Abstract

For years, the modelling of the brain tissue has been widely investigated. Indeed, a biomechanical model of the brain would find applications in fields like image-guided neurosurgery or safety system design (helmets, car manufacturing, security fences design,...).

In the present thesis, we propose an original, fractional calculus-based, constitutive equation of the brain tissue.

Different types of experiments (unconfined compression, relaxation and cyclic tests) were carried out in order to characterize the mechanical behaviour of the brain tissue. The use of the digital image correlation enabled us, for the first time to our best knowledge, to prove the incompressibility of the brain tissue, a widespread assumption.

The constitutive model was calibrated and validated using these experiments. The agreement between the model and the experimental results is very satisfactory. The model reproduces with only a few percent error the stress-strain curves for the compression tests at three different loading rates covering two orders of magnitude as well as the behaviour in the relaxation and cyclic tests.

Keywords: biomechanics, brain tissue modelling, fractional derivative, experimental characterization, digital image correlation, incompressibility.

Résumé

La modélisation du tissu cérébral fait l'objet de nombreuses recherches depuis quelques années. En effet, un modèle biomécanique du cerveau trouverait des applications dans le domaine de la neurochirurgie guidée par l'image et chez les fabricants de système de sécurité (casques, automobiles, barrières de sécurité,...).

Dans cette thèse, nous proposons un modèle d'équation constitutive original pour le tissu cérébral basé sur l'utilisation des dérivées d'ordre réel arbitraire (aussi connues sous le terme de dérivées fractionnaires).

Divers types d'essais (compression, relaxation et essais cycliques) ont également été réalisés afin de caractériser le comportement mécanique du tissu cérébral. L'utilisation de la corrélation d'images numériques a permis, pour la première fois à notre connaissance, de démontrer expérimentalement son incompressibilité, justifiant ainsi une hypothèse couramment rencontrée.

La loi constitutive développée a été calibrée et validée à partir de ces essais. L'accord entre le modèle et les résultats expérimentaux est très satisfaisant en ce qui concerne le comportement en compression à trois vitesse de déformation différentes s'étalant sur deux ordres de grandeur. Il en va de même pour les comportements en relaxation et lors des essais cycliques.

Mots clefs: biomécanique, modélisation du tissu cérébral, dérivation fractionnaire, caractérisation expérimentale, corrélation d'images numériques, incompressibilité.

CONTENTS

LIST OF FIGURES

LIST OF TABLES

Acknowledgments

La rédaction de cette thèse de doctorat est l'occasion pour moi de synthétiser en quelques dizaines de pages le travail effectué pendant 4 années. C'est aussi l'occasion de témoigner ma gratitude à toutes les personnes qui m'ont aidé et soutenu pendant la durée de ma thèse. Il m'est d'ailleurs plus difficile d'écrire ces remerciements, d'abord par peur d'oublier quelqu'un, ensuite parce qu'il est plus ardu de ne prendre que quelques lignes pour souligner tout ce qu'une personne a pu vous apporter pendant plusieurs années. Les mots qui suivent traduisent probablement maladroitement mes pensées, mais sachez, vous à qui ils s'adressent, qu'ils sont sincères.

Je voudrais tout d'abord remercier mon promoteur, Monsieur Serge Cescotto pour m'avoir encadré avec enthousiasme, gentillesse et disponibilité durant ces années de doctorat. Chaque discussion avec lui a été pour moi l'occasion de bénéficier de sa grande expérience. J'ai la faiblesse de croire qu'il m'a témoigné une grande confiance en me laissant totalement libre des mes choix et en ne m'imposant aucune contrainte.

Je remercie ensuite Monsieur Jean-Philippe Ponthot d'avoir accepté d'être membre de mon jury de thèse ainsi que pour ses nombreuses remarques et corrections sur mon travail de D.E.A. qui ont été un moteur pour la suite de mon travail.

Ik dank Mevrouw Liesbet Geris om zo vriendelijk te zijn op het aanbod in te gaan om deel uit te maken van mijn thesisjury. Ook maak ik gebruik van deze gelegenheid om haar succes te wensen in haar nieuwe functie van docent aan de ULg.

Je remercie aussi Mademoiselle Lara Vigneron d'avoir accepté de se replonger pour quelques instant dans le monde universitaire qu'elle a quitté il y a quelques mois après avoir brillamment défendu de sa thèse. J'ai passé avec elle de très bons, et hélas trop brefs, moments dont l'apogée restera sans doute la journée de tournage d'une production Walliwoodienne trop vite oubliée.

Je tiens encore à remercier Monsieur Pierre Robe pour son enthousiasme et l'intérêt qu'il a manifesté pour mon travail, ainsi que pour avoir accepté lui aussi d'être membre du jury. Je remercie son collègue neurochirurgien, Monsieur Didier Martin de m'avoir permis d'assister

à une opération, ce qui m'a permis de remettre mon travail dans un cadre concret quant à son application. Je dois avouer qu'il m'est arrivé de connaître quelques baisses de motivation au long de ces quatre années mais chaque réunion avec Messieurs Robe et/ou Martin me redonnait l'envie de plancher sur le modèle ou peaufiner le protocole expérimental. Les quelques discussions que j'ai eu la chance d'avoir avec eux m'ont conforté dans mon choix de m'être tourné vers l'ingénierie à application médicale.

En regardant un peu plus loin en arrière, je constate que c'est Monsieur David Guiraud qui m'a, le premier, donné l'envie de m'orienter vers cette voie. C'est lors de mon projet de fin d'étude réalisé sous sa supervision à Montpellier qu'il m'a transmis sa grande motivation pour appliquer les techniques de l'ingénierie à des fins médicales. Monsieur Guiraud restera à jamais un modèle pour moi et je lui suis infiniment reconnaissant d'avoir accepté lui aussi de faire partie de mon jury. Je me permets de lui souhaiter le meilleur dans sa vie personnelle et professionnelle, notamment en ce qui concerne le projet DEMAR dont il est le responsable.

Special thanks to Mister Stéphane Bordas for accepting to be a member of the jury. I also thank him for the time he spent answering to me by phone or by email and the interest he showed in my work.

Enfin, je remercie Monsieur Patrick Chabrand d'avoir lui aussi pris de son temps pour faire partie de mon jury de thèse.

Les membres du laboratoire de mécanique des matériaux et structures m'ont été d'une aide précieuse pour la partie expérimentale de mon travail. Je les remercie sincèrement pour leurs encouragements et leur disponibilité. Je suis également reconnaissant à Messieurs Jean-Paul Chéramy et Pierre Drion qui m'ont permis de m'installer dans leur local au C.H.U. de Liège.

De nombreux collègues et amis m'ont fait bénéficier de leur soutien, de leur bonne humeur, de leur expérience et expertise dans des domaines divers. J'adresse donc mes plus chaleureux remerciements à Christophe Mercier, Marlène Mengoni et Léo Studer pour les nombreux temps de midi et autres soirées passés en leur compagnie, où les discussions se sont transformées en bon mots et les bon mots en autres idées. Merci également à mes "gourous" es LaTeX, Alexandre Fournier et Emmanuel Rachelson avec qui je me réjouis d'avoir gardé le contact après mes deux années à Toulouse.

Mes premières années au sein du département ArGEnCo m'ont donné la chance de partager le bureau de Barbara Rossi, qui mériterait 100 fois de gagner le fameux trophée des femmes de cristal. Merci également à Patricia Sepulveda dont le sourire et la bonne humeur ont égayé mes derniers mois de thèse.

J'ai bien entendu eu le plaisir de rencontrer bien d'autres personnes dans les murs de l'université à qui je dois également une pensée: merci donc pêle-mêle à Christophe Henrard, Lam Ly, Sébastien Burton, Patricia Tossings, Frank Wolk, Axel Modave, Romain Boman, Anne-Françoise Gerday, Frédéric Pascon, Renée Schwartz, Séverine Rossomme, Matthieu Delehaye, Boubakar Diouf et Thomas Lelotte. Je garde enfin une place toute particulière pour Jean-Christophe Leyder, l'astrophysicien globe-trotter, qui m'a honoré de son amitié depuis la première candi et Emilie "Caroline" Herwats, ma grande soeur de coeur.

Si une thèse de doctorat s'apparentait à un bâtiment, nul ne pourrait douter de l'importance de ses fondations. Elles sont rarement spectaculaires mais soutiennent la construction depuis le premier jusqu'au dernier jour. Je fais bien sûr référence ici aux personnes dont le soutien m'a été très précieux, qui ont partagé les bons comme les mauvais moments et qui m'ont ainsi permis d'arriver au bout de cette thèse.

Je remercie donc en tout premier lieu mes parents de m'avoir soutenu, réconforté et rendu confiance dans les moments de doutes. Je les remercie aussi d'avoir partagé mes moments d'enthousiasme. Car s'il est dur de se sentir seul quand rien ne va, ce n'est pas non plus évident de ne pas pouvoir communiquer sa joie quand les choses se passent bien. Au dela de leur soutien durant ce doctorat, je voudrais les remercier pour tout ce qu'ils m'ont apporté et pour surtout m'avoir toujours donné une grande liberté dans tous mes choix. Je remercie également ma famille grâce à qui j'ai senti que quoiqu'il arrive, je ne serai jamais seul.

J'ai aussi pu compter sur la solide amitié de longue date de nombreuses personnes, avec qui j'ai passé de merveilleux mais trop rares moments au cours de ces quatres années: Fabienne, François, Laurence, Lauranne, Yseult, Mathieu et Vicky, Brigitte, Lucille, Sophie et Boris.

En parallèle avec la thèse, j'ai débuté le karaté, activité qui m'a apporté énormément de choses positives et de rencontres (bon pour être honnête, ça ma aussi coûté 2-3 fractures, de nombreuses tendinites, une déchirure, de l'arthrose précoce et d'innombrables hématomes, mais bon, je ne vais pas m'attarder sur ces quelques menus détails ici !). Si je ne devais citer qu'un nom, je témoignerais de l'immense gentillesse de Franklin Simain-Sato, mon Maître Wazaaa. Sa disponibilité, sa bonne humeur, sa sagesse et sa bienveillance ont fait de lui le grand frère que j'aurais voulu avoir. Son amitié a, et continuera, de beaucoup compter à mes yeux.

Mais comme je me suis promis de n'oublier personne, je tiens à remercier mes amis du Wado RCAE, du Wado Flémalle et de l'Atémi Visé pour ce qu'ils m'ont apporté sur et en dehors du dojo, dans un ordre qui ne sera pour une fois pas celui des grades, mais bien totalement aléatoire: merci donc à Junior, Laurent, Julien, Catherine, Denis, Ridge, Jean-Luc, Daniel, Philippe, Michel, Marie, Jennifer, Anne-Sophie, Ilgi, Youcha, Joe, Thierry, Sylvain, Sophie, Aurélie, Alain, Phuc et, *last but not least*, Marc.

Enfin, il est une personne qu'il me tient à coeur de remercier à part. Parce que justement c'était une personne exceptionnelle. Il s'agit de ma Mamy, qui nous a malheureusement quitté il y a un peu plus d'un an. Elle qui a pris soin de moi depuis mon plus jeune âge et qui a été comme ma deuxième maman, n'est plus là pour lire ces lignes. Hasard de la vie, la date prévue pour le dépôt de ce document coïncide avec celle de son anniversaire.

Cette thèse lui est dédiée.

Introduction

Motivation

The human brain is a very complex organ from anatomical, functional and material points of view.

As the center of the nervous system, its importance is obvious. Possible internal trauma (such as an internal injury, tumor or hydrocephalus) must therefore be carefully investigated and treated. For this purpose, a complete biomechanical model of the brain can be useful. It would take into account the geometrical complexity of the brain as well as the mechanical properties of its various tissues. The goal of this thesis is to contribute to the knowledge of these mechanical properties.

Two fields of application can be drawn: the neuronavigation and the prediction of traumatic brain injury due to an impact. Both will be discussed in the following subsections. We must pay attention to the fact that the strain rates are very different for each case: neurosurgery deals with much slower strain rates than impact situations. So, we must expect to face major difficulties in designing constitutive laws valid for such a range of strain rates. In the frame of this thesis, the application aimed is the neuronavigation.

Application to neurosurgery

Thanks to the progresses made during the last decades, computer-based medical imaging revolutionized neurosurgery, making it possible for the practitioner to actually see the lesions their patients are suffering from without opening the skull. These imagery protocols include, among others, magnetic resonance imagery (MRI) and positron emission tomography (PET), as shown in Fig. 1.

- The MRI allows the surgeon to distinguish between grey and white matter. It also shows brain structures,
- the MRA (magnetic resonance angiography) gives a map of the blood vessels,
- the DTI (diffusion tensor imaging) is also a MRI technique whose principal application is in the imaging of white matter where location, orientation and anisotropy of the tracts can be measured,

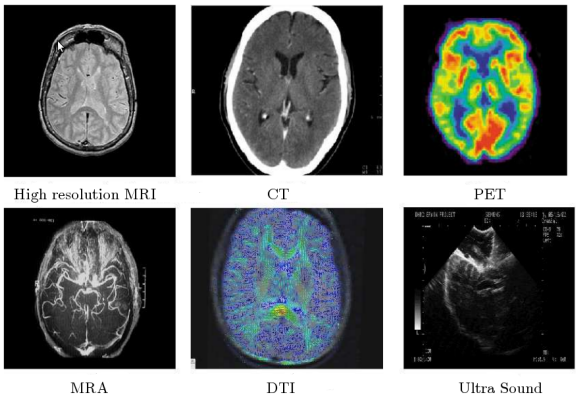

Fig. 1: Different imagery protocols of the brain.

- the CT (computer tomography) is used to evaluate cranial fractures and trauma, to detect increases in intra cranial pressure and intra cranial hemorrhage. It is also used to detect some tumors,

- the PET is used to diagnose tumors and diffuse brain diseases.

The neurosurgeon can rely on these images to plan his intervention. The problem of accuracy is especially important in brain surgery. The brain is a very delicate organ protected by the skull. Thus, the intented craniotomy should be as small as possible to preserve this natural protection. The site of surgical interest (e.g. a tumor to be resected) may not be located at the brain surface but instead under some sane tissues. Nowadays, the precise knowledge of the lesion boundaries allows the neurosurgeon for resections of tumors that were often considered to be inoperable some years ago. It also permits the surgeon to perform a more complete resection.

Although these computer-based imaging techniques seem compelling, it must be stressed that they only produce pictures. Without a suitable reference frame in the operating room by which one could register the image space with the physical space, a neuronavigation system will not allow the surgeon to monitor in real time the location of his instruments in the patient's head. Thus, the current neuronavigation system using optical digitizers combines landmarks in the operating room with the preoperative images. The real time localization is achieved by an opto-electronic system consisting of light-emitting diodes (LED) and CCD cameras that detect their positions. Infrared light is preferably chosen due to its maximal accuracy, decreased sensitivity to ambient light and minimal emitter size. The computation of the 3D position is done by triangulation.

As stated, the problem of accuracy is very important in brain surgery. It is obviously neither desirable that sane tissues be removed or damaged during the process nor that the tumor be incompletely resected. The major issue with the current neuronavigation systems is that they are based on preoperative images that become obsolete as soon as the surgeon performs the craniotomy. Indeed, a displacement of the order of 1 centimetres occurs when the skull is opened. This phenomenon, known as the *brain shift* is illustrated in Fig. 2.

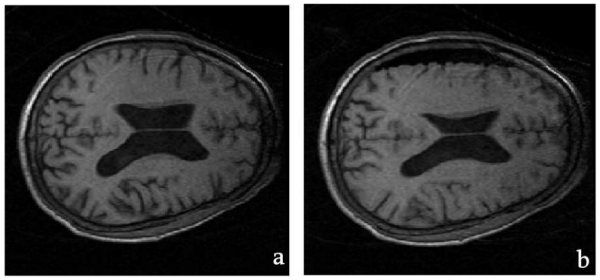

Fig. 2: Illustration of the brain shift: the brain before (a) and after (b) the opening of the skull.

As the intervention takes place, the brain deforms more and more, due to the resection, the pressure exerted by the retractors and others surgical deeds. So, the available images become less and less accurate in the course of time as they no longer reflect the actual situation.

To overcome this problem, new images have to be taken during the operation. It is obviously difficult to move the patient in the PET scan or MRI room, so the scanner has to be brought into the operating room. Then, not all protocols shown in Fig. 1 are available because of the size of the machines. The only possibilities are ultrasound, CT and low field MRI[1] whose image quality is quite poor (Fig. 3).

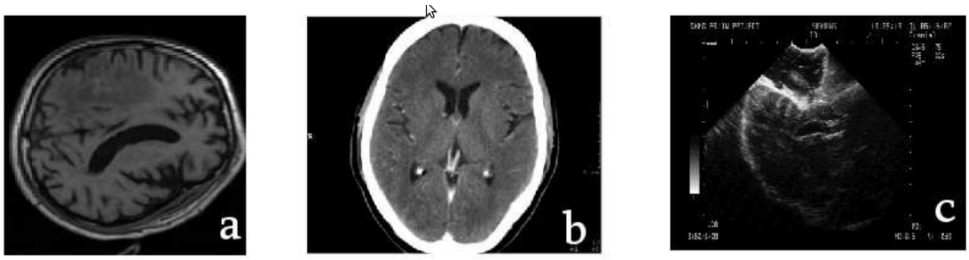

Fig. 3: Interventional imaging: 0.5 Tesla MRI (a), CT (b) and US (c).

Because of this lower quality, the interpretation of the images is very difficult. The surgeon is then left with high quality but outdated and updated but low quality images. The solution would be to merge the data from both sources to obtain sufficiently accurate updated images. This kind of processing is achievable by using a *non rigid registration (NRR)* algorithm. Unlike rigid registration which only uses translations, rotations and scaling to align images into a standard coordinate system, NRR also deals with deformations. To simplify, the idea is basically to perform a non rigid registration of the updated and the preoperative images, to determine the deformation of a part of the brain and then to compute the stresses and the strains and deformations for the whole brain with the help of a biomechanical model. So, suitable constitutive laws are needed in order to design this model.

[1] Traditional structural MRI are performed on 1.5 Tesla (or more) scanners. The expression *low field* refers to $0.5T$ (or less) scanners.

Another application can be imagined involving the design of haptic devices. The term "haptics" refers to the modality of touch and associated sensory feedback. A (well known ?) example is the force feedback wheel used for formula one video games. The basic principle of this technology is quite simple : a robot arm (also called a *stylus*) is connected to a computer. If the user is far away from all the virtual objects displayed on the screen, a zero voltage is sent to the motors of the arm and its move is completely free, as if the user was exploring an empty space. On the other hand, if the system detects a virtual collision between the stylus and an object, it drives the motor so as to exert a force along the exterior normal to the surface being penetrated. The user is then prevented from penetrating the virtual object just as if the stylus collided with a real object. In neurosurgery, this technology could be applied to train the practitioners before the actual intervention. The finite element (FE) model of the brain would then be used to compute the reaction force to transmit to the user following a particular deformation.

Application to trauma prediction

A traumatic brain injury (TBI) is caused by an impact on the head, for example in a traffic accident. A TBI occurs when the local mechanical load exerted on the brain tissue exceeds a given tolerance level.

In order to improve injury protection devices and diagnostic methods, it is imperative to understand how an external mechanical load on the head is transmitted locally to the brain and thus determine the resulting stresses, strains and possible damages.

Such a model would be useful to car designers, who could then evaluate the possible trauma due to an impact. Helmet manufacturers and safety fences designers could be interested as well.

Outline of the thesis

The present document is divided into four parts.

The first part is devoted to the presentation of some tools and concepts that will be extensively used in the rest of the thesis. They are related to the various domains that are mechanics of material, image processing, fractional calculus and neuroanatomy. This first part is intented to provide the reader with the basis to fully understand the rest of the document. Another domain of application is that of sports (boxing,...)

A few elements of neuroanatomy, describing the brain tissue from the cell scale to the macroscopic scale are given in chapter 1.

The digital image correlation is exposed in chapter 2. This optical method, relying on the use of stereoscopic systems of cameras, allows one to compute the displacement and strain fields of a sample. The basic notions of the method, i.e. the calibration of the cameras and the surface reconstruction, are presented. To work properly, this method requires a speckle pattern to be painted on the surface of the analysed sample. The importance of this pattern is underlined.

Chapter 3 presents the notions of constitutive equations for brain modelling. After recalling the general basis about constitutive equations, the different laws used to model the brain tissue are presented, i.e. hyperelastic, poroelastic and viscoelastic laws.

In chapter 4, the notion of fractional derivative is presented. We do not expect the reader to have any previous knowledge of this particular topics, therefore some points are widely developped, like the relationship between the integer order and fractional derivatives. The basic properties are given without demonstration, just to be compared with the better known properties of classical derivatives. We also introduce some analytical and numerical methods of resolution of fractional differential equations.

The second and shortest part present a literature review of the state of the art in brain tissue modelling and experimental characterization.

In the third part, the experimental work on the characterization of the brain tissue is exposed.

Chapter 6 details the experimental protocol designed to enable the use of the digital image correlation for the measurement of the displacements. The application of the speckle pattern on the brain tissue samples and the related challenges are widely detailed. Chapter 7 presents the results obtained for the tests performed, i.e. unconfined compression tests at different loading rate, relaxation tests and cyclic tests. The stress-strain curves obtained with the use of the digital image correlation are compared with the stress-strain curves obtained by using only the outputs of the testing machine. The evolution of the volume ratio during the experiments is also investigated, leading to the experimental proof of the incompressibility of brain tissue. The influence of the imperfection of the initial contact between the superior surface of the sample and the plate of the testing machine is also underlined throughout this chapter. Chapter 8 summarizes and discusses the obtained experimental results.

Finally, the fourth part is devoted to the numerical modelling.

Chapter 9 presents the developments that yield to an original, fractional calculus-based constitutive model of the brain tissue. The result of calibration and the validation of this model using the experimental data presented in part three is exposed in chapter 10. At last, chapter 11 summarizes and discusses the obtained numerical results.

A general conclusion ends this document.

Original contributions

The present thesis contains, to the best knowledge of the author, several original contributions:

- the use of the D.I.C. to measure the displacements that occured in brain tissue samples during compression, relaxation and cyclic experiments,
- the investigation of the volume ratio of the sample during these experiments that led to the experimental proof of the incompressibility of the brain tissue,
- the design of a constitutive law for brain tissue based on fractional derivatives,
- the calibration of this model using unconfined compression tests at three loading rates spreading over two order of magnitude,
- the validation of this model using cyclic and relaxation tests.

Part I

Tools

CHAPTER 1

ELEMENTS OF NEUROANATOMY

1.1 Introduction

The objective of this chapter is to provide the reader with a very basic knowledge in neuroanatomy in order to associate the macroscopic mechanical properties of the brain with its microscopic structure. The geometrical and material points of view are emphasised. The cerebral topography will be briefly discussed, but the distinction between the telencephalon, diencephalon, forebrain, midbrain, ... is omitted. The term "brain" used in this document stands for the cerebrum, i.e. the portion of the central nervous system consisting of two lateral hemispheres joined by a thick band of fibers. It then excludes the cerebellum and the brain stem (see Fig. 1.1).

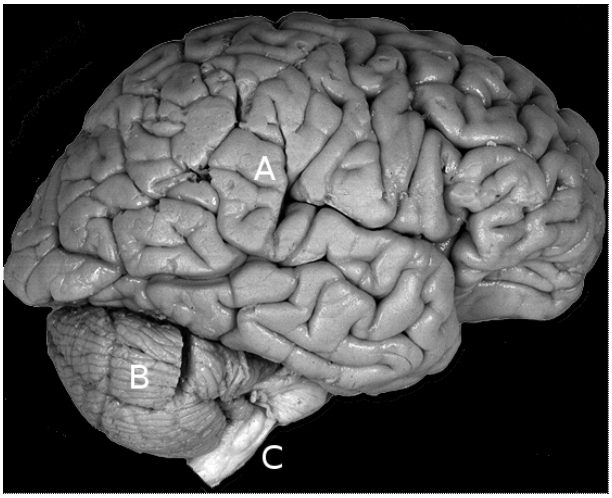

Fig. 1.1: Human cerebrum (A), cerebellum (B) and brain stem (C).
(Credits: digital anatomist project, http://www9.biostr.washington.edu)

The approach we chose is to describe first the anatomy and the composition of the brain cells, the neurons and the neuroglia. Then, their spatial organization is explained, from which

macroscopic mechanical properties are deduced. Finally, the meninges and other membranes are presented and the macroscopic description of the brain geometry is given.

1.2 Neurons and neuroglia

1.2.1 Neurons

The neurons, or nerve cells, are the functional and structural units of the nervous system. Billions of neurons are found in the brain, forming a shell, the *cortex*, at its surface. Fig. 1.2 pictures the schematic representation of a neuron. It roughly consists of two parts: the cell body or *soma* and the *axon*. The soma has multiple poles from which emerges a dendrite and each dendrite divides repeatedly. The axon is connected to the soma and is longer than the dendrites. Its role is to conduct the electrical impulses away from the soma and it is insulated by a sheath of myelin. The axon diameter is of the order of 1 micrometer while the diameter of the soma can vary from 5 to 100 micrometers.

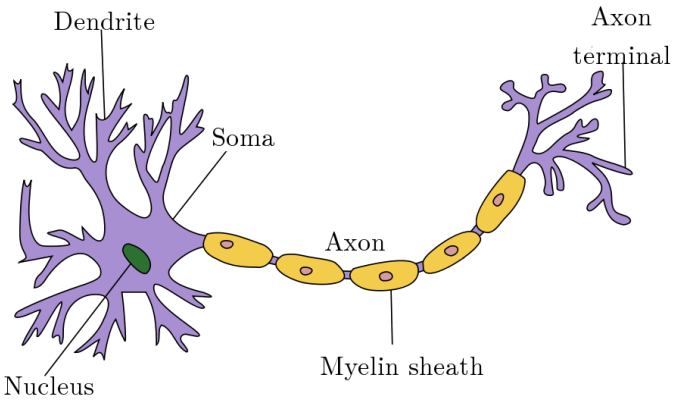

Fig. 1.2: Schematic representation of a neuron. (Credits: http://en.wikipedia.org)

The neurons are mainly composed of water ($\simeq$ 78%) and lipids and proteins (resp. 10% and 8%).

1.2.2 Neuroglia

The neuroglia constitutes the connective tissue of the nervous system. The neuroglia cells are approximatively ten times more numerous than the neurons. They have both supportive and nutritive functions.

Four different types of neuroglia cells are found in the brain. Let's just mention them without entering into the details. The *astrocytes* present a certain degree of rigidity and a spatial organization that make them support the brain as a whole while the *oligodendrocytes* wrap myelin sheaths around the axons. The *ependymal* cells are found in the ventricles (see section 1.5) where they participate in the circulation of the cerebrospinal fluid. The *microglia* have no supportive function but are rather involved in the immunological process.

1.3 Grey and white matters

The grey[1] matter is found at the surface of the brain (in the cortex) and it also forms particular structures within the white matter (e.g. the thalamus and the putamen,...) as shown in Fig. 1.3. It is composed of the astrocytes, oligodendrocytes and the somas of the neurons. Their orientation within the brain is random, so, from a mechanical point of view, an isotropic behaviour is expected from the grey matter.

The white[2] matter forms the internal mass of the brain and is made of bundles of myelinated axons forming fibers. These fibers can be classified into three groups: the association fibers, the commisural fibers and the projection fibers. The direction of the fibers can be determined by diffusion tensor imaging, a magnetic resonance protocol. Fig. 1.4 presents a diffusion tensor image. The color is representative of the direction of the fibers. Local preferred directions are thus easily identified. This leads to the conclusion that, from a mechanical point of view, the white matter is anisotropic.

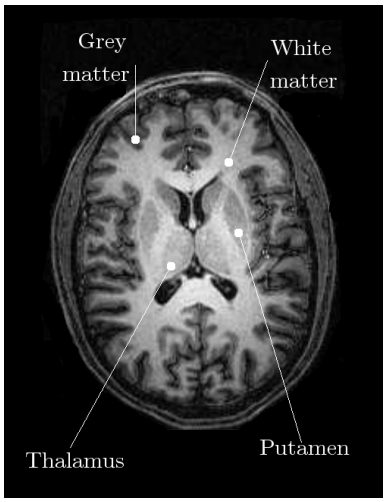

Fig. 1.3: Illustration of the repartition of the white and grey matters within the brain.

According to Miller et al. (1980), the volume ratio of grey matter to white matter changes with age and is equal to 1.3 for 20 years old subjects and 1.1 for 50 years old subjects.

1.4 Meninges

The meninges (Fig. 1.5) surround the brain and are composed of three layers: *the dura mater*, *the arachnoid* and *the pia mater*. Between the arachnoid and the pia is found *the subarachnoid space* which is filled with the *cerebrospinal fluid*. The major role of the meninges is to protect the brain.

The dura mater is the outermost layer and sticks to the skull. It is a few millimeters thick and partially erases some of the small asperities of the skull interior wall. It contains venous

[1] The grey matter appears pinkish to the naked eye.
[2] It appears white to the naked eye because the myelin is mainly composed of lipids.

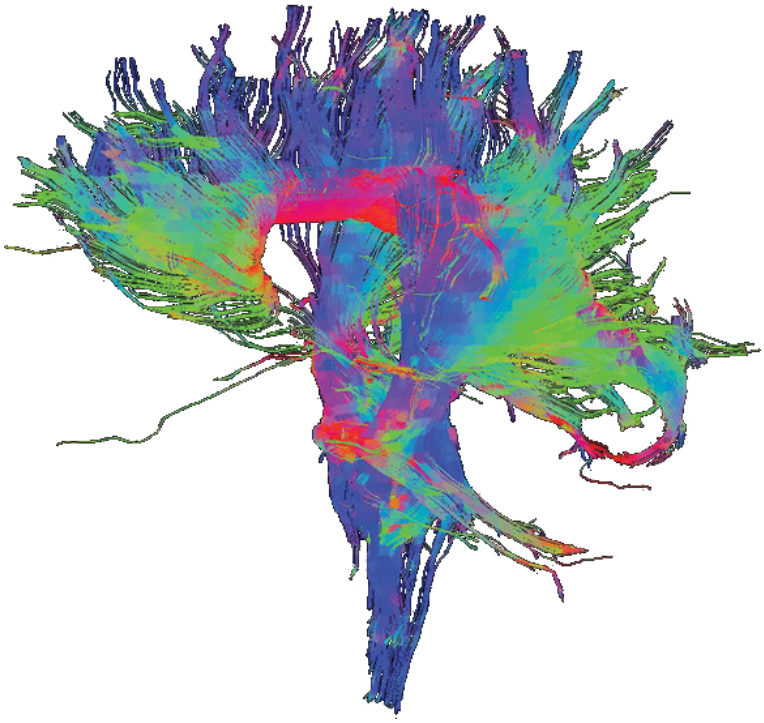

Fig. 1.4: Diffusion tensor image example. (Credits: http://illumination.missouri.edu)

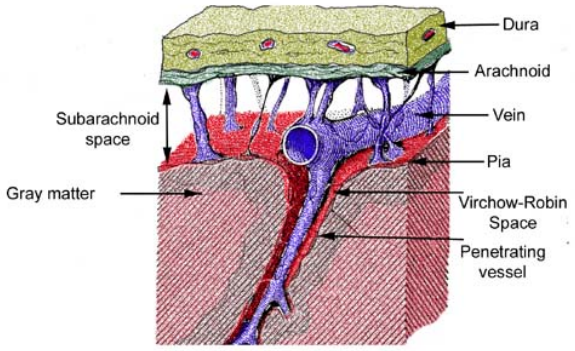

Fig. 1.5: Schematic representation of the meninges. (Credits: http://www.sbtruth.com)

sinuses and gives birth to *the falx cerebri*, which separates the two hemispheres, and to *the tentorium cerebelli* which acts as a tent separating the cerebrum from the cerebellum.

The arachnoid is a 10 micrometers thick membrane. It can slide on the dura mater.

The pia mater is the innermost and thinnest of the meninges: its thickness is of the order of the cell size (a few micrometers). It follows closely the contours of the brain and acts as a bag, keeping the whole volume together.

Finally, the subarachnoid space is a trabecular structure made of interwoven fibers. It can be considered as an anisotropic porous medium filled with cerebrospinal fluid. Its thickness is of the order of a few millimeters.

The interactions of the membranes with each other and the brain should be taken into account when studying the mechanical behaviour of the late.

1.5 Ventricular system and cerebrospinal fluid

The ventricular system comprises four ventricles, interconnected by several channels. The two lateral ventricles, located in the cerebrum, are relatively large and C-shaped. The third and fourth ventricles are located between the two "C branches" and underneath the lateral ventricles respectively. The ventricles are pictured in Fig. 1.6.

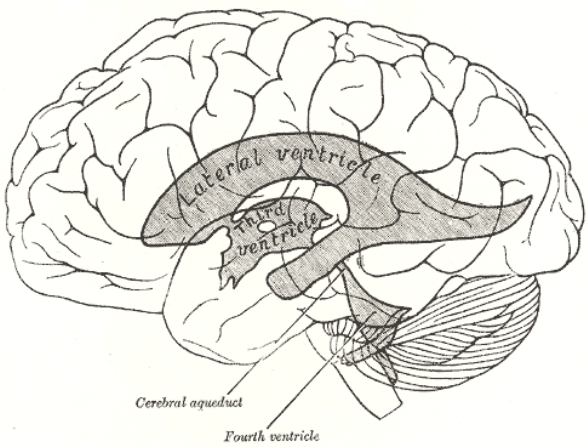

Fig. 1.6: The ventricular system. (Credits: http://en.wikipedia.org)

The ventricles produce the cerebrospinal fluid (CSF) which flows through the subarachnoid space. The volume of CSF in the brain is equal to 125 ml and 500 ml are produced each day resulting in a turnover of the entire volume of CSF equals to 4 times per day.

The CSF acts as a shock damper for the brain. Its influence is essential in all the mechanical processes that can be modelled, from impact situations to hydrocephalus[3].

1.6 Arteries and veins.

Numerous arteries and veins lie in the brain as shown by a magnetic resonance angiography (Fig. 1.7). Those blood vessels probably contribute to the mechanical strength of the brain.

[3]Medical condition resulting in the accumulation of CSF in the ventricles.

When studying the effects of traumatic brain injuries, it is important to model those blood vessels to be able to predict oedemas and hemorrhages through a suitable rupture criterion.

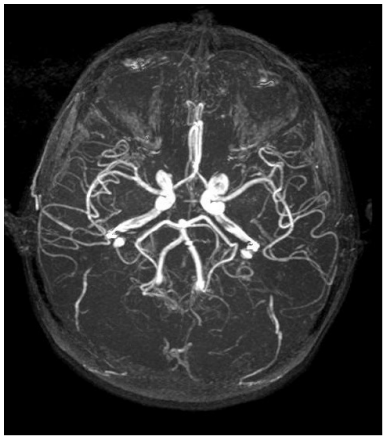

Fig. 1.7: Blood vessels of the brain highlighted by a magnetic resonance angiography. (Credits: http://www.imaginggroupde.com)

1.7 Conclusion

As pictured in Fig. 1.1, the brain presents a succession of swellings and fissures [4] that wander through the surface and give it a wrinkled appearance. Fig. 1.8 presents a lateral cut of the brain, and clearly shows its heterogeneous composition.

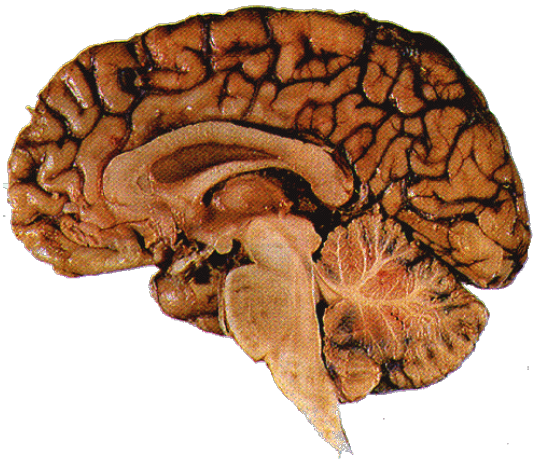

Fig. 1.8: Lateral cut of the brain. (Credits: http://lbc.nihm.gov)

The brain should then be considered as an heterogeneous, partially anisotropic (white matter) medium which comprises a blood and a cerebrospinal fluid circulations. The meninges

[4] Called *gyri* and *sulci*.

add both a geometrical and a mechanical complexities to the modelling of this organ. Not to mention that both the cerebellum and brain stem are excluded of the present work.

The modelling of the brain is thus a challenge and the description of its mechanical behaviour through suitable constitutive laws requires simplifying assumptions.

More details about the anatomy of the brain can be found in the following references: Chusid (1996), Fitzgerald (1995) and Libmann (1991)

CHAPTER 2
DIGITAL IMAGE CORRELATION

2.1 Introduction

This short chapter is devoted to a small overview of the digital image correlation (D.I.C.) technique. To fix the ideas, and without loss of generality, we describe the application of D.I.C. to our particular topic, the surface reconstruction of a brain sample undergoing a compression test. We consider in this chapter only one stereoscopic system composed of two cameras located on the same support. It is assumed that the left camera is the master, i.e. all the coordinate transforms will express the relevant quantities in the reference frame of the left camera.

The D.I.C. is an optical method for the determination of the displacements and strains. The stereoscopic system records the experiment and reconstruct the 3D surface of the sample for each pair of images. Basically, the surface reconstruction of a sample consists in the matching of particular features in the images acquired by both cameras followed by the determination of the disparity map. The disparity map is used for the determination of the 3D coordinates of the sample thanks to a rigid transformation whose parameters are determined by a previous operation, called *calibration*, described in the following section. Each pixel is tracked from one image to the other to allow the computation of the displacements and thus the strains that occur in the sample. Let's recall that a digital picture can be seen as a matrix whose elements represent the intensity of the grey level of the associated pixel. Conventionally, the 0 stands for black and 255 for white.

This chapter constitutes only a small introduction to the digital image correlation. The calibration of the simplest model of camera is described, then the reconstruction and tracking phases are briefly presented. The last section underlines the importance of the preparation of the sample by the application of a suitable speckle pattern.

2.2 Calibration

2.2.1 Definition

The calibration of a camera can be defined as the process of determining its intrinsic and extrinsic parameters such as its focal length or its orientation with respect to the sample (see

). This is achieved by linking the coordinates of a test pattern (Fig. 2.1) expressed in its own coordinate system $\mathcal{R}_\mathcal{M}$ and a coordinate system bound to the image $\mathcal{R}_\mathcal{I}$. It is the knowledge of those parameters that will allow the 3D reconstruction of the sample from N (N $\geq$ 2) pictures taken by N cameras.

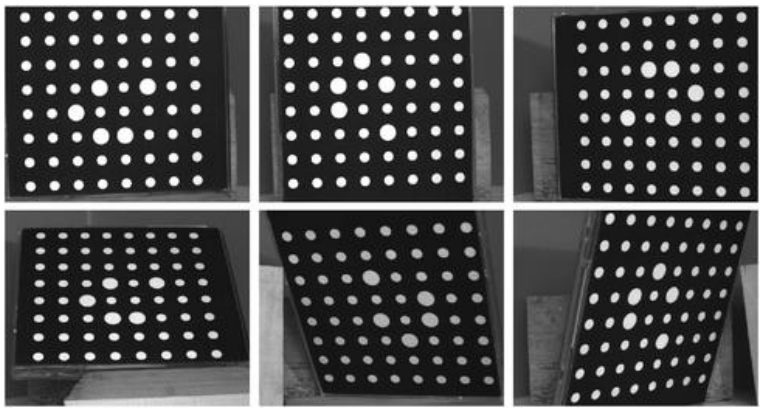

Fig. 2.1: Example of test pattern.

Notations

In this chapter, the following notations will be adopted:

(X, Y, Z)	the coordinates of a point P of the 3D space expressed in $\mathcal{R}_\mathcal{M}$ (generally expressed in millimetres).
(x, y, z)	the coordinates of the same point in the camera coordinate system $\mathcal{R}_\mathcal{C}$ (generally expressed in millimetres).
$(\tilde{x}, \tilde{y}, \tilde{z})$	the coordinates of p, projection of P on the image plane, expressed in $\mathcal{R}_\mathcal{C}$ (generally expressed in millimetres).
(u, v)	the coordinates of p expressed in $\mathcal{R}_\mathcal{I}$ (expressed in pixels).

2.2.2 Modelling of a camera

Let's consider the so-called pinhole model of a camera, in which the objective is considered punctual, represented in Fig. 2.2.

Point C, the origin of the camera coordinate system, is called the center of projection. The principal point O is the intersection of the image plane with the optical axis. The distance between C and O is the focal length f. The coordinates of point P in $\mathcal{R}_\mathcal{C}$ are (x, y, z). Its projection on the image plane is p, the coordinate of which are (u, v) in $\mathcal{R}_\mathcal{I}$.
The objective of the calibration is to find the relationship between the coordinates (X, Y, Z) of P in $\mathcal{R}_\mathcal{M}$ and the coordinates of p in $\mathcal{R}_\mathcal{I}$.

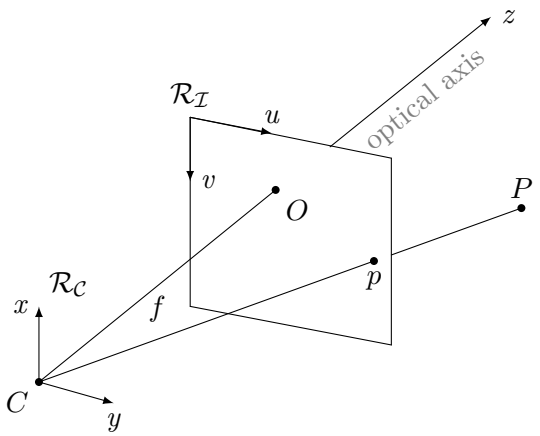

Fig. 2.2: Pinhole model of a camera

2.2.3 Calibration

The coordinates of p are expressed in $\mathcal{R}_\mathcal{C}$ by the formulae:

$$\tilde{x} = \frac{f\,x}{z} \tag{2.1}$$

$$\tilde{y} = \frac{f\,y}{z} \tag{2.2}$$

$$\tilde{z} = f \tag{2.3}$$

This transformation can be represented by the matrix

$$\mathbf{P} = \begin{pmatrix} 1 & 0 & 0 & 0 \\ 0 & 1 & 0 & 0 \\ 0 & 0 & 1 & 0 \\ 0 & 0 & \frac{1}{f} & 0 \end{pmatrix} \tag{2.4}$$

so that

$$\begin{pmatrix} s\tilde{x} \\ s\tilde{y} \\ s\tilde{z} \\ s \end{pmatrix} = \mathbf{P} \begin{pmatrix} x \\ y \\ z \\ 1 \end{pmatrix} \tag{2.5}$$

if the homogeneous coordinates[1] are used.

The coordinate transformation from $\mathcal{R}_\mathcal{C}$ to $\mathcal{R}_\mathcal{I}$ requires, in general, a translation, a rotation and a scaling. Since, by convention, the pixels are counted positively downwards (see Fig. 2.2), the rotation matrix is written:

$$\mathbf{R} = \begin{pmatrix} -1 & 0 & 0 \\ 0 & 1 & 0 \\ 0 & 0 & -1 \end{pmatrix} \tag{2.6}$$

[1]The homogeneous coordinates are used to make calculations in projective space just as the Cartesian coordinates do in the Euclidian space.

and the scaling matrix is written:

$$\mathbf{S} = \begin{pmatrix} k_u & 0 & 0 \\ 0 & k_v & 0 \\ 0 & 0 & 0 \end{pmatrix} \tag{2.7}$$

where k_u and k_v stand for the vertical and horizontal scaling factors. They are expressed in pixels per unit length (generally the millimetre).

Finally, the translation is represented by the vector $\mathbf{t}$

$$\mathbf{t} = \begin{pmatrix} u_0 \\ v_0 \\ w_0 \end{pmatrix} \tag{2.8}$$

the components of which are the coordinates of the principal point. The coordinates transformation finally writes:

$$\begin{pmatrix} u \\ v \\ w \end{pmatrix} = \mathbf{SR} \begin{pmatrix} \tilde{x} \\ \tilde{y} \\ \tilde{z} \end{pmatrix} + \mathbf{t} \tag{2.9}$$

However, it is obvious that the coordinate w is always null for a point in the image. Nevertheless, the third coordinate was kept in order to facilitate the change towards the homogeneous coordinates. Using them, the transformation can be represented by the matrix $\mathbf{K}$

$$\mathbf{K} = \begin{pmatrix} -k_u & 0 & 0 & u_0 \\ 0 & k_v & 0 & v_0 \\ 0 & 0 & 0 & 1 \end{pmatrix} \tag{2.10}$$

so that

$$\begin{pmatrix} u \\ v \\ 1 \end{pmatrix} = \mathbf{K} \begin{pmatrix} \tilde{x} \\ \tilde{y} \\ \tilde{z} \\ 1 \end{pmatrix} \tag{2.11}$$

The change of coordinates from system $\mathcal{R}_\mathcal{C}$ to system $\mathcal{R}_\mathcal{I}$ is achieved by matrix $\mathbf{H}$, combining the projection and the change of coordinates

$$\mathbf{H} = \mathbf{KP} \tag{2.12}$$

$$= \begin{pmatrix} -k_u & 0 & \frac{u_0}{f} & 0 \\ 0 & k_v & \frac{v_0}{f} & 0 \\ 0 & 0 & \frac{1}{f} & 0 \end{pmatrix} \tag{2.13}$$

Since the homogeneous coordinates are defined up to a constant, we can multiply matrix $\mathbf{H}$ defined by Eqn. 2.13 by the focal length f to finally obtain

$$\mathbf{H} = \begin{pmatrix} \alpha_u & 0 & u_0 & 0 \\ 0 & \alpha_v & v_0 & 0 \\ 0 & 0 & 1 & 0 \end{pmatrix} \tag{2.14}$$

with

$$\begin{pmatrix} su \\ sv \\ s \end{pmatrix} = \mathbf{H} \begin{pmatrix} x \\ y \\ z \\ 1 \end{pmatrix} \tag{2.15}$$

The four parameters in the matrix $\mathbf{H}$ are called *the intrinsic parameters*.

The change of coordinates system from $\mathcal{R}_\mathcal{M}$ to $\mathcal{R}_\mathcal{C}$ is achieved by applying a rotation and a translation. The corresponding matrix writes:

$$\mathbf{A} = \begin{pmatrix} r_{11} & r_{12} & r_{13} & t_x \\ r_{21} & r_{22} & r_{23} & t_y \\ r_{31} & r_{32} & r_{33} & t_z \\ 0 & 0 & 0 & 1 \end{pmatrix} \tag{2.16}$$

with

$$\begin{pmatrix} x \\ y \\ z \\ 1 \end{pmatrix} = \mathbf{A} \begin{pmatrix} X \\ Y \\ Z \\ 1 \end{pmatrix} \tag{2.17}$$

Finally, the relationship between the coordinates (u, v) and (X, Y, Z) is described by the matrix equation

$$\begin{pmatrix} su \\ sv \\ s \end{pmatrix} = \begin{pmatrix} m_{11} & m_{12} & m_{13} & m_{14} \\ m_{21} & m_{22} & m_{23} & m_{24} \\ m_{31} & m_{32} & m_{33} & m_{34} \end{pmatrix} \begin{pmatrix} X \\ Y \\ Z \\ 1 \end{pmatrix} \tag{2.18}$$

where the m_{ij} define the matrix $\mathbf{M} = \mathbf{HA}$. Eqn. 2.18 can alternatively be written in a vectorial form

$$\mathbf{u} = \mathbf{MX} \tag{2.19}$$

One can either determine the components of $\mathbf{A}$ and $\mathbf{H}$ separately (for example, if the intrinsic parameters are needed) or directly determine the components of $\mathbf{M}$.

The pinhole model described here and the associated calibration are the simplest: they do not account for the distortion of the lenses and they assume the perfect orthogonality of the u and v axes. More details can be found in Horaud and Monga (1995).

For a stereoscopic system, the location and orientation of one camera with respect to the other must also be computed in order to reconstruct the sample in three dimensions.

2.3 Surface reconstruction and point tracking

The determination of the 3D coordinates basically consists in the resolution of Eqn. 2.19, i.e., to find

$$\mathbf{X} = \mathbf{M}^{-1}\mathbf{u} \tag{2.20}$$

The vector equation 2.20 is equivalent to two scalar equations, which is not enough to determine the three unknowns. But since we use a stereoscopic system constituted of two cameras, the same relationship can be written for the other camera

$$\mathbf{X} = \mathbf{M'}^{-1}\mathbf{u'} \tag{2.21}$$

The resolution of this system of four scalar equations gives the Cartesian coordinates of the sample in $\mathcal{R}_\mathcal{M}$.

This process requires the matching of the pixels from both left and right pictures. The epipolar constraint (presented in the next section) ensures that the pixel in the right picture corresponding to the considered pixel in the left picture is located on a line, called the epipolar line. It thus saves the algorithm from searching a matching point in the entire image, dramatically reducing the computational time.

2.3.1 Epipolar constraint

Let's consider the schematic representation of a stereoscopic system depicted in Fig. 2.3. p_L is the projection of point P in the left picture. Its correspondent in the right picture is p_R.

If we consider only the left image, p_L can be the projection of any point on the line C_LP, such as Q or R whose projections in the right image are q and r. It can be seen that they are on the same line as p_R, which is obvious since the projection of a straight line remains a straight line[2]. Therefore, the correspondent of a pixel in the left image is located on a line, called an *epipolar* line in the right image. This epipolar line is simply the projection of C_LP. The point E_R, called the *epipole* of the right image, is the projection of C_L. All the epipolar lines of an image concur to the epipole. In the particular case of parallel cameras with their centres of projection parallel to the horizontal axis, the epipolar lines are horizontal. It is always possible to compute a rigid transformation, called *the rectification*, to retrieve this particular configuration. The search for a matching point in $\mathcal{R}_\mathcal{I}$ is then significantly simplified for it has now the same ordinate v.

The equations of the epipolar lines can be determined once the stereoscopic system has been calibrated.

2.3.2 Correlation

Let's assume that we work with a pair of rectified images. How can we now associate a pixel in the left image with its correspondent in the right image ?

The first step is to determine the most probable candidate. This is achieved by optimizing, for each pixel in the left image, the following correlation coefficient:

$$c^c_{i,j}(d) = -\frac{\sum_{k,l}\left(\left(I_L(i+k,j+l)-\bar{I}_L(i,j)\right)-\left(I_R(i+d+k,j+l)-\bar{I}_R(i,j)\right)\right)^2}{\sqrt{\sum_{k,l}\left(I_L(i+k,j+l)-\bar{I}_L(i,j)\right)^2}\sqrt{\sum_{k,l}\left(I_R(i+d+k,j+l)-\bar{I}_R(i,j)\right)^2}} \tag{2.22}$$

where I represents the intensity (or the grey level) of the considered pixel and $\bar{I}$ its mean value, (i,j) are the coordinates (in $\mathcal{R}_\mathcal{I}$) of the considered pixel, $k \in [-w,w]$, $l \in [-h,h]$ with

[2]Or a point in a pathological case.

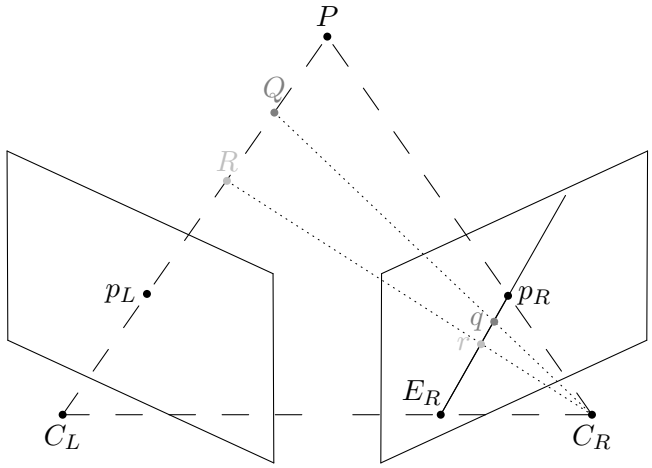

Fig. 2.3: Illustration of an epipolar line and the epipolar constraint.

$2w+1$ and $2h+1$ the width and height of a window centered on (i, j). Fig. 2.4 illustrates this correlation window. The disparity d is the difference of abscissa of the pixel in the right and left images.

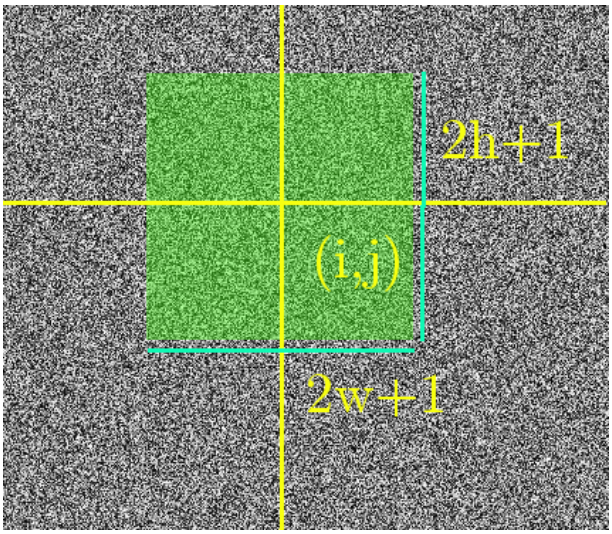

Fig. 2.4: Correlation window.

The correlation coefficient is computed for each possible disparity in the right image. The pixel in the right image with the highest correlation value is kept as the matching candidate[3].

It is then possible to compute the 3D coordinates by solving the system defined by Eqn. 2.20 and Eqn. 2.21.

[3]Other constraints (order, uniqueness,...) are also defined to reject possible bad correspondences.

2.3.3 Tracking

The reconstruction process described here above is valid for one pair of images. To obtain a displacement and a strain map, the algorithm must be able to track each point, i.e., to recognize it from one image of the video flow to the other. Like for the reconstruction phase, this is achieved by the maximization of a correlation coefficient:

$$c^t_{i,j} = -\frac{\sum_{k,l}\left(\left(I(i+k,j+l)-\bar{I}(i,j)\right)-\left(I^*(i^*+k,j^*+l)-\bar{I}^*(i^*,j^*)\right)\right)^2}{\sqrt{\sum_{k,l}\left(I(i+k,j+l)-\bar{I}(i,j)\right)^2}\sqrt{\sum_{k,l}\left(I^*(i^*+k,j^*+l)-\bar{I}^*(i^*,j^*)\right)^2}} \tag{2.23}$$

where $I(i,j)$ stands for the intensity of the pixel (i,j) in the undeformed image, $\bar{I}(i,j)$ for its mean value and $I^*(i^*,j^*)$ represents the intensity of the corresponding pixel now located at (i^*,j^*) in the deformed image.

2.4 Importance of the speckle pattern

The reconstruction and tracking algorithms of the digital image correlation technique are both based on the intensity of the pixels. This underlines the importance of the quality of the speckle pattern applied. In the best case, each pixel would have a unique, distinguishable neighbourhood. Several factors can influence the quality of the pattern and thus of the reconstruction.

Fig. 2.5 shows three examples of pattern. Pattern (a) is very good, as it presents a visually good contrast leading to a unique neighbourhood for each pixel. The contrast of pattern (b) is very poor. Therefore, the correlation coefficient will be almost constant along an epipolar line, making the matching (and the tracking) very difficult. Finally, pattern (c) present an alternance of white and black pixels[4]. Therefore, it is not possible to distinguish between one black pixel from another. The correlation would also fail in this case, despite the excellent contrast of the pattern since each black (resp. white) pixel has the same neighbourhood.

A good speckle pattern has then to be fine, contrasted and random.

The window size (shown in Fig. 2.4) is also an essential factor for a good correlation. Smaller sizes give more details but greater sizes prevent errors. The characteristic size of the spots constituting the pattern must also be taken into account, as shown in Fig. 2.6.

If the window is smaller than the spots, the correlation will not produce good results since there are a lot of points with the same value for the correlation coefficient.

Fig. 2.5(a) shows what a good speckle pattern is. Unfortunately, it is more difficult to obtain on a real-life situation than on a synthetic image.

2.5 Example

To illustrate the concept of disparity map, an example is given for a pair of synthetic images in Fig. 2.7. The closer the object, the higher the value of the disparity between the left and right pictures. The value of the disparity is translated into a grey level for each pixel leading to a picture.

[4]The image was zoomed in order to distinguish the pixels.

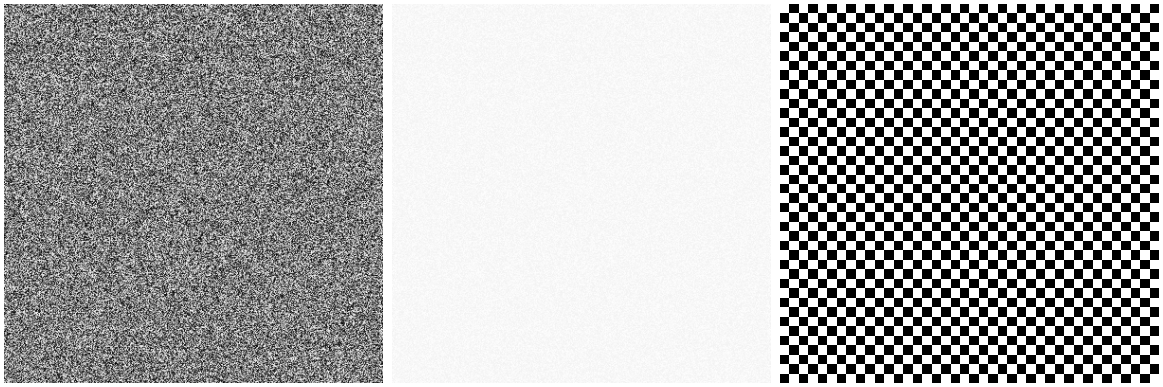

(a) (b) (c)

Fig. 2.5: Examples of speckle patterns: (a) good pattern, random and with a high contrast, (b) random pattern with poor contrast and (c) pattern with a perfect contrast but no randomness.

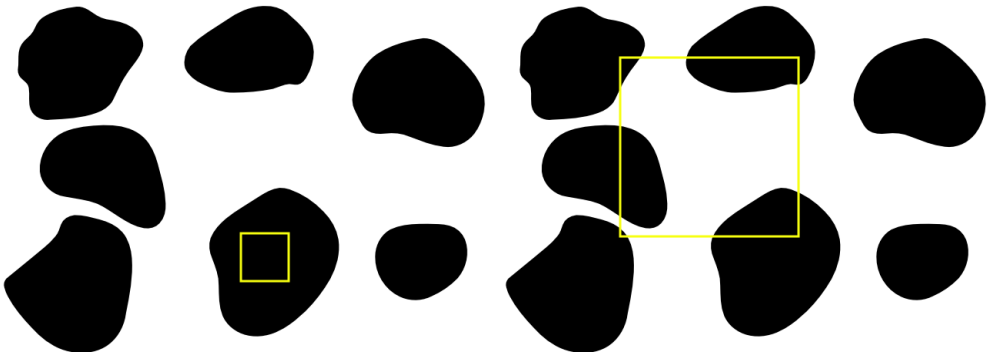

(a) Bad size of the correlation window. (b) Better size of the correlation window.

Fig. 2.6: Importance of the correlation window with respect to the spots size.

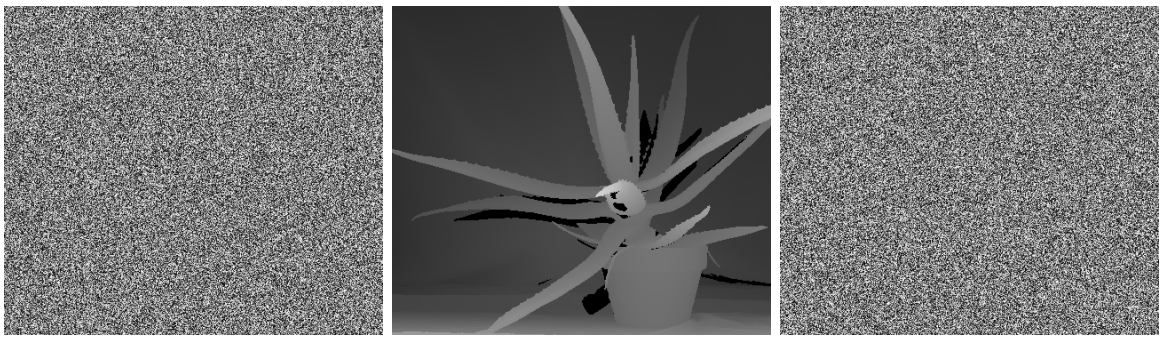

(a) Left picture. (b) Disparity map. (c) Right picture.

Fig. 2.7: Example of disparity map for a pair of synthetic images.

CHAPTER 3

NOTIONS OF CONSTITUTIVE EQUATION FOR BRAIN MODELLING

3.1 Introduction

In this chapter, some generalities about constitutive equations are recalled. Three material behaviors employed in brain tissues modelling are presented; these are hyperelasticity, viscoelasticity and poroelasticity. A larger section will be devoted to viscoelasticity, due to its importance in brain tissue modelling and the numerous existing formulations. All the processes studied are assumed to be isothermal and thus purely mechanical to simplify the developments. For more details, please consult Drozdov (1996, 1998) and Holzapfel (2001).

3.2 Generalities

Notations

In this section, we briefly recall some elements of the continuum mechanics and present the notations used.

Let $\mathbf{x}$ and $\mathbf{X}$ be the positions of a material point in the current (γ) and reference (Γ) configuration respectively as depicted in Fig. 3.1. The deformation gradient tensor $\mathbf{F}$ is defined as

$$\mathbf{F} = \frac{\partial \mathbf{x}}{\partial \mathbf{X}} \tag{3.1}$$

Its determinant, J, is named the *Jacobian* and measures the relative change of volume between γ and Γ in the neighbourhood of the considered material point.

Let's also define the displacement, the velocity and the acceleration :

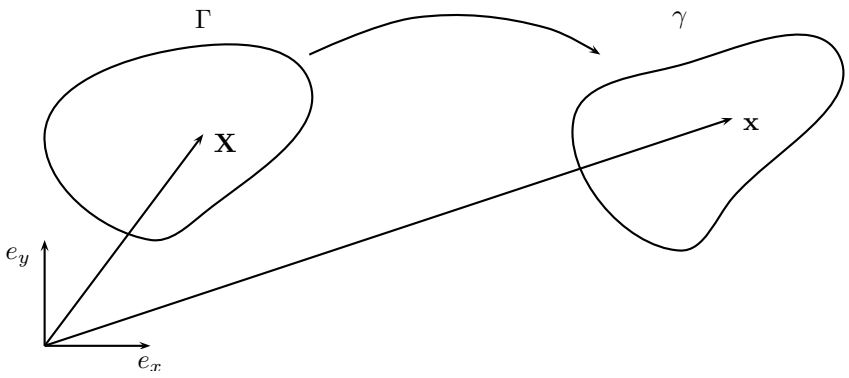

Fig. 3.1: Illustration of the deformation of a solid. A material point associated to vector $\mathbf{X}$ in the initial configuration Γ becomes associated with $\mathbf{x}$ in the deformed configuration γ.

$$\mathbf{u} = \mathbf{x} - \mathbf{X} \tag{3.2}$$
$$\mathbf{v} = \dot{\mathbf{x}} \tag{3.3}$$
$$\mathbf{a} = \ddot{\mathbf{x}} \tag{3.4}$$

The spatial gradient of velocity, $\mathbf{L}$ is written as

$$\mathbf{L} = \frac{\partial \mathbf{v}}{\partial \mathbf{x}} \tag{3.5}$$
$$= \dot{\mathbf{F}}\mathbf{F}^{-1} \tag{3.6}$$

It is decomposed into its symmetric $\mathbf{D}$ and antisymmetric $\mathbf{W}$ parts respectively named the rate of deformation tensor and the spin tensor.

The following strain and stress tensors are generally used in the field of mechanics of material :

Strain tensors

$$\text{Cauchy} \quad \mathbf{C} = \mathbf{F}^T\,\mathbf{F} \tag{3.7}$$

$$\text{Finger} \quad \mathbf{B} = \mathbf{F}\,\mathbf{F}^T \tag{3.8}$$

$$\text{Natural} \quad \mathbf{E}^N = \ln(\sqrt{\mathbf{C}}) \tag{3.9}$$

$$\text{Green-Lagrange} \quad \mathbf{E}^{GL} = \frac{1}{2}(\mathbf{C} - \mathbf{I}) \tag{3.10}$$

Stress tensors

$$\text{Cauchy} \qquad \boldsymbol{\sigma} \tag{3.11}$$

$$\text{Lagrange} \quad \mathbf{T} = J\boldsymbol{\sigma}\ \mathbf{F}^{-t} \tag{3.12}$$

$$\text{Piola-Kirchhoff 2} \quad \mathbf{S} = J\mathbf{F}^{-1}\ \boldsymbol{\sigma}\ \mathbf{F}^{-t} \tag{3.13}$$

Strain invariants

When a material can be considered as isotropic, the constitutive equation is expressed in terms of strain invariants, their number depending on the nature of the material. In hyperelastic constitutive laws, 3 invariants are used (here expressed in term of $\mathbf{C}$):

$$I_1 = \text{Tr}\ \mathbf{C} \tag{3.14}$$

$$I_2 = \frac{1}{2}\left(I_1^2 - \text{Tr}\ \mathbf{C}^2\right) \tag{3.15}$$

$$I_3 = \det \mathbf{C} \tag{3.16}$$

$$= J^2 \tag{3.17}$$

In viscoelastic constitutive laws, 7 additional invariants may be employed :

$$J_1 = \text{Tr}\ \dot{\mathbf{C}} \tag{3.18}$$

$$J_2 = \text{Tr}\ \dot{\mathbf{C}}^2 \tag{3.19}$$

$$J_3 = \text{Tr}\ \dot{\mathbf{C}}^3 \tag{3.20}$$

$$J_4 = \text{Tr}\left(\mathbf{C}\ \dot{\mathbf{C}}\right) \tag{3.21}$$

$$J_5 = \text{Tr}\left(\mathbf{C}^2\ \dot{\mathbf{C}}\right) \tag{3.22}$$

$$J_6 = \text{Tr}\left(\mathbf{C}\ \dot{\mathbf{C}}^2\right) \tag{3.23}$$

$$J_7 = \text{Tr}\left(\mathbf{C}^2\ \dot{\mathbf{C}}^2\right) \tag{3.24}$$

For many materials in which fibers play an important mechanical role (such as collagen fibers in blood vessel walls), the isotropy hypothesis is not valid and two invariants are added to the set of 3.14 to 3.16 . In such a case (see Fig. 3.2), denoting $\mathbf{N}$ the preferred fiber direction in the reference configuration, I_4 and I_5 can be written as

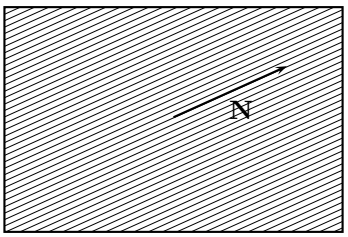

Fig. 3.2: Fibrous material. The fibers are aligned in a preferred direction, denoted by vector **N**.

$$I_4 = \mathbf{N} \,.\, \mathbf{C} \,.\, \mathbf{N} \tag{3.25}$$

$$I_5 = \mathbf{N} \,.\, \mathbf{C}^2 \,.\, \mathbf{N} \tag{3.26}$$

Principle of objectivity

The behavior of a material subjected to a certain loading must be observer independent. A change of reference frame must not result in the alteration of the constitutive law. This is ensured by the **principle of objectivity**

Constitutive equations must be invariant with respect to changes of reference frame; that is two observers, even if in relative motion, observe the same stress tensor in a given body.

The practical consequence is that constitutive laws have to be written only in terms of objective quantities. This constraint is much stronger than invariance under a change of coordinates which is ensured by requiring constitutive equations to be tensor equations.

Let's consider the following change of reference frame:

$$\mathbf{x}^* = \mathbf{c}(t) + \mathbf{Q}(t)\,\mathbf{x} \tag{3.27}$$

$$t^* = t - a \tag{3.28}$$

where $\mathbf{c}(t)$ is a time dependent translation and $\mathbf{Q}(t)$ a time dependent rotation tensor with

$$\mathbf{Q}^T\,\mathbf{Q} = \mathbf{I} \tag{3.29}$$

In Eqn. 3.28, it is also assumed that the origin of the time measure is shifted by a quantity a.

Let now G^* be the quantity G in this other reference frame. To be an objective quantity, the following relations must hold :

$$\text{scalar } g^* = g \tag{3.30}$$

$$\text{vector } \mathbf{g}^* = \mathbf{Q}\,\mathbf{g} \tag{3.31}$$

$$\text{tensor } \mathbf{G}^* = \mathbf{Q}\,\mathbf{G}\,\mathbf{Q}^T \tag{3.32}$$

Most of the quantities continuum mechanics deals with are objective. The following exceptions must be noted : time t, position vector $\mathbf{x}$, velocity $\mathbf{v}$, acceleration $\mathbf{a}$, displacement $\mathbf{u}$, and spin tensor $\mathbf{W}$ are not objective. In general, material derivatives of spatial objective tensors are not objective neither.

Let $g, \mathbf{h}$ and $\mathbf{K}$ be scalar, vector and second order tensor constitutive functions respectively. To respect the principle of objectivity, the following relations must be satisfied :

$$g(\mathbf{A}^*, \mathbf{b}^*, c^*) = g(\mathbf{Q}\ \mathbf{A}\ \mathbf{Q}^T, \mathbf{Q}\ \mathbf{b}, c) = g(\mathbf{A}, \mathbf{b}, c) \tag{3.33}$$

$$\mathbf{h}(\mathbf{A}^*, \mathbf{b}^*, c^*) = \mathbf{h}(\mathbf{Q}\ \mathbf{A}\ \mathbf{Q}^T, \mathbf{Q}\ \mathbf{b}, c) = \mathbf{Q}\ \mathbf{h}(\mathbf{A}, \mathbf{b}, c) \tag{3.34}$$

$$\mathbf{K}(\mathbf{A}^*, \mathbf{b}^*, c^*) = \mathbf{K}(\mathbf{Q}\ \mathbf{A}\ \mathbf{Q}^T, \mathbf{Q}\ \mathbf{b}, c) = \mathbf{Q}\ \mathbf{K}(\mathbf{A}, \mathbf{b}, c)\ \mathbf{Q}^T \tag{3.35}$$

with $\mathbf{A}$ a second order tensor, $\mathbf{b}$ a vector and c a scalar.

3.3 Hyperelasticity

A material is said to be hyperelastic when the stresses can be obtained by derivation of a strain potential W with respect to the strains. A typical example is

$$\mathbf{S} = \frac{\partial W}{\partial \mathbf{E}^{GL}} \tag{3.36}$$

Isotropic material

If the material can be considered as isotropic, the strain potential must be expressed in terms of strain invariants, i.e. $W = W(I_1, I_2, I_3)$. Introducing 3.14 to 3.16 into constitutive relation (3.36) leads to

$$S_{AB}{}^{1} = \frac{\partial W}{\partial I_1}\frac{\partial I_1}{\partial E^{GL}_{AB}} + \frac{\partial W}{\partial I_2}\frac{\partial I_2}{\partial E^{GL}_{AB}} + \frac{\partial W}{\partial I_3}\frac{\partial I_3}{\partial E^{GL}_{AB}} \tag{3.37}$$

The derivatives with respect to E^{GL}_{AB} need a few developments. If δ_{AB} stands for the Kronecker symbol, one gets

$$\frac{\partial I_1}{\partial E^{GL}_{AB}} = 2\delta_{AB} \tag{3.38}$$

$$\frac{\partial I_2}{\partial E^{GL}_{AB}} = 2\left(I_1\delta_{AB} - C_{AB}\right) \tag{3.39}$$

$$\frac{\partial I_3}{\partial E^{GL}_{AB}} = 2I_3 C^{-1}_{AB} \tag{3.40}$$

Defining

$$\Phi = 2\frac{\partial W}{\partial I_1}, \Psi = 2\frac{\partial W}{\partial I_2} \text{ and } p = 2\frac{\partial W}{\partial I_3} \tag{3.41}$$

and substituting finally leads to

$$S_{AB} = \Phi\delta_{AB} + \Psi\left(I_1\delta_{AB} - C_{AB}\right) + pI_3C^{-1}_{AB} \tag{3.42}$$

Isotropic incompressible material

If a material is said to be incompressible, it is not subjected to any volume change. Therefore, the incompressibility constraint is written

$$I_3 = 1 \tag{3.43}$$

and the strain potential is only of function of I_1 and I_2. Eqn. 3.42 becomes

$$S_{AB} = \Phi\delta_{AB} + \Psi\left(I_1\delta_{AB} - C_{AB}\right) + pC^{-1}_{AB} \tag{3.44}$$

where p serves as a Lagrange multiplier which can be determined using the equilibrium equations and the boundary conditions. It can be identified with the hydrostatic pressure. Another way to obtain this result is to define the following potential :

$$W = \hat{W}(I_1, I_2) + \frac{1}{2}p(I_3 - 1) \tag{3.45}$$

Nearly incompressible isotropic material

In practice, no material is strictly incompressible. Instead, it is appropriate to consider about nearly incompressible materials. In this case,

$$I_3 \simeq 1 \tag{3.46}$$

Let's define the modified invariants:

$$\hat{I}_1 = I_1 I_3^{-1/3} \tag{3.47}$$

$$\hat{I}_2 = I_2 I_3^{-2/3} \tag{3.48}$$

$$\hat{I}_3 = I_3^{1/2} \tag{3.49}$$

and the strain potential

$$W(I_1, I_2, I_3) = \hat{W}(\hat{I}_1, \hat{I}_2) + \Xi f(\hat{I}_3 - 1) \tag{3.50}$$

where $f(\hat{I}_3-1)$ is a suitable function (for example $0.5(\hat{I}_3-1)^2$ or $0.5\ln(\hat{I}_3-1)$) and Ξ plays the role of a penalty coefficient. Substituting in relation 3.36 and taking $f(\hat{I}_3-1) = 0.5(\hat{I}_3-1)^2$ leads to

$$S_{AB} = \frac{\partial \hat{W}}{\partial \hat{I}_1}\frac{\partial \hat{I}_1}{\partial E^{GL}_{AB}} + \frac{\partial \hat{W}}{\partial \hat{I}_2}\frac{\partial \hat{I}_2}{\partial E^{GL}_{AB}} + \Xi(\hat{I}_3-1)\frac{\partial \hat{I}_3}{\partial E^{GL}_{AB}} \tag{3.51}$$

with

$$\frac{\partial \hat{I}_1}{\partial E^{GL}_{AB}} = 2I_3^{-1/3}\left(\delta_{AB} - \frac{1}{3}I_1 C^{-1}_{AB}\right) \tag{3.52}$$

$$\frac{\partial \hat{I}_2}{\partial E^{GL}_{AB}} = 2I_3^{-2/3}\left(I_1\delta_{AB} - C_{AB} - \frac{2}{3}I_2 C^{-1}_{AB}\right) \tag{3.53}$$

$$\frac{\partial \hat{I}_3}{\partial E^{GL}_{AB}} = \hat{I}_3 C^{-1}_{AB} \tag{3.54}$$

Examples of energy function

Energy function	Equation	
Mooney-Rivlin	$c_1(I_1-3)+c_2(I_2-3)$	(3.55)
neo-Hookean	$c_1(I_1-3)$	(3.56)
Ogden	$\sum_{p=1}^{N}\frac{\mu_p}{\alpha_p}\left(\lambda_1^{\alpha_p}+\lambda_2^{\alpha_p}+\lambda_3^{\alpha_p}-3\right)$	(3.57)
Varga	$c_1(\lambda_1+\lambda_2+\lambda_3-3)$	(3.58)
Yeoh	$c_1(I_1-3)+c_2(I_1-3)^2+c_3(I_1-3)^3$	(3.59)

The λ_p are the principal stretches, i.e. the eigenvalues of $\mathbf{C}$, the μ_p denote constant shear moduli, the c_i are material parameters and the α_p are dimensionless constants.

3.4 Viscoelasticity

A viscoelastic material exhibits both viscous and elastic properties. The viscous part is responsible for a strain rate dependence (Fig. 3.3). For a given strain, the higher the strain rate, the higher the stress. It is also responsible for hysteresis, i.e. the loss of energy over one loading cycle. Hysteresis is observable on the stress-strain curve (see Fig. 3.4). The

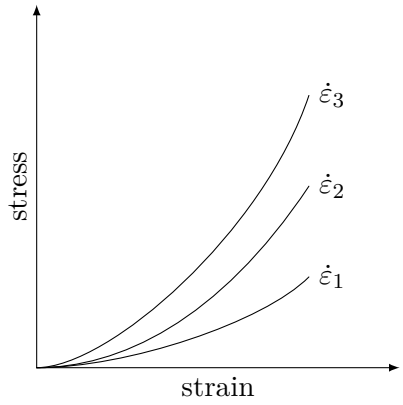

Fig. 3.3: Illustration of strain-rate dependency exhibited by the viscoelastic materials. $\dot{\varepsilon}_3 > \dot{\varepsilon}_2 > \dot{\varepsilon}_1$

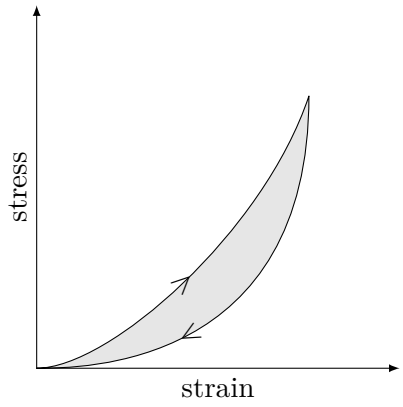

Fig. 3.4: Illustration of the hysteresis exhibited by the viscoelastic materials. The grey area correspond to the energy loss during the cycle.

viscoelastic behavior is also thought of as a dependence of the current stress on the entire history of strains.

Creep, relaxation and recovery are also characteristic behaviors of viscoelasticity. They will be discussed later.

Viscoelasticity is observed in many materials: polymers and plastics, metals and alloys at elevated temperatures, fresh concrete, biological tissues, foodstuffs, ...

Rheological models

First, the rheological models based on two simple elements that are the spring and the dashpot are described. We then see how to combine them to obtain more complex models.

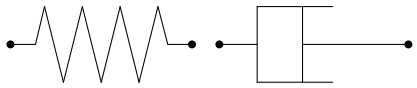

Fig. 3.5: Spring and dashpot rheological models.

The spring (Fig. 3.5 a) obviously represents an elastic element. In a one dimension, small strains case, its constitutive relation is written :

$$\sigma = E\varepsilon \tag{3.60}$$

with E an elastic constant.

The dashpot (Fig. 3.5 b) represents a viscous element. Under the same conditions, its constitutive relation is written

$$\sigma = \eta\dot{\varepsilon} \tag{3.61}$$

with η a viscous constant.

These two elements can be combined in series and in parallel to obtain two elementary models.

Elementary models

The Maxwell fluid model is made up of a spring and a dashpot in series (Fig. 3.6).

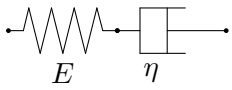

Fig. 3.6: Maxwell model of a viscoelastic material.

Its constitutive relation expresses that the total strain is the sum of the elastic and the viscous ones :

$$\dot{\varepsilon} = \frac{\dot{\sigma}}{E} + \frac{\sigma}{\eta} \tag{3.62}$$

Let's apply a stress step $\sigma_0\Delta(t)$[2]. The resulting strain is given by

$$\varepsilon(t) = \frac{\sigma_0 t}{\eta} + \frac{\sigma_0}{E} \tag{3.63}$$

and is thus a linear function of time. Conversely, let's impose a given strain $\varepsilon_0\Delta(t)$. The stress verifies the equation

$$\dot{\sigma} + \frac{E}{\eta}\sigma = 0 \tag{3.64}$$

whose solution is

$$\sigma(t) = E\varepsilon_0\, e^{-E/\eta\, t} \tag{3.65}$$

Eqn. 3.63 and Eqn. 3.65 illustrates the fluid behavior of this model : a constant stress results in strain growing linearly with time and the stress decreases exponentially to 0 when a constant strain is applied.

The Voigt solid model consists of a spring and a dashpot in parallel (Fig.. 3.7). The governing differential equation is :

$$\sigma = E\varepsilon + \eta\dot{\varepsilon} \tag{3.66}$$

The response to a strain step $\varepsilon_0\Delta(t)$ equals

$$\sigma(t) = E\varepsilon_0 + \eta\delta(t) \tag{3.67}$$

The presence of the Dirac distribution $\delta(t)$ signifies that it is physically impossible to impose a strain step to a Voigt model, since it would require an infinite force.

Let's now apply a stress step $\sigma_0\Delta(t)$. The strain is given by equation 3.68

$$\dot{\varepsilon} + \frac{E}{\eta}\varepsilon = \frac{\sigma_0}{\eta} \tag{3.68}$$

whose solution is

$$\varepsilon(t) = \frac{\sigma_0}{E}\left[1 - e^{-E/\eta\, t}\right] \tag{3.69}$$

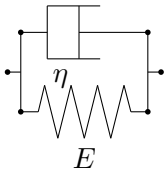

Fig. 3.7: Voigt model of a viscoelastic material.

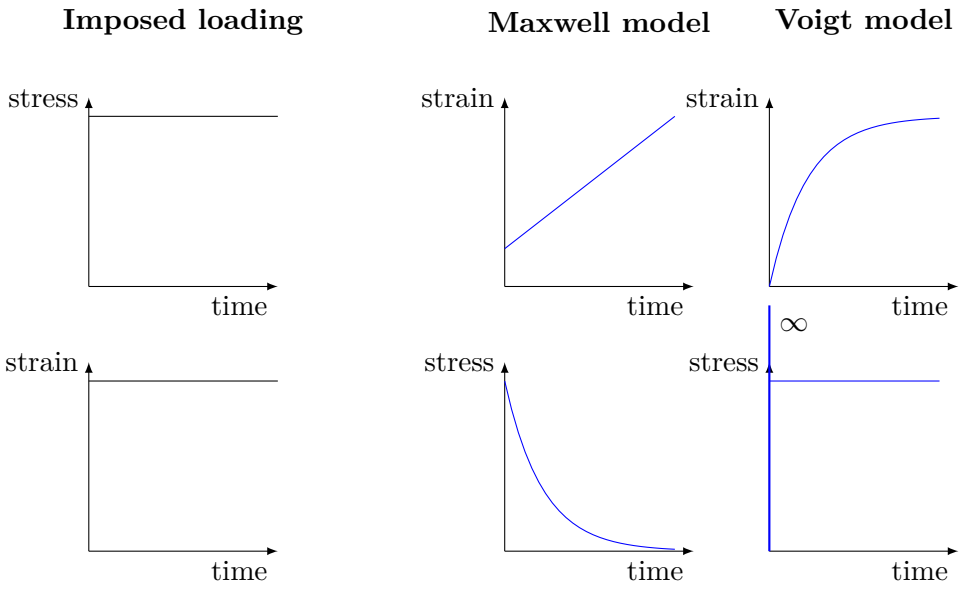

Fig. 3.8: Qualitative responses of Maxwell and Voigt models for constant strain and stress steps.

If subjected to a constant strain, the Voigt model responds with a constant stress $E\varepsilon_0$, like a linear elastic solid. Conversely, if a constant stress is applied, the initial strain is 0 and tends toward σ_0/E when $t \to \infty$. Such a behavior is called *delayed elasticity*. The Voigt model is then much likely to describe a solid.

The responses of the Voigt and Maxwell models to stress and strain steps are summarized in Fig.3.8

More complex models

The spring and dashpot elements as well as the Voigt and Maxwell models can be combined together to obtain more sophisticated models. One of them is the so called 3-parameter solid. It consists in a spring in series with a Voigt solid (Fig.. 3.9) and is governed by Eqn. 3.70

$$\dot{\sigma} + \frac{E_s + E_v}{\eta}\sigma = \frac{E_s E_v}{\eta}\varepsilon + E_s\dot{\varepsilon} \tag{3.70}$$

with E, η and E_v being the rigidity of the first spring and the viscosity and the rigidity of the Voigt model elements respectively.

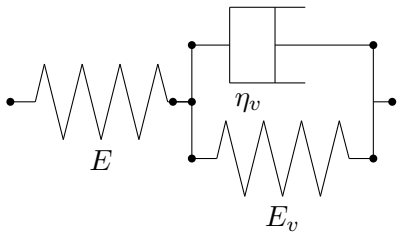

Fig. 3.9: Kelvin model for viscoelastic materials.

The generalized Maxwell model, n Maxwell elements and a spring in parallel (Fig. 3.10), is widely used to model viscoelastic solids. Maxwell elements may be added depending on the number of parameters needed to characterize the material.

[2]We use the notation $\Delta(t)$ to designate the Heaviside function

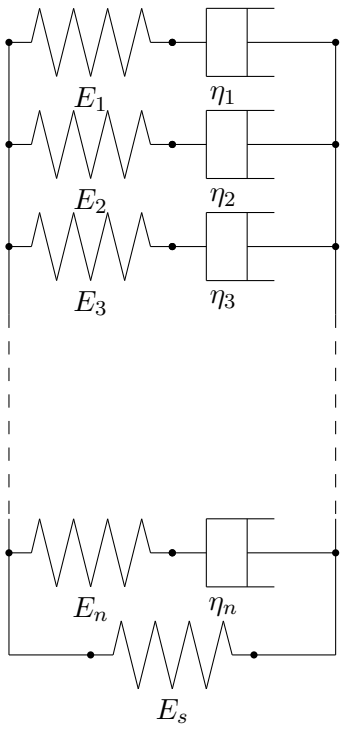

Fig. 3.10: Generalized maxwell model.

Creep, relaxation and recovery

The creep designates the evolution of the strain when a constant stress is imposed. This evolution depends obviously on the viscoelastic material considered. The term relaxation designates the diminution of the stress when a constant strain is applied. Examples have been presented in Fig. 3.8.

A creep compliance $J(t)$ and a relaxation modulus $Y(t)$, both function of time, can be attributed to each model. Such functions characterize the response of the material to a stress and a strain step respectively, i.e. if

$$\varepsilon(t) = f(\sigma(t)) \tag{3.71}$$

then

$$J(t) = f(\sigma_0 \Delta(t)) \tag{3.72}$$

and in the same way, if

$$\sigma(t) = g(\varepsilon(t)) \tag{3.73}$$

then

$$Y(t) = g(\varepsilon_0 \Delta(t)) \tag{3.74}$$

If one of the two functions, either $Y(t)$ or $J(t)$ is determined experimentally, analytically or numerically, the other one can be found thanks to the following relationship

$$\hat{J}(s)\hat{Y}(s) = s^{-2} \tag{3.75}$$

where $\hat{Y}(s)$ and $\hat{J}(s)$ stand for the Laplace transforms of functions $\hat{Y}(t)$ and $J(t)$ respectively and where s is the Laplace independent variable.

Finally, the recovery phenomenon occurs after a stress loading/unloading cycle. A residual strain may remain after the cycle. If no more stress is applied, the material will be subjected to a partial or full recovery. This is illustrated in Fig. 3.11

Hereditary integrals

Rheological models are linked to differential equations. An analytical solution may be obtained for $\sigma(t)$ or $\varepsilon(t)$ thanks to the Laplace transform. This generally implies the appearance of a convolution integral.

An integral formulation is presented here, the hereditary integral. Let's consider the arbitrary function presented in Fig. 3.12. This arbitrary stress function $\sigma(t)$ may be decomposed into a sum of step functions

$$\sigma(t) = \sum_i \sigma_i \Delta(t - t_i) \tag{3.76}$$

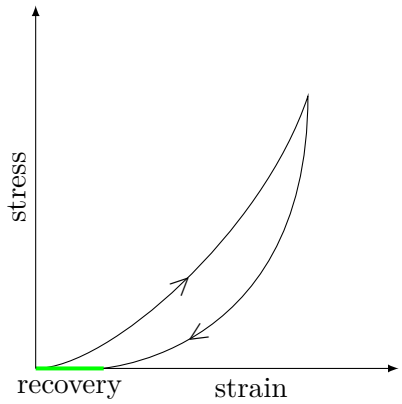

Fig. 3.11: Illustration of the recovery phenomenon exhibited by viscoelastic materials. The recovery may be partial or complete.

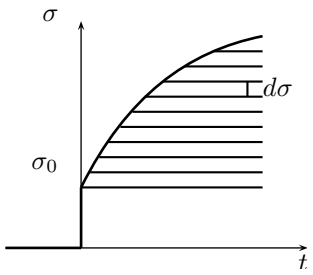

Fig. 3.12: Hereditary integral: decomposition of the stress into a sum of step functions.

where Δ is the Heaviside function. At every time t', an increment $d\sigma$ is added to the function. It may be expressed as

$$d\sigma = \left.\frac{d\sigma}{dt}\right|_{t=t'} dt \tag{3.77}$$

Using the previously defined creep compliance $J(t)$, the strain may be written as

$$\varepsilon(t) = \sigma_0 J(t) + \int_0^\infty J(t-t')\frac{d\sigma}{dt'}\, dt' \tag{3.78}$$

which can be written

$$\varepsilon(t) = J * d\sigma \tag{3.79}$$

Similarly,

$$\sigma(t) = Y * d\varepsilon \tag{3.80}$$

Expressions 3.78 to 3.80 are known as different forms of *hereditary integrals*. They express that the strain (resp. stress) at time t depends on the whole stress (resp. strain) history. The convolution kernel is the creep compliance (resp. relaxation modulus).

Complex compliance

Let $\varepsilon = \varepsilon_0 e^{\imath\omega t}$. Let's define the following operators :

$$\mathcal{P} = \sum_{i=0}^{m} p_i \frac{d^i}{dt^i} \tag{3.81}$$

$$\mathcal{Q} = \sum_{j=0}^{n} q_j \frac{d^j}{dt^j} \tag{3.82}$$

Provided that the coefficients p_i and q_j respect some model-dependent conditions, the differential equation

$$\mathcal{P}\sigma(t) = \mathcal{Q}\varepsilon(t) \tag{3.83}$$

represents a viscoelastic material.
The corresponding stress is of the form of $\sigma(t) = \sigma_0 e^{\imath\omega t}$. The amplitude σ_0 is given by

$$\sigma_0 = \frac{\sum_{k=0}^{n} q_k (\imath\omega)^k}{\sum_{k=0}^{m} p_k (\imath\omega)^k} \tag{3.84}$$

σ_0 is *a priori* complex and then $\sigma_0 = \sigma_1 + \imath\sigma_2$. So,

$$\begin{aligned} \sigma(t) &= \sigma_0 e^{\imath\omega t} && (3.85)\\ &= (\sigma_1 + \imath\sigma_2)(\cos(\omega t) + \imath \sin(\omega t)) && (3.86)\\ &= \underbrace{(\sigma_1 \cos(\omega t) - \sigma_2 \sin(\omega t)}_{\text{response to } \varepsilon_0 \cos(\omega t)} + \imath \underbrace{(\sigma_2 \cos(\omega t) + \sigma_1 \sin(\omega t))}_{\text{response to } \varepsilon_0 \sin(\omega t)} && (3.87) \end{aligned}$$

ε_0 may be chosen complex in a way that the relative phase φ between σ and ε remains unchanged. Thus, the following equality holds

$$\varepsilon_0 = G(\omega)\sigma_0 \tag{3.88}$$

with

$$G(\omega) = G_1(\omega) + \imath G_2(\omega) \tag{3.89}$$

the complex compliance.

G_2 must be negative due to thermodynamical constraints. The complex compliance can be deduced from the creep compliance (or the relaxation modulus, see Eqn. 3.75) :

$$G_1 \cos(\omega t) - G_2 \sin(\omega t) = \lim_{T\to\infty} \left(\cos(\omega t) J(t+T) - \omega \int_{-T}^{t} J(t-t') \sin(\omega t')\, dt' \right) \tag{3.90}$$

For instance, the complex compliance of the Voigt solid is given by

$$G_1 = 1 - \frac{\omega^2}{\lambda^2 + \omega^2} \tag{3.91}$$

$$G_2 = \frac{\lambda\omega}{\lambda^2 + \omega^2} \tag{3.92}$$

where λ stands for $\dfrac{E}{\eta}$
This notion of complex compliance proves to be useful when dealing with cyclic tests to characterize a viscoelastic material.

Extension to the 3D case

The monodimensional cases presented in the previous section are seldom encountered when modelling a material. Generally, they are used as an introduction to viscoelasticity. But once the concepts are understood, the extension to the 3D case is almost immediate.
In 3D viscoelasticity, the stress and strain tensors are decomposed into hydrostatic and deviatoric parts :

$$\boldsymbol{\sigma} = \sigma_m \mathbf{I} + \hat{\boldsymbol{\sigma}} \tag{3.93}$$

$$\boldsymbol{\varepsilon} = \varepsilon_m \mathbf{I} + \hat{\boldsymbol{\varepsilon}} \tag{3.94}$$

with $\sigma_m = 1/3\text{Trace}(\boldsymbol{\sigma})$ and $\varepsilon_m = 1/3\text{Trace}(\boldsymbol{\varepsilon})$.
If the considered viscoelastic material is isotropic, a hydrostatic stress must produce a pure dilatation[3] and no distortion. Hence, the quantities σ_m and ε_m may be connected by

$$\sum_{k=0}^{m''} p''_k \frac{d^k}{dt^k}\sigma_m = \sum_{k=0}^{n''} q''_k \frac{d^k}{dt^k}\varepsilon_m \tag{3.95}$$

Similarly,

$$\sum_{k=0}^{m'} p'_k \frac{d^k}{dt^k}\hat{\boldsymbol{\sigma}} = \sum_{k=0}^{n'} q'_k \frac{d^k}{dt^k}\hat{\boldsymbol{\varepsilon}} \tag{3.96}$$

To achieve a normalization, p'_0 and p''_0 are set to 0. If an operator formulation is used, Eqn. 3.95 and Eqn. 3.96 become

$$\mathcal{P}''\sigma_m = \mathcal{Q}''\varepsilon_m \tag{3.97}$$
$$\mathcal{P}'\hat{\boldsymbol{\sigma}} = \mathcal{Q}'\hat{\boldsymbol{\varepsilon}} \tag{3.98}$$

In particular, if $\mathcal{P}'' = 1, \mathcal{P}' = 1, \mathcal{Q}'' = 3K, \mathcal{Q}' = 2G$, the constitutive law for a linear elastic material is retrieved. Generally, in viscoelastic models, the dilation is assumed to be elastic. For the deviatoric operators, a suitable rheological model may be chosen.

Hyperviscoelasticity

The hyperviscoelasticity behavior directly derives from Eqn. 3.36 and Eqn. 3.80. We will assume that $\mathbf{S}(0) = \mathbf{0}$, i.e. the system has no residual stress in its initial configuration. If the material is hyperelastic, $\mathbf{S}$ in not an explicit function of time, i.e.

$$\frac{d}{dt}\frac{\partial W}{\partial \mathbf{E}^{GL}} = 0 \tag{3.99}$$

If the material follows a hyperviscoelastic law, $W = W(I_1, I_2, I_3, t)$ and therefore $\mathbf{S} = \mathbf{S}(t)$
The hyperviscoelastic potential Ψ is defined by

$$\Psi = \int_0^t Y(t-\tau)\frac{d}{d\tau}W(I_1, I_2, I_3)\, d\tau \tag{3.100}$$

where $W(I_1, I_2, I_3)$ is a hyperelastic strain potential, as those introduced in section 3.3. The constitutive relation for a hyperviscoelastic material is then :

$$\mathbf{S} = \frac{\partial \Psi}{\partial \mathbf{E}} \tag{3.101}$$

The developments made for incompressible materials hold here, provided W is replaced by Ψ.

[3] or contraction

Decoupling

Another way to model a viscoelastic material is to assume a unique decomposition of the stress tensor $\mathbf{S}$ into an elastic part and a viscous part,

$$\mathbf{S} = \mathbf{S}_e + \mathbf{S}_v + \mathcal{I}_{\tau=\delta}^{\infty}\{G(t-\tau);\mathbf{C}\} \tag{3.102}$$

The second term of the right hand side represents the short time memory response while the third term is the delayed contribution, i.e. the long time memory. Both are viscous contributions. The functional $\mathcal{I}$ contains the information about the history of $\mathbf{C}(t)$ and is assumed to be linear[4]. This functional generally identified to an integral and $G(t-\tau)$ to a relaxation function, which defines an hereditary integral.

The elastic and short time stresses may be linked to an elastic and a viscous (or pseudo) potential respectively :

$$\mathbf{S}_e = 2\frac{\partial W_e}{\partial \mathbf{C}} \tag{3.103}$$

$$\mathbf{S}_v = 2\frac{\partial W_v}{\partial \dot{\mathbf{C}}} \tag{3.104}$$

For an isotropic material, $W_e = W_e(I_1, I_2, I_3)$ whereas $W_v = W_v(I_i, J_j) \quad i = 1,2,3\ ; j = 1,...,7$ (see Eqn. 3.18 to Eqn. 3.24). Eqn. 3.105 shows an example of viscous potential (see Pioletti and Rakotomanana (2000)).

$$W_v = \frac{\eta'}{4} J_2 (I_1 - 3) \tag{3.105}$$

Internal variables

The concept of internal variables postulates that the current state at a given point of a dissipative material is specified by the strain tensor $\mathbf{C}$ and a finite number of scalar, vector or tensor internal variables $\mathbf{\Gamma}_1, ..., \mathbf{\Gamma}_m$. The information relative to the whole past of the material is thus contained in the set of internal variables at time t. The viscoelastic potential is here defined by

$$\Psi\left(\mathbf{C}, \mathbf{\Gamma}_1, ...\mathbf{\Gamma}_m\right) = W_e(\mathbf{C}) + \sum_{\alpha=1}^{m} \Upsilon_\alpha(\mathbf{C}, \mathbf{\Gamma}_\alpha) \tag{3.106}$$

The second term of the right hand side is a dissipative potential responsible for the viscoelastic regime. The scalar-valued functions Υ_α represent the so-called **configurational free energy** of the viscoelastic solid and characterize the non-equilibrium state. Each subscript α is related to a relaxation time.

[4] Which does not imply that the response of the material will also be linear

According to experimental data on tissues, it can be assumed that a time-dependent change in the system is caused practically by isochoric deformations. Hence, the volumetric response remains fully elastic. The hyperelastic energy function is then split into a volumetric part and a isochoric part :

$$W_e = W_{vol}(J) + W_{iso}(\bar{\mathbf{C}}) \tag{3.107}$$

where $\mathbf{C} = \left(J^{2/3}\mathbf{I}\right)\bar{\mathbf{C}}$. The first term is associated with volume changing deformations while $\bar{\mathbf{C}}$ is associated with the isochoric deformations of the material. The constitutive law is obtained according to thermodynamics arguments and is written[5]

$$\mathbf{S} = 2\frac{\partial\Psi\left(\mathbf{C}, \mathbf{\Gamma}_1, ..., \mathbf{\Gamma}_m\right)}{\partial\mathbf{C}} \tag{3.108}$$

The PK2 stress tensor $\mathbf{S}$ can also be split into a volume ($\mathbf{S}_{vol}$) and an isochoric ($\mathbf{S}_{iso}$) parts with the following definitions :

$$\mathbf{S}_{vol} = J\,\frac{\partial W_{iso}(J)}{\partial J}\,\mathbf{C}^{-1} \tag{3.109}$$

$$\mathbf{S}_{iso} = \mathbf{S}_{iso}^{\infty} + \sum_{\alpha=1}^{m}\mathbf{Q}_\alpha \tag{3.110}$$

$$\mathbf{S}_{iso}^{\infty} = J^{-2/3}\mathbf{P} \,:\, 2\frac{\partial W_{iso}(\bar{\mathbf{C}})}{\partial\bar{\mathbf{C}}} \tag{3.111}$$

with the fourth order tensor

$$\mathbf{P} = \mathbf{I} - \frac{1}{3}\mathbf{C}^{-1}\otimes\mathbf{C} \tag{3.112}$$

$$\tag{3.113}$$

The non equilibrium stresses $\mathbf{Q}_\alpha$ are defined by the relationship

$$\mathbf{Q}_\alpha = 2\frac{\partial\Upsilon_\alpha(\bar{\mathbf{C}}, \mathbf{\Gamma}_\alpha)}{\partial\mathbf{C}} \tag{3.114}$$

$$= J^{-2/3}\,\mathbf{P} \,:\, \bar{\mathbf{Q}}_\alpha \tag{3.115}$$

The **fictitious non-equilibrium stress** is given by

$$\bar{\mathbf{Q}}_\alpha = -2\frac{\partial\Psi(\mathbf{C}, \mathbf{\Gamma}_\alpha)}{\partial\Gamma_\alpha} \tag{3.116}$$

Motivated by the (mechanical) equilibrium equations for the linear viscoelastic solid, one can conclude that $\bar{\mathbf{Q}}_\alpha$ are variable related (conjugate) to $\mathbf{\Gamma}_\alpha$ with the internal constitutive equation

[5]For more details, please consult Holzapfel (2001)

$$\bar{\mathbf{Q}}_\alpha = -2\frac{\partial \Upsilon(\bar{\mathbf{C}}, \mathbf{\Gamma}_\alpha)}{\partial \mathbf{\Gamma}_\alpha} \tag{3.117}$$

The set of equations already obtained must be completed by a kinetic relation, which describes the evolution of the internal variables. These are of the form of

$$\dot{\mathbf{Q}}_\alpha = f_\alpha\left(\bar{\mathbf{C}}, \mathbf{Q}_1, ..., \mathbf{Q}_m\right) \tag{3.118}$$

3.5 Poroelasticity

A poroelastic medium is composed of a solid matrix and a fluid phase. Geomaterials (rocks, soils,...) are good examples of such medium. The pores of the material are (partially) filled with fluid. The porosity n is defined as the ratio of the volume of the pores over the total volume. The motion of this fluid as well as its pressure play a fundamental role in the considered mechanics. We then first focus on porous media flow.

Porous media flow

Balance equations for monophasic flows express that, in a control volume, the sum of incoming and outgoing fluid is equal to the stored fluid volume . The surface balance equation is written :

$$\mathbf{n}.\mathbf{v} + q = 0 \tag{3.119}$$

and indicates that the imposed flux q is equal to the components of the inner flux along the outer normal to the boundary.

The volume balance equation in its local form is written :

$$\nabla.\mathbf{v} + \dot{S} - Q = 0 \tag{3.120}$$

where Q is a source term and S is the amount of stored fluid. These two equations need to be completed by a constitutive relation. Darcy's law provides this equation

$$\mathbf{v} = \frac{\mathbf{K}}{\rho g}\left(\nabla p + \nabla \rho g z\right) \tag{3.121}$$

$$= \frac{\mathbf{k}}{\mu}\left(\nabla p + \nabla \rho g z\right) \tag{3.122}$$

where $\mathbf{k}$ is the intrinsic permeability tensor, $\mathbf{K}$ the permeability tensor, μ the dynamic viscosity of the fluid, ρ the density of the fluid, g the acceleration of gravity, p the pressure and $\mathbf{v}$ the velocity of the fluid.

In steady state, the balance equations and Darcy's law are sufficient to describe the flow. But in transient regime, the volume of fluid stored in the material may vary, i.e.

$$\dot{S} \neq 0 \tag{3.123}$$

and an evolution equation for S has to be written. Various reasons can explain the variation of S, among them :

- the solid matrix deforms, resulting in a modification of the volume of the pores,
- the fluid is compressible ; a variation in pressure results then in a variation in density,
- the temperature of the fluid varies,
- ...

Obviously, these contributions can combine.

Solid phase mechanics

The solid phase mechanics is driven by the usual balance equations

$$\mathbf{t} = \sigma.\mathbf{n} \tag{3.124}$$
$$\nabla\sigma + \mathbf{F} = 0 \tag{3.125}$$

in surface (3.124) and in volume (3.125). $\mathbf{t}$ stands for the surface traction, $\mathbf{n}$ the outer normal, $\mathbf{F}$ the applied body forces and σ Cauchy stress tensor. The constitutive law is chosen according to the application aimed. For soft tissues, a linear elastic law has generally been chosen[6].

Conclusion

In this chapter, some generalities about constitutive models for brain tissue have been reminded. Three kinds of constitutive laws have been studied, with a particular attention to viscoelasticity. Numerous formulations exist, some heavier than others but all have to take into account the property that the stress state at a given point and a given time depends on the whole strain history at that point. Rheological models are very useful in 1D to understand the viscoelastic processes while hyperviscoelastic or decoupled models seem more practical for 3D calculations.

[6] See Miga et al. (2000a) and Miga et al. (2000b)

CHAPTER 4

FRACTIONAL DERIVATION

4.1 Introduction

The notion of fractional [1] derivative may sound weird the first time it is heard. Indeed, it is neither usual to deal with an expression such as $\left(\frac{d}{dt}\right)^{(1.4)} f(t)$ nor is it to determine its physical meaning if any.

The equations encountered in physics, from quantum mechanics to relativity and from electromagnetism to thermodynamics, are all expressed in terms of integer-order derivatives, and therefore, it is unconceivable for us to imagine that a physical phenomenon could be expressed with a real-order derivative. A parallel can be drawn between the order of derivation and the exponents: we all know that $a^3 = a.a.a$ but we still cannot give a physical meaning to the expression $a^{1.4}$: how can we imagine to multiply a 1.4 times by itself ? However, this expression is used whenever necessary without any trouble. So should be the fractional derivatives.

This concept of fractional derivative was first discussed by L'Hospital and Leibniz in 1695: (Schmidt and Gaul (2002b)).

> "In a letter dated September 30th, 1695 L'Hospital wrote to Leibniz asking him about a particular notation he had used in his publications for the nth-derivative of the linear function $f(x) = x$, $D^{(n)}f(x)$. L'Hospital asked the question to Leibniz, what would the result be if $n = 1/2$. Leibniz's response: "An apparent paradox, from which one day useful consequences will be drawn." "

Many other brilliant mathematicians contributed to the theory of the fractional calculus, amongst them Euler, Abel, Liouville and Riemann. But although the mathematical foundations of the theory were developed prior the turn of the 20^{th} century, it has been only for the last decades that the applications to physical processes have been studied. A short literature review about the use of the fractional derivatives in the field of the characterization of materials is given in section 4.8.

[1] The term "fractional" may mislead to think that only rational numbers are used to define a new kind of derivative; however, it is used to designate any real number. For historical reason, the term fractional is still used.

The aim of this chapter is to provide the reader with the basics of the calculus of fractional derivation. Two small developments show how they are deduced from integer order derivatives. Then some useful properties are given without demonstration. Analytical and numerical methods of resolution of fractional differential equations are presented. As far as the numerical methods are concerned, some developments are given to provide the reader with the essential ideas underlaying the methods.

4.2 From integer order to fractional order operators

In this section, we derive two expressions of the fractional derivative from the definitions of the differential quotient and the integral. This should help the reader unfamiliar with these notions to link it to well known concepts.

4.2.1 Grunwald-Letnikov derivative

The starting point that will lead us to the expression of the Grunwald-Letnikov (GL) derivative is the definition of the first order derivative as the limit of the differential quotient:

$$D_t^{(1)} f(t) = \lim_{\Delta t \to 0} \frac{1}{\Delta t} \left(f(t) - f(t - \Delta t) \right) \tag{4.1}$$

Repeated applications lead to

$$D_t^{(2)} f(t) = \lim_{\Delta t \to 0} \frac{1}{(\Delta t)^2} \left(f(t) - 2f(t - \Delta t) + f(t - 2\Delta t) \right) \tag{4.2}$$

$$D_t^{(3)} f(t) = \lim_{\Delta t \to 0} \frac{1}{(\Delta t)^3} \left(f(t) - 3f(t - \Delta t) + 3f(t - 2\Delta t) - f(t - 3\Delta t) \right) \tag{4.3}$$

which can be generalized in

$$D_t^{(n)} f(t) = \lim_{\Delta t \to 0} \frac{1}{(\Delta t)^n} \left(\sum_{j=0}^{n} (-1)^j \binom{n}{j} f(t - j\Delta t) \right) \tag{4.4}$$

where

$$\binom{n}{j} = \frac{n!}{j!\,(n-j)!} \tag{4.5}$$

Using the Γ function[2]

$$\Gamma(x) = \int_0^\infty t^{x-1} e^{-t}\, dt \tag{4.6}$$

[2]See appendix E for more details

Eqn. 4.5 can be rewritten:

$$\binom{n}{j} = \frac{\Gamma(n+1)}{\Gamma(j+1)\Gamma(n-j+1)} \tag{4.7}$$

which allows a generalization if n is no longer an integer.

Definition 4.4 then becomes

$$D_t^{(n)} f(t) = \lim_{\Delta t \to 0} \frac{1}{(\Delta t)^n} \left(\sum_{j=0}^{n} (-1)^j \frac{\Gamma(n+1)}{\Gamma(j+1)\Gamma(n-j+1)} f(t - j\Delta t) \right) \tag{4.8}$$

Let's now write consider the function $Df_{\Delta t}^p(t)$ defined from the right hand side of Eqn. 4.8, with $p \leq n$:

$$Df_{\Delta t}^p(t) = \frac{1}{(\Delta t)^p} \left(\sum_{j=0}^{n} (-1)^j \frac{\Gamma(p+1)}{\Gamma(j+1)\Gamma(p-j+1)} f(t - j\Delta t) \right) \tag{4.9}$$

If $\Delta t \to 0$, Eqn. 4.9 identifies with $D^{(p)} f(t)$ since the coefficients following

$$\left. \frac{\Gamma(p+1)}{\Gamma(j+1)\Gamma(p-j+1)} \right|_{j=p} \tag{4.10}$$

in the sum are all equal to 0, according to the property $\Gamma(z) \to \infty \; \forall z \in \{0, -1, -2, \cdots\} = \mathbb{Z}^-$ (see appendix E).

Now, if we take $p \in \mathbb{Z}^-$ and let $\Delta t \to 0$, $Df_{\Delta t}^p(t) \to 0$ which is not a very interesting result. The only way to get a non zero value is to extent the sum in Eqn. 4.9 to M rather than n with $M \to \infty$ as $\Delta t \to 0$. This is the case if we introduce the substitution:

$$\Delta t = \frac{t}{M} \tag{4.11}$$

With $M \to \infty$, Eqn. 4.8 becomes

$$D_t^{(n)} f(t) = \lim_{M \to \infty} \frac{1}{(t/M)^n} \left(\sum_{j=0}^{M} (-1)^j \frac{\Gamma(n+1)}{\Gamma(j+1)\Gamma(n-j+1)} f(t - jt/M) \right) \tag{4.12}$$

The Grunwald-Letnikov fractional derivative is finally obtained by replacing the integer n with a real number α:

$$D_t^{(\alpha)} f(t) = \lim_{M \to \infty} \frac{1}{(t/M)^\alpha} \left(\sum_{j=0}^{M} (-1)^j \frac{\Gamma(\alpha+1)}{\Gamma(j+1)\Gamma(\alpha-j+1)} f(t - jt/M) \right) \tag{4.13}$$

4.2.2 Riemann-Liouville derivative

The expression of the Riemann-Liouville (RL) derivative is established from the definition of the first order integral:

$$I^{(1)}f(t) = \int_0^t f(x)\,dx \tag{4.14}$$

It is possible to express the second order integral with only one integration operator:

$$I^{(2)}f(t) = \int_0^t dt_2 \int_0^{t_2} f(t_1)\,dt_1 \tag{4.15}$$

$$= \int_0^t f(t_1)dt_1 \int_{t_1}^t dt_2 \tag{4.16}$$

$$= \int_0^t f(t_1)(t-t_1)\,dt_1 \tag{4.17}$$

$$= \int_0^t f(x)(t-x)dx \tag{4.18}$$

The order of integration was permuted between Eqn. 4.15 and Eqn. 4.16. Eqn. 4.18 can be extended to the nth order of integration, leading to:

$$I^{(n)}f(t) = \frac{1}{(n-1)!}\int_0^t f(x)(t-x)^{n-1}\,dx \tag{4.19}$$

Let's adopt the convention that $D_t^{(k)}$ $k \in \mathbb{Z}$ stands for the derivation operator with respect to t if $k > 0$ and the integration operator with respect to t if $k < 0$. As we did for the Grunwald-Letnikov definition, we replace the factorial operator by the Γ function

The following relation holds $\forall n \geq 1$:

$$D_t^{(k-n)}f(t) = \frac{1}{\Gamma(n)}D_t^{(k)}\int_0^t f(x)(t-x)^{n-1}\,dx \tag{4.20}$$

The Riemann-Liouville definition of the fractional derivative is obtained by replacing the integer n by a real number $\alpha > 0$ in Eqn. 4.20:

$$D_t^{(k-\alpha)} = \frac{1}{\Gamma(\alpha)}D_t^{(k)}\int_0^t f(x)(t-x)^{\alpha-1}\,dx \tag{4.21}$$

Like the Riemann-Liouville definition, the Grunwald-Letnikov formulation can be interpreted as an integral, being the limit of a sum over a large number of infinitesimal intervals. The classical integer-order derivatives are obviously retrieved if α is replaced by an integer value n in both definitions.

According to Podlubny (1999), both definitions are equivalent for the fractional index $p, 0 < p < n$, if the function $f(t)$ is $(n-1)$-times continuously differentiable in the interval $[0, T]$ and if $f^{(n)}(t)$ is integrable in $[0, T]$. This property proves to be useful as definition (4.13) is more convenient for numerical evaluation and (4.21) for analytical calculus.

4.3 Basic properties

Now that we established two formulations for the fractional derivative, it is useful to examine some of their properties. We assume that the conditions under which expressions 4.21 and 4.13 are equivalent are fulfilled and we focus on the Riemann-Liouville formulation, easier to deal with in analytical calculus.

Non locality

It appears directly from the examination of Eqn. 4.21 that the fractional derivative is non local: all the past values of the function are needed to compute $D_t^{(\alpha)} f$ at time t. However, the kernel is of the form of $1/(t-x)^{1+\alpha}$ and thus exhibits a rapidly decreasing behaviour. Therefore, the weight of the values of $f(t)$ located in a distant past tend towards 0. This property is exploited in the numerical algorithms used to compute the fractional derivatives.

The first coefficients $(-1)^j \dfrac{\Gamma(\alpha+1)}{\Gamma(j+1)\Gamma(\alpha-j+1)}$ of the Grunwald-Letnikov derivative are plotted in Fig. 4.1. The coefficients corresponding to a non-integer value of α present a damped oscillatory behaviour and tend to 0, while the coefficients corresponding to the integer order value p are exactly equal to 0 from the $(p+1)^{\text{th}}$ one.

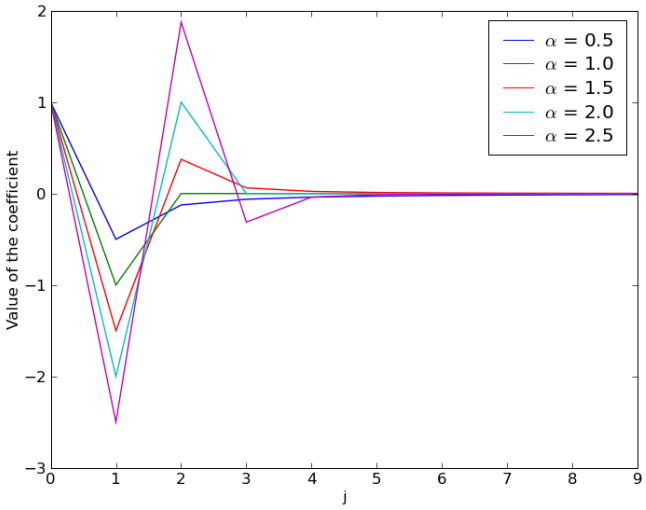

Fig. 4.1: First coefficients of the Grunwald-Letnikov fractional derivative for several values of α.

Linearity

Classical derivation operators are linear :

$$D_t^{(n)}\left[\lambda f(t) + \mu g(t)\right] = \lambda D_t^{(n)} f(t) + \mu D_t^{(n)} g(t) \tag{4.22}$$

The same holds for the fractional counterpart :

$$D_t^{(\alpha)}\left[\lambda f(t)+\mu g(t)\right] = \lambda D_t^{(\alpha)} f(t)+\mu D_t^{(\alpha)} g(t) \tag{4.23}$$

Leibniz rule

The classical first derivative of a product is well known :

$$D_t^{(1)}\left[f(t)g(t)\right] = g(t)D_t^{(1)} f(t)+f(t)D_t^{(1)} g(t) \tag{4.24}$$

The extension to the n^{th} derivative is known as the Leibniz rule :

$$D_t^{(n)}\left[f(t)g(t)\right] = \sum_{k=0}^{n}\binom{n}{k} D_t^{(k)} f(t)\; D_t^{(n-k)} g(t) \tag{4.25}$$

A similar form can be written for the fractional derivative of a product :

$$D_t^{(\alpha)}\left[f(t)g(t)\right] = \sum_{k=0}^{\infty}\binom{\alpha}{k} D_t^{(k)} f(t)\; D_t^{(\alpha-k)} g(t) \tag{4.26}$$

Inverse operator

One of the most important properties of the Riemann-Liouville derivative is that

$$D_t^{(\alpha)}\left[D_t^{(-\alpha)} f(t)\right] = f(t) \tag{4.27}$$

but it does not mean that the operators commute, since, for $k-1<\alpha\leq k$

$$D_t^{(-\alpha)}\left[D_t^{(\alpha)} f(t)\right] = f(t)-\sum_{j=1}^{k}\left[D_t^{(\alpha-j)} f(t)\right]_{t=0}\frac{t^{\alpha-j}}{\Gamma(\alpha-j+1)} \tag{4.28}$$

This is not surprising, since classical integration and derivation operators do not commute neither

Composition with integer-order derivatives

Fractional and classical derivatives do not generally commute since :

$$D_t^{(n)}\left[D_t^{(\alpha)} f(t)\right] = D_t^{(n+\alpha)} f(t) \tag{4.29}$$

$$D_t^{(\alpha)}\left[D_t^{(n)} f(t)\right] = D_t^{(n+\alpha)} f(t)+\sum_{j=0}^{n-1}\left[D_t^{(j)} f(t)\right]_{t=0}\frac{t^{j}}{\Gamma(j+1)} \tag{4.30}$$

One only has to use the definition 4.21 to prove it.
Therefore, operators $D_t^{(\alpha)}$ and $D_t^{(n)}$ commute if the function $f(t)$ satisfies

$$D_t^{(j)} f(t)\Big|_{t=0} = 0,\quad (j=0,1,....,n-1) \tag{4.31}$$

Composition with fractional derivative

As a consequence of 4.28, the composition of fractional derivatives of orders α and β does not result in an operator of order $\alpha+\beta$. Assuming $m-1<\alpha\leq m$ and $n-1<\beta<n$ leads to

$$D_t^{(\alpha)}\left[D_t^{(\beta)}f(t)\right] = D_t^{(\alpha+\beta)}f(t)-\sum_{j=1}^{n}\left[D_t^{(\beta-j)}f(t)\right]_{t=0}\frac{t^{-\alpha-j}}{\Gamma(-\alpha-j+1)} \tag{4.32}$$

$$D_t^{(\beta)}\left[D_t^{(\alpha)}f(t)\right] = D_t^{(\alpha+\beta)}f(t)-\sum_{j=1}^{n}\left[D_t^{(\alpha-j)}f(t)\right]_{t=0}\frac{t^{-\beta-j}}{\Gamma(-\beta-j+1)} \tag{4.33}$$

Hence,both fractional derivation operators commute if and only if both sums in the right hand sides of 4.32 and 4.33 vanish. For this, the following condition must be fulfilled[3] :

$$D_t^{(j)}f(t)\Big|_{t=0} = 0,\quad (j=0,1,...,r-1) \tag{4.34}$$

with $r=\max(n,m)$

On the other hand, fractional integration operators always commute.

Laplace transform

The Laplace transform is very useful as it allows to turn differential equations into algebraic ones. It proves to be indispensable when dealing with viscoelastic rheological models, for example.
First, let's recall its basic properties. The Laplace transform of a function $f(x)$ is defined by

$$F(s) = \mathcal{L}\{f(t);s\}=\int_0^\infty e^{-st}f(t)\,dt \tag{4.35}$$

where s is a complex variable.

The original function $f(t)$ can be restored with the help of the inverse transform

$$f(t) = \mathcal{L}^{-1}\{F(s);t\}=\int_0^\infty e^{st}F(s)\,ds \tag{4.36}$$

The Laplace transform of a convolution product is simply the product of the transformed functions :

$$\mathcal{L}\{f(t)*g(t);s\} = F(s)G(s) \tag{4.37}$$

At last, another useful property is the formula for the Laplace transform of the integer order n derivative of the function $f(t)$

[3]The simple form of this condition comes from the equivalence between Riemann and Grunwald definitions.

$$\mathcal{L}\{D_t^{(n)} f(t); s\} = s^n F(s) - \sum_{k=0}^{n-1} s^{n-k-1} \left[D_t^{(k)} f(t)\right]_{t=0} \tag{4.38}$$

$$= s^n F(s) - \sum_{k=0}^{n-1} s^k \left[D_t^{(n-k-1)} f(t)\right]_{t=0} \tag{4.39}$$

We will now turn to the evaluation of the Laplace transform of the Riemann-Liouville derivative. Once more, let's assume that $n-1 < \alpha \leq n$. The expression of the Laplace transform writes

$$\mathcal{L}\{D_t^{(\alpha)} f(t); s\} = s^\alpha F(s) - \sum_{k=0}^{n-1} s^k \left[D_t^{(\alpha-k-1)} f(t)\right]_{t=0} \tag{4.40}$$

4.4 A few examples

Derivation of $a(t-c)^\beta$

The following result requires a few developments, which will not be reproduced here.

$$D_t^{(\alpha)} a(t-c)^\beta = a\frac{\Gamma(1+\beta)}{\Gamma(1+\beta-\alpha)}(t-c)^{\beta-\alpha} \tag{4.41}$$

Two particular cases are presented.
The first case corresponds to $\beta = c = 0$, i.e. the derivation of a constant:

$$D_t^{(\alpha)} a = a\frac{1}{\Gamma(1-\alpha)}t^{-\alpha} \tag{4.42}$$

The second case, corresponding to $\alpha, \beta = p, q \in \mathbb{N}$, shows that the result of the classical, integer order derivative is retrieved:

$$D_t^{(p)}(t-c)^q = \frac{q!}{(q-p)!}(t-c)^{q-p} \tag{4.43}$$

Eqn. 4.42 provides an interesting but unexpected result: the fractional derivative of a constant is not 0 but rather a real-order power of the independent variable.

Derivation of e^t

$$D_t^{(\alpha)} e^t = D_t^{(\alpha)} \left[\sum_{k=0}^{\infty} \frac{t^k}{k!}\right] \tag{4.44}$$

$$= \sum_{k=0}^{\infty} \frac{t^{k-\alpha}}{\Gamma(1+k-\alpha)} \tag{4.45}$$

$$= E^\alpha(t) \tag{4.46}$$

where the result from Eqn. 4.41 was used. The function $E^\alpha(t)$ is called the generalized exponential. A few examples of this function for different values of α are given in Tab. 4.1. We can notice that $E^n(x) = e^x \ \ \forall n \in \mathbb{N}$ which justifies the term "generalized exponential".

$E^0(t)$	$=$	e^t
$E^1(t)$	$=$	e^t
$E^{1/2}(t)$	$=$	$\dfrac{1 + e^t\sqrt{\pi t}\ \mathrm{Erf}\left(\sqrt{t}\right)}{\sqrt{\pi t}}$
$E^{-1/2}(t)$	$=$	$e^t\ \mathrm{Erf}\left(\sqrt{t}\right)$
$E^{-1}(t)$	$=$	$e^t - 1$

Tab. 4.1: Some examples of the generalized exponential function.

Derivative of sine and cosine

Finally, we can also compute the fractional derivatives of the trigonometrical functions. Let's recall that the sine and cosine can be expressed in terms of exponentials:

$$\cos(t) = \frac{e^{\imath t} + e^{-\imath t}}{2} \tag{4.47}$$

$$\sin(t) = \frac{e^{\imath t} - e^{-\imath t}}{2\imath} \tag{4.48}$$

Using the previous results, we deduce

$$D_t^{(\alpha)} \cos(t) = \frac{\imath^\alpha E^\alpha(\imath t) + (-\imath^\alpha) E^\alpha(-\imath t)}{2} \tag{4.49}$$

$$D_t^{(\alpha)} \sin(t) = \frac{\imath^\alpha E^\alpha(\imath t) - (-\imath^\alpha) E^\alpha(-\imath t)}{2\imath} \tag{4.50}$$

Once again, we recover the classical results if α is an integer.

Discussion

In this section, we presented fractional derivatives of some common functions. In most of the cases, the results for integer order derivatives can be recovered by setting $\alpha = n,\ n \in \mathbb{N}$ except when deriving a constant. This proves to be a major problem when dealing with fractional differential equations, particularly with initial conditions. More details are given in Podlubny (1999).

4.5 The Caputo derivative

Riemann derivative, as previously stated, is very useful for mathematical purpose. Its definition, involving a convolution integral, makes it more practical for analytical calculus than the Grunwald definition. For decades, this operator played a major role in the development of the theory of fractional derivatives and integrals and for its application in the pure mathematical field (solution of differential equations, definition of new function classes...). However, since physical processes have been modelled with the help of fractional derivatives, the theory needed to be, if not revised, at least extended. Indeed, the result shown in Eqn. 4.42 implies that the use of Riemann derivative in the frame of fractional differential equations will lead to impose fractional initial conditions, which do not have an immediate physical interpretation, unlike usual ones. Despite efforts of some authors (Podlubny and Heymans (2005)) on this particular topics, it would useful to find to way to continue to use integer-order initial conditions.

The alternative is then to use another fractional derivative which returns 0 when deriving a constant. The Caputo derivative has been designed specifically to present this property. Its definition is given by expression 4.51

$$ {}^{C}D_t^{(\alpha)} f(t) \quad = \quad \frac{1}{\Gamma(n-\alpha)} \int_0^t \frac{D_x^{(n)} f(x)}{(t-x)^{\alpha+1-n}}\, dx, \quad n-1 < \alpha \leq n,\ n \in \mathbb{N} \tag{4.51} $$

If α becomes a positive integer n, the classical integer order derivative is recovered

$$ \lim_{\alpha \to n} {}^{C}D_t^{(\alpha)} f(t) \quad = \quad D_t^{(n)} f(t) \tag{4.52} $$

The Caputo and the Riemann formulations are equivalent for the fractional order α with $m-1 < \alpha \leq m$, if $D_t^{(j)} f(t)\Big|_{t=0} = 0\ j = 0, 1, \cdots, m-1$.

Not all of the properties presented previously will be discussed in the frame of the Caputo derivative. Only the Laplace transform will be briefly discussed, for its possible application in the resolution of fractional differential equations. In Eqn. 4.40, fractional derivatives appear in the right hand side. These turn into integer order ones if the Caputo derivative is used instead of the Riemann-Liouville derivative:

$$ \mathcal{L}\{{}^{C}D_t^{(\alpha)} f(t); s\} \quad = \quad s^{\alpha} F(s) - \sum_{k=0}^{n-1} s^{\alpha-k-1}\, D_t^{(k)} f(t)\Big|_{t=0} \tag{4.53} $$

From the foregoing, we will only use the Caputo operator, therefore the superscript ^{C} will be omitted.

4.6 The Mittag-Leffler function

The Mittag-Leffler function plays a major role in the framework of the fractional differential equations. Like the generalized exponential function (Eqn. 4.46), it is defined as a series:

$E_{1,1}(t)$	$=$	e^t
$E_{1,2}(t)$	$=$	$\frac{e^t-1}{t}$
$E_{2,1}(t^2)$	$=$	$\cosh(t)$
$E_{2,2}(t^2)$	$=$	$\frac{\sinh(t)}{t}$

Tab. 4.2: Some examples of usual functions expressed in terms of Mittag-Leffler function

$$E_{\alpha,\beta}(z) = \sum_{k=0}^{\infty} \frac{z^k}{\Gamma(\alpha k+\beta)},\ \alpha,\beta>0, |z|<\infty \tag{4.54}$$

Usual functions can be expressed in terms of Mittag-Leffler function. A few examples are given in Tab. 4.2

Two more identities are needed in order to be able to solve fractional differential equations using Laplace transform. Let's assume m and $k \in \mathbb{N}, \alpha$ and $\beta \in \mathbb{R}$

$$D_t^{(m)}\left(t^{\beta-1}E_{\alpha,\beta}(t^\alpha)\right) = t^{\beta-m-1}E_{\alpha,\beta-m}(t^\alpha) \tag{4.55}$$

$$\int_0^\infty e^{-st}t^{\alpha k+\beta-1}E_{\alpha,\beta}^{(k)}(\pm at^\alpha)\,dt = \frac{k!s^{\alpha-\beta}}{(s^\alpha \mp a)^{k+1}} \tag{4.56}$$

Eqn. 4.56 gives a pair of Laplace transform of the function $t^{\alpha k+\beta-1}E_{\alpha,\beta}^{(k)}(\pm zt^\alpha)$ while Eqn. 4.55 provides a way to compute the m^{th} derivative of the Mittag-Leffler function.

4.7 Fractional differential equations (FDE)

4.7.1 Existence and uniqueness

Let's consider a linear fractional differential equation:

$$D_t^{(\alpha_n)}y(t) + \sum_{j=1}^{n-1} p_j(t)D_t^{(\alpha_{n-j})}y(t) + p_n(t)y(t) = f(t) \tag{4.57}$$

with $p_j(t)$ $j=1,\cdots,n$ and $f(t)$ given functions and with initial conditions

$$D_t^{(k)}y(t)\Big|_{t=0} = y_0^k \quad k=0,1,...,n-1 \tag{4.58}$$

on the unknown function $y(t)$.

We must first make sure that a solution exists and is unique. This is the case if some weak conditions are fulfilled :

If $f(t) \in L_1]0,T[$, and $p_j(t)$, $(j = 1, 2, ..., n)$ are continuous functions in the closed interval [0,T], then the initial-value problem 4.57 has a unique solution $y(t) \in L_1]0,T[$

An existence and uniqueness theorem also exists for nonlinear equations such as $D_t^{(\alpha)} y(t) = f(t, y(t))$. There will be no further development as we will only deal with linear fractional differential equations.

4.7.2 Analytical methods of resolution

In some cases, it is useful to have an analytical solution available, to evaluate the error of a numerical method for instance. A lot of methods coexist, some are adapted to a class of problems, other are more generals. The aim of this section is not to present the whole panel of available methods but rather to focus on the Laplace transform.

Given the following equation, with $0 < \alpha < 1$[4]
and the initial condition $f(0) = f_0$

$$D_t^{(\alpha)} f(t) + af(t) = 0, \tag{4.59}$$

the application of the Laplace transform leads to

$$s^\alpha F(s) - s^{\alpha-1} f_0 + aF(s) = 0 \tag{4.60}$$

and then

$$F(s) = f_0 \frac{s^{\alpha-1}}{s^\alpha + a} \tag{4.61}$$

Identifying the parameters in expression 4.56 and performing the inverse transform produces the result

$$f(t) = f_0 E_{\alpha,1}(-at^\alpha) \tag{4.62}$$

The Mittag-Leffler function thus plays the same role as the exponential in the frame of fractional differential equations.

Let's now consider a non homogeneous linear FDE under non zero initial conditions $D_t^{(k)} f(t)\Big|_{t=0} = b_k,\ k = 0, .., n-1$:

$$D_t^{(\alpha)} y(t) - \lambda y(t) = h(t) \tag{4.63}$$

The Laplace transform yields

[4]The case $\alpha > 1$ is just longer to deal with, not more difficult

$$s^\alpha Y(s) - \lambda Y(s) = H(s) + \sum_{k=0}^{n-1} b_k s^{\alpha-k-1} \tag{4.64}$$

and the inverse Laplace transform gives the solution

$$y(t) = \sum_{k=0}^{n-1} b_k t^k E_{\alpha,k+1}(\lambda t^\alpha) + \int_0^t (t-\tau)^{\alpha-1} E_{\alpha,\alpha}(\lambda(t-\tau)^\alpha) h(\tau)\, d\tau \tag{4.65}$$

4.7.3 Numerical methods of resolution

This section is devoted to the review of existing algorithms for the resolution of fractional differential equations. It does not aim at being exhaustive and providing all the mathematical developments on which the presented methods are based. However, it seemed interesting to show different algorithms and explain the reasons why a particular one was chosen.

Evaluation of the fractional derivative

According to Eqn. 4.51, the n (where $n-1 < \alpha \leq n$) first derivatives of y are required to compute $D_t^{(\alpha)} y(t)$, which is not very practical. Diethelm et al. (2005) propose to repeat integrations by parts, which eventually leads to expression (4.66).

$$D_t^{(\alpha)} y(t) = \frac{1}{\Gamma(-\alpha)} \int_0^t \frac{y(x)}{(t-x)^{\alpha+1}}\, dx \tag{4.66}$$

Here, function y directly appears instead of its derivative. The drawback of this formulation is that the convolution kernel now presents a strong singularity, so the integral must be interpreted as a Hadamard-finite-part integral. It is however not difficult to design a numerical algorthim which overcomes this difficulty.

According to Diethelm et al. (2005), fractional derivatives with $\alpha > 2$ seldom appear in physical problems. Therefore, their method takes $0 < \alpha < 2,\ \alpha \neq 1$.

The derivative is computed on an equispaced grid $t_j = nh\ j = 0, 1, ..., N$. The discretized version of (4.66) then writes:

$$D_t^{(\alpha)} y(t_N) = \frac{h^{-\alpha}}{\Gamma(2-\alpha)} \sum_{n=0}^{N} a_{n,N} \left(y_{N-n} - \sum_{k=0}^{\lfloor\alpha\rfloor} \frac{(N-n)^k h^k}{k!} y_0^{(k)} \right) \tag{4.67}$$

where $a_{n,N}$ are quadrature weights.

Diethelm (1997b) proved that the order of this approximation is $O(h^{2-\alpha})$. The quadrature weights are derived from a trapezoidal rule and are written:

$$a_{n,N} = \begin{cases} 1 & \text{if } n = 0 \quad (4.68) \\ (n+1)^{1-\alpha} - 2n^{1-\alpha} + (n-1)^{1-\alpha} & \text{if } 0 < n < N \quad (4.69) \\ (1-\alpha)N^{-\alpha} - N^{1-\alpha} + (N-1)^{1-\alpha} & \text{if } n = N \quad (4.70) \end{cases}$$

Another method, proposed by Odibat (2006), uses a modified trapezoidal rule to compute the Caputo derivative. Nevertheless, it requires the values of the m^{th} $(m-1 < \alpha < m)$ derivative at each point of an equispace grid, making it less pratical than the first method.

Resolution of fractional differential equations

Predictor-corrector algorithm

Diethelm and Freed (2006a) proposed a modified Adams-Moulton[5] method suitable for the resolution of the fractional differential equation. For a classical differential equation $D_t^{(1)} y(t) = f(t, y(t))$, the keypoint of the Adams-Moulton method is to write a relationship of the form of

$$y(t_{n+1}) = y(t_n) + \int_{t_n}^{t_{n+1}} f(x, y(x))\, dx \tag{4.71}$$

Let's consider the general problem

$$D_t^{(\alpha)} y(t) = f(t, y(t)) \tag{4.72}$$
$$D_t^{(k)} y(t)\Big|_{t=0} = y_0^{(k)} \tag{4.73}$$

Diethelm (1997a) proved that this problem is equivalent to the Volterra equation

$$y(t) = \sum_{k=0}^{n-1} y_0^{(k)} \frac{x^k}{k!} + \frac{1}{\Gamma(\alpha)} \int_0^t (t-x)^{\alpha-1} f(x, y(x))\, dx \tag{4.74}$$

Eqn. 4.74 is of the type of 4.71 but looks somewhat different because the range of integration now starts at 0 instead of t_n. This is a consequence of the non-local structure of the fractional derivative. This however does not cause a major problem in the attempt to generalize the Adams-Moulton method. The trapezoidal quadrature formula is used to replace the integral.

If $\bar{f}_{n+1}$ stands for the piecewise linear interpolant for f, the following approximation holds:

$$\int_0^{t_{n+1}} (t_{n+1}-x)^{\alpha-1} f(x)\, dx \simeq \int_0^{t_{n+1}} (t_{n+1}-x)^{\alpha-1} \bar{f}_{n+1}(x)\, dx \tag{4.75}$$

Using standard techniques of the quadrature theory, the right hand side of 4.75 can be written as

$$\int_0^{t_{n+1}} (t_{n+1}-x)^{\alpha-1} \bar{f}_{n+1}(x)\, dx = \frac{h^\alpha}{\alpha(\alpha+1)} \sum_{j=0}^{n+1} a_{j,n+1} f(t_j) \tag{4.76}$$

[5] For a detailled explanation of the Adams-Moulton method, please consult Press (1992) or any introductorial book on numerical analysis.

where the quadrature weights take the following values:

$$a_{j,n+1} = \begin{cases} n^{\alpha+1} - (n-\alpha)(n+1)^{\alpha}, & \text{if } j = 0, \\ (n-j+2)^{\alpha+1} + (n-j)^{\alpha+1} - 2(n-j+1)^{\alpha+1}, & \text{if } 1 \leq j \leq n, \\ 1, & \text{if } j = n+1 \end{cases}$$

This gives the fractional variant of the one-step Adams-Moulton method, i.e. the corrector :

$$y_{corr}(t_{n+1}) = \sum_{k=0}^{m-1} \frac{t_{n+1}^k}{k!} y_0^{(k)} + \frac{h^\alpha}{\Gamma(\alpha+2)} f(t_{n+1}, y_{pred}(t_{n+1})) + \frac{h^\alpha}{\Gamma\alpha+2} \sum_{j=0}^{m} a_{j,m+1} f(t_j, y_{corr}(t_j)) \quad (4.77)$$

where $m-1 < \alpha < m$ and $y^{(k)(0)} = D_t^{(k)} y(t)\Big|_{t=0}$.

The remaining problem is to find an expression for the predictor formula to compute the value $y_{pred}(t_{n+1})$. The following approximation is made :

$$\int_0^{t_{n+1}} (t_{n+1} - x)^{\alpha-1} f(x)\, dx \quad \simeq \quad \sum_{j=0}^{n} b_{j,n+1} f(t_j) \quad (4.78)$$

where

$$b_{j,n+1} \quad = \quad \frac{h^\alpha}{\alpha} \left((n+1-j)^\alpha - (n-j)^\alpha \right) \quad (4.79)$$

The predicted value $y_{pred}(t_{n+1})$ is then given by the fractional method :

$$y_{pred}(t_{n+1}) \quad = \quad \sum_{k=0}^{m-1} \frac{t_{n+1}^k}{k!} y_0^{(k)} + \frac{1}{\Gamma(\alpha)} \sum_{j=0}^{n} b_{j,n+1} f(t_j, y_{corr}(t_j)) \quad (4.80)$$

where $m-1 < \alpha < m$, which completes to describe the method. The error is expected to behave as

$$\max_{j=0,1,\ldots,N} |y(t_j) - y_{corr}(t_j)| \quad = \quad O(h^p) \quad (4.81)$$

with

$$p \quad = \quad \min(2, 1+\alpha) \quad (4.82)$$

Some improvements may be added to increase the precision of the algorithm given by 4.75 to 4.80 including additional corrector iterations and Richardson's extrapolation. See Diethelm and Freed (2006a) for more details.

Adomian's decomposition method

The Adomian's decomposition method (ADM) is used to find approximate solutions to nonlinear equations as an infinite series converging to the exact solution.

Let's consider the nonlinear equation

$$f(x) = 0 \tag{4.83}$$

for a given funtion f which is sufficiently smooth in the neighborhood of a simple root x^*. Eqn. 4.83 can be rewritten in the so-called canonical form

$$x = c + N(x) \tag{4.84}$$

where N is a nonlinear function and c is a constant.

According to the ADM, the solution x of Eqn. 4.84 is expressed as the series:

$$x = \sum_{n=0}^{\infty} x_n \tag{4.85}$$

and the nonlinear function N is decomposed over the Adomian's polynomials:

$$N(x) = \sum_{n=0}^{\infty} A_n \tag{4.86}$$

where

$$A_n = \frac{1}{n!} D_{\lambda}^{(n)} \left[N\left(\sum_{i=0}^{\infty} \lambda^i x_i \right) \right]_{\lambda=0}, \quad n = 0, 1, 2, ... \tag{4.87}$$

Substituing into Eqn. 4.84 yields to

$$\sum_{n=0}^{\infty} x_n = c + \sum_{n=0}^{\infty} A_n \tag{4.88}$$

Identifying the first component

$$x_0 = c \tag{4.89}$$

leads to the recursive relationship

$$x_{n+1} = A_n \tag{4.90}$$

Let $S_m = x_0 + x_1 + ... + x_m$. Then, $S_m = c + A_0 + A_1 + ... + A_{m-1}$ is the $m + 1$ terms approximation of the solution x.

The first Adomian's polynomials are given by:

$$A_0 = N(x_0) \tag{4.91}$$
$$A_1 = x_1 \left[D_x^{(1)} N(x)\right]_{x=x_0} \tag{4.92}$$
$$A_2 = x_2 \left[D_x^{(1)} N(x)\right]_{x=x_0} + 0.5x_1^2 \left[D_x^{(2)} N(x)\right]_{x=x_0} \tag{4.93}$$

The n^{th} polynomial is a function of $x_0, x_1, \cdots, x_n$. It is then often writen as $A_n(x_0, x_1, \cdots, x_n)$.

The Adomian decomposition can also be used in the framework of differential equations, both fractional and ordinary. Let's begin with the latter and consider the following system of nonlinear differential equations:

$$y_i'(x) = \sum_{j=1}^{n} b_{ij}(x) y_j + N_i(x, y_1, y_2, \cdots, y_n) + g_i(x), \quad y_i(0) = c_i \tag{4.94}$$

where $b_{ij}(x)$ and $g_i(x) \in C_0$ and the functions N_i are nonlinear continuous functions. The integration of Eqn. 4.94 leads to

$$y_i(x) = c_i + \int_0^x g_i(u)du + \int_0^x \sum_{j=1}^{n} b_{ij}(u) y_j(u)\, du + \int_0^x N_i(u, y_1, y_2, \cdots, y_n)\, du \tag{4.95}$$

The ADM consists in writing the solution as the series

$$y_i(x) = \sum_{m=0}^{\infty} y_{im}(x) \tag{4.96}$$

and the nonlinear terms as an infinite series of Adomian's polynomials

$$N_i(x, y_1, y_2, \cdots, y_n) = \sum_{m=0}^{\infty} A_{im} \tag{4.97}$$

with

$$A_{im} = \frac{1}{m!} D_x^{(m)} \left[N_i \left(x, \sum_{m=0}^{\infty} y_{1m}\lambda_m, \cdots, \sum_{m=0}^{\infty} y_{nm}\lambda_m \right) \right]_{\lambda=0} \tag{4.98}$$

The ADM allows a recursive computation of the y_{im}:

$$y_{i0}(x) = c_i + \int_0^x g_i(u)\, du \tag{4.99}$$

$$y_{i,m+1}(x) = \int_0^x \sum_{j=1}^{n} b_{ij}(u) y_{jm}\, du + \int_0^x A_{im}\, du \tag{4.100}$$

The real solution $y_i(x)$ is approximated by the truncated series

$$\varphi_i(x) = \sum_{m=0}^{k-1} y_{im}(x) \tag{4.101}$$

with

$$\lim_{k\to\infty} \varphi_i(x) = y_i(x) \tag{4.102}$$

A revised version (rADM) was developed by Jafari and Daftardar-Gejji (2006). They set

$$y_{10}(x) = c_1 + \int_0^x g_1(u)\, du \tag{4.103}$$

$$y_{1,m+1}(x) = \int_0^x \sum_{j=1}^{n} b_{1j}(u) y_{jm}\, du + \int_0^x A_{1m}\, du \tag{4.104}$$

$$y_{l0}(x) = c_l + \int_0^x g_l(u)\, du + \int_0^x \sum_{j=1}^{l-1} b_{ij}(u) y_{j0}\, du \tag{4.105}$$

$$y_{l,m+1} = \int_0^x \sum_{j=1}^{l-1} b_{ij}(u) y_{j,m+1}\, du + \int_0^x \sum_{0}^{x} \sum_{j=1}^{n} b_{ij}(u) y_{jm}\, du + \int_0^x A^*_{lm}\, du \tag{4.106}$$

where A^*_{lm} is defined as:

$$A^*_{l,m} = \begin{cases} A_{l,m+1} & \text{if } N_l \text{ are independent of } y_l, y_{l+1}, \cdots, y_n \\ A^1_{l,m+1} + A^2_{l,m} & \text{if } N_l(y_1, \cdots, y_n) = N^1_l(y_1, \cdots, y_{l-1}) + N^2_l(y_l, \cdots, y_n) \\ A_{lm} & \text{otherwise} \end{cases} \tag{4.107}$$

According to Jafari and Daftardar-Gejji (2006), the revised ADM converges faster and produces results closer to the analytical solution than the classical one. The authors also present some illustrations of the method.

The ADM and its revised version can also be used to solve fractional differential equations of the form:

$$D_x^{(\alpha)} y_i = \sum_{j=1}^{n} \varphi_{ij}(x) y_j + \sum_{j=1}^{n} \gamma_{ij} D_x^{\alpha_{(ij)}} y_j + N_i(x, y_1, \cdots, y_n) + g_i(x) \tag{4.108}$$

with $y_i^{(k)}(0) = c_k^i,\ 0 \le k \le m_i,\ \alpha_{ij} \le \alpha_i,\ m_i < \alpha_i \le m_i + 1,\ 1 \le i \le n$, where α_i and $\alpha_{ij} \in \mathbb{R}$. The use of the standard ADM yields to:

$$\begin{aligned} \sum_{m=0}^{\infty} y_{im} = \sum_{k=0}^{m_i} c_k^i \frac{x^k}{k!} + I^{(\alpha_i)} g_i(x) - \sum_{j=1}^{n} \gamma_{ij} \sum_{k=0}^{m_{ij}} c_k^j \frac{x^{\alpha_i - \alpha_{ij} + k}}{\Gamma(\alpha_i - \alpha_{ij} + k + 1)} \\ + \sum_{m=0}^{\infty} \left(\sum_{j=1}^{n} (I^{r\alpha_i}) \varphi_{ij}(x) + \gamma_{ij} I^{(\alpha_i - \alpha_{ij})}) y_{jm}(x) \right) \\ + I^{(\alpha_i)} \sum_{m=0}^{\infty} A_{im}(y_{10}, \cdots, y_{1m}, \cdots, y_{n0}, \cdots, y_{nm}) \end{aligned} \tag{4.109}$$

with the recurrence relations:

$$y_{i0}(x) = \sum_{k=0}^{m_i} c_i^k \frac{x^k}{k!} + I^{(\alpha_i)} g_i(x) - \sum_{j=1}^{n} \gamma_{ij} \sum_{k=0}^{m_{ij}} c_k^j \frac{x^{\alpha_i - \alpha_{ij} + k}}{\Gamma(\alpha_i - \alpha_{ij} + k + 1)} \quad (4.110)$$

$$y_{i,m+1}(x) = \sum_{j=1}^{n} (I^{(\alpha_i)} \varphi_{ij}(x) + \gamma_{ij} I^{\alpha_i - \alpha_{ij}}) y_{jm}(x) + I^{(\alpha_i)} A_{im} \quad (4.111)$$

The revised ADM writes

$$y_{10}(x) = \sum_{k=0}^{m_1} c_1^k \frac{x^k}{k!} + I^{(\alpha_1)} g_1(x) - \sum_{j=1}^{n} \gamma_{1j} \sum_{k=0}^{m_{1j}} c_k^j \frac{x^{\alpha_1 - \alpha_{1j} + k}}{\Gamma(\alpha_i - \alpha_{ij} + k + 1)} \quad (4.112)$$

$$y_{1,m+1}(x) = \sum_{j=1}^{n} (I^{(\alpha_1)} \varphi_{1j}(x) + \gamma_{1j} I^{(\alpha_1 - \alpha_{1j})}) y_{jm}(x) + I^{(\alpha_1)} A_{1m} \quad (4.113)$$

$$y_{l0}(x) = \sum_{k=0}^{m_l} c_1^k \frac{x^k}{k!} + I^{(\alpha_l)} g_l(x) - \sum_{j=1}^{n} \gamma_{lj} \sum_{k=0}^{m_{lj}} c_k^j \frac{x^{\alpha_l - \alpha_{lj} + k}}{\Gamma(\alpha_l - \alpha_{lj} + k + 1)} + \sum_{j=1}^{l-1} (I^{(\alpha_l)} \varphi_{lj}(x) + \gamma_{lj} I^{(\alpha_l - \alpha_{lj})}) y_{j0}(x) \quad (4.114)$$

$$y_{l,m+1} = \sum_{j=1}^{l-1} (I^{(\alpha_l)} \varphi_{lj}(x) + \gamma_{lj} I^{(\alpha_l - \alpha_{lj})}) y_{jm+1}(x) + \sum_{j=l}^{n} (I^{(\alpha_l)} \varphi_{lj}(x) + \gamma_{lj} I^{(\alpha_l - \alpha_{lj})}) y_{jm}(x) + I^{(\alpha_1)} A^*_{lm} \quad (4.115)$$

where the A^*_{lm} are defined in Eqn. 4.107. It is noticeable from equation Eqn. 4.108 that the ADM and rADM can deal with multiple orders of fractional dynamics, leading to a very rich description of a system.

Momani (2006) proposed a numerical implementation of the ADM for the resolution of Eqn. 4.108.

Expansion formula

In the expansion formula method developed by Atanackovic and Stankovic (2008), a single fractional differential equation is shown to be equivalent to an infinity of first order ordinary differential equations. The development is summarized hereafter. The starting point is the Riemann-Liouville derivative with $0 < \alpha < 1$:

$$D_t^{(\alpha)} f(t) = \frac{1}{\Gamma(1-\alpha)} D_t^{(1)} \int_0^t \frac{f(t)}{(t-\tau)^\alpha} \, d\tau \quad (4.116)$$

$$= \frac{1}{\Gamma(1-\alpha)} \left[\frac{f(0)}{t^\alpha} + \int_0^t \frac{D_t^{(1)} f(t)}{(t-\tau)^\alpha} \, d\tau \right] \quad (4.117)$$

A partial integration leads to

$$D_t^{(\alpha)} f(t) = \frac{1}{\Gamma(1-\alpha)} f(0) t^{-\alpha} + \frac{1}{\Gamma(2-\alpha)} \left[D_t^{(1)} f(t) \right]_{t=0} t^{1-\alpha} + \frac{1}{\Gamma(2-\alpha)} \int_0^t (t-\tau)^{1-\alpha} \, D_t^{(2)} f(\tau) \, d\tau \tag{4.118}$$

The last term is modified according to the binomial formula

$$(1+z)^\gamma = \sum_{p=0}^{\infty} \binom{\gamma}{p} z^p \tag{4.119}$$

$$= \sum_{p=0}^{\infty} \frac{(-1)^p \, \Gamma(p-\gamma)}{\Gamma(-\gamma) \, p!} z^p \tag{4.120}$$

for $|z| < 1$. Eqn. 4.120 still holds for $z = 1$ if and only if $\gamma > -1$ and for $z = -1$ if and only if $\gamma > 0$.

Using Eqn. 4.120 to evaluate $(t-\tau)^{1-\alpha}$, Eqn. 4.118 becomes

$$D_t^{(\alpha)} f(t) = \frac{1}{\Gamma(1-\alpha)} f(0) t^{-\alpha} + \frac{1}{\Gamma(2-\alpha)} \left[D_t^{(1)} f(t) \right]_{t=0} t^{1-\alpha} + \frac{t^{1-\alpha}}{\Gamma(2-\alpha)} \int_0^t D_t^{(2)} f(\tau) \left(\sum_{p=0}^{\infty} \frac{\Gamma(p-1+\alpha)}{\Gamma(\alpha-1)p!} \left(\frac{\tau}{t} \right)^p \right) d\tau \tag{4.121}$$

Integrating by parts the last term of Eqn. 4.121 leads to

$$D_t^{(\alpha)} f(t) = \frac{1}{\Gamma(1-\alpha)} f(0) t^{-\alpha} + \frac{t^{1-\alpha}}{\Gamma(2-\alpha)} \sum_{p=1}^{\infty} \frac{\Gamma(p-1+\alpha)}{\Gamma(\alpha-1)p!} \left(D_t^{(1)} f^(t) - \frac{p}{t^p} V_{p-1}(D_t^{(1)} f(t)) \right) + \frac{t^{1-\alpha}}{\Gamma(2-\alpha)} D_t^{(1)} f(t) \tag{4.122}$$

where $V_n(D_t^{(p)} f(t)),\ n, p \in \mathbb{N}$ stands for the nth moment of the pth derivative of function f and is written

$$V_n(D_t^{(p)} f(t)) = \int_0^t D_\tau^{(p)} f(\tau) \tau^n \, d\tau \tag{4.123}$$

Finally, another integration by parts of Eqn. 4.122 results in

$$D_t^{(\alpha)} f(t) = \frac{f(t) t^{-\alpha}}{\Gamma 1 - \alpha} + \frac{1}{\Gamma(2-\alpha)} \left\{ D_t^{(1)} f(t) \left[1 + \sum_{p=1}^{\infty} \frac{\Gamma(p-1+\alpha)}{\Gamma(\alpha-1)p!} \right] t^{1-\alpha} - \sum_{p=2}^{\infty} \frac{\Gamma(p-1+\alpha)}{\Gamma(\alpha-1)(p-1)!} \left(\frac{f(t)}{t^\alpha} + \frac{V_p^*(t)}{t^{p-1+\alpha}} \right) \right\} \tag{4.124}$$

where $f(0)$ was assumed to be null and

$$V_p^*(t) = -(p-1)\int_0^t \tau^{p-2} f(\tau)\, d\tau \tag{4.125}$$

The moments $V_p^*(t)$ satisfy the following system of differential equations:

$$D_t^{(1)} V_p^*(t) = -(p-1)t^{p-2} f(t),\ V_p^*(0) = 0 \tag{4.126}$$

From Eqn. 4.124, another approximation of the fractional derivative is drawn by Atanackovic and Stankovic (2008). It is written:

$$D_t^{(\alpha)} f(t) \simeq \frac{f(t)}{t^\alpha}\left[\frac{1}{\Gamma(1-\alpha)} - \frac{1}{\Gamma(\alpha-1)\Gamma(2-\alpha)} \sum_{p=2}^{\infty} \frac{\Gamma(p-1+\alpha)}{(p-1)!}\right] - \frac{1}{\Gamma(\alpha-1)\Gamma(2-\alpha)} \sum_{p=2}^{\infty} \frac{\Gamma(p-1+\alpha)}{(p-1)!} \frac{V_p^*(t)}{t^{p-1+\alpha}} \tag{4.127}$$

In Eqn. 4.127, the fractional derivative is expressed in terms of $f(t)$ and an infinite number of "internal variables" $V_p^*(t)$ satisfying the system of differential equations Eqn. 4.126. Thus comes the stunning result: a fractional differential equation can be turned into an infinite system of ordinary differential equations. Obviously, a finite number N of terms is kept in the sums for computational applications.

Once Eqn. 4.127 is established, its application to the resolution of FDE is straightforward. Consider the nonlinear equation

$$D_t^{(\alpha)} x(t) + F(x,t) = 0 \tag{4.128}$$

where[6] $\alpha \in]0,1[$, subjected to the initial condition $x(0) = 0$[7].
Applying the operator $D^{(1-\alpha)}$ to both sides of Eqn. (4.128) leads to

$$D_t^{(1)} x(t) = -D^{(1-\alpha)} F(x,t) \tag{4.129}$$

Then, using (4.127), the FDE (4.129) turns into a system of $N+1$ first order ODE:

$$D_t^{(1)} x(t) \simeq \frac{-F(x,t)}{t^\alpha}\left[\frac{1}{\Gamma(1-\alpha)} - \frac{1}{\Gamma(\alpha-1)\Gamma(2-\alpha)} \sum_{p=2}^{N} \frac{\Gamma(p-1+\alpha)}{(p-1)!}\right] - \frac{1}{\Gamma(\alpha-1)\Gamma(2-\alpha)} \sum_{p=2}^{N} \frac{\Gamma(p-1+\alpha)}{(p-1)!} \frac{V_p^*(t)}{t^{p-1+\alpha}} \tag{4.130}$$

The same developments can be made for the Caputo derivative, which permits the use of the method in case of non homogeneous initial conditions.

[6] The case of Eqn. 4.128 where $\alpha > 1$ can be treated in the same way
[7] Indeed, this is a necessary condition to apply operator $D^{1-\alpha}$, see section 4.3

4.7.4 Methods for accelerating the computation

The major drawback of fractional operators is inherent to their very definition: as the whole past of the function is needed to evaluate the derivative at time t, the time required for solving a FDE is much larger than for the resolution of the corresponding ordinary differential equation (ODE). Three approaches presented is this section allow the reduction of the computation time.

Fixed memory principle (FMP)

The simplest approach is to consider only the recent past at each step, i.e. to perform the integration over a fixed period. This can be done thanks to the fading memory property of fractional derivatives. This is commonly referred as the *fixed memory principle* and was described by Podlubny (1999).

Let $T < t$ be the length of the chosen integration period. The Caputo derivativewith $0 < \alpha < 1$ may be approximated by

$$D_t^{(\alpha)} f(t) \simeq \frac{1}{\Gamma(1-\alpha)} \int_{t-T}^{t} \frac{D_x^{(1)} f(x)}{(t-x)^\alpha}\, dx \tag{4.131}$$

The truncation error is equal to

$$E = \left| \frac{1}{\Gamma(1-\alpha)} \int_{0}^{t-T} \frac{D_x^{(1)} f(x)}{(t-x)^\alpha}\, dx \right| \tag{4.132}$$

Let $M = \sup_{x\in[0,t]} D_x^{(1)} f(x)$. Then

$$E \leq \left| \frac{M}{\Gamma(1-\alpha)} \int_{0}^{t-T} \frac{1}{(t-x)^\alpha}\, dx \right| \tag{4.133}$$

$$\leq \left| \frac{M}{\Gamma(2-\alpha)} \left(t^{1-\alpha} - T^{1-\alpha} \right) \right| \tag{4.134}$$

and the error vanishes for $T = t$. But for a fixed T, this approach results in a loss of precision order in the numerical method. This method dramatically reduces the computational time for sufficiently small T.

Short memory principle (SMD)

The short memory principle was proposed by Deng (2007). The version proposed here assumes that the fractional order of derivation $\alpha \in]0, 1[$.

The SMP consists in rewriting Eqn. 4.74 so that the convolution kernel decreases faster, thus decreasing the error commited when applying the FMP.

The first step is to split the integration domain in Eqn. 4.74

$$\begin{aligned} y(t_{n+1}) &= y(t_n) + \frac{1}{\Gamma(\alpha)} \int_{t_n}^{t_{n+1}} (t_{n+1} - \tau)^{\alpha-1} f(\tau, y(\tau))\, d\tau \\ &+ \frac{1}{\Gamma(\alpha)} \int_0^{t_n} \left((t_{n+1} - \tau)^{\alpha-1} - (t_n - \tau)^{\alpha-1} \right) f(\tau, y(\tau))\, d\tau \end{aligned} \tag{4.135}$$

The last term in Eqn. 4.135 is obviously related to the non local property of the fractional derivative operator. Written in this form, the convolution kernel exhitis a decay of order $2 - \alpha$ rather than $1 - \alpha$. Indeed, assuming that the equation is solved on a regular grid, the following equalities hold:

$$\begin{aligned} &\frac{1}{\Gamma(\alpha)} \int_0^{t_n} \left((t_{(n+1)} - \tau)^{\alpha-1} - (t_n - \tau)^{\alpha-1} \right) f(\tau, y(\tau))\, d\tau \\ &= \frac{1}{\Gamma(\alpha)(\alpha-1)} \int_0^{t_n} \left(\int_{t_n-\tau}^{t_{n+1}-\tau} z^{\alpha-2}\, dz \right) f(\tau, y(\tau))\, d\tau \\ &= \frac{1}{\Gamma(\alpha)(\alpha-1)} \int_{t_{n-1}}^{t_n} \left(\int_{t_n-\tau}^{t_{n+1}-\tau} z^{\alpha-2}\, dz \right) f(\tau, y(\tau))\, d\tau \\ &+ \frac{1}{\Gamma(\alpha)(\alpha-1)} \int_{t_{n-2}}^{t_{n-1}} \left(\int_{t_n-\tau}^{t_{n+1}-\tau} z^{\alpha-2}\, dz \right) f(\tau, y(\tau))\, d\tau \\ &+ \cdots + \frac{1}{\Gamma(\alpha)(\alpha-1)} \int_0^{t_1} \left(\int_{t_n-\tau}^{t_{n+1}-\tau} z^{\alpha-2}\, dz \right) f(\tau, y(\tau))\, d\tau \\ &= \sum_{k=0}^{n-1} \left(\frac{h}{\Gamma(\alpha)(\alpha-1)} \int_{t_{n-k-1}}^{t_{n-k}} (z_{k+1}^*)^{\alpha-2} f(\tau, y(\tau))\, d\tau \right) \end{aligned}$$

where $z_k^* \in [t_{k-1}, t_{k+1}]$. This faster decay of the convolution kernel allows to use the fixed memory principle with a lesser error than with the FMP since a lighter weight is assigned to the most distant values of the function f. The error e obtained by truncating the series after T terms satisfies the inequality:

$$e < \left| \frac{M}{\Gamma(\alpha)} T^{\alpha-1} h \right| \tag{4.136}$$

where

$$M = \max_{0 \le \tau \le t_n - T} f(\tau, y(\tau)) \tag{4.137}$$

Logarithmic memory principle (LMP)

The logarithmic memory principle was introduced by Ford and Simpson (2001). The basic idea is very simple: rather than discarding the value from the distant past, this method uses a logarithmic rather than a linear sampling of the time axis. Let's begin with the scaling property of the fractional derivative. For $w \in \mathbb{R}^+$ and $\alpha \in]0, 1[$, we have

$$D_t^{(\alpha)} f(t) = \frac{1}{\Gamma(1-\alpha)} \int_0^t \frac{D_x^{(1)} f(x)}{(t-x)^\alpha}\, dx \tag{4.138}$$

Hence, with w as above,

$$D_t^{(\alpha)} f(wt) = \frac{1}{\Gamma(1-\alpha)} \int_0^{wt} \frac{D_x^{(1)} f(x)}{(wt-x)^\alpha}\, dx \tag{4.139}$$

Substituting x by wx leads to

$$D_t^{(\alpha)} f(wt) = w^\alpha \frac{1}{\Gamma(1-\alpha)} \int_0^{t} \frac{D_x^{(1)} f(wx)}{(t-x)^\alpha}\, dx \tag{4.140}$$

Additionally, for $p \in \mathbb{N}$:

$$D_t^{(\alpha)} f(w^p t) = w^{p\alpha} \frac{1}{\Gamma(1-\alpha)} \int_0^{t} \frac{D_x^{(1)} f(w^p x)}{(t-x)^\alpha}\, dx \tag{4.141}$$

Thus, if a numerical scheme is used to compute a discrete approximate of the convolution integral, the weights necessary to calculate $\Omega_h^\alpha f(nh) \simeq I^{(\alpha)} f(nh)$ using a step length h can be used to calculate $\Omega_{w^p h}^\alpha f(nw^p h) \simeq I^{(\alpha)} f(nw^p h)$ using a step length $w^p h$ simply by multiplying the resulting sum by $w^{p\alpha}$

$$\Omega_h^\alpha f(nh) = \sum_{j=0}^{n} a_{n-j} D^{(1)} f(jh) \tag{4.142}$$

$$\Omega_{w^p h}^\alpha f(nw^p h) = w^{p\alpha} \sum_{j=0}^{n} a_{n-j} D^{(1)} f(jw^p h) \tag{4.143}$$

The practical implementation requires the following decomposition of the time interval:

$$\begin{aligned}[0,t] = {} & [0, t-w^m T] \cup [t-w^m T, t-w^{m-1} T] \cup ... \\ & \cup [t-wT, t-T] \cup [t-T, t]\end{aligned} \tag{4.144}$$

where $T > 0$. A step length h is used over the most recent time intervals $[t-T, t]$ and [t-wT,t-T]. Then this step length is multiplied by w, keeping the number of function evaluations constant over each interval. The fractional derivative can now be rewritten as

$$D_{[0,t]}^{(\alpha)} f(t) = D_{[t-T,t]}^{(\alpha)} f(t) + \sum_{j=0}^{m-1} D_{[t-w^{i+1}T, t-w^i T]}^{(\alpha)} f(t) + D_{[0,t-w^m T]}^{(\alpha)} f(t) \tag{4.145}$$

$$= D_{[t-T,t]}^{(\alpha)} f(t) + \sum_{j=0}^{m-1} D_{[t-wT, t-T]}^{(\alpha)} f(w^i t) + w^{m\alpha} D_{[0,t-w^m T]}^{(\alpha)} f(w^m t) \tag{4.146}$$

The last term in the right hand side of Eqn. 4.146 is generally dropped as the interval length is seldom an exact multiple of the step $w^m T$. It could be computed using a different scheme but in practice, the fading memory property ensures that the order of the method is

preserved without this extra computational time cost.

The following theorem has very important practical consequences :

> The logarithmic memory principle preserves the order of the underlying quadrature rule on which is based

Hence, if the error of the numerical scheme used to resolve a FDE is $O(h^p)$, the error made by using the LMP in this scheme will remain $O(h^p)$.

According to Ford and Simpson (2001), the computational cost of an algorithm using full memory over the interval $[0, w^m T]$ is $O(w^{2m})$ while the LMP is $O(w^{m+1})$.

4.8 Application of fractional derivation to the characterization of materials

During the last decade, the fractional derivatives have become a valuable tool in the modelling of viscoelastic materials such as polymers Soula and Chevalier (1998). This short section does not aim at providing the reader with a complete literature survey but presents a brief overview of the history of the use of fractional calculus in the characterization of materials.

Nutting (1921) found that fractional powers of time caused a better fit of stress relaxation curves of some materials. A few years later, Gemant (1936) observed that fractional powers of frequency better fit the stiffness and the damping properties of viscoelastic materials. Scott Blair and Caffyn (1949) suggested that the use of fractional time derivatives was required to meet the observations of Nutting and Gemant.

Caputo and Mainardi (1971) also found good agreement with experimental results when using fractional derivatives for the description of viscoelastic materials. They also established the relationship between fractional derivatives and the theory of linear viscoelasticiy. Bagley and Torvik (1983) then proposed a physical justification for the use of the fractional operator in the framework of viscoelastic material modelling. They then established the equation of motion of a plate immersed in a Newtonian fluid and connected by a spring to a point (Bagley and Torvik (1984)). They also determined the constraints to apply to a three-parameters fractional viscoelatic solid, ensuring that the model predicts a non negative rate of energy dissipation and internal work.

More recently, Schmidt and Gaul (2002b) proposed an implementation of a fractional constitutive law in the finite element method. Diethelm (2006a) designed an efficient algorithm for the evaluation of convolution integrals, suitable for the evaluation of solutions of fractional differential equations. This algorithm implements the logarithmic memory principle and does not assume an equispaced time grid to discretize the solution, making it suitable for a finite element code.

Fractional constitutive models have been studied on a theoretical point of view by Adolfsson (2003) and Adolfsson and Enelund (2003). Diethelm and Freed (2006b) applied fractional calculus to the modelling of calcaneal fat pad.

4.9 Conclusion

The fractional derivation operator is a tool discovered centuries ago but which has only been used recently for the modelling of the behaviour of viscoelastic materials.

The fractional derivatives extend the well known properties of the integer-order derivatives. While the Riemann operator was intensively investigated by the mathematicians, the Caputo operator is preferred in practical problems, as it sets the derivative of a constant to zero, contrarily to the other.

The fractional derivation operator proved to be able to give a complete description of a system since it was shown that only one fractional differential equation of order $\alpha \in]0, 1[$ is equivalent to an infinite system of first order ordinary differential equations.

This remarkable result is likely to be a consequence of the non local structure of the fractional derivatives. The counterpart is that their evaluation, as well as the resolution of fractional differential equations, are more time consuming compared to the traditional derivatives. Fortunately, their convolution kernel exhibits a fast decay, leading to the development of three computation acceleration methods: the fixed memory, the logarithmic memory and the short memory.

Part II

Literature review

CHAPTER 5
LITERATURE REVIEW

5.1 Introduction

This chapter is devoted to the review of the existing literature on the modelling and the experimental characterization of brain tissue.

The design of a biomechanical model of the brain aims at two major applications: the image-guided neurosurgery (including the planning of the operation) and the prediction of traumatic injuries (T.B.I.). These two applications involve considerably different loading velocities and time scales, it is thus not surprising that they use model of different kinds. For example, it is commonly admitted that the hydrocephalus is better represented with the poroelastic formulation while hyperelastic and viscoelastic models are used in the framework of traumatic brain injury prediction (see section 5.2).

Like the models, the experimental protocols aiming at the characterization of brain tissue depend on the studied phenomenon. In the case of T.B.I., shear experiments are mainly carried out contrarily to the surgical application where compression and tensile tests are also achieved.

The field of brain biomechanics has been investigated for more than 40 years now and there is still no consensus within the community on topics such as the fluid or solid nature of the brain, or its compressibility. Since the experiments are seldom conducted in the same conditions from one author to another, it is very difficult to compare the results and the properties observed.

5.2 Modelling of the brain tissue

5.2.1 Elastic models

Linear elastic models

Although it was proven experimentally that brain tissue exhibits properties such as relaxation and a strong strain-rate dependence of the stresses (see section 5.3), some authors model it as a linear elastic material. Clatz et al. (2004b) used a linear elastic model in the framework of the prediction of brain deformation during neurosurgical procedures. Vigneron

(2009) used both linear elastic and viscoelastic formulations in her thesis focused on the non rigid registration of peroperative images with preoperative ones. In the particular case of the brain shift[1], Wittek et al. (2008) showed that the maximum difference in displacement between a linear elastic and a hyperviscoelastic model did not exceed 0.2 mm which is below the resolution of the traditional MRI scanners (0.5mm - 1 mm).

Hault et al. (2005) also used a linear elastic model of the brain tissue to concentrate on the influence of the cerebrospinal fluid when the brain is subjected to an impact. Mehdizadeh et al. (2008) used the Bridgman method (see Ling (1996)) to describe the behavior of white and grey matters in tension taking the necking phenomenon into account.

Finally, Ueno et al. (1995) used a linear elastic model for brain tissue in a finite element simulation for the modelling of an impact.

Nonlinear elastic models

In their finite element modelling of brain tumour mass-effect, Mohamed and Davatzikos (2005) considered a hyperelastic formulation to describe the behaviour of the brain. They ignored the viscous effects since the characteristic time of tumor growth is much larger than the relaxation time. They also considered that the brain is weakly compressible. Their strain energy density function is based on Ogden's one (see section 3.3) and is of the form of:

$$W = \frac{2\mu}{\alpha^2}\left(\bar{\lambda}_1 + \bar{\lambda}_2 + \bar{\lambda}_3 - 3\right) + \frac{1}{D_1}\left(\frac{J}{J_{th}} - 1\right)^2 \tag{5.1}$$

where $\bar{\lambda}_i = J^{-1/3}\lambda_i$, λ_i $(i = 1, 2, 3)$ are the principal stretches, J is the Jacobian and J_{th} is the thermal volume ratio. μ and D_1 are material parameters.

Meaney (2003) used a different approach: he tried to determine the relationship between the structure of the white matter and its macroscopic behaviour. From a reasoning about the structure of the axons, he derived an expression for the tensile force needed to stretch them. He then compared this value to ones obtained from three different hyperelastic strain energy density functions. Let's note that the first one is used to model isotropic material.

$$W(I_1, I_2) = \frac{\mu_1}{2}(I_1 - 3) + \frac{\mu_2}{2}(I_2 - 3) \tag{5.2}$$

$$W(I_1, I_4) = C\left(\exp(C_1(I_1 - 3) + C_2(I_4 - 1)^2)) - 1\right) \tag{5.3}$$

$$W(\lambda, I_4) = \frac{2\mu_g}{\alpha_g^2}\left(\lambda^{\alpha_g} + 2\lambda^{-\alpha_g/2} - 3\right) + \frac{2\mu_a}{\alpha_a^2}\left(I_4^{\alpha_a/2} + 2I_4^{-\alpha_a/4} - 3\right) \tag{5.4}$$

Eqn. 5.2 describes a classical Mooney-Rivlin model (see section 3.3), Eqn. 5.3 is due to Fung (1981) and Eqn. 5.4 comes from Ogden (1984). Subscripts a and g stand for the axonal fibers and the glia respectively (see section 1.2). The reason why Meaney chose a hyperelastic functions rather than (hyper)viscoelastic ones is the sake of simplicity.

Meaney derived an expression for the Lagrange stress T[2] for the white matter of the guinea pig optic nerve in the case of a tensile test. Firstly, he defined the undulation U as

[1] The initial displacement and/or deformation of the brain following the opening of the skull.

[2] Since the only non-zero component of the stress tensor is in the loading direction, the index is omitted.

the ratio

$$U = \frac{l_t}{l_0} \tag{5.5}$$

where l_0 is the end-to-end distance and l_t is the true axonal length, as illustrated in Fig. 5.1.

In a tensile test, an axon can only be stretched if the stretch ratio λ is greater than the

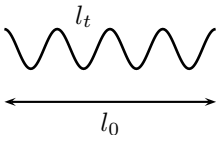

Fig. 5.1: End-to-end (l_0) and true (l_t) axonal length.

undulation value U. This leads to the definition of the axon stretch ratio λ_a

$$\lambda_a = \frac{\lambda}{U} \tag{5.6}$$

Meaney then assumed that the mechanical behaviour of a single axon is described by a neo-Hookean constitutive equation (see section 3.3), which, in the case of a tensile loading, is written

$$T_{axon} = C\left(\lambda_a - \frac{1}{\lambda_a^2}\right) \tag{5.7}$$

The total force exerted on the axons is obtained by summing the contributions:

$$F_{axons} = \int_{U=1}^{U=U_{max}} N\, A_{axon}\, f(U)\, C\left(\frac{\lambda}{U} - \frac{U^2}{\lambda^2}\right) dU \tag{5.8}$$

where N is the total number of axons, A_{axon} the mean cross section of the axons and $f(U)$ a probability density function. Since the white matter is not only made of axons but also of glial cells (see section 1.2), another contribution must be taken into account:

$$F_{glia} = 0.033C\left(\lambda - \frac{1}{\lambda^2}\right) A_{nerve} \tag{5.9}$$

The Lagrange stress is finally expressed as the weighted sum of the contribution from the glia and the axons.

By comparing hyperelastic models with structural models, Meaney hopes to be able to predict the circumstances that will lead to axonal injuries in the white matter of humans.

Finally, Velardi et al. (2006) used the model defined by Eqn. 5.4 to characterize separately the behaviour of grey and white matters both in tension and compression. Contrarily to Meaney who chose hyperelastic law for their simplicity (compared to hyperviscoelastic ones), Velardi et al. claims that the viscous effects can be disregarded in impact loading as they have limited influence on the short term response of the brain tissue. By comparing the results from the model to their experimental data, Velardi et al. reached the conclusion that the model must be refined and should have at least two terms for the isochoric part (one for the response in tension, the other for the response in compression) and at least one term for the

fiber reinforcing part. The corresponding strain density function would thus be of the form of

$$W = \sum_{n=1}^{N} \frac{\mu_n}{\alpha_n} (\lambda_1^{\alpha_n} + \lambda_2^{\alpha_n} + \lambda_3^{\alpha_n} - 3) + \sum_{r=1}^{R} \left(\nu_r I_4^{\beta_r} + \xi_r I_4^{\gamma_r} - \nu_r - \xi_r \right), \ \lambda_1 \lambda_2 \lambda_3 = 1 \quad (5.10)$$

5.2.2 Poroelastic models

Since the brain is a highly hydrated tissue, some authors chose the poroelastic formalism to describe its mechanical behaviour. Despite stating that there is indubitably viscoelasticity in brain tissue, Miga et al. (2000b) asserted that a pure viscoelastic description would be limited given the inherent coupling between deformation and hydrodynamic behaviour. The model they designed assumes that the solid matrix is linear elastic, isotropic and follows small strains approximation. Hooke's law is thus employed. The interstitial fluid flows according to Darcy's law. Because of the lack of knowledge in this domain, the solid matrix is assumed to be saturated with fluid. In their global model of the brain, Miga et al. did not take the flows of the ventricular system into account. The strain-rate dependence is ensured by the existence of a finite permeability[3]. However, poroelastic models are solely used in neurosurgical applications and hydrocephalus studies. Miga et al. (2000a) validated their model by comparing the results of finite element analysis with in vivo compression experiments on three pigs. The model achieved a 75 to 85 percent predictive capability of the displacements.

The study of the hydrocephalus and of oedemas was treated with the poroelastic formalism by Nagashima et al. (1987, 1990, 1994) and Kazmarec et al. (1997).

Cheng and Bilston (2007) proposed a poroviscoelastic model. To the governing equations presented in section 3.5, they added the relaxation through the use of the Prony series:

$$G(t) = G_0 \left(1 - \sum_{k=1}^{N} g_k^p (1 - \exp(-t/\tau_k)) \right) \quad (5.11)$$

where $G(t)$ (resp. G_0) is the time-dependent (resp. initial) shear relaxation modulus, the g_k^p are the relaxation coefficients and the τ_k are the relaxation times. According to these authors, the poroelastic models can only take long term relaxation into account while poroviscoelastic ones are able to deal with shorter characteristic times.

Franceschini (2006) claimed that, regarding the results of her strain experiments under controlled drainage conditions, the brain tissue behaves like a porous solid. She also found that the tissue exhibits a stress softening. This property is taken into account by using a modified Ogden strain energy density (Ogden and Roxburgh (1999))

$$W(\lambda, \eta) = \eta W(\lambda) + \varphi(\eta) \quad (5.12)$$

Eqn. 5.12 is called a *pseudo-energy function*. $W(\lambda)$ is the classical Ogden energy density function.

The function η is of the form of

$$\eta = 1 - \frac{1}{r} \operatorname{erf} \left(\frac{1}{m} (W(\lambda_m) - W(\lambda)) \right) \quad (5.13)$$

[3]Sometimes called *hydraulic conductivity*

where r and m are material parameters and λ_m is the stretch at which the unloading begins. Although she acknowledged the existence of a viscous component of the brain tissue, Franceschini stated that her results proved that it is less important than the consolidation mechanism (Terzaghi (1943)) for the delayed volumetric deformation.

Finally, let's mention that a 2d finite element model in plane stress state was designed in our department by Lecomte (2006). A lateral ventricle, the subarachnoid space and white and grey matters were included in this model. They were all described, even the ventricle, by poroelastic solids with different parameters. The following initial conditions were used (see Fig. 5.2):

- the displacements are imposed for each node of the subarachnoid space in contact with the skull,
- the contacts of the ventricle with the cerebellum and the spinal cord are taken into account by springs elements (k_1 and k_2)
- similarly, a small glide between white and grey matters and the skull was allowed, modelling the presence of membranes (springs k_3),
- the pressure was fixed initially to a hydrostatic distribution with the 0 level placed at the highest nodes of the brain

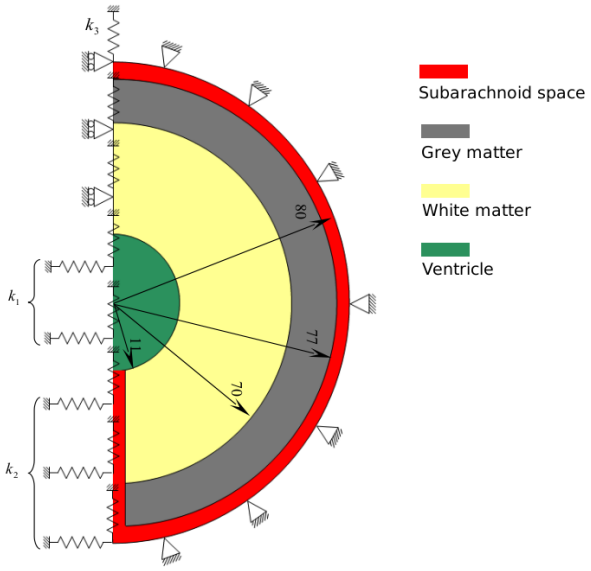

Fig. 5.2: Lateral view of the simplified brain model. The distances are in millimetres.

The aim of the study was to determine the displacements that occur in the brain after a craniotomy through a step by step calculus with equilibrium iterations. The simulation was divided in three phases :

1. The patient is laid on the operation table. The brain is subjected to gravity. The final time is such that equilibrium is reached,

2. the pressure of the exterior nodes of the elements where the skull is opened is decreased to zero,

3. the embedded degrees of freedom where opening takes place are freed.

This artificial decomposition allowed to find the root of possible problems.

The displacements obtained were at least 1 order of magnitude smaller than those observed during brain shift. Numerous explanations can be given : the number of parameters to be adjusted, the simplified geometry,... This praiseworthy attempt nevertheless took several interactions into account and deserves to be further explored.

are six times higher than at a "slow"[4] one. Biphasic models are unable to reproduce this behavior due to the underlying assumption of solid matrix (hyper)elasticity.

5.2.3 Viscoelastic models

Analog models

The analog models were the first viscoelastic models used in the framework of brain tissue modelling. Despite their spring and dashpot representation may suggest that they are only used for the description in tension and compression, the analog models were also used to identify the behaviour in shear. Tab. 5.1 presents some analog models encountered in the literature.

The first two models and the generalized Maxwell models are linear, while the others contain one or several nonlinear component(s) (symbolized by an oblique arrow). The four-parameters models are said to be fluid models because of the dashpot in series, while Donnelly and Medige (1997) intentionally used a solid model. According to them, the fluid models cannot represent the quasistatic behaviour of the brain.

Bandak (1995) used a Maxwell model in parallel with a spring for his study on traumatic brain injuries. He enriched this model with a cumulative strain damage measure which makes it able to reproduce the stress softening behaviour.

Skrinjar et al. (2002) designed a viscoelastic global brain model for real time applications. A linear stress-strain relationship was chosen. In this damped spring-mass model, nodes are linked through a Voigt model. The main problem is that the model parameters are mesh dependent, i.e. if a denser (or sparser) mesh is desired, the model should be readjusted to obtain the same behavior, which is everything but practical.

Hyperviscoelastic models

The brain modelling for neurosurgical application can hardly be separated from the name of Professor Karol Miller. Since the late 90's, he concentrated his effort on the design of constitutive equations for brain tissue.

The first model Miller and Chinzei (1997a) proposed was based on the hyperviscoelastic formulation. The extended Mooney-Rivlin-based potential was written :

[4] 0.005mm/min

Reference	Loading	Model
Galford and McElhaney (1970)	Compression	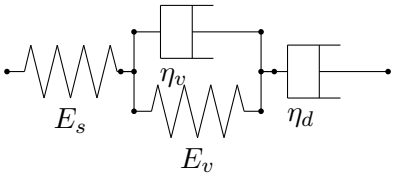
Shuck and Advani (1972)	Shear	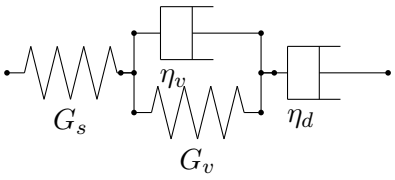
Pamidi and Advani (1978)	Compression	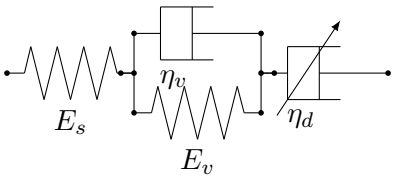
Pamidi and Advani (1978)	Compression	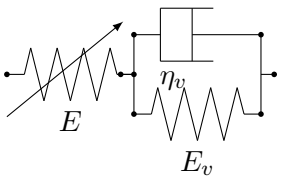
Donnelly and Medige (1997)	Shear	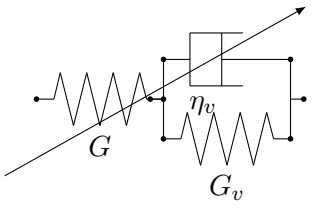
Brands (2002)	Shear	Generalized Maxwell model (5 branches)
Hrapko et al. (2005)	Shear	Generalized Maxwell model (3 branches)

Tab. 5.1: Review of analog models.

$$W = \int_0^t \left\{ \sum_{i+j=1}^{N} \left[C_{ij0} \left(1 - \sum_{k=1}^{n} g_k (1 - e^{(\tau - t)/\tau_k}) \right) \right] \frac{d}{d\tau} \left[(I_1 - 3)^i \ (I_2 - 3)^j \right] \right\} d\tau \quad (5.14)$$

In expression 5.14, the C_{ij0} are hyperelastic coefficients, the τ_k are relaxation times and the g_k are relaxation coefficients. For infinitesimal strain conditions, the sum of constants C_{100} and C_{010} has the physical meaning of one half of the instantaneous shear modulus. The relaxation function is a Prony series. Unconfined compression tests were performed to identify the parameters of the model.

Like Velardi et al. (2006) and Franceschini (2006), Miller and Chinzei (2002) found that the brain tissue behaves differently in tension and in compression. They then replaced the Mooney-Rivlin strain energy density by the Ogden one with $p = 1$ (see section 3.3). The resulting potential is of the form of

$$W = \frac{2}{\alpha^2} \int_0^t \left[\mu_0 \left(1 - \sum_{k=1}^{n} g_k \left(1 - e^{-t/\tau_k} \right) \right) \frac{d}{d\tau} \left(\lambda_1^\alpha + \lambda_2^\alpha + \lambda_3^\alpha - 3 \right) \right] d\tau \quad (5.15)$$

where μ_0 stands for the instantaneous shear modulus in undeformed state and α is a parameter.

Gao et al. (2006) exploited the constitutive equation Eqn. 5.15 in the modelling of the human brain with detailed anatomy. The anatomical features, including the ventricles and several sub cortical structures, came from a brain atlas and not from pictures from an actual patient. Prange and Margulies (2002) also used that type of constitutive equation.

Nava et al. (2004) enriched a constitutive equation based on a Prony series and an extended Mooney-Rivlin strain energy density function, like the one described in Eqn. 5.14, with a damage model suitable for the modelling of the stress softening of the material. To that purpose, the hyperelastic coefficients were modified according to

$$C_{ij0} = \frac{\bar{C}_{ij0}}{1 + SV} \quad (5.16)$$

$$\dot{SV} = \beta \left(\bar{I}_1 - 3 \right) \quad (5.17)$$

where $\bar{C_{ij0}}$ are the hyperelastic coefficient before any loading and SV is the damage. β is a material coefficient.

Nonlinear viscoelasticity

Brands et al. (2004) focused on the design of a 3D nonlinear viscoelastic constitutive model for brain tissue during impact. They used a differential decoupled 3D constitutive law. According to them, hyperviscoelastic models are more often used than the decoupled ones but are unable to reproduce the full nonlinear behavior that appears at frequencies above 44 Hz. The volumetric part of the model is assumed to be purely elastic, while several relaxation modes are included in the deviatoric equation leading to a large number of parameters to identify[5]. The ith viscous mode is described by the equation

$$\mathbf{D}_i = \frac{\boldsymbol{\sigma}_i^v}{2\eta_i} \quad (5.18)$$

[5] A differential model due to Bilston et al. (2001) counts no less than 30 parameters. According to Bilston this causes the identification to be very laborious but she argues that it is improbable to get a realistic model with less coefficients.

where η denotes the viscosity coefficient, $\mathbf{D}$ is rate of deformation tensor and $\boldsymbol{\sigma}^v$ is the viscous part of the stress. This model can reproduce the non-<F11> linear shear softening that occurs in stress relaxation experiments as well as the nonlinear shear hardening in oscillatory experiments. The model was implemented in a finite element code to simulate the transient phase in shear relaxation experiments. The stresses are overestimated by more than 30%, whatever the strains. Furthermore, if the strain exceeds 27%, the stiffness matrix becomes negative. This can be corrected by using a Ogden model instead of a Mooney-Rivlin model, but it is then unable to reproduce shear softening.

Darvish and Crandall (2001) agreed with the nonlinear viscoelastic behaviour of the brain when subjected to deformation impulses with a duration of only a few milliseconds. According to them, the nonlinear effects in the brain constitutive relation are of particular importance for two reasons :

1. a nonlinear model is more accurate for finite deformations,
2. the injury pattern predicted by a nonlinear model can potentially differ from that of a linear one. According to the linear theory of materials with memory, the waves produced by a step-wise input are diffusive in character, broadening with time, whereas the nonlinear theory permits the development of discontinuities in the form of shock or acceleration waves.

The model used is composed of 3 hereditary integrals and is of the form of

$$\Sigma_{12} = \int_0^t \Psi_1(t-\tau_1)\dot{E}_{12}(\tau_1)d\tau_1 + 4\int_0^t\int_0^t \Psi_2(t-\tau_1,t-\tau_2)\dot{E}_{12}(\tau_1)\dot{E}_{12}(\tau_2)d\tau_1 d\tau_2 + \int_0^t\int_0^t\int_0^t \Psi_3(t-\tau_1,t-\tau_2,t-\tau_3)\dot{E}_{12}(\tau_1)\dot{E}_{12}(\tau_2)\dot{E}_{12}(\tau_3)d\tau_1 d\tau_2 d\tau_3 \quad (5.19)$$

where Σ_{12} is shear component the pulled back Cauchy stress tensor to the frame that is rotated with the rotation component of the deformation gradient and E_{12} is the (1,2) component of the Green Lagrange strain tensor[6]. According to the authors, that kind of formulation can describe all the possible nonlinearities in the response of materials with memory.

Shear tests were performed to calibrate the model. These experiments showed a strongly nonlinear behavior, even for strains as small as 1%.

To our best knowledge, El Sayed et al. (2008) were the only authors to propose a model including a plasticity component. The global potential they define is the sum of an elastic, a viscoelastic and a plastic potentials:

$$A = W^e(e^e_j,\theta^e) + W^p(e^p,\theta^p) + \sum_{i=1}^{M} W^e_i(e^e_{ij},\theta^e_i) \quad (5.20)$$

where $i = 1,\cdots,M$ is the number of viscoelastic mechanisms, W^e and W^e_i are elastic strain energy densities, W^p is the plastic stored energy, e^e, e^e_i, e^p are elastic and plastic logarithmic shear strains, e^e_j, e^e_{ij} are the eigenvalues of the elastic logarithmic shear strains and $\theta^e, \theta^e_i, \theta^p$ are elastic and plastic logarithmic volumetric strains. $j = 1,2,3$ indicates eigen-components

[6]The superscript GL was omitted to make Eqn. 5.19 clearer.

and i stands for the number of the viscoelastic mode. The elastic strain energy density is chosen to be a sum of Ogden functions (see section 3.3). The plastic function is written

$$W^p(e^p, \theta^p) = \frac{n\sigma_0 e_0^p}{n+1}\left(1+\frac{e^p}{e_0^p}\right)^{\frac{n+1}{n}} + \frac{n\sigma_0 e_0^p}{n+1} N_v \frac{4\pi a^3}{3} g(\theta^p, n) \tag{5.21}$$

where σ_0 is the yield stress, e_0^p is the reference plastic strain, n is the hardening exponent, N_v designates the void density per unit undeformed volume of the material, a is the void radius and

$$g(\theta^p, n) = \int_1^{1/f} \left(1+\frac{2}{3\varepsilon_0^p}\log\left(\frac{x}{x-1+\frac{f_0}{f_0+\exp(\theta^p-1)}}\right)\right)^{\frac{n+1}{n}} dx \tag{5.22}$$

where f_0 and f are respectively the initial and current volume fractions. The first term on the right hand side of Eqn. 5.21 models the permanent shear damage and the second term models the growth of voids in the material. The reader should refer to El Sayed et al. (2008) and references therein for more information about this model.

5.3 Experimental characterization

5.3.1 In vitro tests

In vitro tests are generally carried out on tissues obtained as by products at slaughterhouses. It is possible to perform a large number of experiments since those tissues are free and available in large quantities. However, there is no control on what happened to the brains before they are collected.

The way the sample is carved is important since it may cause permanent stresses and/or strains in the sample. The most commonly encountered technique is the use of a dice cutter, but other tools were tested by Aimedieu (2004).

If the geometry of the sample is computed with the digital image correlation technique (see chapter 2), the application of the speckle pattern must not change the mechanical properties of the tissues.

The samples can be composed of white matter, grey matter or both. In the first two cases, they are smaller and require more care when handled. The postmortem time and the method of conservation of the samples as well as their origin (porcine, bovine, human) are also important factors that may influence the results.

Compression and tensile tests

The compression and tensile tests are generally performed to characterize the brain tissue in the framework of neurosurgical applications. Indeed, the loading velocities of the testing machine used in literature do not exceed 1000 mm min^{-1}, which, for the size of the tested samples, do not lead to strain rates representative of impact loading situations where they are superior to 10 s^{-1} (Brands et al. (2004)).

Miller and Chinzei (1997a) performed compression tests at three loading velocities (0.005 mm min^{-1}, 5 mm min^{-1} and 500 mm min^{-1}) on cylindrical samples carved from swine brains. The diameter and height of those samples were equal to 30 mm and 13 mm respectively. To illustrate the scatter of the results, the curves they obtained are shown in Fig. 5.3

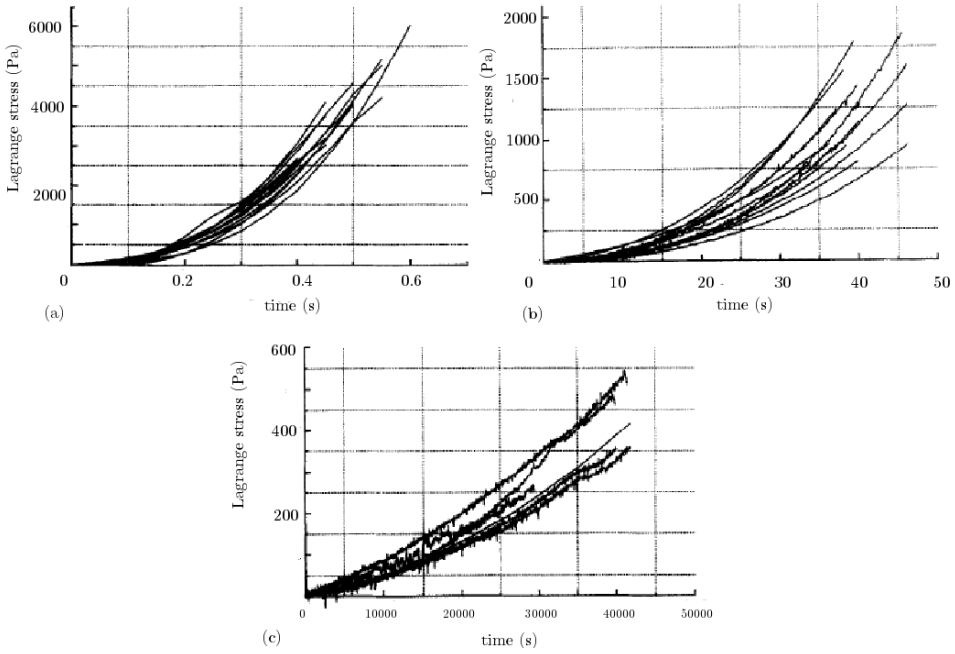

Fig. 5.3: Compression test: scatter of the results. Loading velocities: (a) 500 min mm^{-1}, (b) 5 min mm^{-1} and (c) 0.005 min mm^{-1}. (Reference: Miller and Chinzei (1997a))

Cheng and Bilston (2007) also conducted unconfined compression tests on calve brains. Contrarily to Miller and Chinzei (1997a), they performed a preconditioning of their samples before each test. The preconditioning consists in applying a preloading to the samples so that they are assumed to be in the same state before the actual experiment.

Aimedieu et al. (2001) performed compression tests on white matter samples from porcine brains to prove its anisotropy. The samples were taken in two perpendicular directions and the white matter reveals to be anisotropic for compression factor $\lambda \geq 25\%$, $(\lambda = l/l_{initial})$.

By using a split Hopkinson pressure bar, Pervin and Chen (2009) were able to test both white matter and grey matter at strain rates ranging from 0.01 s^{-1} to 3000 s^{-1}.

The boundary condition at the tissue-compression plate interface is very important. Numerical simulations performed by Wu et al. (2004) showed that the stresses vary by more than 50% between the friction and frictionless cases. To deal with this problem, some authors, like Miller and Chinzei (1997a), glued their samples to the plate while others, like Prange and Margulies (2002), lubricated the plates to eliminate the friction.

Miller (2001) proposed a method to test the brain tissue in tension. He used a surgical glue to fix the cylindrical sample to the plates of the testing machine and analytically determined the shape of the deformed sample. This technique was then applied by Miller and Chinzei (2002) where they demonstrated that the stiffness of the brain is larger in compression that in tension. Mehdizadeh et al. (2008) used the same protocol as Miller and Chinzei for their tensile tests on bovine white and grey matters.

Velardi et al. (2006) used strips of white and grey matters (4-6 cm long, 1 cm wide, 0.2-0.5 mm thick) from bovine brains. The strips were placed between grips and the no-slip condition was checked by visual inspection. The imposed displacement was imposed at a rate of 5 mm

s^{-1}.

Franceschini (2006) performed cyclic tension-compression experiments at 5 mm min^{-1} on human brain tissues. The samples were cylindrical and prismatic shaped and taken at different orientation and location within the brain. She successfully demonstrated the heterogeneity of the mechanical properties of the brain, as shown in Fig. 5.4

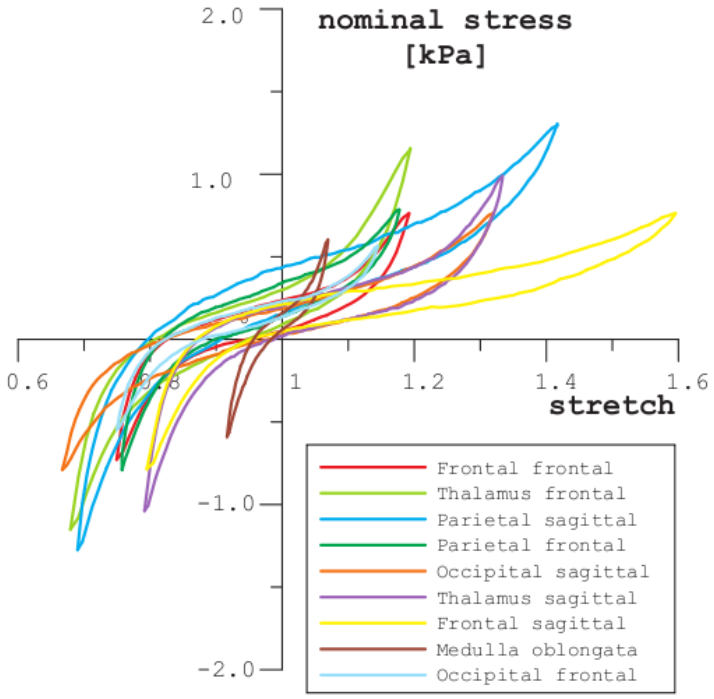

Fig. 5.4: Nominal stress versus stretch for tension/compression tests on prismatic specimen of white and grey matters.(Reference: Franceschini (2006)).

Shear tests

The shear tests are mainly used in the framework of traumatic brain injury prediction, the reason being that the shear modulus of the brain is a few order of magnitude smaller than its bulk modulus (Donnelly and Medige (1997)).

In typical shear tests, the sample is glued to the plates. Either a rotative motion (for torsion) or a translation (for pure shear) is imposed to the plates. In impact situations, high frequencies are reached and cannot always be reproduced in a laboratory. The time-temperature superposition principle (see appendix C) is then used to extend the range of frequency.

Hrapko et al. (2005) performed shear cycle experiments (in torsion) on porcine brain tissues at different frequencies (0.16 Hz, 1.6 Hz and 16 Hz). The loading was repeated, with increasing amplitude and/or frequency on the same sample and relaxation took place between the loadings to study the possible damage due to a previous strain history. These tests

showed that the immediate damage is negligible and that the samples stiffen with increasing frequencies.

Darvish and Crandall (2001) carried out cyclic shear tests on bovine brain tissues at frequencies ranging from 0.5 Hz to 200 Hz and with amplitudes up to 20% Green Lagrange shear strain. Their input signal was a superposition of three sines and surprisingly, non-integer harmonics were found in the output force signal. Their results showed that a quasi linear viscoelastic model (like hyperviscoelastic ones) is unable to predict the behaviour of the brain at high (>44 Hz) frequencies, contrarily to their fully nonlinear model described by Eqn. 5.19.

5.3.2 In vivo tests

The in vivo tests have the great advantage to take account of the blood circulation. However, it is generally more difficult to get accurate measures of the displacements and the strains.

Indentation tests

During the indentation tests, a part of the skull of the animal is removed. A metallic shaft, the indentor, is used to impose a displacement on a part of the brain, as illustrated in Fig. 5.5

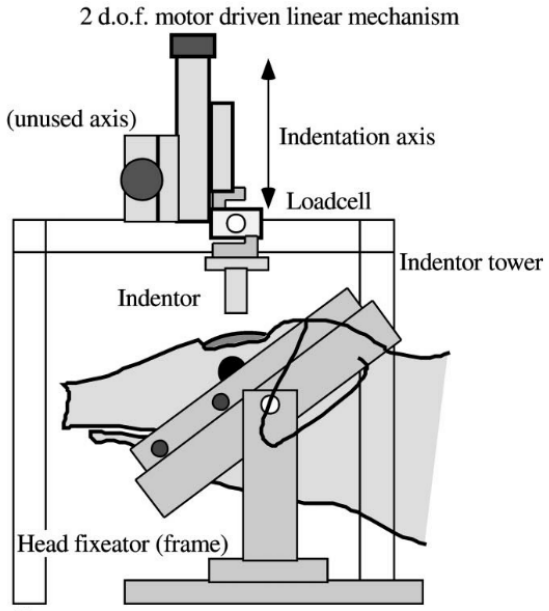

Fig. 5.5: Schematic view of the in vivo indentation experiment on a swine brain. (Reference: Miller et al. (2000))

Miller et al. (2000) used this technique on a swine. They compared the experimental results with the output of a finite element model and found that the force predicted by the model was 30 % lower than that measured in vivo.

Miga et al. (2000b) employed the same technique on a porcine subject. They monitored the displacement of specific points in the brain by inserting 20 small (1 mm) stainless steel beads in the tissue. Their positions were determined throughout the experiment by performing CT scans.

Aspiration tests

In aspirations tests, a small transparent tube is placed in contact with the tissue. A weak vacuum is then created in the tube yielding to the aspiration, and thus the deformation, of the tissue inside the tube. The intensity of the vacuum is modified and recorded during the tests. The deformation of the surface is recorded by a digital camera and analysed to result in a quantitative measure. The principle of the device is presented in Fig. 5.6

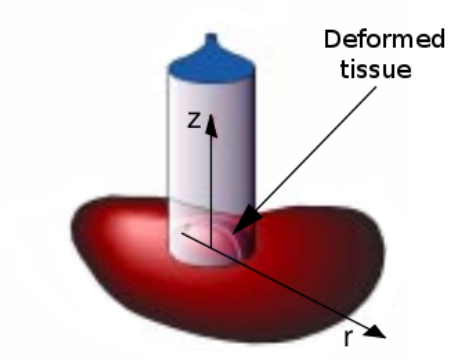

Fig. 5.6: Principle of the aspiration device. (Reference: Vuskovic et al. (1999))

This device is due to Vuskovic et al. (1999), who investigated the behaviour of bovine liver, and was used by Ozawa et al. (2001) on grey and white matter. The major problem when using this device, according to Vuskovic, is the estimation of the initial configuration. The stress free state is then assumed.

Non invasive in vivo measurements

The magnetic resonance elastography (M.R.E.) is a non invasive technique of measurement of brain mechanical properties. A vibration is applied to the head of the subject and the mechanical response of the brain tissue is monitored by a M.R.I. scanner (see Greenleaf et al. (2003)).

Sack et al. (2009) performed M.R.E. on 55 volunteers to determine the impact of aging and gender on brain viscoelasticity. They showed that the brain undergoes a constant "liquefaction", i.e. a steady decrease of the elasticity combined with an increase of the viscosity with the age. A significant difference was also observed regarding the gender, the female brain being on average 9% more solid-like than the male one.

5.3.3 Measurements with the D.I.C.

Lauret (2007) measured the acceleration-induced strains in porcine brain slices. Before applying the speckle pattern, she prepared the slices according to this protocol:

- take the slice out of the CSF in which it was laying and remove the CSF layer with paper tissue,
- use cold air from an air drier until the surface is dry enough for the paint to adhere,
- apply the pattern,
- use cold air to dry the paint

The black paint constituting the speckle pattern was applied with an airbrush. This is the only reported case, to our best knowledge, of the use of the D.I.C. in the framework of brain tissue characterization.

Zhang and Arola (2004) proposed general advice concerning the use of the D.I.C. for the measurement on soft tissues. They successfully used the method on arterial tissue, hoof horn and loosening in cemented total hip replacement. Although their experiments were in vitro, they think that the method could be transposed to in vivo experiments.

5.3.4 Influence of the testing parameters

When dealing with soft tissues, special care must be taken on the carving and the handling of the samples as well as on the environmental conditions. Furthermore, a number of testing parameters may influence the results, such as the temperature, the humidity, the animals chosen to perform the experiments, their age, ...

Searching causes for the dispersion of the experimental results in the literature, Hrapko et al. (2008) studied the effects of three parameters on the results of shear tests: the temperature, the anisotropy of the tissue and the preconditioning. They established that the mechanical behaviour of the brain is temperature-dependent and is affected by a preconditioning. They observed that increasing the preconditioning compression force from 5 mN to 10 mN increases the shear modulus by 20%. They also confirmed preceding conclusions about the anisotropy of the brain. They concluded that the experimental protocol used should be carefully and exhaustively documented.

Garo et al. (2007) investigated the effects of postmortem time and sample preparation on the response of the porcine brain tissue in oscillatory shear tests. Two methods were used to cut a slices from the brains, a vibrating blade and a rotating disk vertical slicer. From the slices, cylindrical samples were taken with a cork bore. The postmortem time at which the samples were tested ranged from 150 min to 480 min. Garo et al. reached the conclusion that the results obtained are strongly influenced by the postmortem time and by the stress/strain history induced by the cutting procedure. According to them, the tissues must be tested within 6 hours after the death in order to get reproducible results. They quantified the increase of shear modulus at 27 Pa h^{-1} after this time.

Gefen and Margulies (2004) compared the results of in vivo and in situ indentation experiments on a porcine subject. For the in situ case, the pig was dead but a device ensured that the blood circulation was maintained. They discovered that only the long-term constant of relaxation τ_{long} significantly differed between *in vivo* and *in situ*. The data they collected

showed no significant difference with perfusion pressure in any properties, except for τ_{long}. They then concluded that the pressurized vasculature of the brain does not represent a major contribution to the mechanical properties of cortical brain tissue. They also showed that the confinement of the brain within the skull may affect some measured properties. Since most of the tissue properties seem to be perfusion pressure independent, Gefen & Margulies suggest that the brain's mechanical characteristics could be determined , in a manner free from boundary conditions or potential test mode artifacts. They also stated that intra- and inter-species variability and testing protocols were responsible for discrepancies, but not as much as the postmortem time for testing. Only properties measured in fresh (or nearly fresh) brain tissue should be compared.

5.4 Validation on clinical case

Wittek et al. (2007) implemented the constitutive equation Eqn. 5.15 in a patient-specific FE model. The aim was to study the displacements due to the brain shift. The mesh was realized using MRI preoperative images of a patient undergoing brain tumor surgery. They were processed and then fed a mesh generator[7]. The resulting mesh counted about 15,000 elements. The pia matter and the falx cerebri were modelled with the help of membrane elements. The ventricles were assigned properties of a very soft compressible elastic solid with Young's modulus of $10Pa$ and Poisson's ratio of 0.1 to allow volume decrease during the brain shift. No data on mechanical properties of brain tumors are available in the literature, but it is commonly acknowledged that they are associated with stiffer tissue. Constitutive equation (5.15) was used with a μ_0 three times larger than for a healthy tissue. The results are very encouraging, as shown in Fig. 5.7 and 5.8. The maximal error on the displacement is equal to 2.96 mm.

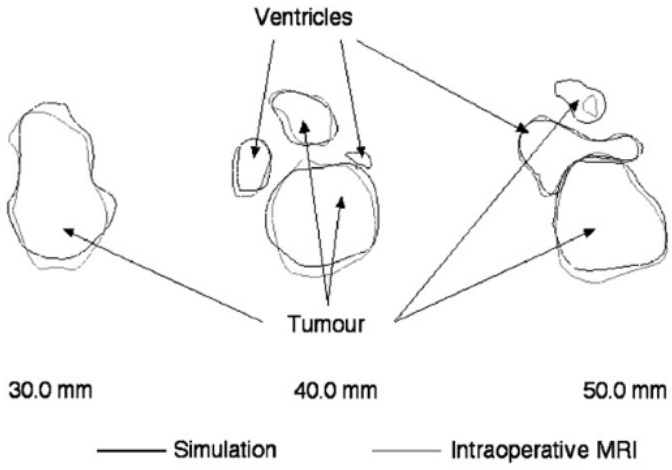

Fig. 5.7: Comparison of contours of coronal sections of ventricles and tumour obtained from the MRI intraoperative images and the model. (Reference: Wittek et al. (2007))

[7] $HyperMesh$, Altair Engineering, Troy, Michigan, USA

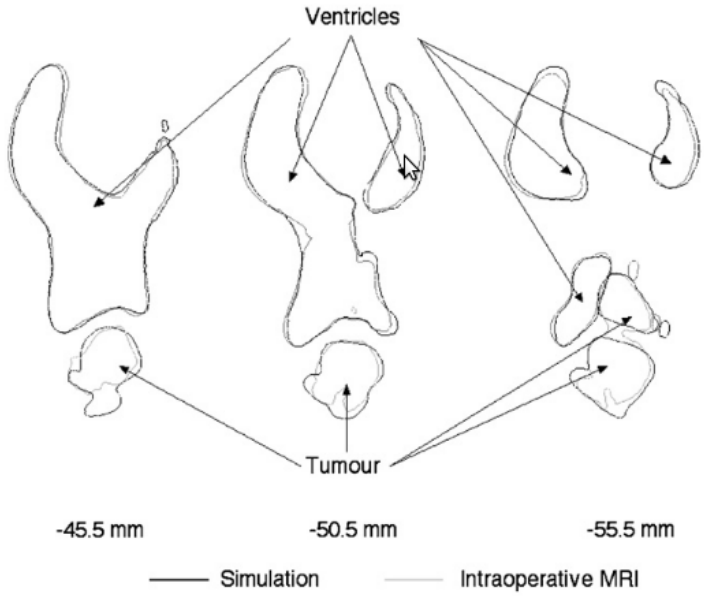

Fig. 5.8: Comparison of contours of axial sections of ventricles and tumour obtained from the MRI intraoperative images and the model. (Reference: Wittek et al. (2007))

5.5 Conclusion

This literature review summarized the existing constitutive models for the brain tissue and the experimental techniques used to characterize it and identify the parameters of the models.

Two main applications are aimed at the design of a biomechanical model of the brain: the neurosurgery and the traumatic brain injury prediction. The approaches related with those applications are quite different. To roughly sum up, the researches focused on the T.B.I. require a viscoelastic formulation and the response of the material at high frequencies in shear while the study aimed at neurosurgical applications use viscoelastic or poro(visco)elastic constitutive models and tensile/compression tests.

Hrapko et al. (2008), Garo et al. (2007) and Gefen and Margulies (2004) stressed the importance of factors such as the temperature, the postmortem time, the anisotropy, the vasculature, the preconditioning and the sample preparation. Wu et al. (2004) demonstrated the importance of the friction between the testing device and the tissue, while Franceschini (2006) showed the dependence of the stress-stretch curves with respect to the location where the samples were taken.

Other studies could be lead on the influence of the humidity of the sample: while Miller and Chinzei (1997a) (for overnight experiments), Aimedieu (2004) used a moisture chamber to preserve the humidity of the tissues, Mehdizadeh et al. (2008) did not but observed no sign of dehydration.

The origin of the brain, human, porcine, bovine, may also be responsible for the differences in mechanical properties found in the literature. But it is remarkable to say that the results

presented by Wittek et al. (2007) for their clinical validation were obtained with a model whose parameters were determined by in vitro experiments on swine brains.

The in vivo and in vitro protocols should not be regarded as concurrents but as complementary. The in vivo experiments are adapted to the validation of a model on realistic conditions (in the case of neurosurgery) while the in vitro experiments focus on the tests of features of the brain (blood vessels, white matter, grey matter, ...) and allows the use of accurate measurement techniques such as the digital image correlation.

Despite being studied for more than 40 years, the determination of the mechanical properties of brain tissue is still an open challenge with unanswered questions such as the solid or fluid nature and the incompressibility of the brain tissue (Kyriacou et al. (2002))

Finally, let's mention that researches are also carried out on the simulation of brain tumor growth (Clatz et al. (2004a)) as well as in the modelling of anisotropic growth in biological tissues (Menzel (2005)). The non rigid registration of peroperative images is a field extensively investigated (Coupé et al. (2005), Hastretier et al. (2000), Vigneron (2009). The modelling of retraction and successive resections for peroperative image update was also investigated (Vigneron et al. (2009)). The effect of the vasculature on the response of the brain tissue was the object of a numerical study (Omori et al. (2000)).

Part III

Experimental characterization

CHAPTER 6

EXPERIMENTAL PROTOCOL

6.1 Introduction

In this chapter is described the experimental protocol defined for the experimental characterization of the mechanical properties of brain tissue. Unconfined compression, relaxation and cyclic tests were performed. The aim of these experiments is to enrich the existing database of stress-strain curves, determine qualitative and quantitative data on the behavior of the brain tissue and verify the incompressibility assumption. The results will be used to calibrate the model described in chapter 9. The tests were carried out on swine brains as they are available in large quantities and their collect does not require any special authorization from the Belgium federal agency for the safety of the food chain.

The digital image correlation technique (D.I.C.) was used to reconstruct the surface of the sample, from which the deformed height, radius and cross section were computed. From there, the true stresses could be determined as well as the volume variation.
This D.I.C. method requires the application of a speckle pattern on the sample, which is not straightforward due to the hydrated nature of the tissue. Other precautions are to be taken when working with soft biological tissues because of their large deformability and the postmortem alterations of the mechanical properties, the influence of the test temperature,...

Although the brain is presented as a complex organ from the geometric and material points of view in chapter 1, considerable simplifications were made in order to get exploitable results. The corresponding assumptions are presented and justified is this chapter.

The equipment used to perform the experiments is also briefly presented.

Finally, the complete and detailed experimental procedure is recalled.

6.2 Equipment

6.2.1 Testing machine

The testing machine we used is a TesT[1] 106-2kN H universal testing machine. The force transducer can measure forces up to 10N with an announced accuracy of 0.05% at full scale,

[1] TesT GmbH., Erkrath, Germany

i.e. 0.005 N. This machine allows displacement and force driven tests with a maximum velocity of 500 mm min^{-1}. The software TesTWinner 922 was used to conduct the experiments and export raw data.

6.2.2 Optical measurement system

Due to the softness of the tissue, it was unthinkable to stick strain gages at the surface of the sample. A contactless method was therefore to be used. The material chosen consisted in three stereoscopic systems, brought by Limess[2]. Each system consists of two cameras mounted on a tripod. The cameras use CCD captors with a VGA (640x480) resolution at 205 Hz[3]. The announced displacement accuracy is 0.01 pixel. When deployed, the system covers the sample with an angle of 240° . The VicSnap and Vic3D software were used for data acquisition and post treatment respectively. Fig. 6.1 shows the testing machine and a stereoscopic system.

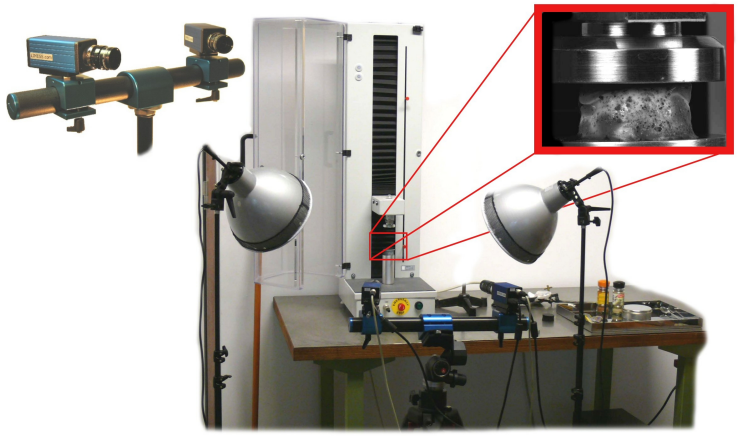

Fig. 6.1: Universal testing machine and one stereoscopic system

6.3 Samples preparation

6.3.1 Notations

In this chapter and till the end of the document, the following notations will be used:

π_s: sagittal plane
π_c: coronal plane
π_t: transverse plane

The term "sagittal (resp. coronal and transverse) cut" will refer to a cut along the sagittal (resp. coronal and transverse) plane. These different planes are shown in Fig. 6.2

[2]Limess Messtechnik und Software GmbH, Pforzheim, Germany

[3]This is a theoretical value. Practically, when using the full system with the 6 cameras, the maximum frequency reached was 30 Hz.

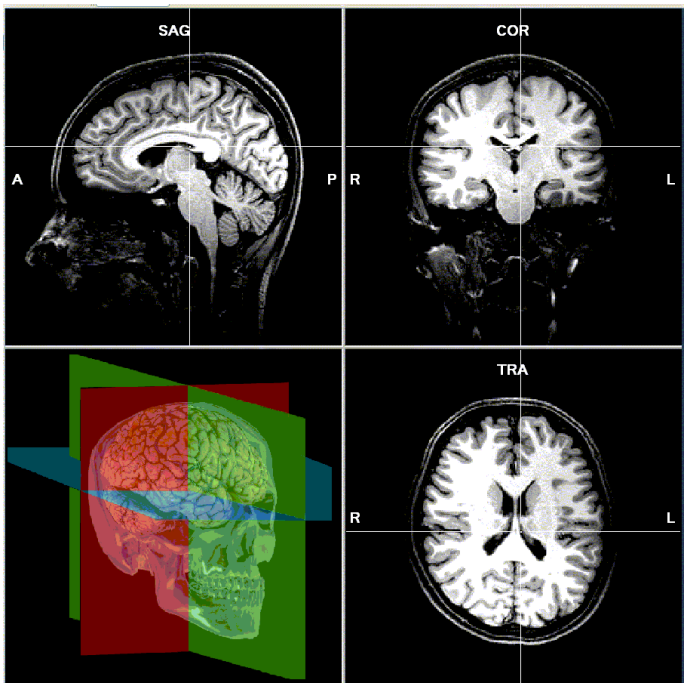

Fig. 6.2: Sagittal, coronal and transverse cuts from magnetic resonance imaging and 3D view of the cut-planes.

6.3.2 Transport and conservation

When dealing with brain tissues and biological tissues in general, some precautions must be taken so that no alteration is caused by the handling of these particular materials. According to Garo et al. (2007) and references therein, the mechanical properties of the brain tissues experience a postmortem degeneration caused by several reasons such as rigor mortis, osmotic swelling and autolysis. This degeneration can be slowed down by keeping the tissues at a lower temperature than the body temperature, provided they are immersed in a physiological fluid to prevent the cells deterioration due to osmosis. Contradictory results exist on the translation of this biological degeneration into a measurable change in mechanical properties. Some authors state that no change is observed with increasing postmortem time [Reference trouvée dans hrapko] while others found small differences in those mechanical properties [References]. To minimize the possible influence of the degradation of the tissues, the tests were performed within 5 hours of sample collection at the slaughterhouse.

The brains used for this study came from 6 months old swines and were collected at the local slaughterhouse [4]. Swine brains were used because they are not subjected to any regulation by the Belgium federal agency for the safety of the food chain (AFSCA). There is, however, a major drawback using these particular tissues: according to the standard slaughtering procedure, the swines are cut into two parts in the length direction just after death, so only half brains are available and they do not necessarily correspond to the hemispheres, as pictured in Fig. 6.3. Thus, the samples were only taken perpendicularly to the sagittal

[4] Abattoirs publics de Liège-Waremme SC, Rue de Droixhe 15, Liege

plane, in the left-right direction.

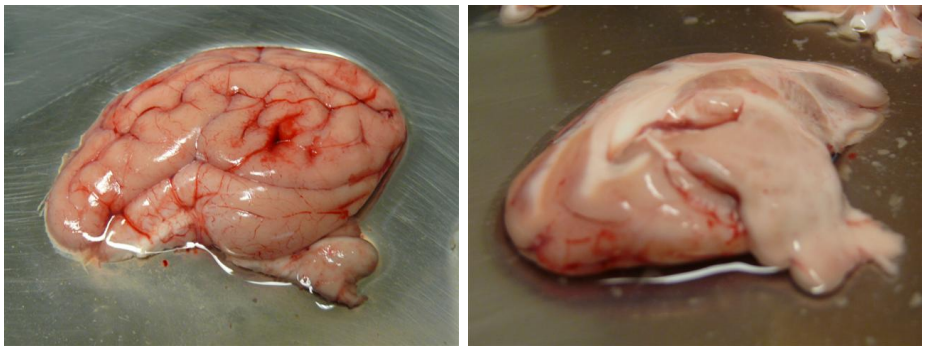

Fig. 6.3: Examples of brains collected at the slaughterhouse

Once collected, the brains were kept in physiological fluid. This fluid had been placed in a refrigerator at 6°C the preceding night. The duration of the transportation never exceeded half an hour.
In the lab, the brains were put in a refrigerator at about the same temperature (6°C to 8°C). They were taken out half an hour before testing and the physiological fluid was replaced with one at the room temperature in order to warm the brains. The experiments were carried out at room temperature (see section 6.6).

6.3.3 Carving and handling

The human brain is described as a "soft yielding structure that is not as stiff as a gel or as plastic as a paste" (Kyriacou et al. (2002)). Due to its softness, it is very difficult to handle. It also tends to deform, and sometimes to collapse, under its own weight. Furthermore, it is very sticky: Fig. 6.4 shows that a brain sample naturally adheres to a stainless steel scalpel when it is lifted. To prevent the adherence of the sample to the bottom of the carving tray, a thin film of physiological fluid was created.

Fig. 6.4: The brain is a very sticky material, the white matter being stickier than the grey one.

As previously stated, the samples were taken in the direction perpendicular to the sagittal plane. The pia mater was delicately removed before the samples, containing both white

matter and grey matter, were cut at the room temperature using a cylindrical stainless steel die cutter. The die diameter and height were chosen to be 20 mm and 10 mm respectively. These dimensions were chosen taking account of the following constrains:

- if the sample height is too large with respect to its diameter, it collapses under its own weight. In our case, an aspect ratio of 1:2 was determined as acceptable to avoid this phenomenon,
- the size of the black dots composing the speckle pattern largely determines the quality of the surface reconstruction at the end of the test. The smaller the sample, the harder the application of the painting in a way to produce a satisfactory pattern (see section 2.4).
- the displacement accuracy of the digital image correlation method is expressed as a fraction of a pixel (e.g. 0.01 pixel). A better accuracy implies a larger size of the sample on the picture. The latter is constraint by the minimum focal length of the camera. With the proposed dimensions, the theoretical relative accuracy is 0.5%.

A surgical scalpel was used to cut the tissues surrounding the cylinder. Surgical tools were used to flatten the superior surface in order to maximize the contact area between the test machine plate and the sample. The challenges encountered when cutting the samples can be imagined by looking at Fig. 6.3: the surface is anything but regular, it presents sulcii (furrows) and gyrii (ridges) which makes it very difficult to obtain a regular shape. Furthermore, extreme care must be taken when cutting the sample since the softness of the tissues yields in their large deformability. This can induce stresses in the specimen, leading to an unknown initial state and/or alter its shape in such a way that it cannot be approximated by a cylinder anymore. For the sake of simplicity, the sample is assumed to keep its cylindrical shape throughout the test, which is equivalent to assert that the barrel effect is negligible. This reduces the study to the evolution of the height and the radius of the cylinder, quantities that can be calculated without resorting to a finite element code. Obviously, this assumption must be justified during the tests. Therefore, the sample must be as cylindrical as possible.

6.3.4 Speckle pattern application

The application of a speckle pattern on the sample is the key point that allows the proper use of the digital image correlation method. The importance of this step is explained, as well as the general principles of the D.I.C. in chapter 2.

Due to its biological nature, it is far more challenging to use the D.I.C. on brain samples than on metallic test pieces. The problems encountered are related to the soft, hydrated nature of the tissue. Indeed, the hydration results in reflective areas, as seen in Fig. 6.5. Those reflections must be avoided since the D.I.C. software is not able to match and/or track the pixels in those areas. Furthermore, the applied speckle pattern must not change the mechanical properties of the brain sample. When applying such a pattern on a metallic test piece, it is not a problem to wait till the paint is dry. Since the material is very rigid, the application of the painting will not result in an alteration of the metal's mechanical properties. However, it is not possible to state the same for the brain tissue.

To summarize, the method designed to apply the speckle pattern should respect the following constraints:

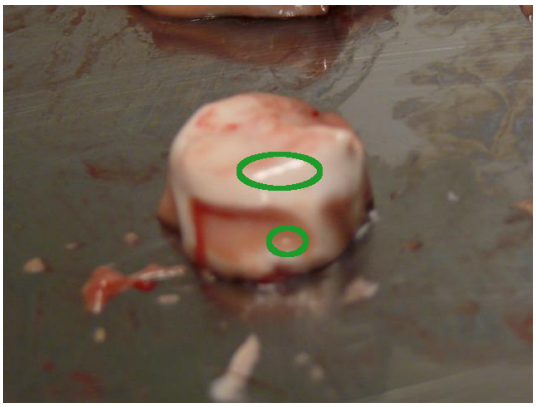

Fig. 6.5: A sample showing reflections (green circles). The software is not able to match and track the pixels in those areas.

- preventing the reflections,
- not altering the mechanical properties of the tissue.

Several techniques have been tried to fulfil the first constraint: the application of a mat powder, the use of a hair dryer or paper towel. The last one must be rejected: it adheres to the sample and thus cannot be used to remove the liquid film at the surface. It is almost impossible to take it off without inducing deformations to the sample.
Cold air from a hair drier was used by Lauret (2007) to dry the surface of a 4 mm thick brain slice so that the paint correctly adheres. No remark was made whether this treatment changes or not the observed mechanical properties. We could speculate that this drying will cause a dehydration of the sample and thus makes it stiffer. In order to investigate this hypothesis, we performed 3 displacement-driven compression tests at the same loading rate for both dried and control (undried) samples. Fig. 6.6 shows the resulting force vs displacement curves. It appears that the force needed is higher for the dried samples, confirming our assumption.

To prevent the reflections, talcum powder was used, as it has a twofold advantage: it creates a mat and white background on which the black pattern can be applied. To maximize the contrast, we chose to paint a white background on the sample with a spray can before the application of the talcum. A spray gun may be preferred for it is easier to set the air and paint flows right. Unfortunately, it was not possible to use it in our lab. The spray can must be held at a sufficient distance so that the compressed air does not exert a pressure on the sample. A home-made spray gun was realized with a one-handed bar clamp (best known as "quick grip") to regulate the flow (see Fig. 6.7).

The talcum powder was shuffled just after the application of the painting. The absence of reflection was checked visually with the cameras. The speckle pattern was created by spraying black paint, with or without the help of the home-made spray gun on the sample. The result of this treatment is shown in Fig. 6.8.

Once again, we should wonder whether this treatment changes the mechanical properties of the test piece or not. To answer that question,10 displacement-driven compression tests at 120 mm min^{-1} were performed on both prepared and control samples. The force vs displacement

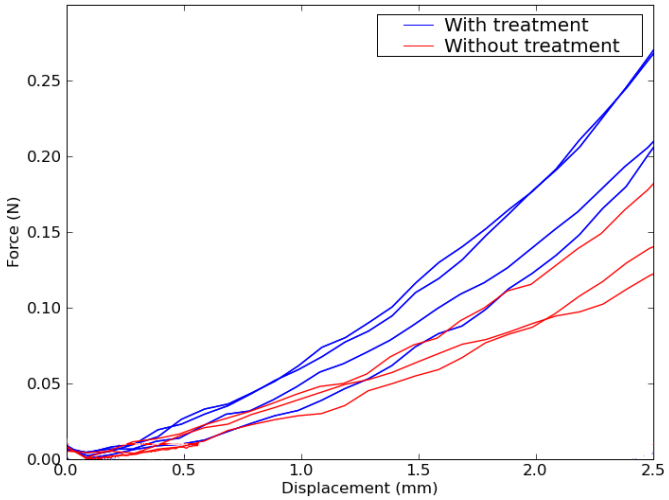

Fig. 6.6: Force vs displacement curves for unconfined compression tests at the same loading velocity (12 mm min^{-1}) of dried (with treatement) and control (without treatment) samples.

Fig. 6.7: Quick grip used as a spray gun. The spray can is place between the jaws and the pressure is regulated by the trigger.

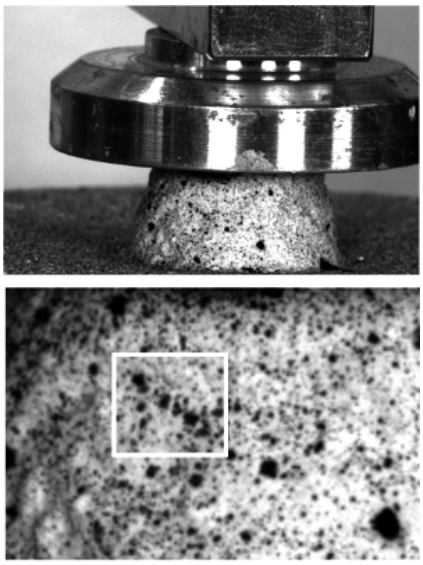

Fig. 6.8: Speckle pattern applied on a sample.

curves are presented in Fig. 6.9, from which we can only state that the envelope of both series of curve is the same. This indicates that no significant difference can be attributed to the application of the speckle pattern. Nevertheless, only a rigorous[5] statistical hypothesis test can verify this assumption. To this end, a unilateral Student test was performed. The first step was to compute the mean and the unbiased standard deviation of the maximal force value for both control (C) and treated (SP) samples. We used the skewness and kurtosis tests to ensure that the distributions of those forces could be considered as normal (or Gaussian). The Fisher-Snedecor test was used to test the homogeneity of the variances. With all these preliminary tests positive, we performed the actual Student test. The null hypothesis, the equality of the means, was verified with the significance level of the test (α) set to 10%. Fig. 6.10 and Tab. 6.1 show the theoretical distributions and their parameters respectively. It can be observed that the maximum of the SP curve falls into $[\bar{X}_C - \tilde{\sigma}_C, \bar{X}_C + \tilde{\sigma}_C]$, where $\bar{X}$ and $\tilde{\sigma}$ stand for the mean and the standard deviation of the control tests respectively.

	mean (N)	standard deviation (N)
control	0.257	0.071
prepared	0.299	0.091

Tab. 6.1: Parameters of the maximum force distribution for control and prepared samples.

The talcum powder is applied directly on the paint and thus cannot be responsible for a possible dehydration of the sample; no sign of dehydration was observed anyway. The time required for a test never exceeded 3 minutes, so that the risk of chemical contamination of the sample by the paint is very low. The sole physical reason for which there could exist a

[5]See any basic course of statistics for more information about the concept used in this paragraph.

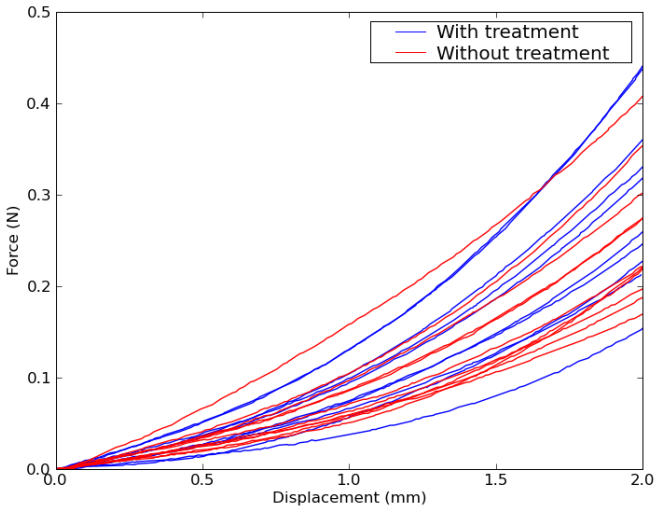

Fig. 6.9: Force vs displacement curves for prepared (with treatment) and control (without treatment) samples.

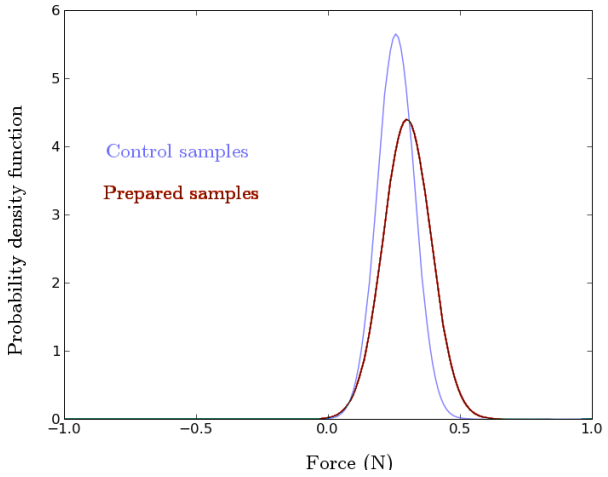

Fig. 6.10: Normal distribution of control and prepared samples.

significant difference between the results for the control and prepared samples would be that the stiffness of the paint layer is of the same order than the brain's. This seems improbable.

From these tests, the following conclusion can be drawn: there is no significant difference between the control samples and the ones with a speckle pattern. This observation is confirmed by a Student test with a 10% significance level. The assumption that the application of the pattern does not change the mechanical properties is confirmed.

6.4 Assumptions

Due to the fact that all the samples were taken in the same direction (π_s) because only half-brains were available, it was not possible to test the anisotropy of the brain. The results presented in the next chapter are valid for the sagittal direction. If the model is used in a finite element model, the isotropy of the tissue will have to be assumed.
The dimensions of the sample did not allow us to test the homogeneity neither. The brain was then supposed to be homogeneous, despite the results found by Franceschini (2006). For the same reason, no distinction was made between grey and white matters. Indeed, the only way we could quantify their respective proportions would be to image the samples in a MRI scanner, which would be very difficult from a practical point of view. Nevertheless the idea of considering the brain as a single homogeneous and isotropic material is not absurd: the aimed application is to insert the constitutive equation for brain tissue(s) in a finite element code. Nowadays, there exists, to our knowledge, no mesh of the brain that separates the two matters and take the heterogeneity and anisotropy into account. But it is obvious that an important effort is to be made from an experimental point of view in the next years to improve the results, regarding those particular points.
Furthermore, the barrelling effect was neglected since the plates were lubricated with physiological fluid prior to each test. The friction coefficient is then assumed to be null. The shape of the sample is supposed to remain cylindrical during the test, making the calculations easier. This assumption was justified by the visual examination of the samples before and after a compression test, Fig. 6.11. Finally, the samples were assumed to be stress-free at the beginning of the test.

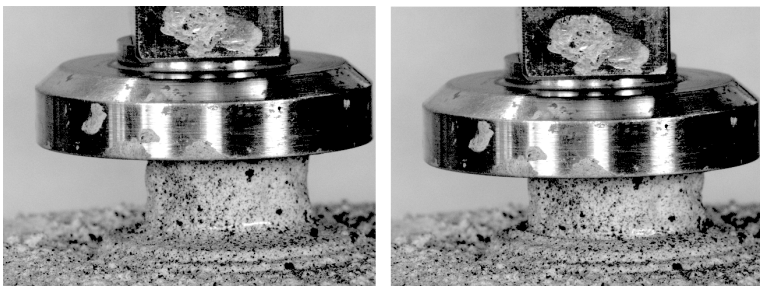

Fig. 6.11: Sample before and after a compression test. The shape remains cylindrical.

6.5 Description of the tests

The experiments that were carried out had a twofold objective:

- to enrich the existing stress-strain curves database to calibrate the numerical model,
- to verify the incompressibility assumption,

With this end in view, we chose to perform three kinds of tests: unconfined compression, relaxation and cyclic tests.

The three stereoscopic systems were calibrated the evening before each experimental day. As mentioned in section 6.2.2, the 6 cameras covered about 2/3 of the sample surface, which correspond to a 240° angle (see Fig. 6.12). The disposition is constrained by the available space in the room[6].

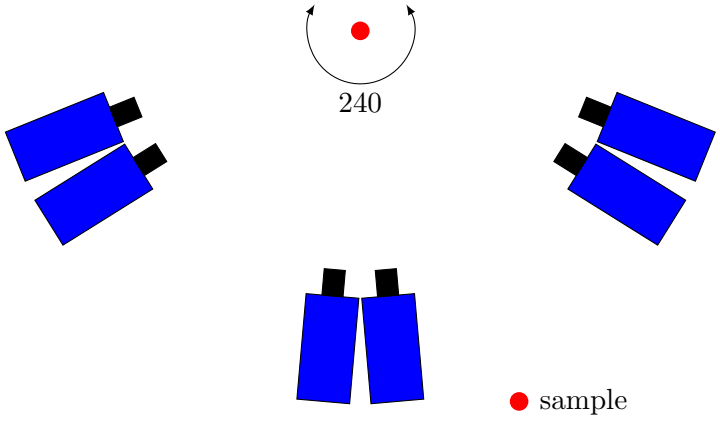

Fig. 6.12: Disposition of the three stereoscopic systems (not to scale).

The superior faces of the samples were never perfectly flat, making impossible a uniform contact with the superior plate. Several options were considered to maximize the contact area:

- to perform a preconditioning,
- to launch the compression sequence when the plate is not yet in contact with the sample,
- to ensure that the whole superior surface of the sample is in contact with the plate,
- to maximize the contact area while keeping the pre-compression force under a threshold.

Let's examine each of these options. The initial situation for each case is the plate brushing the sample.

[6]Dissection room, Tower 3, Centre Hospitalier Universitaire de Liege.

Compression & discharge preconditioning: in the initial situation (Fig. 6.13.a), only a part of the surface is in contact with the moving plate of the testing machine. Then, a compression is performed in such a way that the whole superior surface of the sample comes in contact with the plate (Fig. 6.13.b). This compression should be performed at a lower loading velocity than the actual test for two reasons: firstly, since the sample is considered as viscoelastic, the relaxation process occurs concomitantly to the compression, thus lowering the stress and secondly, the stress increases with the loading velocity. These two effects help limiting the force reached and thus make the initial stress-free assumption more valid. At the end of this phase, a compression field exists in the zone indicated by a green ellipse in Fig. 6.13.b.
After this phase, the plate is moved back to its initial position. The whole surface of the sample is now in contact with the plate, with the initial lower part now undergoing a tensile force in the zone indicated by a yellow ellipse in Fig. 6.13.c. The relaxation process being uncomplete, there exists a residual force, resultant of both tensile and compression forces. The absolute value of this force depends on the gap existing in the initial situation.

Furthermore, the sample may sometimes unstick from the plate.

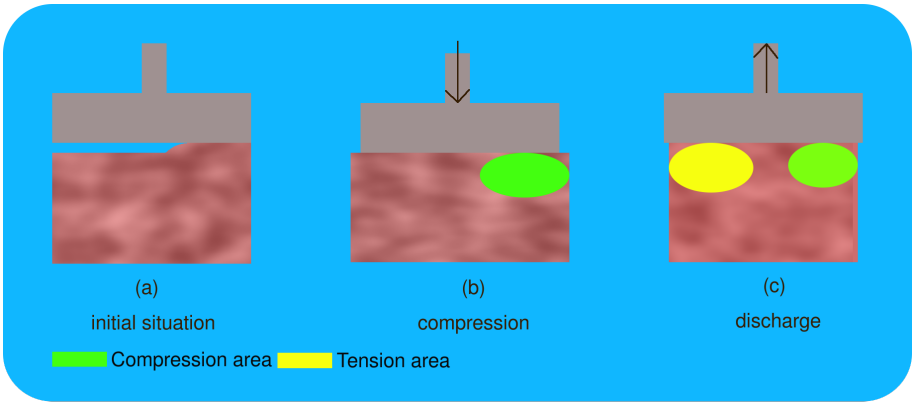

Fig. 6.13: Schematic description of the compression and discharge preconditioning.

Compression preconditioning: in this operation, a displacement is applied to the plate so that it comes in contact with the whole superior surface of the sample and a relaxation occurs. It corresponds to the first phase of the compression & discharge preconditioning. The value of the residual force is higher in this case.

Compression preconditioning with a force threshold: the major issue with the preceding procedures is that the initial force may not be negligible with respect to its final value obtained during the actual test. The proposed method is a compromise between optimizing the contact surface and minimizing the residual initial force. A single compression test is performed on a dummy sample at a smaller loading velocity than the actual test. A threshold is fixed at 5% of the maximal value of the force. A series of compression-relaxation processes is carried out to gradually reach this threshold. The imperfection of the contact is reduced (and sometimes eliminated), while the initial residual force remains limited (Fig. 6.15).

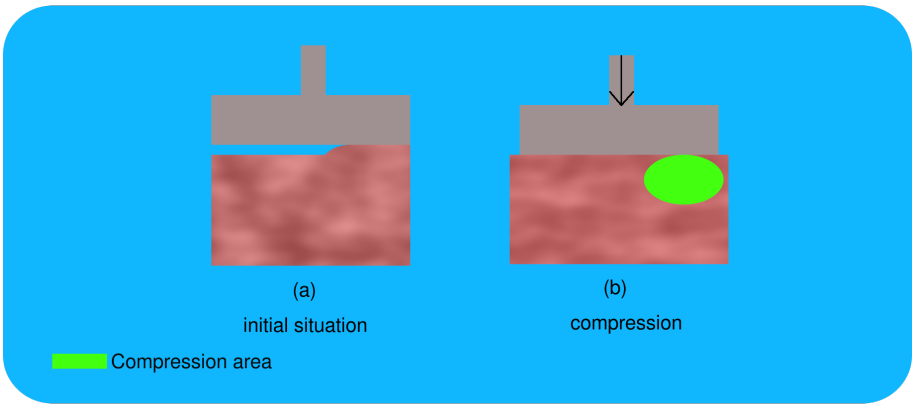

Fig. 6.14: Schematic description of the compression preconditioning.

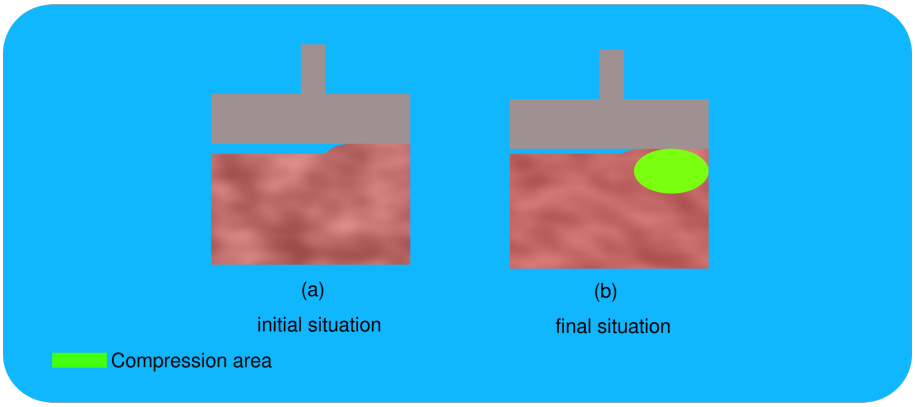

Fig. 6.15: Schematic description of the compression preconditioning with a force threshold.

Direct testing: in this last case, the test sequence is launched from the initial situation. Thus, the vertical displacement of the superior surface of the sample recorded by the cameras is not uniform. This can lead to the miscalculation of the strain along the compression direction as explained in section 7.4.

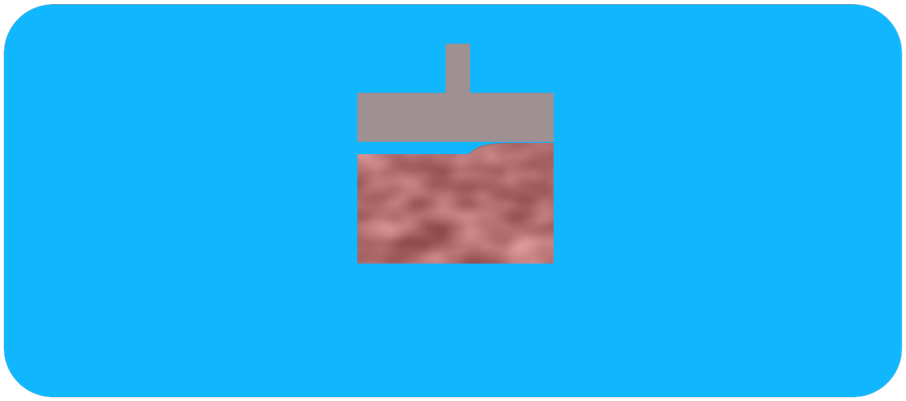

Fig. 6.16: Schematic description of the direct testing method.

None of these solution is better than the others. They all present advantages and drawbacks. Because it seems to represent a good compromise, the compression preconditioning with a force threshold was chosen. In practice, the duration of this preconditioning phase was of the order of a few dozens of seconds, which is not sufficient to alter the mechanical properties of the sample.

The compression and cyclic experiments were all displacement-driven. The maximum displacement of the superior plate of the testing machine was fixed to 2 mm. Once again this value results from a compromise: on the one hand, a sufficiently high value is needed in order to characterize the tissue in the finite strain domain, as the deformation encountered in the aimed application (neurosurgery) are not infinitesimal, and on the other hand, a too large value of the displacement would alter the quality of the surface reconstruction. Indeed, some of the spots of the pattern would be too deformed to be recognized and tracked by the post-treatment software from one picture to an other.

The compression tests were performed at different loading rates: 1.2, 12 and 120 mm min^{-1}. The upper limitation was imposed by the frequency of the cameras: only 30 images per second can be acquired when the full system (6 cameras) is deployed. This corresponds to 30 pictures for the highest velocity, and thus to a maximum of 30 points on the stress versus strain curve, which proved to be sufficient for the exploitation of the experimental data.

As far as the cyclic tests are concerned, the loading velocity was arbitrarily fixed to 60 mm min^{-1} and the maximum displacement was set to 2 mm. These experiments consisted in 3 loading/unloading cycles. Preliminary tests showed that irreversible damages could happen to the samples (e.g. cracks) if more that 3 cycles were performed.

At last, for the relaxation tests, the samples underwent a compression at 60 mm min^{-1} until a 0.5 N force was reached. The time for the relaxation was fixed to 1 minute.

6.5.1 Post test verifications

After each completed test, the sample was cut in half and no sign of dehydration was observed.

When a crack occurred on the surface seen by the cameras, the surface of the sample was delicately washed to remove the paints and the talcum, so that it could be observed whether the crack was only a superficial crack in the pattern or was really present in the sample. In every cases, the crack could be observed in the tissues, confirming the assumption that the application of the pattern does not alter the mechanical properties of the tissues. The corresponding tests were discarded.

6.6 About the temperature

All the experiments were performed at room temperature ($\approx 21°C$) rather than at body temperature. Testing at body temperature was considered but quickly abandoned. Indeed, a steam room was used to warm the samples at 37°C, but they were subjected to a 7°C decrease by the time they were placed on the plate. A spirally-shaped radiative resistor was placed around the plate to keep the environment at 37°C. A thermocouple, placed just behind the sample, measured the temperature and controlled the intensity of the electric current flowing in the resistor. This system, pictured in Fig 6.17, proved to be too imprecise and hazardous both for the operator and the testing machine. Indeed, the temperature of the resistor could reach more than 100°C and some plastic parts of the testing machine began to mold. It was impossible to place the spires closer since they would have been in front of the sample and thus making it impossible to measure the deformation with the cameras.

A possible solution was to enclose the sample in a chamber at 37°C, but it would have made almost impossible to use correctly the D.I.C. since glass or plastic walls would have caused unwanted reflections.

Since Hrapko et al. (2008) showed that the temperature sensitively influences the observed stress, a solution must be found to test the sample at body temperature. The only solution we can figure out is to work in a room warmed at body temperature, which was not possible during our experimental campaign.

Fig. 6.17: Schematic view of the warming system.

6.7 Summary of the protocol.

The day before the experiments.

01. Calibrate the three stereoscopic systems by doing a reconstruction on a dummy sample with the same dimensions as the actual samples.
02. Put a bottle (at least 500 ml) of physiological fluid (PF) in the refrigerator at 6°C.

The day of the experiments.

03. Pour the cooled PF in isotherm containers and fill a non-isotherm one with PF at room temperature .
04. Collect the half brains at the slaughterhouse. Place them in the isotherm containers in such a way that no one is likely to be flatten out by the weight of the others.
05. Once in the lab, place all the isotherm containers in the refrigerator (at approximatively 6°C).
06. Remove the cooled PF from the remaining container and re-fill it with PF at room temperature.
07. Remove the pia mater and carve a sample.
08. Inspect the superior face and try to remove parts if necessary to make it the flattest you can.
09. Apply white paint with a spray can or a spray gun. Be careful that the compressed air exerts a pressure on the sample. Maintain a minimal distance between the can and the sample.
10. Delicately shuffle talcum powder on the sample.
11. Check the presence of reflection with the cameras. If any, go back to point 10
12. Apply the pattern with the black paint. The smaller the dots, the better the result.
13. Lubricate the compression plates with PF.
14. Perform the test.
15. If a crack occurred, delicately wash the sample and check if the crack was due to the paint, the talcum powder or if it actually began in the sample. The corresponding test is to be rejected since the post treatment software will not be able to perform the surface reconstruction.
16. Cut the sample in half and check any sign of dehydration.
17. The full preparation process should not take more than 15 minutes. 30 to 40 minutes before running out of samples (i.e. when, in the currently used container, there remains enough material to prepare 2 or 3 samples), remove one of the containers from the refrigerator so that the half brains warm up and go back to point 6.
18. Go back to point 7.

CHAPTER 7

EXPERIMENTAL RESULTS

7.1 Introduction

In this chapter are presented the results of the experiments. Each type of experiment (unconfined compression, relaxation and cyclic) was repeated at least 15 times in the same conditions to estimate the scatter of the results.They consist in stress versus strain, force versus displacement and volume ratio curves.

The first section explains how these quantities were computed. The curves are then presented and commented. The use of the D.I.C. underlines the influence of the geometry and the imperfection of the contact between the superior plate and the sample. The incompressibility of the brain tissue is proved thanks to this image correlation technique. With that property granted, the opportunity of performing the tests without the optical measurement system is discussed. Finally, some sources of dispersion of the results are mentioned and commented.

7.2 Stress, strain and volume computation

7.2.1 Surface reconstruction

Prior to the surface reconstruction, i.e. the determination of the 3D coordinates of the sample by the post treatment software, the acquired pictures must be checked. Indeed, for some unknown reason, a desynchronization of the cameras may have occurred. Although this problem can easily be detected, it means the data are unexploitable, since the same displacement is shown at different times for each stereoscopic system. These tests are therefore discarded before the surface reconstruction step.

After a successful reconstruction, the number of points for which the software successfully computed the 3D coordinates [1] was examined: if more than 20% of the points were lost between the initial and the final picture, the whole sequence was discarded to ensure that the loss of those points did not influence too much the results.

[1] The term *data points* will be used in the rest of this document.

Here, an awkward deficiency of the Vic3D software must be emphasized: it is not able to perform a combination of three data files and a best fit cylinder, although the contrary was first claimed by Limess. The combination process consists in putting together the data files from several data acquisition systems into one file containing all the data points. Since a cylindrical shape was assumed for the sample, only the height and radius were needed. But the software is not able to compute those parameters AND perform the combination. Accordingly, the best fit cylinder was determined separately for each of the three data acquisition systems and the radii and heights were averaged to get only one value for each sample.

7.2.2 Data processing

A data processing code was written in Python to process the output files from the testing machine and Vic3D softwares.

The forces (F) from the testing machine were matched with the corresponding radii (r) and heights (h) from the Vic3D software. The deformed cross section area (a), the true (or Cauchy) stress σ, the elongation λ and the natural strain ε were then computed according the formulae:

$$a = \pi r^2 \tag{7.1}$$

$$\sigma = \frac{F}{a} \tag{7.2}$$

$$\lambda = \frac{h}{h_0} \tag{7.3}$$

$$\varepsilon = \ln(\lambda) \tag{7.4}$$

were h_0 stands for the initial height. It should be precised that the term 'height' does not stand for the actual height of the sample for two reasons:

- due to the small size of the sample with respect to the focal length, it was very difficult to prevent the cameras from pointing slightly downward. As a result, a small part of the sample, close to the machine plate, was in the shadow of that plate and could not be seen by the cameras. Furthermore, the area defined as the region of interest (green part in Fig. 7.1) does not always perfectly fit the edges of the sample;
- only the points that are in the middle of the subset window see their 3D coordinates computed (yellow window and its central point in Fig. 7.1). As a result, the points belonging to the border (red frame in Fig. 7.1) of the region of interest are not exploited.

The term 'height' thus designates the height of the region of interest reduced by the size of the subset window. It actually does not matter for the computation of the strain, since the elongation λ is a relative quantity. Indeed, the relation between the deformed vertical coordinate z and the initial one Z is written:

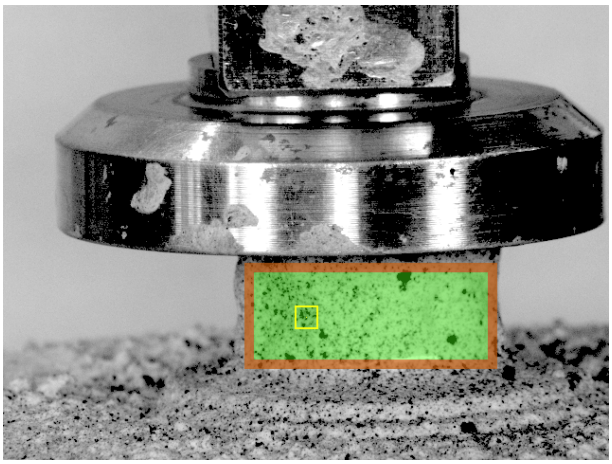

Fig. 7.1: Region of interest (green) defined for the surface reconstruction. The red frame represents the pixels for which the correlation coefficient is not computed. The width of this frame is equal to half of the width of the subset window (yellow).

$$z = \lambda Z \tag{7.5}$$

Let's consider 2 particular coordinates z_1 and z_2 in the deformed geometry, corresponding to the coordinate Z_1 and Z_2 in the initial one. Then the following equalities hold:

$$z_2 - z_1 = \lambda Z_2 - \lambda Z_1 \tag{7.6}$$
$$= \lambda (Z_2 - Z_1) \tag{7.7}$$

which means that, whatever the choice for the vertical coordinates, the elongation λ is the same. So, although it does not reflect the actual geometry of the sample, the term 'height' will still be used in the rest of this document, with the herebefore explained meaning.

The volume ratio was also computed with the help of the formula

$$\frac{v}{V} = \frac{R^2\ H}{r^2\ h} \tag{7.8}$$

where v (resp. V) stands for the current (resp. initial) volume. Here again, it does not matter that h (resp. H) does not stand for the actual height. Indeed, expression 7.8 can be rewritten:

$$\frac{v}{V} = \frac{R^2\ H}{r^2\ \lambda\ H} \tag{7.9}$$

$$= \frac{R^2}{\lambda\ r^2} \tag{7.10}$$

A rejection module was integrated in the data processing code to ensure the enforcement of some constraints:

- for compression tests, λ must be strictly decreasing,
- for cyclic tests, λ must be strictly decreasing (resp. increasing) during the compression (resp. unloading) phase,
- for relaxation tests, λ must be strictly decreasing during the compression phase and must not exceed a fixed threshold during the relaxation phase.

These simple constraints are imposed by the good sense. Each point on the stress-strain curve that does not respect the corresponding condition is rejected. If more than 25% of the points are rejected, the whole curve is not taken into account.

The remaining curves corresponding to the experiments performed in the same conditions are interpolated so that a mean value may be obtained, both for the stress vs strain and the volume ratio curves. This operation sometimes led to further loss of curves; indeed, the largest interpolation abscissa value is limited by the smallest abscissa of the curves. Only the curves with a maximal strain greater or equal to 0.12 (in absolute value) were kept. This value of 0.12 was chosen by the observation of the figures. It ensures that a sufficient number of curves participate to the computation of the mean while the maximum strain is not too small. An example is presented in Fig. 7.2. No extrapolation of the curves was made, since this numerical operation may yield to a poor result. For instance, the quality of the linear extrapolation will only depend on the slope of the line defined by the two last points. It is obviously hazardous to try and represent the behaviour of any system just considering so little information. An extrapolation of higher order (e.g. cubic spline) would induce unwanted oscillations that can greatly distort the results.

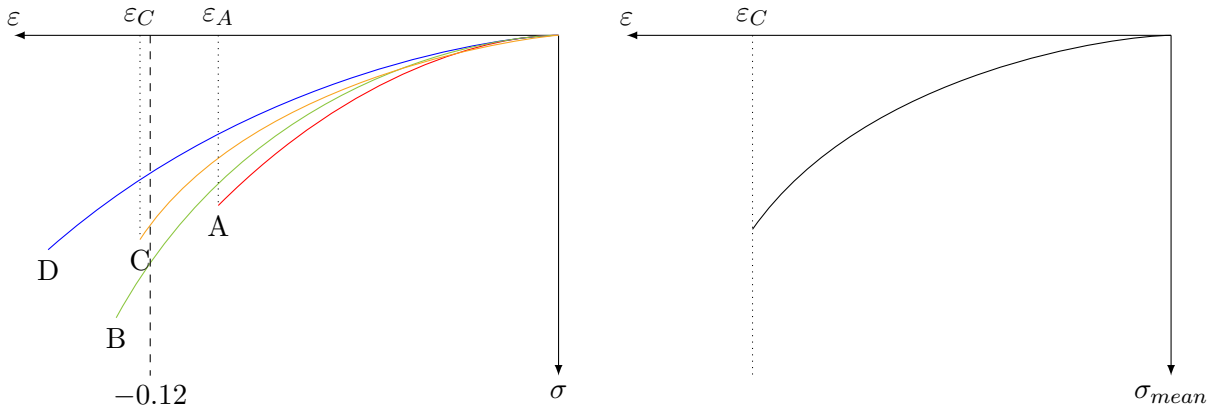

Fig. 7.2: Interpolation criterion: curve A is rejected because $|\varepsilon_A| < 0.12$. The mean curve is computed from curves B,C and D up to ε_C.

7.3 Results

7.3.1 Unconfined compression tests

Here are the results for the unconfined compression tests at 120 mm min^{-1}.

Fig. 7.3 shows a significant scatter, the causes of which are discussed in section 7.6. More than 20 experiments were carried out and only 5 were used to compute the mean curve shown in Fig. 7.4, according to the rejection process described hereabove. This shows the difficulty of working, and getting results, with very soft tissues.

This mean curve shows a linear behaviour, which is not surprising since the maximum strain in absolute value is moderate. This observation also holds for the results of the other compression tests at various loading rates as seen in Fig. 7.8, Fig. 7.12 and Fig. 7.16.

Besides these stress-strain diagrams, the other variable of interest was the evolution of the volume ratio during the experiments. Fig. 7.5 shows this volume ratio with respect to the natural strain. Most of the curves are increasing with the strain, indicating an augmentation of the volume, which seems weird from a physical point of view. On the mean curve presented in Fig. 7.6, this tendency is lessened thanks to the averaging. The maximal value of the volume ratio is 1.02, which would indicate only a 2 % error *if the incompressibility assumption is verified*, a point treated in section 7.3.4. Anyway, for a compressible material, the thermodynamics imposes that the volume ratio must strictly decrease over time (or with increasing strain) during a compression experiment, which is clearly not the case here.

The same set of figures were plotted for the compression tests at 12, 1.2 and 60 mm min^{-1}.

The three volume ratio mean curves presented in Fig. 7.10, Fig. 7.14 and Fig. 7.18 are always comprised between the value 0.99 and 1.02 and are most of the time very close to 1.0. The scatter is far less important compared that of the stress-strain mean curves observed in Fig. 7.8, Fig. 7.12 and Fig. 7.16. The linear behaviour already observed in Fig. 7.4 is clearly visible on those curves too.

Even at those low strains, the effect of the loading rate on the stresses is clearly noticeable. For the sake of comparison, the mean curves were grouped in Fig. 7.19.

The final value of the curve obtained at 120 mm min^{-1} is more than twice the one at 1.2 mm min^{-1}. The loading velocity effect is less pronounced for the intermediary curves at 60 and 12 mm min^{-1}.

From the unconfined compression tests, the following conclusions can be reached:

- an effect of the loading velocity on the value of the stress exits: for a given strain, the higher the loading velocity, the higher the stress,
- the volume ratio curves show that the value stays very close to 1, tending to confirm the incompressibility assumption.

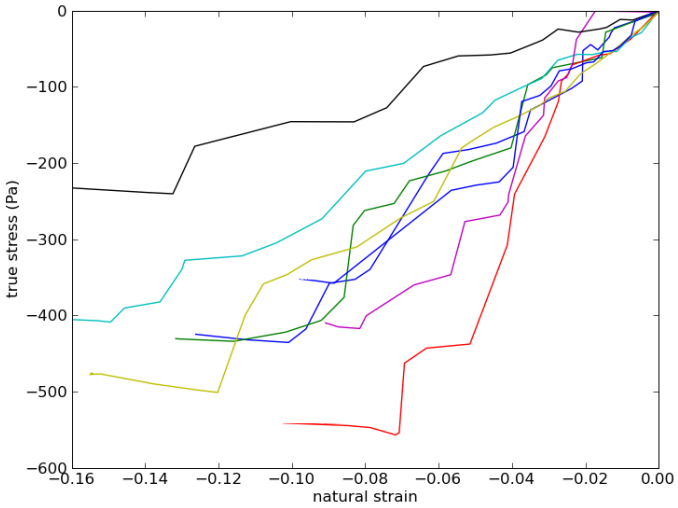

Fig. 7.3: Stress-strain curves for the unconfined compression tests a 120 mm min^{-1}

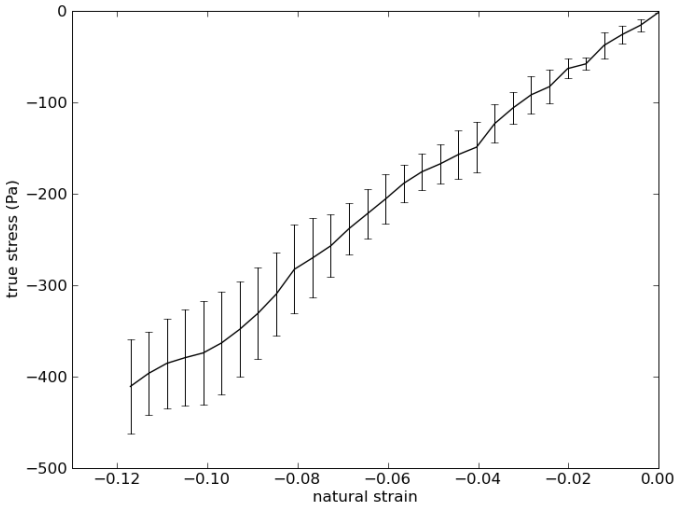

Fig. 7.4: Stress-strain mean curve for the unconfined compression tests at 120 mm min^{-1}.

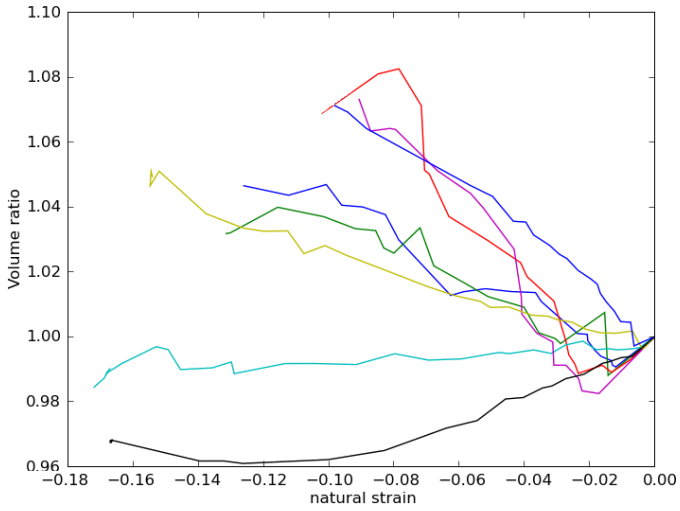

Fig. 7.5: Evolution of the volume ratio during the unconfined compression tests at 120 mm min^{-1}.

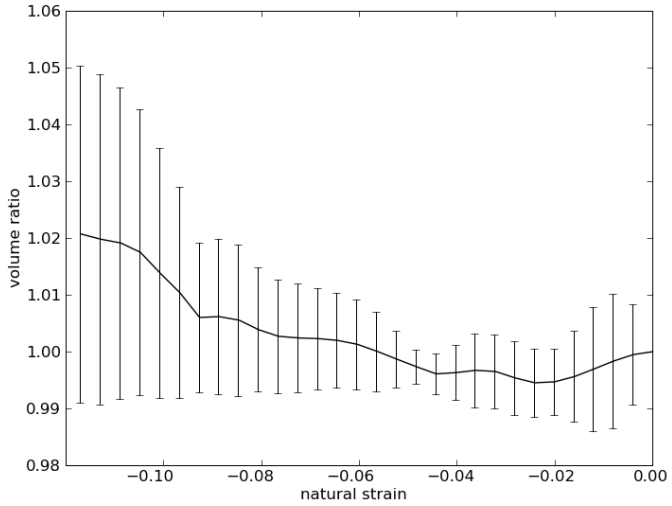

Fig. 7.6: Averaged evolution of the volume ratio during the unconfined compression tests at 120mm min^{-1}.

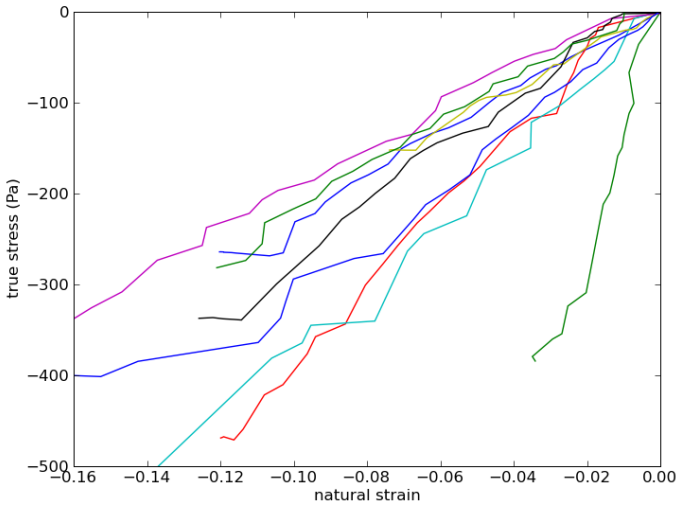

Fig. 7.7: Stress-strain curves for the unconfined compression tests at 60 mm min^{-1}.

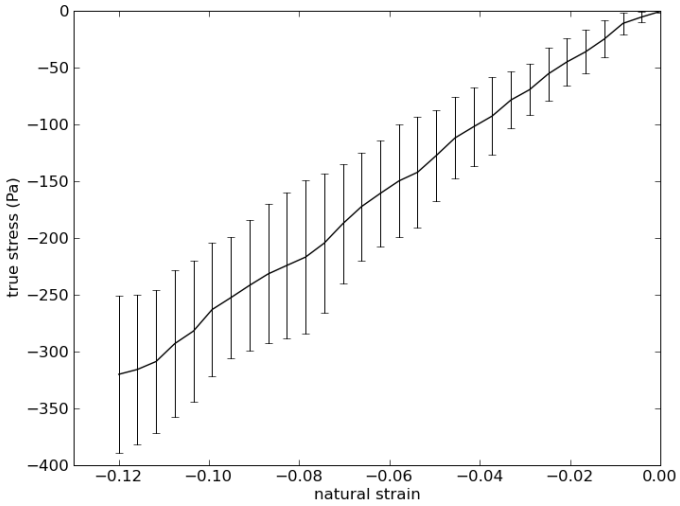

Fig. 7.8: Stress-strain mean curve for the unconfined compression tests at 60 mm min^{-1}.

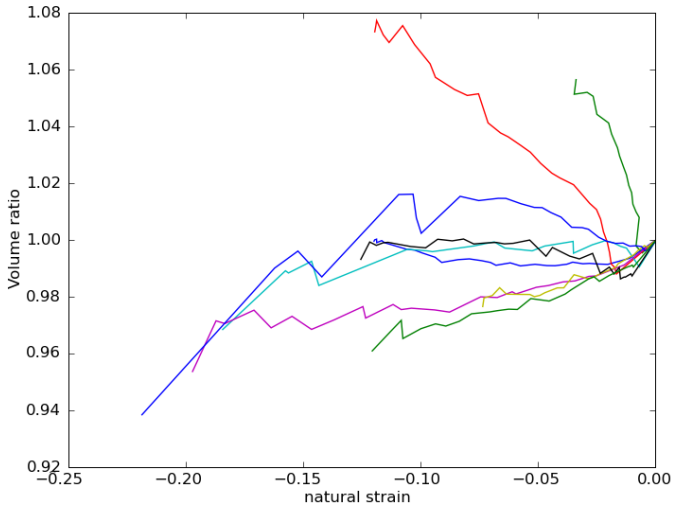

Fig. 7.9: Evolution of the volume ratio during the unconfined compression tests at 60 mm min^{-1}.

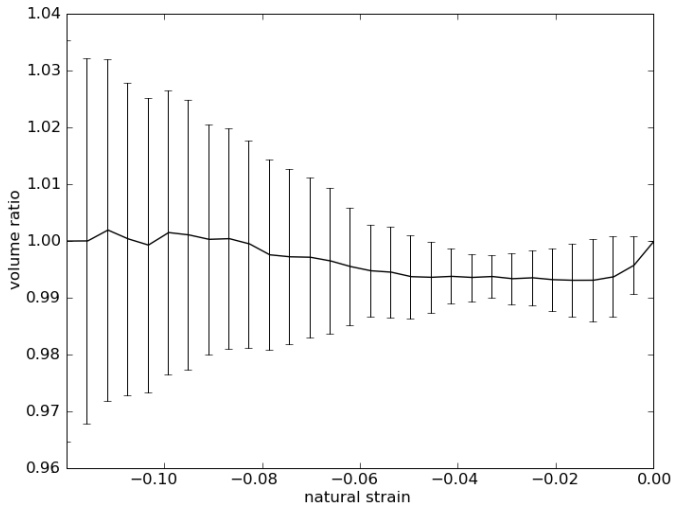

Fig. 7.10: Averaged evolution of the volume ratio during the unconfined compression tests at 60 mm min^{-1}

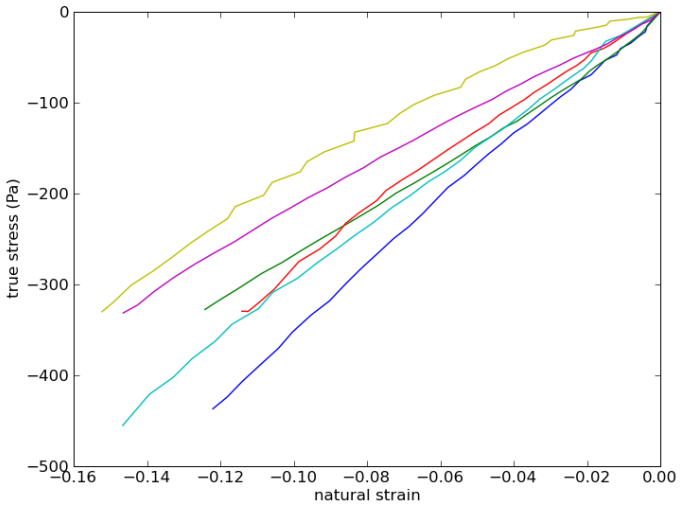

Fig. 7.11: Stress-strain curves for the unconfined compression tests at 12 mm min^{-1}.

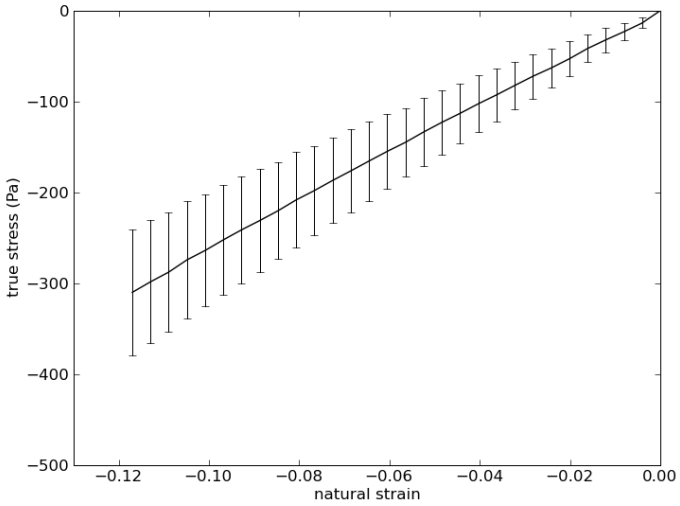

Fig. 7.12: Stress-strain mean curve for the unconfined compression tests at 12 mm min^{-1}.

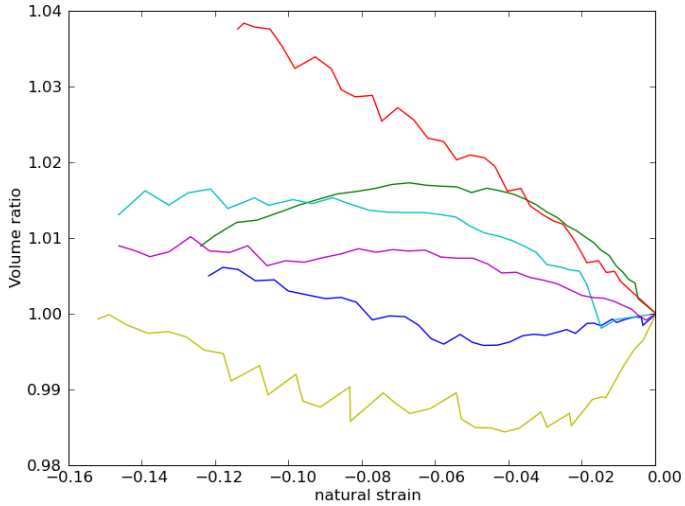

Fig. 7.13: Evolution of the volume ratio during the unconfined compression tests at 12 mm min^{-1}.

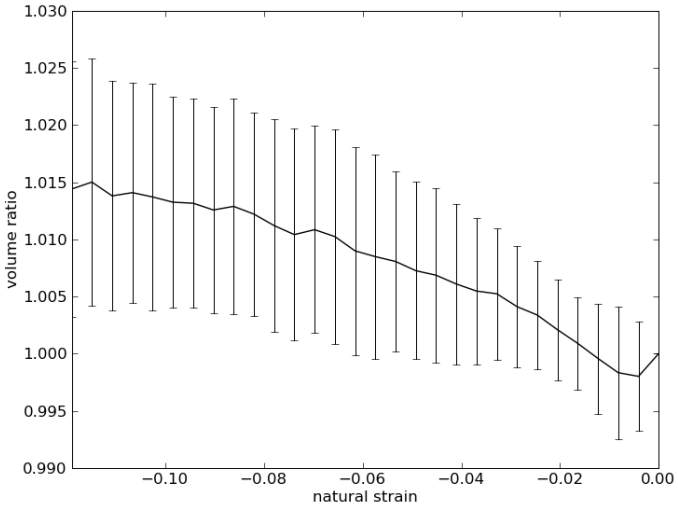

Fig. 7.14: Averaged evolution of the volume ratio during the unconfined compression tests at 12 mm min^{-1}

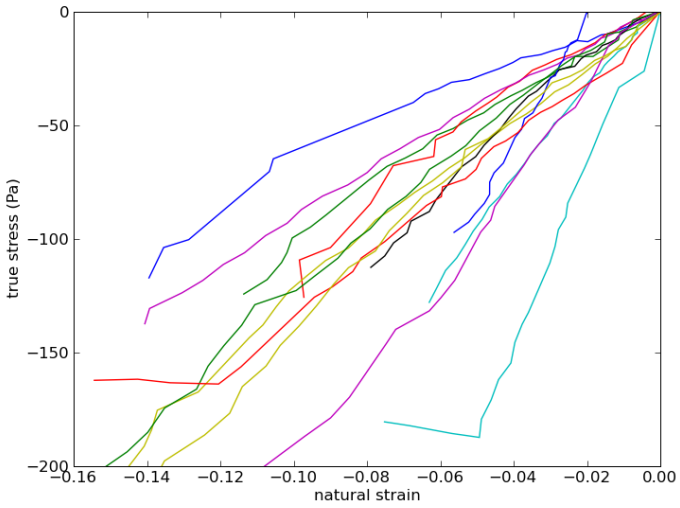

Fig. 7.15: Stress-strain curves for the unconfined compression tests at 1.2 mm min^{-1}.

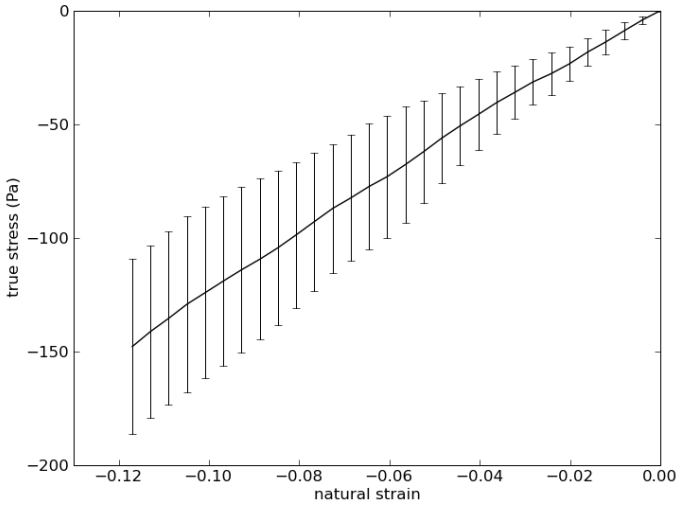

Fig. 7.16: Stress-strain mean curve for the unconfined compression tests at 1.2 mm min^{-1}.

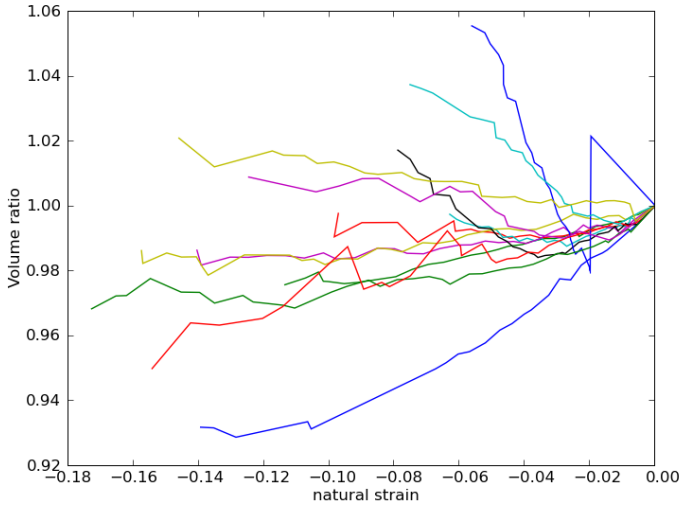

Fig. 7.17: Evolution of the volume ratio during the unconfined compression tests at 1.2 mm min^{-1}.

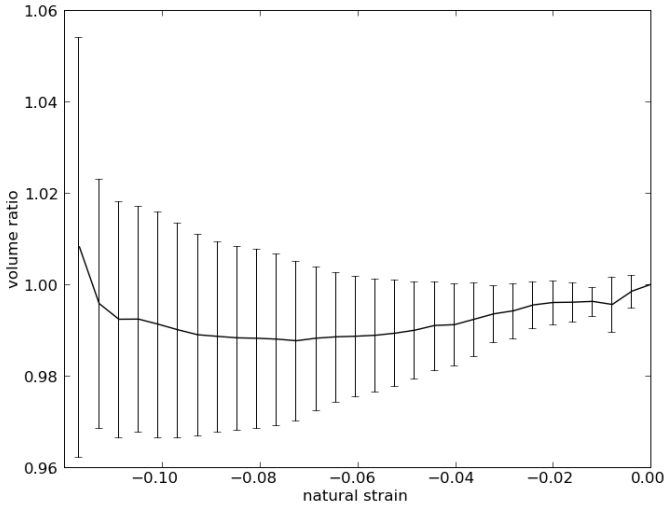

Fig. 7.18: Averaged evolution of the volume ratio during the unconfined compression tests at 1.2 mm min^{-1}

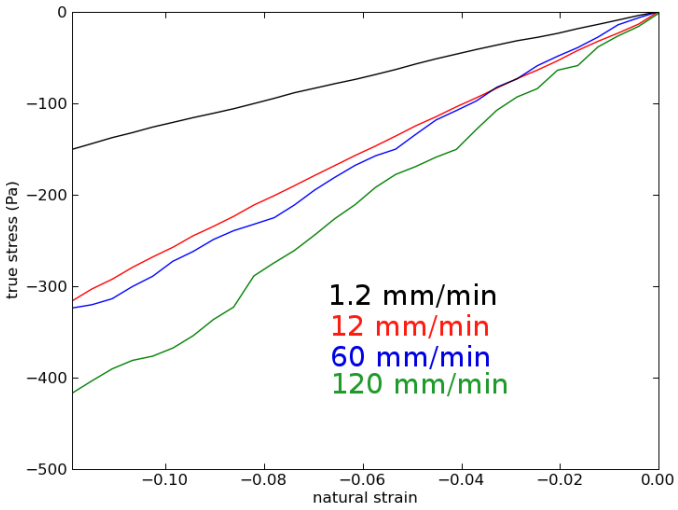

Fig. 7.19: Stress vs strain curves: effect of the loading rate.

7.3.2 Relaxation tests

For the relaxation experiments, the initial compression was performed sufficiently quickly to minimize the effect of the relaxation during this phase. A value of 60 mm min^{-1} was chosen so that it was possible to acquire data with the stereoscopic system during the compression. The superior plate was imposed to reach a force of 0.5 N; it was then hold in position for one minute. Fig. 7.20 shows the resulting force versus time curves from which several comments can be made. Firstly, it appears that the imposed value of 0.5 for the force was not perfectly respected. This is due to the inertia of the testing machine. Secondly, the scatter of the curves is less than for the compression tests results. The force quickly (less than 5 seconds) drops to half its peak value and then continues to decrease but at a much smaller rate.

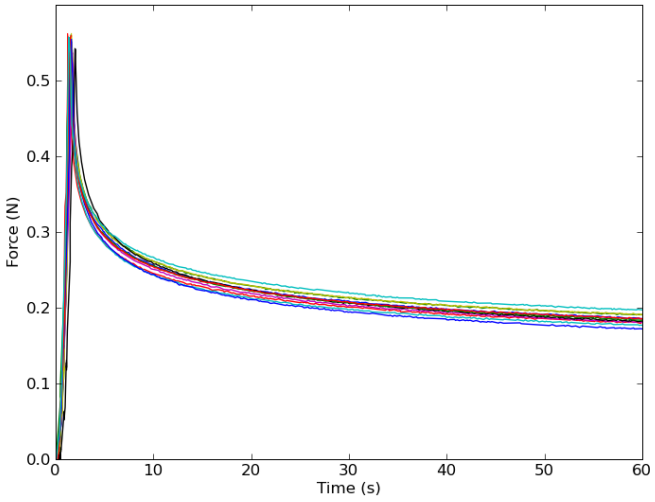

Fig. 7.20: Force versus time curves for the relaxation experiments.

The strictly speaking relaxation curves were isolated obtain Fig. 7.23 and averaged on Fig. 7.24. No exponential function of the form

$$f(t) \quad = \quad C\exp(-t/\tau) \tag{7.11}$$

is able to reproduce the relaxation behaviour of the brain tissue with a reasonable accuracy. To prove it, the logarithm of the force was plotted versus time (Fig. 7.21). The obtained curve is clearly not the straight line expected in the case of an exponential. Fig. 7.22 shows the best fit exponential, which does not fit the experimental curve at all.

This is of remarkable importance as a modelling issue. If the constitutive model is expressed as a differential equation, a first order cannot be considered. Thus, the notion of characteristic (or *relaxation* in this case) time generally used with the decaying exponentials is not transposable here. Indeed, the relaxation presents two different dynamics: a short-term fast decaying and a long-term, slow decrease. Two new characteristic times are defined to describe the shape of the curve: let's introduce the **time of first relaxation** $\tau_\mathbf{1}$ as the time at which the force reaches half of its initial value. The *steady state time* $\tau_\mathbf{m}$ is the time for

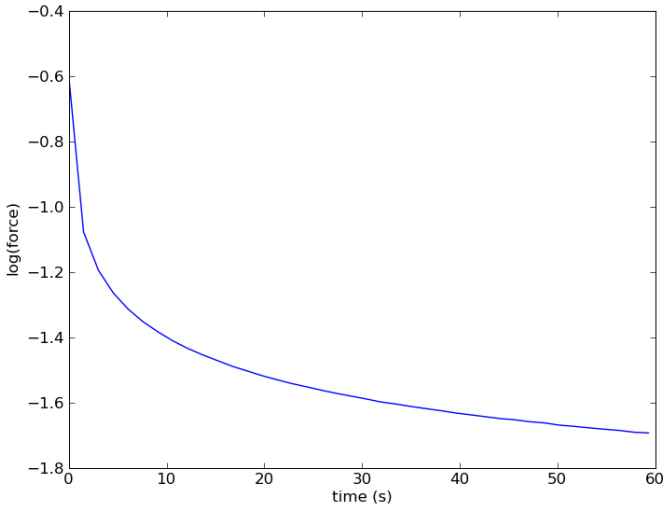

Fig. 7.21: Logarithm of the experimental relaxation force versus time.

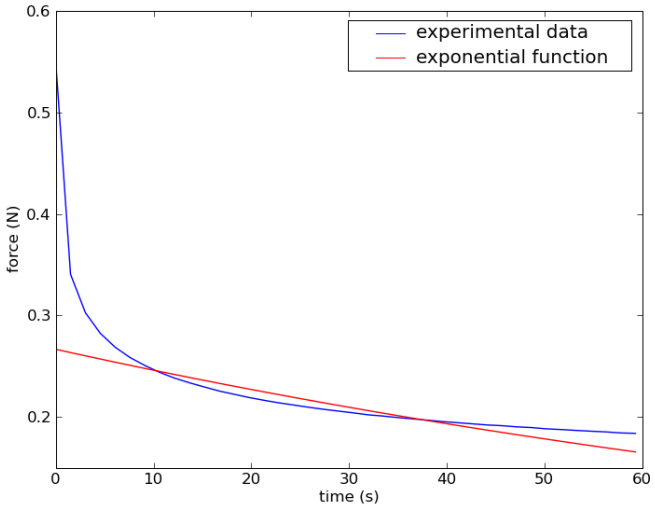

Fig. 7.22: Comparison of the experimental relaxation curve and the best fit exponential $y = 0.27 * \exp(-t/124.5)$.

which the slope of the curve becomes smaller than m. In this case, m was arbitrarily fixed to 0.001 (N s^{-1}). These two variables, determined for the mean relaxation curve (Fig. 7.24), are equal to:

$$\begin{aligned} \tau_1 &= 6.08\ s \\ \tau_{0.001} &= 33.43\ s \end{aligned}$$

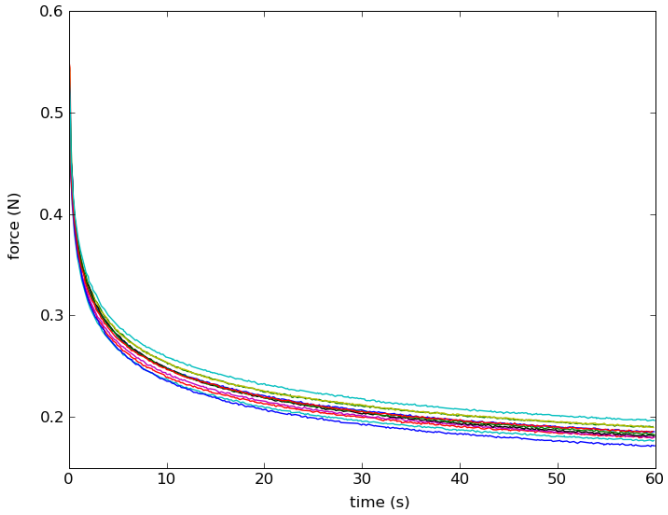

Fig. 7.23: Force versus time curves for the relaxation experiments during the relaxation phase.

One more experiment was conducted on a longer time. The aim was to determine if the force reached a constant value after a "sufficiently long time". The duration of this experiment was set to 500 seconds. The result is plotted in Fig. 7.25. The variation of the slope at the end of the curve cannot be distinguished from the noise, therefore it can be considered as constant.

As for the compression tests, the volume ratio was computed and plotted versus the strain in Fig. 7.26 and Fig. 7.27.

As seen in Fig. 7.27, the mean curve exhibits a more important standard deviation than for the compression tests. A compressible material should have here presented a strictly decreasing slope during the compression phase and a plateau during the relaxation phase (as it is the case for the black, yellow and purple curves). But this is not the behaviour observed for the mean curve. This is again a fact in favor of the incompressibility of the brain tissue.

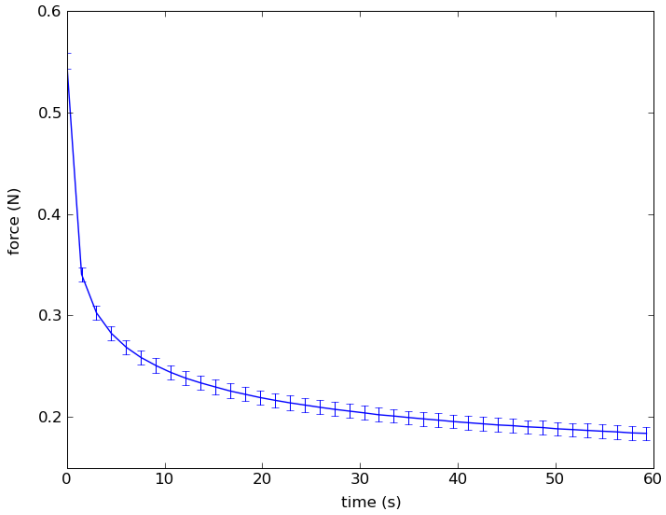

Fig. 7.24: Force versus time mean curve for the relaxation experiments during the relaxation phase.

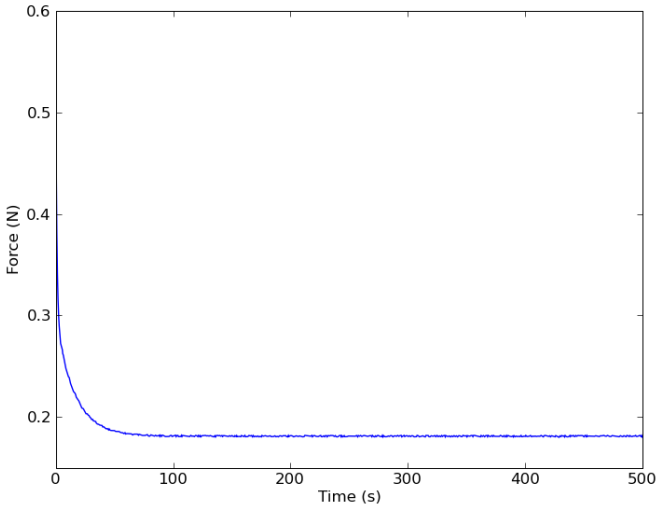

Fig. 7.25: Force versus time for the 500 seconds relaxation test

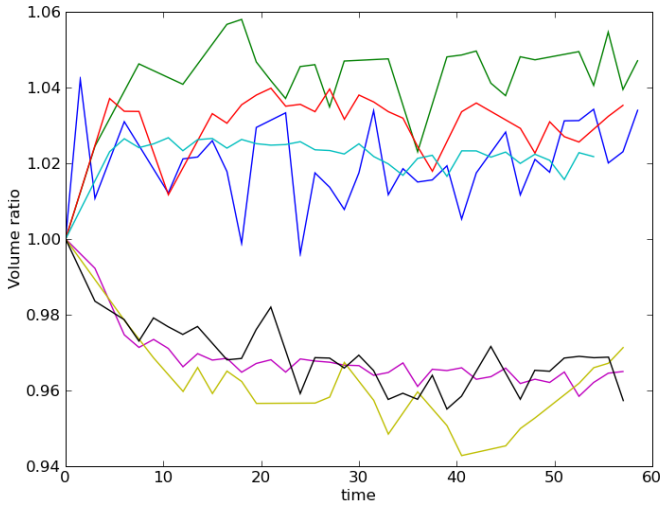

Fig. 7.26: Evolution of the volume ratio during the relaxation experiments.

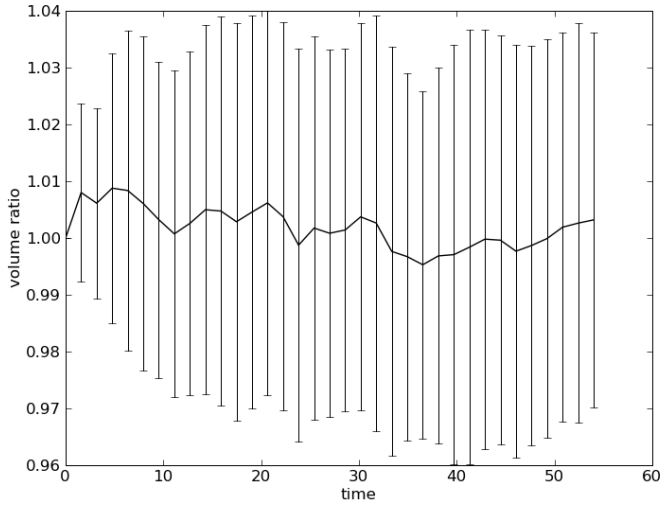

Fig. 7.27: Evolution of the averaged volume ratio during the relaxation experiments.

From the relaxation tests, the following conclusions are reached:

- the behaviour of the brain tissue in relaxation cannot be described by a single exponential, therefore at least two characteristic times are needed to define it,
- during the relaxation process, the force (or equivalently, the stress) reaches an non-zero steady value,
- the averaged volume ratio is very close to 1 throughout the tests.

7.3.3 Cyclic tests

The cyclic tests consisted in the repetition of three cycles of unconfined compression test followed by an unloading phase which brought back the superior plate at its initial position. The number of repetitions was fixed after observing that a larger number prevented the proper use of the correlation algorithm due to irreversible deformation of the samples (such as cracks). The displacement of the superior plate was fixed to 2 mm and its speed to 60 mm min^{-1}. A special care was taken as far as the contact is concern. The maximal threshold force value authorized during the compression preconditioning (explained in section 6.5) was reduced to 1% of the peak value.
Due to the important rejection of data points, it was not possible to obtain a proper set of stress-strain curves. However, those cyclic tests may be used to determine the qualitative response of the brain tissue to a periodic loading. Therefore, the analysis will be performed on the force versus displacement curves plotted in Fig. 7.28 and Fig. 7.29. For the sake of readability, only one experiment was plotted. However, the observations made for this particular curve (randomly chosen) are valid for all the tests carried out.

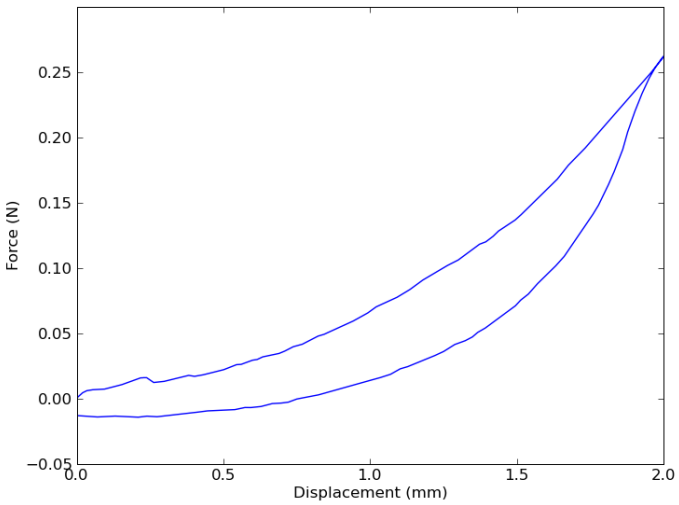

Fig. 7.28: Force versus displacement curve for the first cycle of a cyclic test.

Some observations can be made when looking at Fig. 7.28. Firstly, this curve clearly shows that, at the considered loading velocity, the brain tissue is not a conservative material. The surface comprised between the two parts of the curve, corresponding to the loading and the unloading, represents the energy dissipated over the cycle. Secondly, the value of the force after the cycle is slightly negative. This value may be explained by the relaxation that takes place during the test. Since the force decreases faster during the unloading phase and since the superior face of the sample adheres to the plate, it yields in a state of tension when the compression plates comes back to its initial location. The relaxation is also responsible for the nearly horizontal slope on the curve at the end of the cycle.

Fig. 7.29 shows a 3-cycles experiment and brings several other information:

1. the peak value of the force decreases as the number of the cycle increases, as does the dissipated energy,

2. the decrease of the peak force is less important between cycles 2 and 3 than between cycles 1 and 2, which could indicate that a steady value is approached.

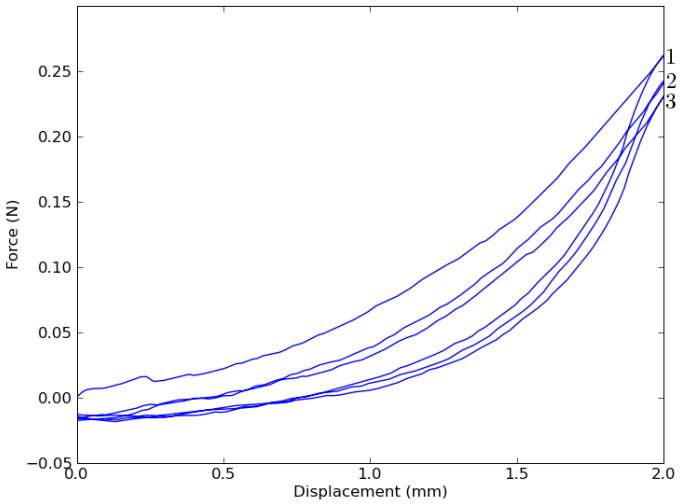

Fig. 7.29: Force versus displacement curve for a three cycles experiment.

This decrease can be attributed either to a softening of the brain tissue or to the fact that from the second cycle the initial force is negative, thus reducing the maximal value. A combination of those two effects can also be assumed. To investigate further those questions, a 50 cycles test was carried out. The result is shown in Fig. 7.30. The decrease of the peak force is clearly visible and a steady value seems to be reached. Fig. 7.31 shows that this steady value is reached around the 40^{th} cycle and is about $\frac{2}{3}$ the initial peak value. If the curves on Fig. 7.32 are examined, it can be concluded that there exists no obvious correlation between the value of the force at the end of one cycle and the next peak value. Thus, although

the decrease of the first few peak values can partially be attributed to the negative value of the minimum force, it cannot be denied that a softening phenomenon of the brain tissue exists.

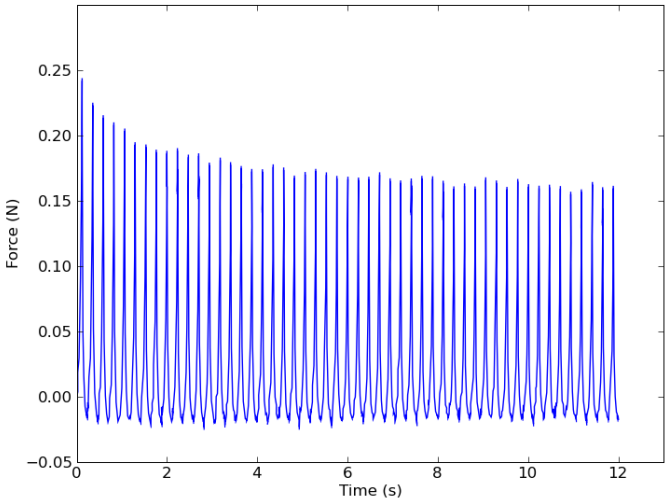

Fig. 7.30: Force versus time curve for the 50 cycles experiment.

As far as the dissipated energy is concerned, Fig. 7.33 points out that it also decreases with the number of cycles and reaches a steady value that is less than $\frac{1}{3}$ of the value corresponding to the initial cycle.

The volume ratio was obviously computed for all the 3 cycles experiments. The results are presented in Fig. 7.34 and Fig. 7.35.

The cycles are visible in Fig. 7.34, suggesting some volume variation during the test, but once again the averaged curve (Fig. 7.35) is almost constant and close to 1, with an erratic data point in the middle. No particular pattern is seen on this mean curve.

The cyclic tests supplied interesting information that yields to the following conclusions:

- the brain tissue presents a softening property and is a dissipative material,
- at least 40 cycles of compression/unloading are necessary to reach a steady value for the compression force,
- the cyclic tests tend to confirm the incompressibility assumption.

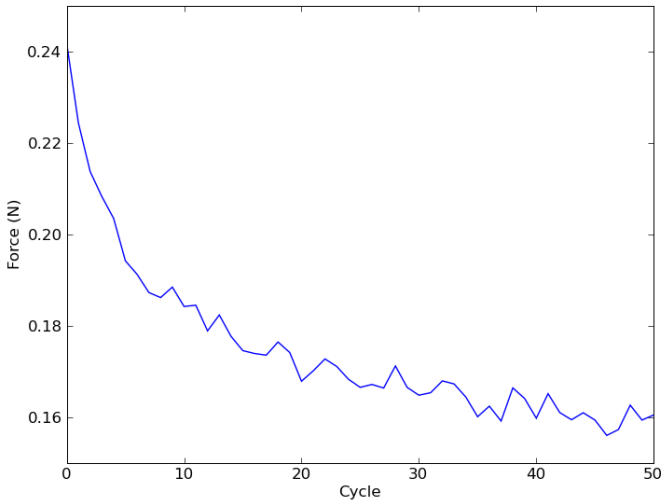

Fig. 7.31: Peak force versus the number of the cycle for the 50 cycles experiment.

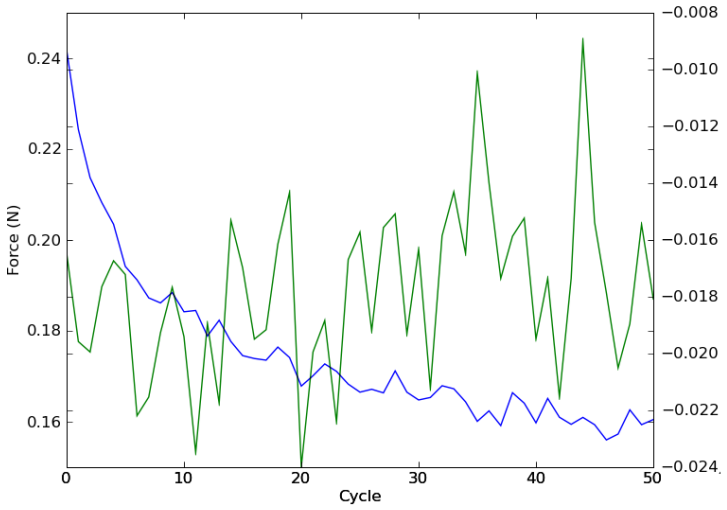

Fig. 7.32: Peak (blue, left scale) and minimal (green, right scale) forces versus the number of the cycle for the 50 cycles experiment.

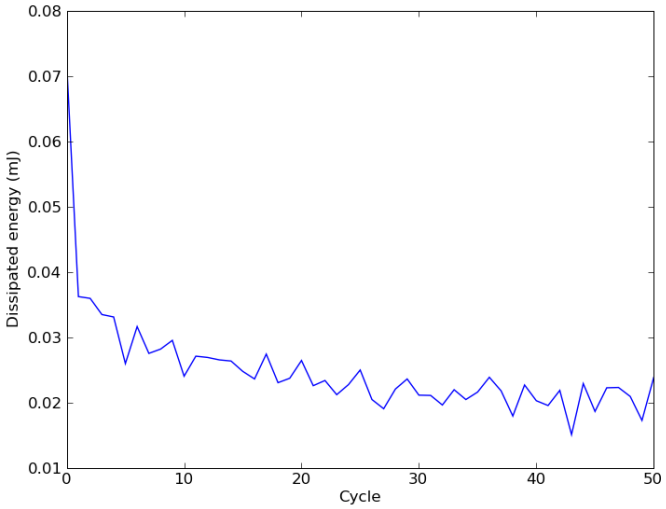

Fig. 7.33: Dissipated energy versus the number of the cycle for the 50 cycles experiment.

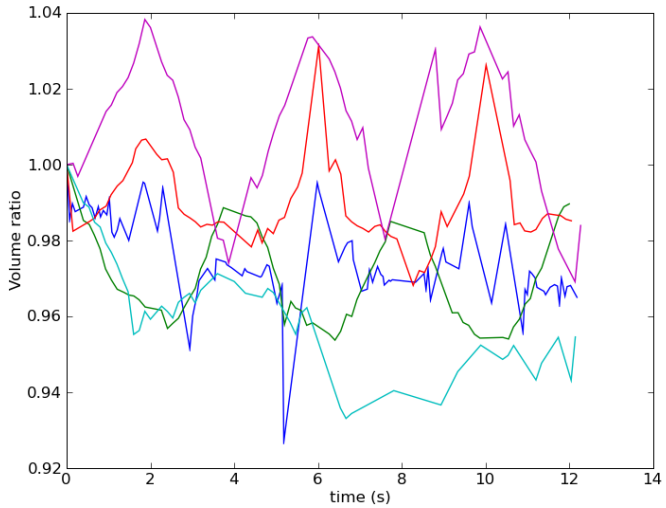

Fig. 7.34: Evolution of the volume ratio during the cyclic tests.

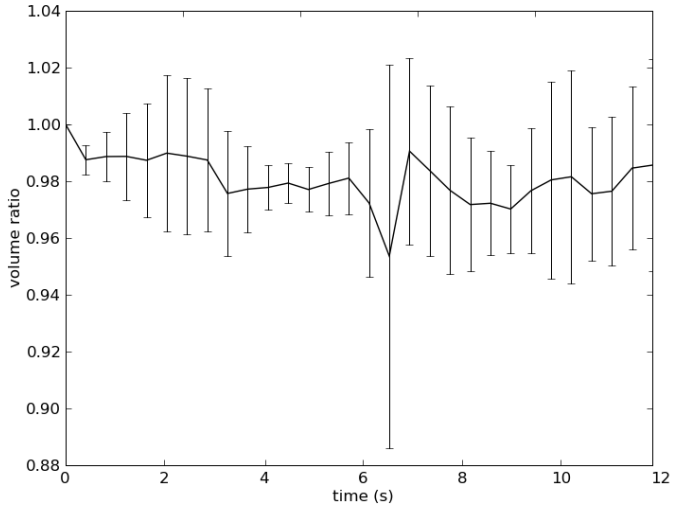

Fig. 7.35: Evolution of the mean volume ration during the cyclic tests.

7.3.4 Incompressibility of the brain tissue.

No material is known to be perfectly incompressible. The unavoidable measurement imprecisions prevent to claim that a medium is perfectly incompressible. However, incompressibility is a very useful approximation for some analytical and/or computational applications. When using the concept of incompressibility, it is tacitly admitted that we refer to a very very low compressibility.

In the previous sections, the volume ratio was computed and plotted versus time (or natural strain) for various types of tests. The averaged curves were almost constant and close to 1, which tends to prove the incompressibility assumption generally admitted for the brain tissue. No test-specific trend appears on those mean curves, as one could have expected in the case of a compressible medium.
Only a few (typically 5 or 6) curves were available for each type of experiment and the maximum standard deviation generally consisted of a [-0.03,+0.03] interval around the mean value.

In order to try to decrease this scatter, all the volume ratio curves were brought together over a fictitious time interval and averaged to produce the results seen in Fig. 7.36 and 7.37.

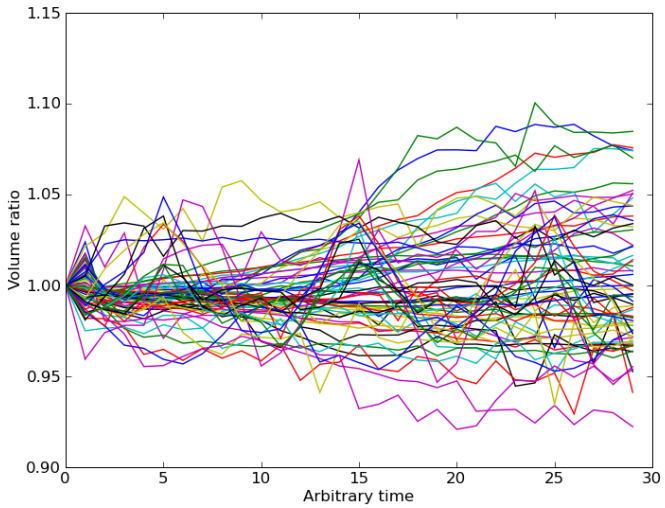

Fig. 7.36: Evolution of the volume ratio with respect to a fictitious time for all the experiments carried out.

Fig. 7.36 shows the evolution of the volume ratio for 65 experiments. The values are strictly contained between 0.93 and 1.10, but most of the curves have only a few points outside the [0.96,1.04] interval. The mean curve plotted in Fig. 7.37 exhibits an almost constant value of 1. It is instructive to consider the Fig. 7.38 presenting the mean value recomputed without the 15 curves containing the most extreme values.

It is remarkable that this operation does not affect the value of the mean but only slightly decrease the size of the standard deviation bars (as could be obviously expected). This is an indication that the extreme values are not due to a physical phenomenon but are

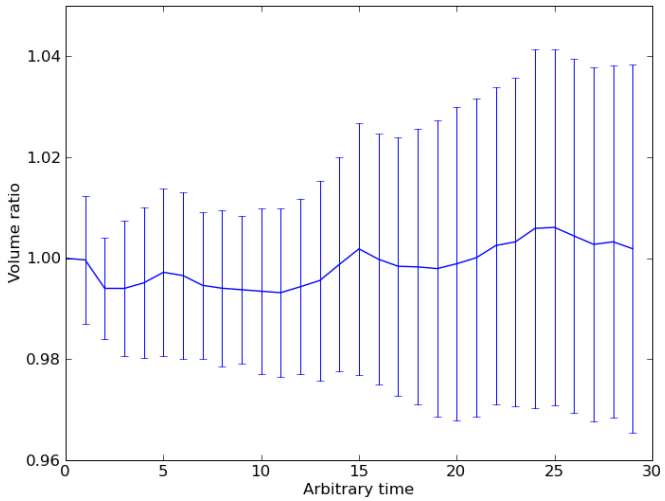

Fig. 7.37: Evolution of the averaged volume ratio with respect to a fictitious time.

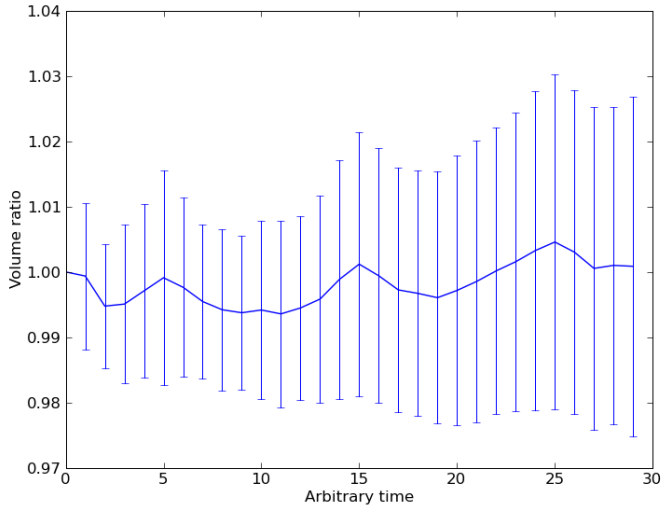

Fig. 7.38: Evolution of the corrected averaged volume ratio with respect to a fictitious time.

rather due to random errors in the experimental results. This is confirmed by the fact that several data points indicates a volume ratio superior to 1. Either the brain tissue is able to increase its volume when compressed or those values result from measurement errors. From a thermodynamic point of view, the first hypothesis cannot be accepted in a continuum. Hence, this apparent volume increase can only be attributed either to the opening of cracks in the tested samples (in such a case, they are not any more a continuum) or to measurement errors. The two possibilities deserve consideration. As stated in section 6.5, the tests were discarded when a crack was observed on the sample, on the field of view of the cameras. If the crack was located outside the 240°C angle covered by the three stereoscopic system, we had no possible knowledge of it. The fact that the volume ratio is superior to 1 for several data points can more likely be attributed to measurement errors, raising the question of the reliability of the optical measurement system.

The problem comes from the fact that it is impossible with our software, and although it was one requirement for the purchase of the material, to combine the results from the three stereoscopic systems into one data file from which the average radius and height of the sample could be determined directly. The decision was then made to use the three systems independently and average their results for the desired variables. This option was however less interesting than the combination of the results. Indeed, instead of having one best-fit cylinder for the whole sample, the system came with three local approximations of the shape of the test piece. Despite the care taken when cutting the samples, the shape was not perfectly regular and sometimes, the radii seen by two systems could differ from 0.5 to 1 mm (for a radius of the order of 10 mm). It is then not impossible that the averaged radius and height led to the computation of a volume ratio greater than 1. Although not physical, these data points should be considered affected by the same kind of error than the ones with a value inferior or equal to 1.

Nevertheless, it is remarkable that the standard deviation on the volume ratio is of the order of a few percents, i.e. about 10 times less than the scatter on the stress-strain curves.

Considering these results and comments, the use of the digital image correlation method allowed us to prove the very near incompressibility of the brain. To the author's knowledge, the present work is the first to bring an experimental proof of the near incompressibility of the brain tissue.

7.3.5 Remark on the values of the compression factor λ

The samples are theoretically 10 mm high and their diameter is 20 mm. Since a 2 mm displacement was set for the unconfined and cyclic tests, a compression factor λ (resp. a natural strain ε) of 0.8 (resp. -0.22) is expected. Practically, the height of the samples were generally smaller than 10 mm for they deformed under their own weight, and larger values of λ and ε are encountered. However, the maximal (in absolute value) natural strain that appears on the stress vs strain curves in section 7.3 never exceeds 0.16, which would correspond to an initial height of the sample of 13.5 mm if the displacement is kept at 2 mm. This is clearly impossible since the carving procedure ensured that the height of the sample never exceeded 10 mm. Thus, the explanation of this small value of the maximum strain must be sought elsewhere.

As stated previously, λ is computed from the stereoscopic system data files. Because of the imperfect contact between the plate and the specimen (Fig. 7.39), at the beginning of the test, the contact with the machine plate starts earlier on one side of the specimen. The

material line AB is first subjected to the compression and thus presents a non-zero strain while line CD does not. Later in the test, line CD is also compressed but its strain remains inferior to that of line AB. The strains appearing in the stress vs strain curves of section 7.3 are averaged strains over the specimen surface computed by the 3D reconstruction software. Hence, it is not surprising that the maximum absolute value of ε does not correspond to a 2 mm compression.

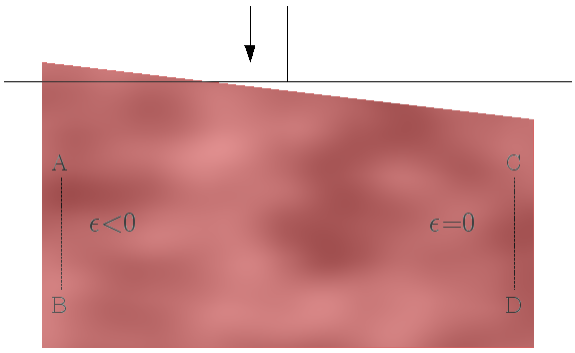

Fig. 7.39: Schematic compression of a specimen with uneven superior face represented in its initial geometry.

7.4 Influence of the geometry of the sample.

The plates of the testing machine were lubricated to ensure that the sample kept its cylindrical shape during the experiment. This assumption is essential to simplify the computation of the stresses and was generally in good agreement with the experimental observations.

With this shape conservation and the tissue incompressibility granted, the question whether a stereoscopic system is still useful for future tests can be asked. Indeed, the preparation in order to apply the speckle pattern requires a lot of manipulations of the fragile sample and may cause unwanted deformations.

A solution would be to cut the sample, place it directly on the plate and perform the test. The initial geometry of the sample would be the dice cutter's one and the displacement of the machine plate would be used to compute the strain. This option would present two immediately identifiable drawbacks:

- the imperfection of the contact would not be taken into account,
- since the sample collapses under its own weight, the initial height (resp. radius) would be smaller (resp. greater) than the dice cutter's ones.

Let's forget the contact issue for a moment to concentrate on the initial geometry. Thanks to the stereoscopic systems, the initial radius was determined for all the samples that were placed in the testing machine, before any rejection was made. The radius distribution is presented in Fig. 7.40. Since this curve is obviously not symmetrical, it cannot be fitted by a Gaussian distribution.

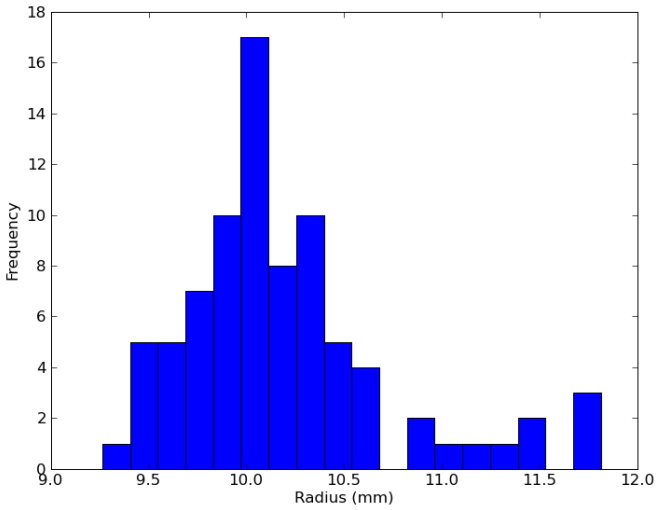

Fig. 7.40: Measured distribution of the samples radius

About 80% of the values are comprised between 9.5 mm and 10.6 mm, with the mean equals to 10.2 mm. Hence, taking the radius of the dice cutter as the initial value of the radius of the sample does not seem to be a bad approximation. However, it should be noted that about 20% of the radii are greater than 10.8 mm.

The relative error on the stress due to an error on the radius solely is easily obtained as follows:

$$\begin{aligned} \sigma &= \frac{F}{\pi r^2} \\ \Delta\sigma|_F &= -\frac{2F}{\pi r^3}\Delta r \\ \left.\frac{\Delta\sigma}{\sigma}\right|_F &= -2\frac{\Delta r}{r} \end{aligned} \tag{7.12}$$

When using only the information (force and displacement) of the testing machine, an error of 8% is committed before the test if the sample radius exceeds the dice radius by 0.4 mm. It is unavoidable that the sample becomes shorter (and then larger in diameter) due to the gravity force, therefore, the value of 10.2 mm should be used as the initial radius in order to minimize the initial error. Correspondingly, an initial height of 9.6 mm should be used to respect the incompressibility of the sample.
Fig. 7.41 illustrates the influence of the initial radius on the stress-strain curves.

Practically, the imprecision on the radius cannot be dissociated from the imprecision on the height because of the incompressibility of the brain tissue. An error on the radius will

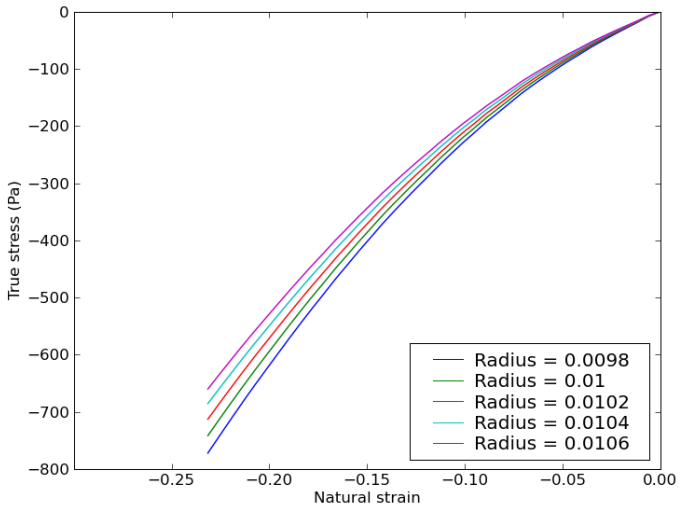

Fig. 7.41: Influence of the initial radius on the stress-strain curves

have a repercussion on the value of the height according to Eqn. 7.13.

$$\begin{aligned} V &= \pi h r^2 \\ \Delta V &= \pi r^2 \Delta h + 2\pi h r \Delta r \\ \frac{\Delta h}{h} &= -\frac{1}{2}\frac{\Delta r}{r} \end{aligned} \tag{7.13}$$

Finally, a simple development connects the relative errors on the strain and the height:

$$\begin{aligned} \frac{\Delta \varepsilon}{\varepsilon} &= \frac{\Delta \lambda}{\lambda \ln \lambda} \\ &= \frac{1}{\ln \lambda}\frac{d}{(h-d)}\frac{\Delta h}{h} \end{aligned} \tag{7.14}$$

where $\lambda = \dfrac{(h-d)}{h}$ and d is the imposed displacement. For the described compression experiments, expression 7.14 reduces to

$$\frac{\Delta \varepsilon}{\varepsilon} = \frac{1}{4 \ln \lambda}\frac{\Delta h}{h} \tag{7.15}$$

To summarize, an initial error on the radius will directly cause an error on the stress. Furthermore, because of the incompressibility constraint, the height will be affected and so will the strain. Therefore, the stress-strain curve will be altered by two effects coming from the same source. To this must be added the error on λ coming from the imperfection of the contact between the plate and the sample. Indeed, due to this flaw, the real compression factor λ^* is greater than the theoretical one λ_{th} as it is illustrated by the following reasoning.

Fig. 7.42 shows the initial and final geometries of a real sample. The ideal sample's superior surface is perfectly flat and its height is h_0, while the superior surface of an actual

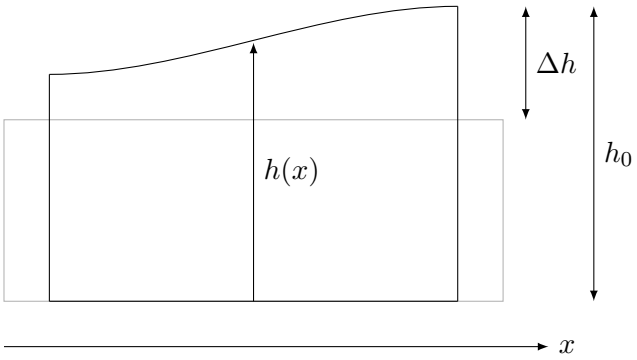

Fig. 7.42: Initial and final geometries of a real sample.

sample is irregular and described by a function h(x)[2]. Let's recall that the theoretical, ideal, compression factor λ_{th} is expressed as

$$\lambda_{th} = \frac{h_0 - \Delta h}{h_0} \tag{7.16}$$

For the real sample pictured in Fig. 7.42, λ is a function of x:

$$\lambda^*(x) = \frac{h(x) - \delta h(x)}{h(x)} \tag{7.17}$$

where $\delta h(x)$ is the local height reduction that can be expressed by:

$$\delta h(x) = \Delta h - (h_0 - h(x)) \tag{7.18}$$

Thus, Eqn. 7.17 becomes:

$$\begin{aligned} \lambda^*(x) &= \frac{h_0 - \Delta h}{h(x)} \\ &= \lambda_{th} \frac{h_0}{h(x)} \end{aligned} \tag{7.19}$$

The ratio $\frac{h_0}{h(x)}$ is superior or equal to 1. In the correlation software Vic3D, the value of λ^* was averaged over the reconstructed surface of the sample. Designating the averaged value by $\bar{\lambda}$, the following inequality holds:

$$\bar{\lambda} \geq \lambda_{th} \tag{7.20}$$

[2]A simplified 2d case is considered here.

In the preceding development, the time dependence of the variables was not explicitly expressed. Let's now define the time function $\varphi(t)$ so that

$$\bar{\lambda} = \varphi(t)\,\lambda_{th} \tag{7.21}$$

with $1 \leq \varphi(t) < \infty$. Thus, the relationship between the theoretical and actual strain is written:

$$\begin{aligned} \bar{\varepsilon} &= \ln \bar{\lambda} \\ &= \ln(\varphi(t)\lambda_{th}) \\ &= \varepsilon_{th} + \ln(\varphi(t)) \end{aligned} \tag{7.22}$$

Using Eq. 7.22, the relative error on the strain is

$$\frac{\bar{\varepsilon} - \varepsilon_{th}}{\varepsilon_{th}} = \frac{\ln(\varphi(t))}{\varepsilon_{th}} \tag{7.23}$$

Let's particularize formula 7.23 to a realistic case: the theoretical strain is equal to -0.25 and, at the considered time, $\varphi = 1.05$, i.e., there is a 5% relative error on λ. The actual strain is then -0.20 and the relative error on ε is 20% ! This "scale expansion" of the strains, which are the abscissae in the stress-strain diagrams, results in an underestimation of the stresses ! Therefore, unless the imperfection of the contact between the plate and the sample can be neglected, the displacement should be estimated by another way than from the vertical displacement of the plate, e.g. an optical measurement system. To illustrate this discussion, the stresses and strains were computed from the output of the testing machine only and compared with the results obtained with the optical system. The Cauchy[3] stresses and natural strains were computed assuming the initial sample's dimensions were $r = 10.2\ mm$ and $h = 9.6\ mm$ which correspond to the previously determined mean values. The resulting curves are presented in Fig. 7.43, Fig. 7.44 and Fig. 7.45.

[3]Despite having the same definition, the term "Cauchy stresses" will be employed instead of "true stress" when referring to a fictitious sample.

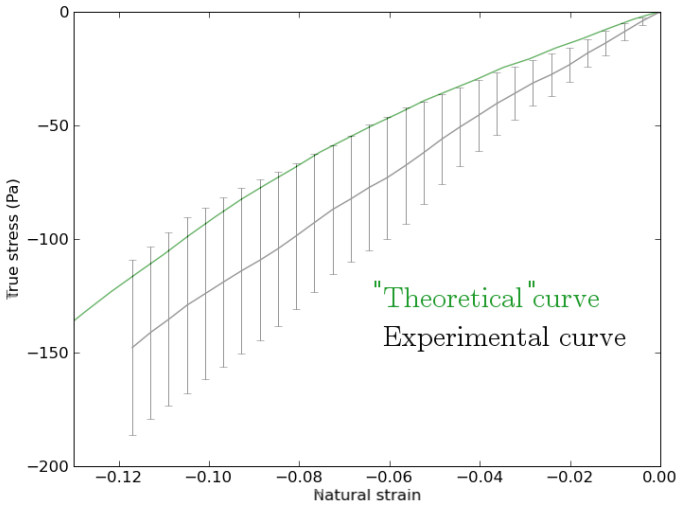

Fig. 7.43: Comparison of the stress vs strain experimental mean curve and the "theoretical" curve based on an ideal sample for the unconfined compression experiment at 1.2 mm min^{-1}.

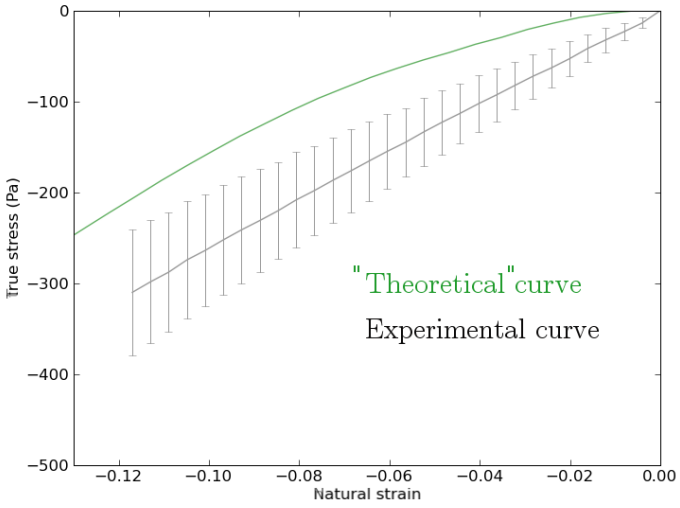

Fig. 7.44: Comparison of the stress vs strain experimental mean curve and the "theoretical" curve based on an ideal sample for the unconfined compression experiment at 12 mm min^{-1}.

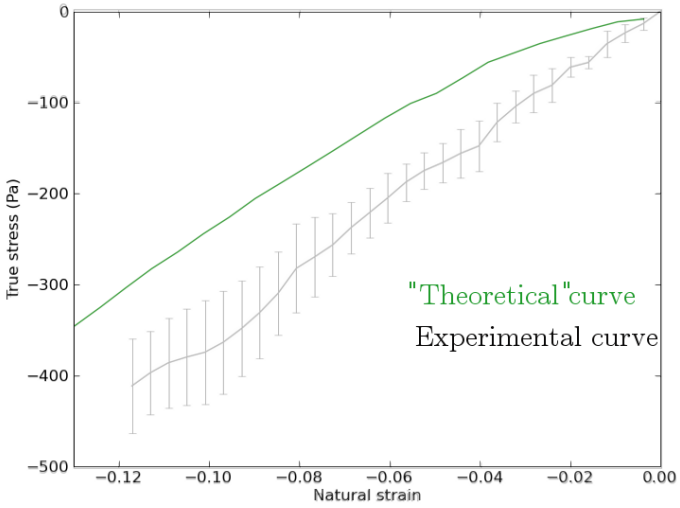

Fig. 7.45: Comparison of the stress vs strain experimental mean curve and the "theoretical" curve based on an ideal sample for the unconfined compression experiment at 120 mm min^{-1}.

The underestimation of the stress clearly appears on those curves. The so-called "theoretical" curves only cross the uncertainty bars in the case of the slowest experiment. The distance between the "theoretical" and experimental curves increases with the loading velocity. The error committed here is bigger than the scatter of the experimental curves, proving the necessity of the precise measurement of the geometry.

It can be verified that the error is compatible with the expression 7.22. The compression factor was plotted versus time for the 12 mm min^{-1} experiment, as shown in Fig. 7.46. Let's consider a particular time, for example 5 s, for which $\Delta h = 1$ mm. The corresponding experimental compression factor is $\bar{\lambda} = 0.955$. The "theoretical" value is

$$\lambda_{th} \quad \frac{h_0 - \Delta h}{h_0} = \frac{9.6 - 1}{9.6}$$

$$= \quad 0.896 \tag{7.24}$$

The value of the correction factor $\varphi(t = 5s)$ is equal to 1.066. Therefore, the following relation holds:

$$\bar{\varepsilon} = \ln(\varphi(t = 5s)) + \ln \lambda_{th} \tag{7.25}$$

$$= -0.046 \tag{7.26}$$

The "theoretical" value of the strain is equal to $\ln(0.896) = -0.11$. Hence, the stress value at $\varepsilon = -0.11$ of the green curve in Fig. 7.45 should be translated at $\varepsilon = -0.046$ and thus fall within the uncertainty bars. The other sources of error (initial radius, ...) must be taken into

account to retrieve the experimental curves but this illustration shows that the imperfection of the contact is the major source of error when performing compression tests.

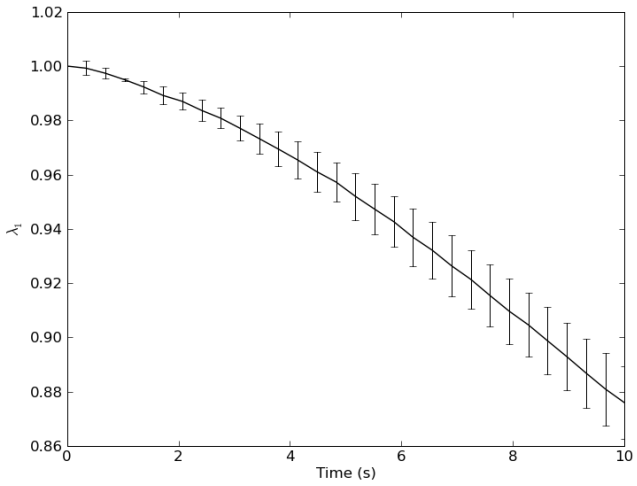

Fig. 7.46: Compression factor λ versus time for the 12 mm min^{-1} unconfined compression experiment.

7.5 Qualitative behaviour at higher strains.

The diagrams presented in section 7.3 show a quasi linear relationship between the stresses and the strains. It was concluded that this behaviour is due to the smallness of the strains. To further investigate the relationship between σ and ε at higher strains, the force versus displacement curves were used. It was assumed that the tests were performed on an ideal sample, the dimensions of which are $r = 10.2\ mm$, the mean value of the distribution, and $h = 9.6\ mm$, the corresponding height using the incompressibility constraint. No quantitative data can obviously be obtained by this way, but qualitative information will be extracted.

Fig. 7.47 shows that the stress-strain curves are nonlinear, so must be the constitutive model. The scatter is very important and will be further discussed in section 7.6. Fig. 7.48, Fig. 7.49 and 7.50 present the averaged curves for the unconfined compression tests at 1.2 mm min^{-1}, 12 mm min^{-1}, 120 mm min^{-1}. They are superimposed in Fig. 7.51. The final value of the stress, as well as the final slope of the curve, increase with increasing loading velocities, which is the expected behaviour of a viscoelastic material. Two points may be underlined: firstly, the difference between the 1.2 mm min^{-1} and 12 mm min^{-1} curves is greater than between the 12 mm min^{-1} and 120 mm min^{-1} curves and secondly, there seems to be an "accident" at the beginning of the 120 mm min^{-1} curve, since it is above the 12 mm min^{-1} one. There is no obvious physical reason to this, so this must be an artifact. Indeed, the initial slope of the curve should also increase with the loading velocity.

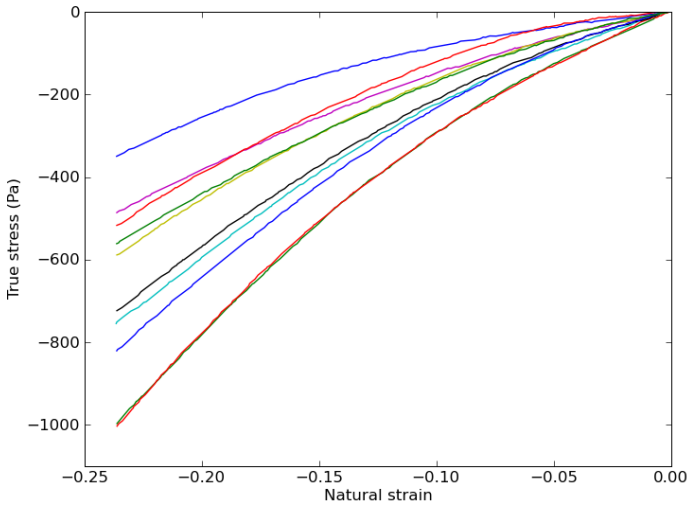

Fig. 7.47: Stress-strain curves for the unconfined compression tests at 12 mm min^{-1}.

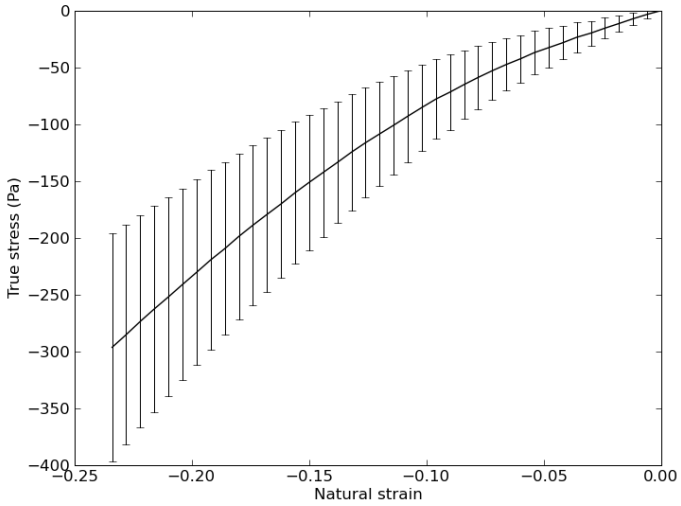

Fig. 7.48: Stress-strain mean curve for the unconfined compression tests at 1.2 mm min^{-1}.

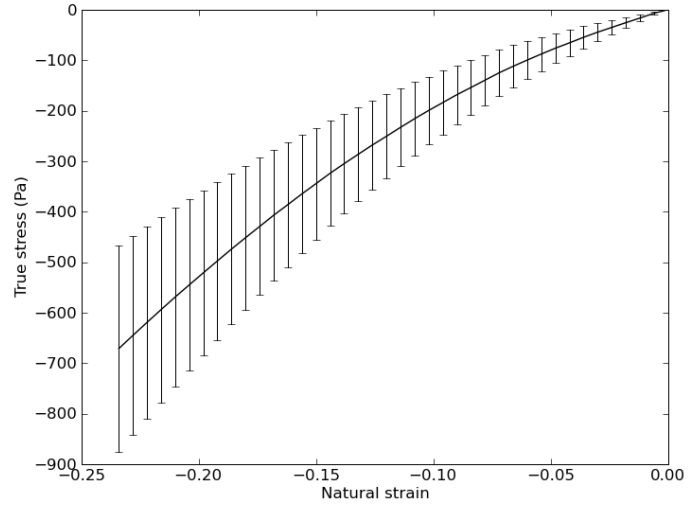

Fig. 7.49: Stress-strain mean curve for the unconfined compression tests at 12 mm min^{-1}.

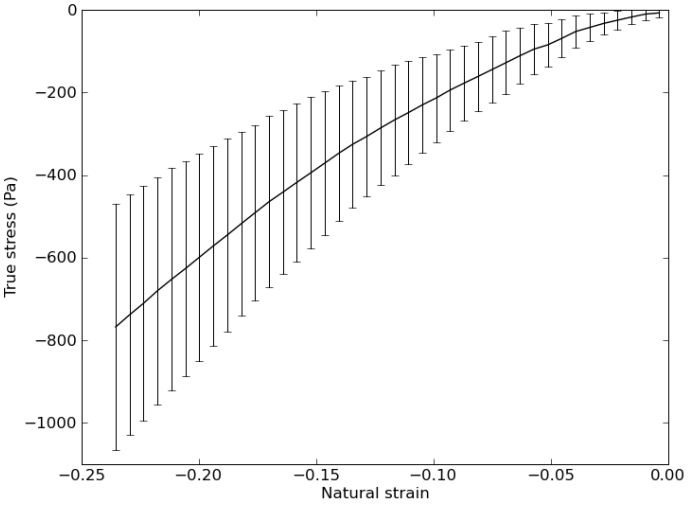

Fig. 7.50: Stress-strain mean curve for the unconfined compression tests at 120 mm min^{-1}.

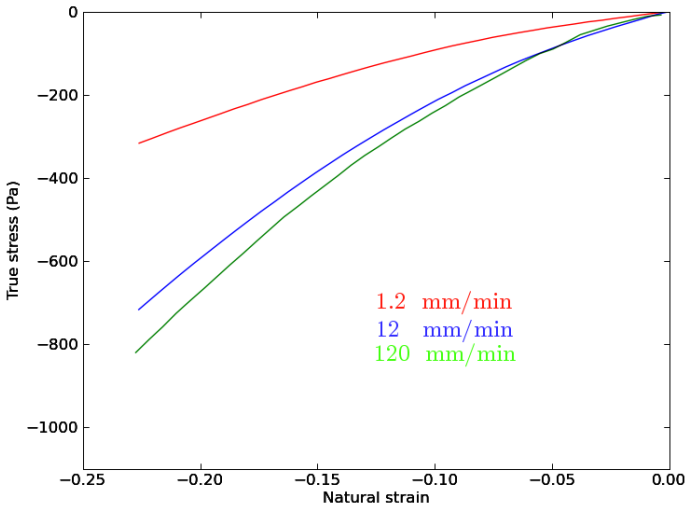

Fig. 7.51: Stress-strain mean curves for the 3 unconfined compression tests.

7.6 Dispersion of the curves.

Due to the different testing conditions, the results presented by different teams are generally quite different (see Hrapko et al. (2008)) . But even amongst the results of a particular team, an important dispersion exists. A reason often given is the intrinsic variability relative to the biological nature of the tissue. Along with this cause, three other sources of dispersion are proposed:

1. the heterogeneity of the brain tissue mechanical properties,
2. the imperfection of the contact, which is related to the irregularity of the superior face of the sample,
3. the "preconditioning" caused by the preparation of the sample and its handling in general.

These points have already been evoked in this document. Let's recall them. The brain tissue was proved to be heterogeneous (Franceschini (2006)). Due to the constraints on the size of the sample and the size of the brains available, it was impossible to take the samples at the same location in the brain. Because of the softness of the tissue and the operations required to apply the speckle pattern, random stresses and/or deformations may have been generated in the samples. At last, the imperfection of the contact and its consequence have been widely discussed above.

The first issue could be solved using bigger brains. Unfortunately, they are not as easy to collect than the swine ones. Another solution would be to use completely different techniques of testing and measurement. As issue 2. is concerned, the use of the digital image correlation

coupled with a finite element code would allow to work with the actual geometry and to get rid of the contact problem, thus bringing more accuracy to the results. The initial geometry would be computed thanks to the D.I.C and would constitute the initial mesh for the F.E. The irregularities of the sample would then be taken into account in the computation of the stresses and the strains. An inverse method would be used to determine the parameters of the proposed model.
However, it is more difficult to solve issue 3. since the preparation of the sample is mandatory to use the D.I.C.

CHAPTER 8
DISCUSSION OF THE EXPERIMENTAL RESULTS

8.1 Introduction

In this short chapter, we discuss one by one the main topics encountered in the two previous chapters.

8.2 Assumptions

In chapter 1, the brain is presented as a very complex organ from geometrical and material points of view, made of white and grey matters as well as membranes and blood vessels. It also comprises a circulatory system for the cerebrospinal fluid. The white matter, constituted by the neurons' axons, was said to be anisotropic while the grey matter is assumed isotropic. Due to the cited twofold complexity, the brain is more likely to be heterogeneous, as shown by Franceschini (2006).

But when trying to characterize the brain tissue, it was assumed to be homogeneous, isotropic and no distinction was made between white and grey matters. The main reasons are the size of the swine (half) brains that were available and the fact that we wanted to use the D.I.C. to measure the deformations of the samples. The stress state of the sample was also assumed to be homogeneous to simplify their computation.

The applications aimed for a global biomechanical model of the brain, neurosurgery as well as traumatic brain injury prediction, involve the finite element method (F.E.M.). Thus, the design of constitutive equations must be developed concurrently with the meshing of the brain, a field bound to the automatic segmentation of clinical images. This late topic is evolving considerably rapidly nowadays, so should the experimental characterization. The development of a model of the brain thus requires a large team and a lot of work.

The experimental characterization performed in the frame of this PhD thesis is not accurate enough to be part of a project which would consist of a software able to compute accurate stresses and strains under a given loading coherent with the loading velocities used in laboratory. However, it is suitable in a simplified meshing. In addition, for modelling issues, it is very important to have a statistically validated experimental proof of the near incompressibility of the brain tissue. In this respect, the results of this chapter provide a sound basis for the use of the near incompressibility hypothesis in brain modelling.

8.3 Dispersion of the results

Contrarily to manufactured materials, it is very difficult to get accurate and reproducible results when dealing with soft tissues such as the brain. Their softness makes them extremely difficult to manipulate. It is also very hard to obtain a regular shape when carving the sample and the change in geometry from one sample to another constitutes a source of dispersion. The imperfection of the contact, widely discussed in the previous chapter also contributes to the scatter of the results. Since it was very difficult to carve the samples at the same locations for each test, the heterogeneity of the brain tissue certainly accounts for the dispersion too. At last, let's mention that an intra-species variability is present in the mechanical properties, the quantitative influence of which is unknown.

All the aforementioned points create an important dispersion of the results. They were averaged to obtain representative curves, but the question is : "representative of what ?" Let's forget a moment that the results were obtained on swine brains. The interest of characterizing the tissue is to provide a model together with the right parameters. If the same scattering of the stress versus strain curves is found for the human brain, would the mean curve really be significant ? In the case of neurosurgery, what if the considered patient's brain mechanical properties were quite different from the mean ?

The dispersion of the experimental results must be diminished to a reasonable level, while a non invasive technique must be developed to adapt the parameters of the model to a particular individual. The magnetic resonance elastometry (M.R.E.) (see Weaver et al. (2001)) seems to be a good start.

8.4 Use of the D.I.C.

When dealing with material so soft that it is impossible to attach strain gauges on them, the digital image correlation technique provides a interesting way of getting measurements. Besides its accuracy, it gives a full map of the displacements and the strains while extensometers only provide a local information.

In the framework of this thesis, the D.I.C. was used to compute the variation of height and radius of the samples, allowing to compute the deformed crossed section and then the true stresses and to monitor the evolution of the volume.

However, the stress (or strain) level reached is limited by the capacity of the correlation software to track the pixels during the deformation. The quality of the speckle pattern is an important related factor but there exists no other instrument that the eyes (and the experience) of the experimentater to judge this quality.

8.5 Influence of the contact

Section 7.4 stresses out the importance of the imperfection of the contact between the superior plate and the sample. Dramatic errors can be commited on the computation of the strains if the contact is assumed ideal.

To cope with this imperfection, one could use the D.I.C. to determine the real initial shape of the sample in the field of view of the cameras. It would then be meshed and a F.E. simulation would reproduce the test. The full maps of the displacements and strains would be used to compute the stresses. An inverse method would be used to determine the

parameters of the implemented model. More precise, this method would also require more computational time. No more assumption would be required on the geometry. With 5 systems and a favorable configuration, it would be possible to reconstruct the whole lateral surface of the sample ! Let's notice, however, that no experimental information is available as far as the inside of the sample is concern.

8.6 In vivo versus in vitro

As reproducible and accurate could be the in vitro tests, they do not take into account the blood and cerebrospinal fluid circulations and the associated change in mechanical properties. The realization of in vivo tests would allow to consider these effects, not to mention that both the temperature and the postmortem degradation of the tissue problems would no longer exist. Furthermore, it would also take the interaction between the different tissues and membranes into account.

Technically speaking, the use of the D.I.C. would be more challenging than in the in vitro case. Firstly, an important part of the skull should be removed to access to largest possible view of the tissues. Secondly, the application of the speckle pattern would be as difficult as in the in vitro case. Ethically speaking, it would be very difficult to ask for painting the brain of a living animal. Not to mention the transposition to the characterization of human tissues.

The alternate way is to work on a brain from a dead animal but still perfused to reproduce the in vivo conditions. This technique has been used by Gefen and Margulies (2004). The difficulty here is to achieve the perfusion. The whole brain surface would be available to record measurements and a skull-shaped plate would be used to maintain the brain. This method could be applicable to fresh human cadavers. But once again, if an important dispersion is observed, the mean curve would be of limited interest when using the model with an actual patient. The perfused, ex vivo method should be coupled with non invasive tests to particularize, or refine, the value of the parameters of the model to a particular individual.

8.7 Conclusion

The experiments performed confirmed the important scatter of the stress versus strain curves observed in the literature. The use of the digital image correlation allowed to compute the true stresses as well as the evolution of the volume of the samples during the tests. The incompressibility assumption was confirmed. The D.I.C. also permitted to stress the importance of the contact between the superior plate of the testing machine and the sample. The error associated to the "perfect contact" assumption was calculated and shown to be significant. The results also showed that the brain tissue exhibits a softening behaviour when submitted to cyclic tests and presents a dynamics in relaxation with two characteristic times.

8.8 Perspectives

From an experimental point a view, and in our humble opinion, the priority goes to the reduction of the scattering of the results. The protocols need to be refined so that the results become more reproducible.

The next phase would then be to use the perfused ex vivo method to get reliable quantitative data. This could allow the characterization of tumorous tissues as well as sane ones.

Part IV

Numerical modelling

CHAPTER 9
A FRACTIONAL VISCOELASTIC LAW

9.1 Introduction

In this chapter are presented the developments that led to the design of an original fractional calculus-based model. The starting point is the first viscoelastic law proposed by Miller and Chinzei (1997a). An equivalent formulation is provided as a differential equation. Then, the basic idea is to replace the time derivatives by a single fractional derivation and see what happens.

The classical and fractional models are compared and a sensitivity analysis is performed on the parameters.

Finally, the methods for accelerating the resolution of the fractional differential equations are implemented and tested. The experimental data used in this chapter come from Miller and Chinzei (1997a).

9.2 From an integral to a differential formulation

9.2.1 Integral formulation

Let's recall the hyperviscoelatic potential[1] proposed by Miller and Chinzei (1997a) defined in Eqn. 5.14:

$$W = \int_0^t \left\{ \sum_{i+j=1}^{N} \left[C_{ij0} \left(1 - \sum_{k=1}^{n} g_k (1 - e^{(\tau - t)/\tau_k}) \right) \right] \frac{d}{d\tau} \left[(I_1 - 3)^i \ (I_2 - 3)^j \right] \right\} d\tau \quad (9.1)$$

Since the incompressibility of the brain tissue is assumed, and using the Lagrange stress tensor, the constitutive equation is written:

[1] Another potential, using the Ogden strain energy density function was also defined. The developments presented in this section are potential-independent.

$$T_{iA} = \frac{\partial W}{\partial F_{iA}} - pF_{iA}^{-T} \tag{9.2}$$

$$= T_{iA}^{*} - pF_{iA}^{-T} \tag{9.3}$$

with p a hydrostatic pressure.

Substituting W by its expression (Eqn. 9.1) leads to

$$T_{iA}^{*}(t) = \int_0^t \left\{ \sum_{i+j=1}^{N} \left[C_{ij0} \left(1 - \sum_{k=1}^{n} g_k (1 - e^{(\tau - t)/\tau_k}) \right) \right] \frac{d}{d\tau} \frac{\partial}{\partial F_{iA}} \left[(I_1 - 3)^i \ (I_2 - 3)^j \right] \right\} d\tau \tag{9.4}$$

Two relaxation times were used ($n = 2$) and second degree terms of the strain invariants were retained ($N = 2$) to characterize the material (Miller and Chinzei (1997a)). The following assumptions were made for the elastic coefficients C_{ij0} :

$$C_{100} = C_{010} \tag{9.5}$$

$$C_{200} = C_{020} \tag{9.6}$$

$$C_{110} = 0 \tag{9.7}$$

9.2.2 Towards a differential formulation

Let $G(t)$ be a function[2] of the form of a particular convolution integral:

$$G(t) = \int_0^t p(\tau) \left(1 - e^{\frac{\tau - t}{\alpha}} \right) d\tau \tag{9.8}$$

where $p(\tau)$ stands for an arbitrary continuous function and α for a time constant.

This function $G(t)$ can be decomposed in a sum of two functions according to:

$$G(t) = \int_0^t p(\tau) \, d\tau - \int_0^t p(\tau) e^{\frac{\tau - t}{\alpha}} \, d\tau \tag{9.9}$$

$$= G_p(t) - G_e(t) \tag{9.10}$$

Using the parametric integral derivation formula and Eqn. 9.10, we can compute the time derivative of $G(t)$

[2]The development is presented here for a scalar valued function. The extension to vector or tensor valued functions is immediate.

$$\frac{dG}{dt} = p(t) + \frac{1}{\alpha}\int_0^t p(\tau)e^{\frac{\tau-t}{\alpha}}d\tau - p(t) \tag{9.11}$$

$$= \frac{1}{\alpha}G_e(t) \tag{9.12}$$

$$= \frac{1}{\alpha}\left(G_p(t) - G(t)\right) \tag{9.13}$$

$$= -\frac{1}{\alpha}G(t) + \frac{1}{\alpha}G_p(t) \tag{9.14}$$

Each component of the stress tensor defined in Eqn. 9.4 is a scalar that can be rewritten[3] in the form of Eqn. 9.10:

$$T^*(t) = G_p(t) - \sum_{k=1}^{2} g_k \left(G_p(t) - G_{e,k}(t)\right) \tag{9.15}$$

provided that

$$p(t) = \sum_{i+j=1}^{2} C_{ij0}\,\frac{d}{dt}\left[\frac{\partial}{\partial F}\left(\left(I_1-3\right)^i\left(I_2-3\right)^j\right)\right] \tag{9.16}$$

and

$$G_{e,k} = \int_0^t p(\tau)\exp\frac{\tau-t}{\tau_k} \tag{9.17}$$

The extension of the differential equation Eqn. 9.14 to a sum of $G_{e,k}$ functions requires a further development.

Let's consider $T(t)$ (Eqn. 9.10 and its derivatives:

$$T^*(t) = G_p(t) - \sum_{k=1}^{2} g_k\left[G_p(t) - G_{e,k}(t)\right]$$

$$= G_p(t)\underbrace{\left(1-g_1-g_2\right)}_{\gamma} + g_1\,G_{e,1}(t) + g_2\,G_{e,2}(t) \tag{9.18}$$

$$\dot{T}^*(t) = p(t) - \frac{g_1}{\tau_1}G_{e,1}(t) - \frac{g_2}{\tau_2}G_{e,2}(t) \tag{9.19}$$

$$\ddot{T}^*(t) = \dot{p}(t) + \frac{g_1}{\tau_1^2}G_{e,1}(t) + \frac{g_2}{\tau_2^2}G_{e,2}(t) - \left(\frac{1}{\tau_1}+\frac{1}{\tau_2}\right)p(t) \tag{9.20}$$

[3]The subscript iA is omitted to make the expressions more readable.

Using Eqn. 9.18 and Eqn. 9.19, we can extract the values of $G_{e,1}$ and $G_{e,2}$

$$G_{e,1}(t) = \frac{\tau_1\tau_2}{g_1\,(\tau_1-\tau_2)}\left(\dot{T}^*(t)+\frac{1}{\tau_2}T^*(t)-p(t)-\frac{\gamma}{\tau_2}G_p(t)\right) \tag{9.21}$$

$$G_{e,2}(t) = \frac{\tau_1\tau_2}{g_2\,(\tau_2-\tau_1)}\left(\dot{T}^*(t)+\frac{1}{\tau_1}T^*(t)-p(t)-\frac{\gamma}{\tau_1}G_p(t)\right) \tag{9.22}$$

If we substitute these results in Eqn. 9.20, we get

$$\ddot{T}^*(t)+\beta\dot{T}^*(t)+\frac{1}{\tau_1\tau_2}T^*(t)-\mathcal{H}(t) = 0 \tag{9.23}$$

with

$$\beta = \frac{1}{\tau_1}+\frac{1}{\tau_2} \tag{9.24}$$

$$\mathcal{H}(t) = \dot{p}+\frac{\gamma}{\tau_1\tau_2}\,G_p(t) \tag{9.25}$$

Consequently, we can state the equivalence between the formulations 9.23 and 9.26 :

$$T^*(t)=\int_0^t\left\{\sum_{i+j=1}^{2}\left[C_{ij0}\left(1-\sum_{k=1}^{2}g_k(1-e^{(\tau-t)/\tau_k})\right)\right]\frac{d}{d\tau}\frac{\partial}{\partial f}\left[(I_1-3)^i\;(I_2-3)^j\right]\right\}d\tau \tag{9.26}$$

where f stands for the component F_{ij} of the deformation gradient tensor.

Unfortunately, the scalar equation Eqn. 9.23 cannot be directly extended to the Lagrange stress tensor $\mathbf{T}$. Indeed, its time derivative is not an objective quantity. If $\mathbf{Q}$ is such that $\mathbf{Q}^{-1}=\mathbf{Q}^T$, we have

$$\dot{\mathbf{T}}^+ = \dot{\overbrace{\mathbf{QTQ}^T}} \tag{9.27}$$

$$= \dot{\mathbf{Q}}\mathbf{T}\mathbf{Q}^T+\mathbf{Q}\dot{\mathbf{T}}\mathbf{Q}^T+\mathbf{Q}\mathbf{T}\dot{\mathbf{Q}}^T \tag{9.28}$$

$$\neq \mathbf{Q}\dot{\mathbf{T}}\mathbf{Q}^T \tag{9.29}$$

Hence, to extend Eqn. 9.23 to a tensor, a natural solution consists in choosing a couple of stress and strain tensors the time derivatives of which are objective.

It can be easily shown that after a change of reference frame :

$$\mathbf{C}^+ = \mathbf{C} \tag{9.30}$$

$$\mathbf{S}^+ = \mathbf{S} \tag{9.31}$$

and thus

$$\frac{d\mathbf{C}^+}{dt} = \frac{d\mathbf{C}}{dt} \tag{9.32}$$

$$\frac{d\mathbf{S}^+}{dt} = \frac{d\mathbf{S}}{dt} \tag{9.33}$$

Hence, we propose the following objective differential equation which is equivalent to the hyperviscoelastic constitutive law based on Miller's work:

$$\ddot{\mathbf{S}}^* + \beta\dot{\mathbf{S}}^* + \frac{1}{\tau_1\tau_2}\mathbf{S}^* = \mathbf{H}(t) \tag{9.34}$$

with

$$\mathbf{H}(t) = \dot{\mathbf{p}} + \frac{\gamma}{\tau_1\tau_2}\mathbf{G}_\mathbf{p}(t) \tag{9.35}$$

$$\mathbf{G}_\mathbf{p}(t) = \int_0^t \mathbf{p}(\tau)d\tau \tag{9.36}$$

in which $\mathbf{p}(t)$ is a Lagrangian quantity redefined as

$$\mathbf{p}(\tau) = \sum_{i+j=1}^{2} C_{ij0}\,\frac{d}{d\tau}\left[\frac{\partial}{\partial\mathbf{C}}\left((I_1-3)^i\,(I_2-3)^j\right)\right] \tag{9.37}$$

Then, the PK2 stresses are given by

$$\mathbf{S} = \mathbf{S}^* - p\mathbf{C}^{-1} \tag{9.38}$$

with p the hydrostatic pressure which is not defined in the constitutive equation because of incompressibility.

The solution of the homogeneous problem relative to 9.34 describes the relaxation of the material while the right hand side term is related to the instantaneous applied strain.

9.3 Fractional formulation (I)

While reviewing the literature, Fig. 9.1 attracted our attention to the existence of the fractional derivative (see chapter 4). This mathematical tool proved to be adapted to the study of viscoelastic materials, so it seemed to be a good idea to try to apply it to the modelling of brain tissue.

The basic idea is to replace Eqn. 9.34 with a fractional differential equation, namely

$$D_t^{(\alpha)}\mathbf{S}^* + b\mathbf{S}^* = \mathbf{M}(t) \tag{9.39}$$

A single fractional term was retained, as it was established by Atanackovic and Stankovic (2008) that a single FDE was equivalent to an infinite system of first order ordinary differential equations (see section 4.7.3). Therefore, the operator

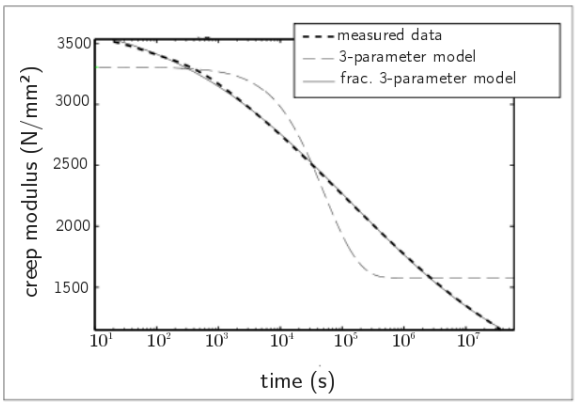

Fig. 9.1: Creep modulus vs time from Schmidt and Gaul (2002a)

$$\mathcal{L}_\alpha(t) \quad = \quad D_t^{(\alpha)} + a \tag{9.40}$$

should be able to reproduce the behaviour of

$$\mathcal{L}_D(t) \quad = \quad D_t^{(2)} + b\, D_t^{(1)} + c \tag{9.41}$$

The right hand side of Eqn. 9.39 must be adapted to be dimensionally coherent. Therefore, we choose

$$\mathbf{M} \quad = \quad \eta \dot{\mathbf{p}}(t) + \zeta \mathbf{G}_\mathbf{p}(t) \tag{9.42}$$

The dimensions of ζ and η are respectively $T^{-\alpha}$and $T^{2-\alpha}$.
The fractional constitutive law for the brain tissue then writes:

$$D_t^{(\alpha)}\mathbf{S}^* + b\mathbf{S}^* \quad = \quad \mathbf{M}(t) \tag{9.43}$$

$$\mathbf{S} \quad = \quad \mathbf{S}^* - p\mathbf{C}^{-1} \tag{9.44}$$

This model counts 6 parameters: $\alpha, b, \eta, \zeta, C_{100}$ and C_{200}. The parameter b can be rewritten as

$$b \quad = \quad \left(\frac{1}{\tau}\right)^\alpha = \tau^{-\alpha} \tag{9.45}$$

in which τ has the dimension of a time and can thus be regarded as a characteristic time.
The numerical method chosen for the resolution of Eqn. 9.43 is the predictor-corrector algorithm (section 4.7.3). There are two reasons to this choice:

1. it is, to our opinion, the simplest to implement,

2. the logarithmic memory and the short memory have been developed for that kind of scheme.

As a first test to evaluate this model, we calibrated its parameters on the unconfined compression experiments at 500 mm min^{-1} and 5 mm min^{-1} found in Miller and Chinzei (1997a). The determination of the six parameters of the model was achieved through the use of the simulated annealing algorithm (see Appendix B). They are grouped in Tab. 9.1.

Parameter	Interpretation	Value	Units
α	order of derivation	0.98	
b	inverse of characteristic time to the power α	$8.581\ 10^{-3}$	$s^{-\alpha}$
C_{100}	elastic coefficient	3463.7	Pa
C_{200}	elastic coefficient	35.9	Pa
η	generalized viscous coefficient	1.0	$s^{2-\alpha}$
ζ	generalized viscous coefficient	$5.0\ 10^{-2}$	$s^{1-\alpha}$
τ	characteristic time	128.4	s

Tab. 9.1: Coefficients of the hyperviscoelastic fractional differential model.

No constraint was applied to the values of the parameters during optimization.

The unconfined compression tests were also simulated for the differential model involving classical derivatives (described by Eqn. 9.34) with the parameters determined by Miller and Chinzei (1997a). The hydrostatic pressure p that appears in both model (Eqn. 9.38 and Eqn 9.44) was determined by setting the components S_{11} and S_{22} of the stress tensor to 0, since the direction of the compression was chosen to be $\mathbf{e_3}$. Thus, the following relations hold:

$$S_{11} = S^*_{11} - pC^{-1}_{11} = 0 \tag{9.46}$$

$$p = \frac{S^*_{11}}{C^{-1}_{11}} \tag{9.47}$$

The resulting stress-strain curves are plotted in Fig. 9.2 and Fig. 9.3.

The fractional model fits better the beginning of the curves than the model with classical derivatives. It is almost perfect for strains up to -0.25 for both loading rates. Apart from the end of the curve in Fig. 9.2 (for strains greater than 0.25 in absolute values), the fractional model completely outmatches the classical hyperviscoelastic model for the same number of parameters.

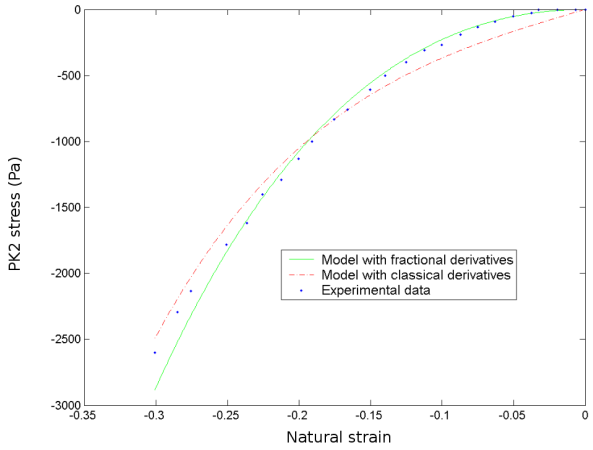

Fig. 9.2: Comparison between the fractional and integer-order differential models for unconfined compression test performed at 500 mm min^{-1}

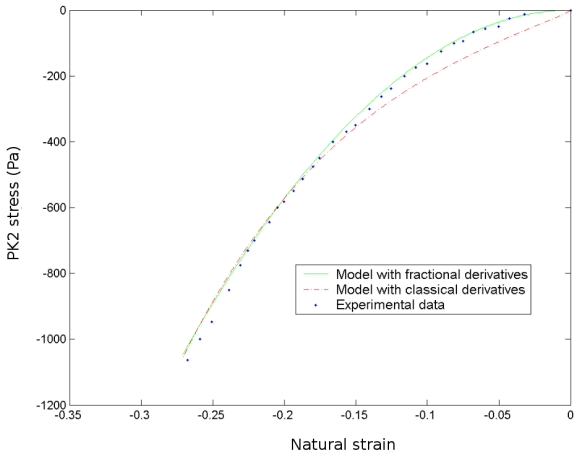

Fig. 9.3: Comparison between the fractional and integer-order differential models for unconfined compression test performed at 5 mm min^{-1}

9.4 Hyperelasticity as a particular case of hypervicoelasticity

For an incompressible material, the constitutive law in term of PK2 stress and Cauchy strain tensors is written

$$\mathbf{S} = 2\frac{\partial W}{\partial \mathbf{C}} - p\mathbf{C}^{-1} \tag{9.48}$$

for a hyperelastic material and

$$\mathbf{S} = 2\frac{\partial \Psi}{\partial \mathbf{C}} - p\mathbf{C}^{-1} \tag{9.49}$$

for a hyperviscoelastic material. The general form of a hyperviscoelastic potential defined in Eqn. 3.100 is recalled here

$$\Psi = \int_0^t Y(t-\tau)\frac{dW}{d\tau}\, d\tau \tag{9.50}$$

Hence, for a hyperviscoelastic material, we have

$$\mathbf{S} = 2\frac{\partial}{\partial \mathbf{C}}\int_0^t Y(t-\tau)\,\frac{dW}{d\tau}\, d\tau \tag{9.51}$$

$$= 2\int_0^t Y(t-\tau)\,\frac{\partial}{\partial \mathbf{C}}\left[\frac{dW}{d\tau}\right]\, d\tau \tag{9.52}$$

However, Eqn. 9.4 (from Miller and Chinzei (1997a)), rewritten in terms of $\mathbf{S}$ and $\mathbf{C}$, has the form

$$\mathbf{S} = 2\int_0^t Y(t-\tau)\frac{d}{d\tau}\frac{\partial W}{\partial \mathbf{C}}\, d\tau - p\mathbf{C}^{-1} \tag{9.53}$$

It differs from Eqn. 9.52 by the permutation of $\frac{d}{d\tau}$ andd $\frac{\partial}{\partial \mathbf{C}}$.

The hyperelastic constitutive law should be a particular case of the hyperviscoelastic one when the relaxation function Y is removed. If we do so, Eqn. 9.53 becomes

$$\mathbf{S} = 2\int_0^t \frac{d}{d\tau}\frac{\partial W}{\partial \mathbf{C}}\, d\tau - p\mathbf{C}^{-1} \tag{9.54}$$

The integration yields in

$$\mathbf{S} = 2\left(\frac{\partial W}{\partial \mathbf{C}}\right)_t - 2\left(\frac{\partial W}{\partial \mathbf{C}}\right)_{t=0} - p\mathbf{C}^{-1} \tag{9.55}$$

Eqn. 9.55 can be identified with the constitutive relation Eqn. 9.48 if and only if

$$\left(\frac{\partial W}{\partial \mathbf{C}}\right)_{t=0} = 0 \tag{9.56}$$

which is generally not the case.

This issue is due to the illegal permutation of the derivatives $\frac{d}{dt}$ and $\frac{\partial}{\partial \mathbf{C}}$. Since the fractional model described in Eqn. 9.43 is derived from Miller's model (Eqn. 9.4) and although it fits the experimental curves very well, it is based on an illegal mathematical operation that prevents hyperelasticity to be a particular case of hyperviscoelasticity as expected. The model should therefore be corrected. This is the goal of the next section.

9.5 Fractional formulation (II)

We need to find a formulation for which the hyperelastic formulation is retrieved when no viscous effects are observed. We thus propose the following constitutive equation:

$$\mathbf{S} = \mathbf{S}^H + \mathbf{S}^V - p\mathbf{C}^{-1} \tag{9.57}$$

$$= 2\frac{\partial W}{\partial \mathbf{C}} + \mathbf{S}^V - p\mathbf{C}^{-1} \tag{9.58}$$

with

$$D_t^{(\alpha)}\mathbf{S}^V + \beta\mathbf{S}^V = F(\boldsymbol{\zeta}, \dot{\boldsymbol{\zeta}}, \ddot{\boldsymbol{\zeta}}) \tag{9.59}$$

$$\boldsymbol{\zeta} = \frac{\partial U}{\partial \mathbf{C}} \tag{9.60}$$

W and U are strain energy density functions. This formulation allows one to separate the hyperelastic from the viscous effects. It no longer requires an unnecessary integration for the hyperelatic part. In the calculation of $\dot{\zeta}$ and $\ddot{\zeta}$, no permutation of the derivations is used. The time derivative are calculated after calculating Eqn. 9.60.

This model was also implemented using the predictor-corrector algorithm (section 4.7.3). The extended Mooney-Rivlin was kept as the strain energy density function for both W and U and the function F in the right hand side of Eqn.9.59 was assumed to be linear, i.e.

$$F(\boldsymbol{\zeta}, \dot{\boldsymbol{\zeta}}, \ddot{\boldsymbol{\zeta}}) = a\boldsymbol{\zeta} + b\dot{\boldsymbol{\zeta}} + c\ddot{\boldsymbol{\zeta}} \tag{9.61}$$

This model counts 9 parameters: $\alpha, \beta, a, b, c, C_{100}^W, C_{200}^W, C_{100}^U$ and C_{200}^U.

The result of the calibration is shown in Fig. 9.4 and Fig. 9.5. The same set of parameters was used for both curves. The mean relative error (MRE) was computed for each curve as follows:

$$MRE = \frac{\sum_{i=1}^{N} |num_i - exp_i|}{\sum_{i=1}^{N} |exp_i|} \tag{9.62}$$

where N stands for the number of experimental points and num_i and exp_i designate the points computed from the model and the experimental points respectively. It corresponds to the area between the two curves divided by the area below the experimental curve. The values found for the curve in Fig. 9.4 and Fig. 9.5 are 2.8% and 1.6 %.

The new model is better than the first one, fitting perfectly both experimental curves. But this time, it counts 9 parameters which are presented in Tab. 9.2. The characteristic time τ is derived from the coefficient β in Eqn. 9.59: $\beta = \tau^{-\alpha}$. It worths noting that the elastic coefficients corresponding to the purely elastic part of the model are close to 0. Therefore, the term $\mathbf{S}^H$ in Eqn. 9.57 can be forgotten in that particular case and the model then counts 7 parameters. This simplification does not alter the values of the MRE.

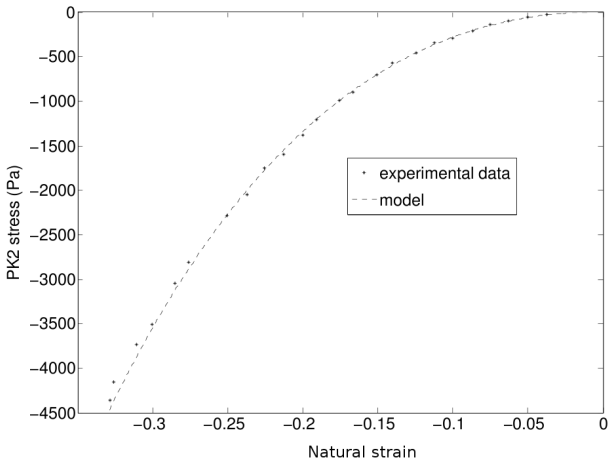

Fig. 9.4: Result of the calibration of the fractional differential model for the unconfined compression test at 500 mm min^{-1}

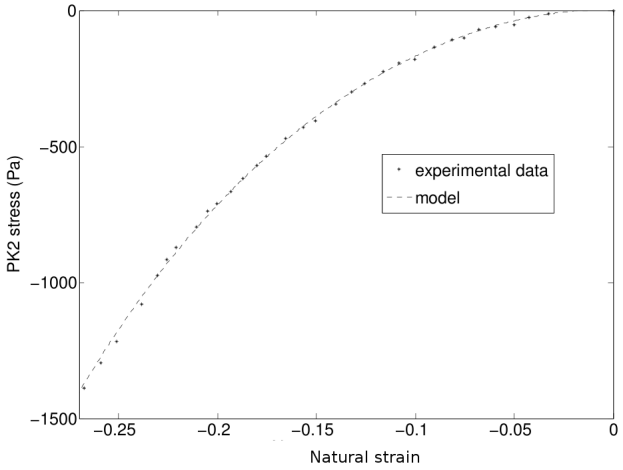

Fig. 9.5: Result of the calibration of the fractional differential model for the unconfined compression test at 5 mm min^{-1}

Parameter	Interpretation	Value	Units
α	order of derivation	0.98	
τ	characteristic time	28.3	s
C_{100}^{W}	elastic coefficient (W)	3.34 10^{-3}	Pa
C_{200}^{W}	elastic coefficient (W)	1.11 10^{-3}	Pa
C_{100}^{U}	elastic coefficient (U)	250.65	Pa
C_{200}^{U}	elastic coefficient (U)	235.15	Pa
a	generalized viscous coefficient	1.0	$s^{-\alpha}$
b	generalized viscous coefficient	0.18	$s^{1-\alpha}$
c	generalized viscous coefficient	0.22	$s^{2-\alpha}$

Tab. 9.2: Parameters of the final fractional differential model.

9.6 Use of the LMP and SMP

The excellent fit between the model and the experimental curves is achieved through a higher computational cost than for the resolution of ordinary differential equations. In section 4.7.4 were presented the logarithmic memory and the short memory principles. They were both implemented in the fractional differential equation solver. Once the model is calibrated, what is the order of magnitude of the error if one of these accelerators is used ? The curve at 500 mm min^{-1} was chosen to compare the methods. The values of the model are computed over 500 points.

Let's start with the LMP. The parameters are w and T (see section 4.7.4). w was fixed to 2 and T was initially fixed to 50, i.e. one tenth of the length of the integration interval. The result is presented in Fig. 9.6. The model stays close to the experimental data, but oscillations are clearly visible. They appear after a time equals to $2T$, accordingly to the method.

The amplitude of the oscillations increases with decreasing T, as it is observable in Fig. 9.7 were T was set to 25.

These oscillations can easily be explained. In Eqn. 4.146, the last term is dropped whenever the interval length is not an exact multiple of the step $w^m T$. Therefore, the difference between the curve with the full memory and the LMP is minimal when it occurs and increases as more terms are dropped, yielding in the observed oscillations.

An averaging filter could be used to reduce the amplitude of the oscillations, since they are not visually pleasing, although they do not seem to significantly increase the error between the curve and the experimental data. But before investigating further on the LMP, let's have a look at the results obtained with the SMP.

Fig. 9.8 shows that the fit between the model and the experimental data is still very good when using the SMP with a fixed memory equals to 50 points, i.e. one tenth of the integration interval.

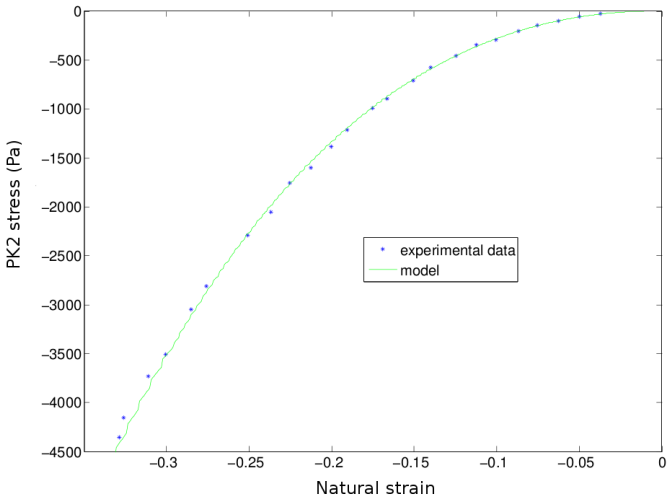

Fig. 9.6: Numerical model using the logarithmic memory ($w = 2.0$, $T = 50$).

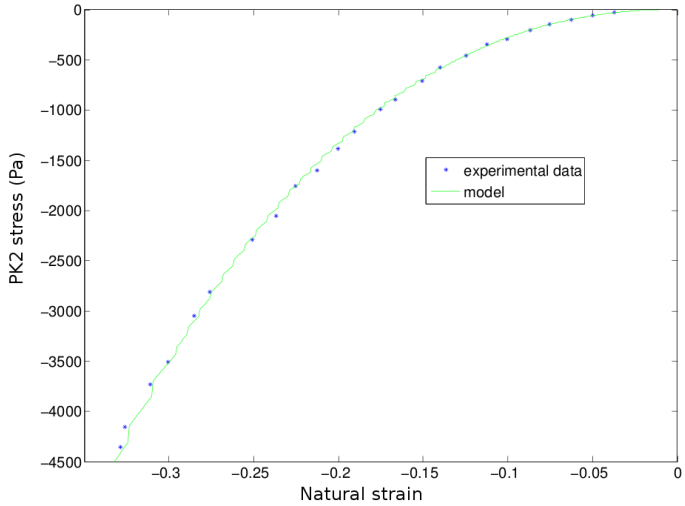

Fig. 9.7: Numerical model using the logarithmic memory ($w = 2.0$, $T = 25$).

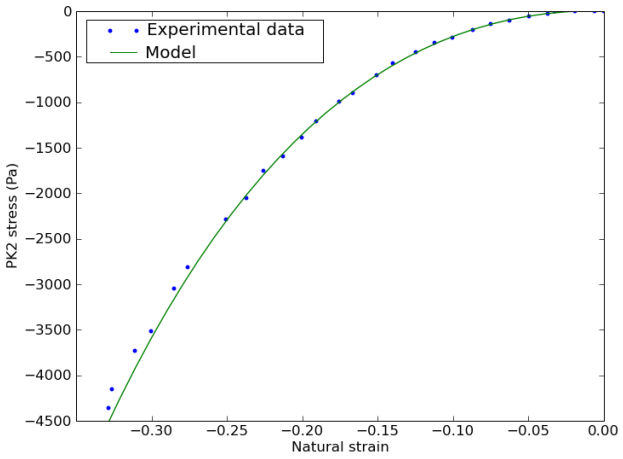

Fig. 9.8: Experimental data (unconfined compression test at 500 mm min^{-1}) and fractional model using the short memory principle with 50 points kept.

To investigate the influence of the memory length on the quality of the result, a mean relative error was defined as

$$MRE_{short\ memory} = \frac{\sum_{i=1}^{N} |numSMP_i - numFullMemory_i|}{\sum_{i=1}^{N} |numFullMemory_i|} \tag{9.63}$$

where N is the number of data points and $numSMP_i$ (resp. $numFullMemory_i$) the value of the curve using the SMP (resp. the full memory) for the data point i.

This mean error is plotted in Fig. 9.9. For a memory length of 10, the difference is less than 2% while the number of evaluations of the fractional derivative is divided by 25. Therefore, the SMP presents a very good compromise between the computational time and the accuracy of the result.

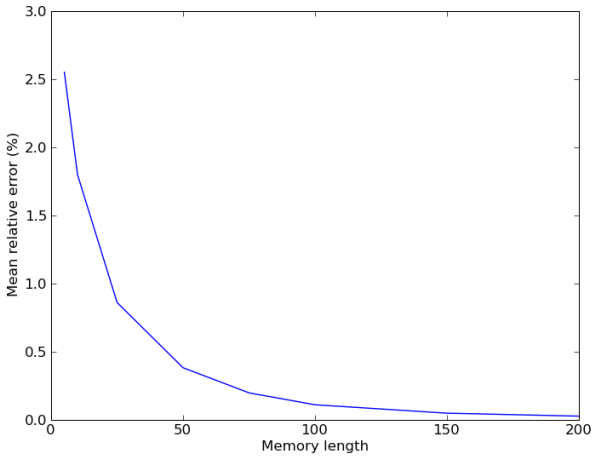

Fig. 9.9: Mean relative error between the fraction model using the full memory and the model using the SMP versus the memory length. The error was computed for the curve corresponding to the unconfined compression test at 500 mm min^{-1}

9.7 Analysis of the parameters

The physical meaning of some parameters of the model, like the fractional derivation order, does not appear as obvious. In order to gain more physical understanding of the model, we propose a sensitivity analysis.

Sensitivity to the fractional derivation order α

As we had no idea of the influence of the parameter α on the stress-strain curves, we first chose to sweep a wide range of values, from 0.2 to 0.98 while the other parameters keep the values of Tab. 9.2 except C_{100}^W and C_{200}^W which are set to 0 as mentioned at the end of section 9.5. The results for the unconfined compression curves at 500 mm min^{-1} and 5 mm min^{-1} are presented in Fig. 9.10 and Fig. 9.11. One can immediatly notice that the influence of α is greater for the stress-strain curve at the highest loading rate (Fig. 9.10) where it seems to determine its curvature and its initial slope. Interesting observations can be made by looking at Fig. 9.11: firstly, the curves cross each other (not exactly at the same point as the figure might suggest) and secondly, the evolution of the curves as α decreases is exactly the opposite of that found in Fig. 9.10: the smaller the value of α, the smaller the stress for a given strain (after the curves met). This is remarkable but we have no simple and direct explanation to this phenomenon.

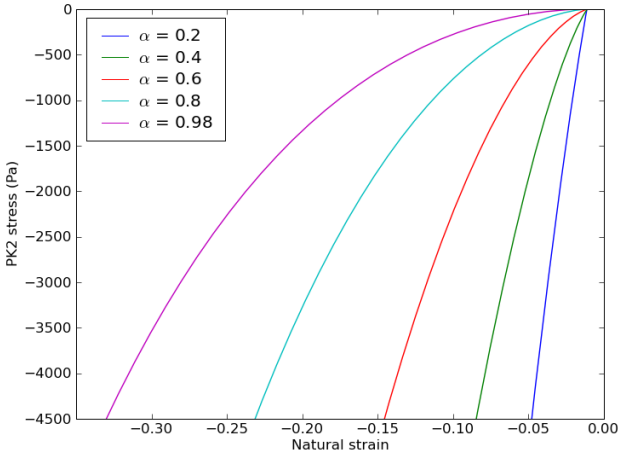

Fig. 9.10: Stress-strain curves for the unconfined compression test at 500 mm min^{-1} obtained for several values of $\alpha \in [0.2, 0.98]$

To further investigate the importance of the fractional derivation order, we chose to restrict the range of variation to $[0.9, 0.98]$. Fig. 9.12 shows that for a given strain equals to -0.25, there is a gap of about 1000 Pa between the two extreme curves, which correspond to a 30% relative difference on the stress for a 10 % relative difference on α. Almost no difference at all is observed at the lower loading rate, as seen in Fig. 9.13.

This strong loading-rate sensitivity is a very interesting fact although it is difficult to interpret. However, it still does not provide a physical meaning to α, if any. To investigate

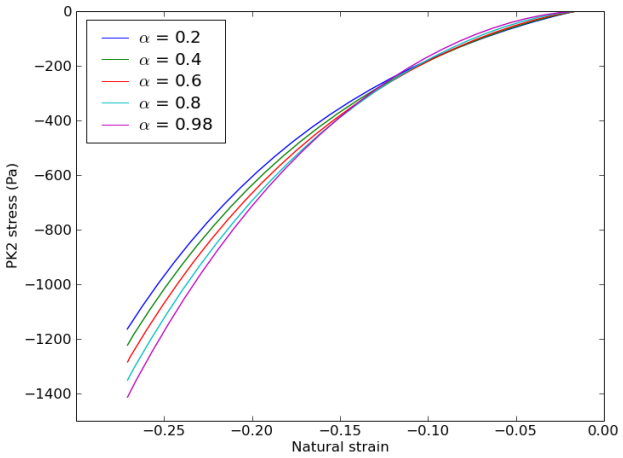

Fig. 9.11: Stress-strain curves for the unconfined compression test at 5 mm min^{-1} obtained for several values of $\alpha \in [0.2, 0.98]$

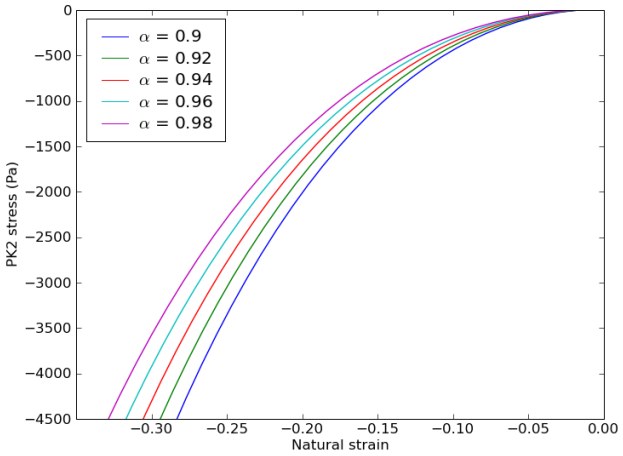

Fig. 9.12: Stress-strain curves for the unconfined compression test at 500 mm min^{-1} obtained for several values of $\alpha \in [0.9, 0.98]$

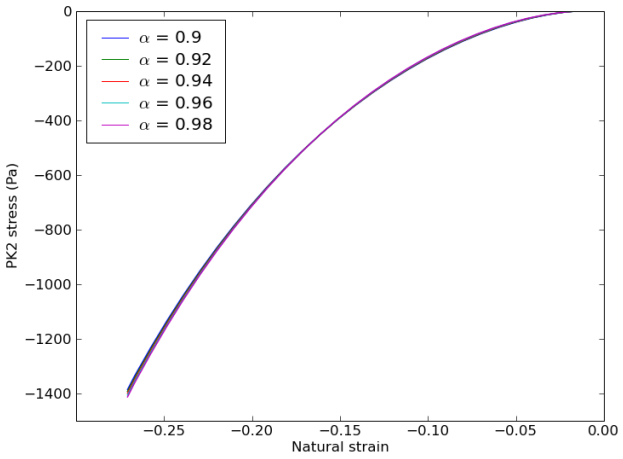

Fig. 9.13: Stress-strain curves for the unconfined compression test at 5 mm min^{-1} obtained for several values of $\alpha \in [0.9, 0.98]$

this particular point, let's consider Eqn. 9.59. Using the analytical method of resolution presented in section 4.7.2, the solution writes

$$\mathbf{S}^V = \int_0^t (t-u)^{\alpha-1} E_{\alpha,\alpha}\left(-\beta(t-u)^\alpha\right)\ \mathbf{F}(\boldsymbol{\zeta}, \dot{\boldsymbol{\zeta}}, \ddot{\boldsymbol{\zeta}})\, du \tag{9.64}$$

Eqn. 9.64 is the fractional counterpart of the traditional hyperviscoelastic model (see section 3.4). In this expression, $f(t-u) = (t-u)^{\alpha-1} E_{\alpha,\alpha}\left(-\beta(t-u)^\alpha\right)$, or equivalently, $f(x) = x^{\alpha-1} E_{\alpha,\alpha}\left(-\beta x^\alpha\right)$ stands for the relaxation function. It is plotted in Fig. 9.14 and Fig. 9.15 for several values of $\alpha \in]0, 1[$. One can immediately notice that these curves present a weak singularity for $x = 0$. However, the integral exists in the sense of Hadamard finite part (see appendix A). The function is strictly decreasing for all the values of $\alpha \in]0, 1[$ and thus deserves to be assimilated to a relaxation function.

The variation of α influences the curvature as well as the behaviour at the origin of the curves. It then seems to be an interesting function to use for the modelling of a viscoelastic material, as it should be able to fit a large number of relaxation behaviours.

Further developments are devoted to the problem of the singularity of the convolution kernel of Eqn. 9.64 in appendix D.

Sensitivity to the characteristic time τ

The experimental results showed that it is not possible to fit the relaxation curve with a single exponential (section 7.3.2). Therefore, it is difficult to define a relaxation time in the way it is generally done. Eqn. 9.64 shows that τ, or equivalently β, is a parameter of the relaxation function. The value obtained is of the order of magnitude of the steady state time $\tau_{0.001}$ defined in section 7.3.2, but there is no mean to confirm that it corresponds to this quantity.

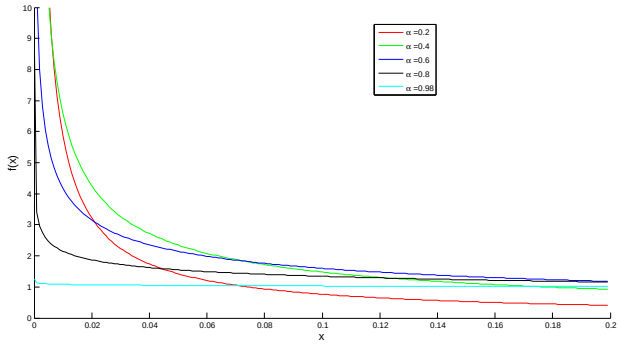

Fig. 9.14: Relaxation function $x^{\alpha-1}E_{\alpha,\alpha}\left(-\beta x^{\alpha}\right)$ for several values of $\alpha \in]0.2, 0.98[$

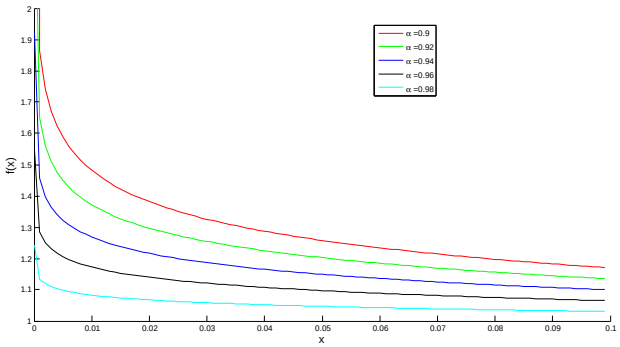

Fig. 9.15: Relaxation function $x^{\alpha-1}E_{\alpha,\alpha}\left(-\beta x^{\alpha}\right)$ for several values of $\alpha \in]0.9, 0.98[$

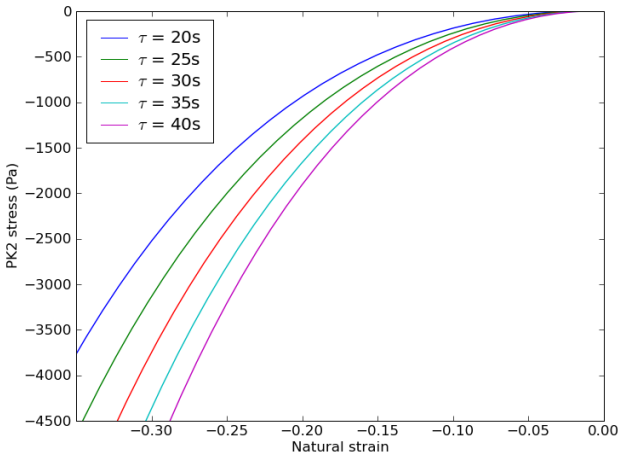

Fig. 9.16: Stress-strain curves for the unconfined compression test at 500 mm min^{-1} obtained for several values of $\tau \in [20, 40]$

Fig. 9.16 and 9.17 show the influence of τ on the stress-strain curve. As it was the case with α, this influence depends on the loading velocity, although the effect is less dramatic here. We can also notice that there is again an inversion in the behaviour of the curves with respect to increasing values of τ, making it difficult to associate τ with a physical characteristic time. Furthermore, this inversion lets think that there may exist a loading rate for which all the curves for various τ are superimposed. Another loading rate should provide the same result for α. This is more likely to be a side effect of the model rather than a property of the tissue.

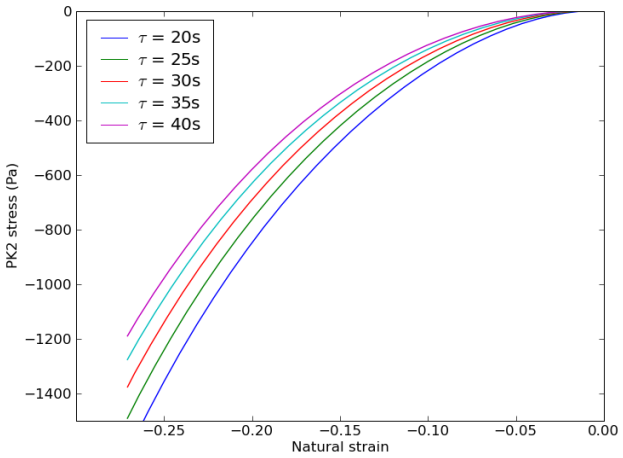

Fig. 9.17: Stress-strain curves for the unconfined compression test at 5 mm min^{-1} obtained for several values of $\tau \in [20, 40]$

The effect of τ on the relaxation function $x^{\alpha-1}E_{\alpha,\alpha}\left(-\beta x^{\alpha}\right)$ is presented in Fig. 9.18. It

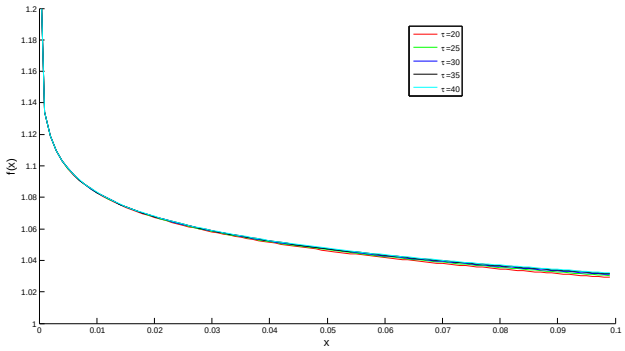

Fig. 9.18: Relaxation function $x^{\alpha-1}E_{\alpha,\alpha}\left(-\beta x^{\alpha}\right)$ for several values of $\tau \in]20, 40[$

is not very sensitive to the variation of τ, which leads to the conclusion that α is the most important parameter describing the relaxation behaviour of the model.

Sensitivity to the elastic coefficients C_{100} and C_{200}

There are only a few words to say about the parameters C_{100} and C_{200}. Fig. 9.19 to Fig. 9.22 show the expected behaviour of elastic coefficients: the stress increases with increasing values of C_{100} and C_{200}. The order of magnitude of their values correspond to what was found in the literature.

Sensititivty to the generalized viscous coefficients a, b and c

The generalized viscous coefficients indicates the relative importance of the function $\boldsymbol{\zeta}$ with respect to its first and second time derivatives.

The model is not very sensitive to the parameter b (related to the instantaneous loading rate) as shown in Fig. 9.25 and Fig. 9.26.

As far as a and c are concerned, we can again observe a loading rate dependency (Fig. 9.23, Fig. 9.24, Fig. 9.27 and Fig. 9.28), particularly dramatic in the case of c. a is the only parameter of the model whose variation results in a larger scatter in the curves obtained for the lowest loading rate.

This short analysis of the sensitivity of the model with respect to its parameters gives us interesting informations. However, it is very difficult to interpret them from a physical point of view. Only the elastic coefficients C_{100} and C_{200} have a straightforward physical meaning. The value of τ could correspond to the steady state time $\tau_{0.001}$ but nothing can prove it.

The difficulty to find a physical meaning to some parameters, particularly the order of derivation α, is maybe the price to pay when using fractional derivatives to obtain a perfect agreement between the experimental data and the model.

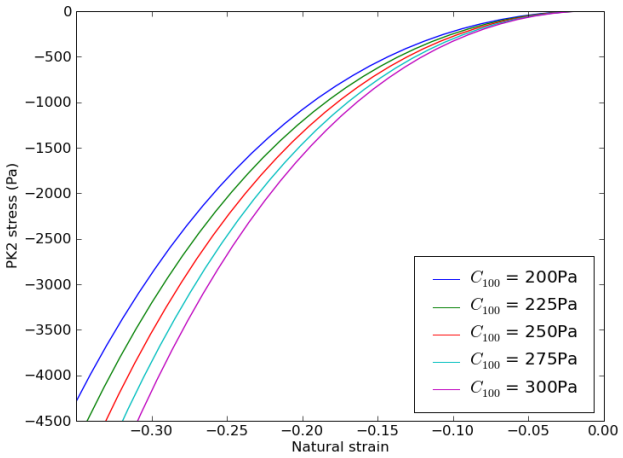

Fig. 9.19: Stress-strain curves for the unconfined compression test at 500 mm min^{-1} obtained with the optimized parameters for several values of $C_{100} \in [200, 300]$

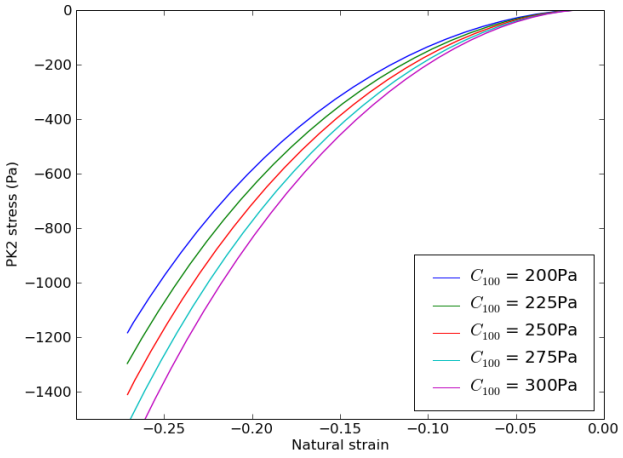

Fig. 9.20: Stress-strain curves for the unconfined compression test at 5 mm min^{-1} obtained with the optimized parameters for several values of $C_{100} \in [200, 300]$

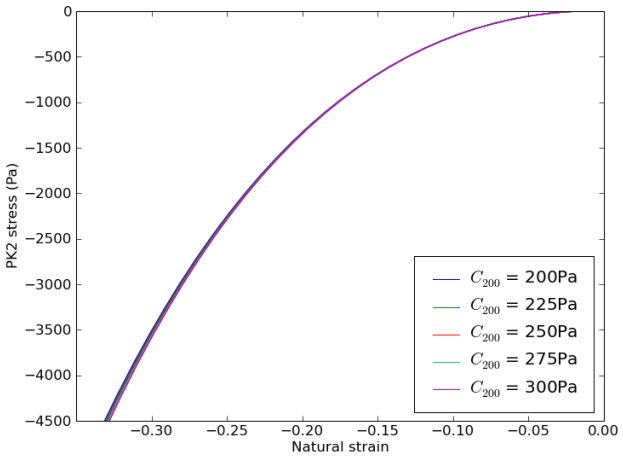

Fig. 9.21: Stress-strain curves for the unconfined compression test at 500 mm min^{-1} obtained with the optimized parameters for several values of $C_{200} \in [200, 300]$

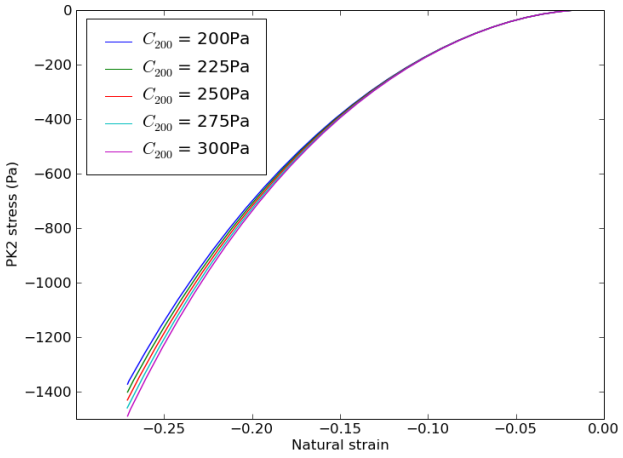

Fig. 9.22: Stress-strain curves for the unconfined compression test at 5 mm min^{-1} obtained with the optimized parameters for several values of $C_{200} \in [200, 300]$

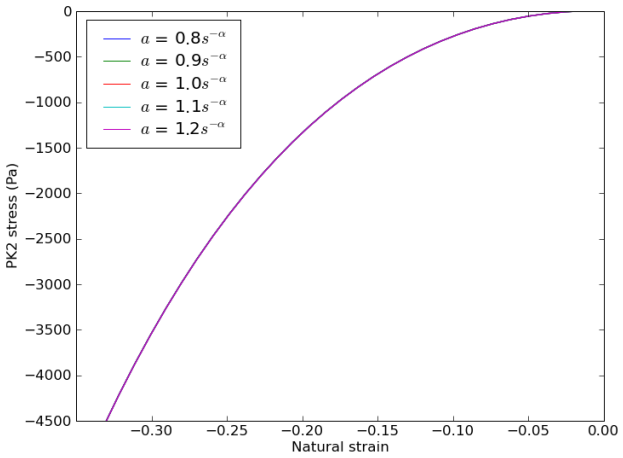

Fig. 9.23: Stress-strain curves for the unconfined compression test at 500 mm min^{-1} obtained for several values of $a \in [0.8, 1.2]$

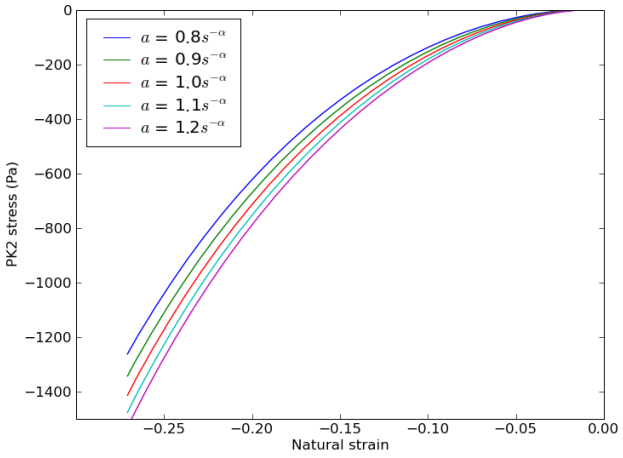

Fig. 9.24: Stress-strain curves for the unconfined compression test at 5 mm min^{-1} obtained for several values of $a \in [0.8, 1.2]$

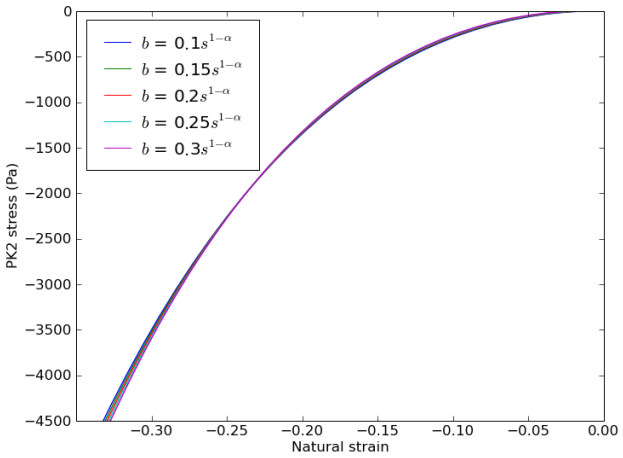

Fig. 9.25: Stress-strain curves for the unconfined compression test at 500 mm min^{-1} obtained for several values of $b \in [0.1, 0.3]$

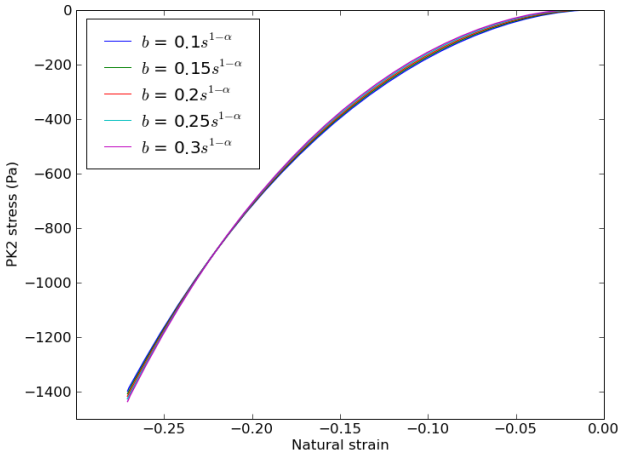

Fig. 9.26: Stress-strain curves for the unconfined compression test at 5 mm min^{-1} obtained for several values of $b \in [0.1, 0.3]$

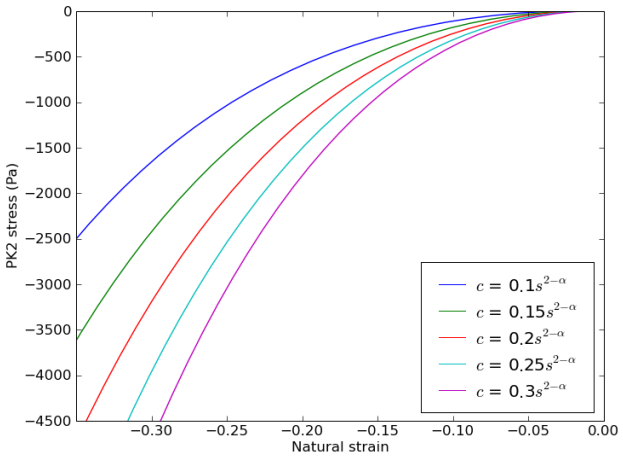

Fig. 9.27: Stress-strain curves for the unconfined compression test at 500 mm min^{-1} obtained for several values of $c \in [0.1, 0.3]$

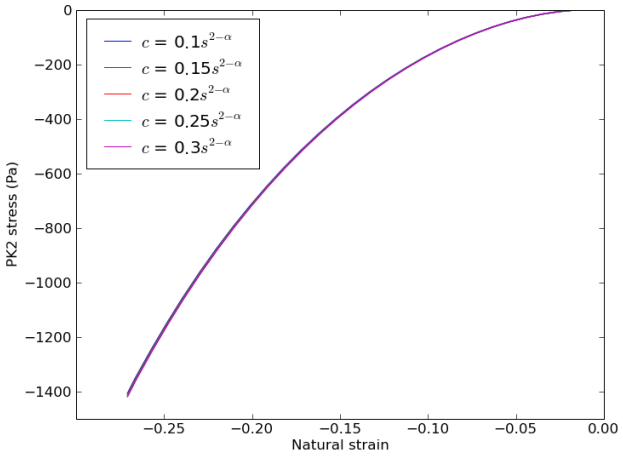

Fig. 9.28: Stress-strain curves for the unconfined compression test at 5 mm min^{-1} obtained for several values of $c \in [0.1, 0.3]$

CHAPTER 10
CALIBRATION AND VALIDATION

10.1 Introduction

In this short chapter, the parameters of the constitutive model presented in section 9.5 are identified from the experimental results of the unconfined compression tests presented in chapter 7. The relaxation and cyclic tests are used to validate the model.

10.2 Calibration

The determination of the parameters of the model developed in section 9.5 was performed independently for the results with and without the use of the D.I.C.

With the parameters presented in Tab. 10.1, the model fits almost perfectly the experimental curves as shown in Fig. 10.1 to Fig. 10.3. The corresponding mean relative errors (MRE) are equal to 3.3% for the test at the highest loading rate, 1.3% for the medium loading rate and 1.1% for the slowest loading rate. Since the stress-strain curves are linear, it only proves that the model can reproduce the behaviour of the brain tissue at three different loading rate in a ratio 100:10:1, i.e. over two orders of magnitude. The examination of Tab. 10.1 shows that this time again, only 7 parameters out of 9 are required to calibrate the model. The values of the elastic coefficients are lower than the ones found in literature (see Miller and Chinzei (1997a) for example).

For the reasons explained in section 7.3.5, the stress-strain curves obtained with the use of the D.I.C. are limited to strains equal to -0.12. Therefore, their nonlinearity is rather small.

The stress-strain curves obtained using only the outputs of the universal testing machines are clearly nonlinear (see section 7.5), as are the curves found in the literature used to perform the sensitivity analysis. The good results presented in section 9.5 showed that the model is able to reproduce a nonlinear behaviour over two orders of magnitude of the loading rate.

Therefore, we re-calibrated the model on our experimental stress-strain curves in order to go further in its assessment.

The results of this new calibration are presented in Fig. 10.4 to Fig. 10.6. Once again the model fits quite well the experimental data, with an exception of the few last points of the curve in Fig. 10.6. The MRE, classified by decreasing order of the loading rates, are equals to 1.3%, 3.4% and 9.7%. None of the parameter is null this time (compared to the hyperelastic

coefficients in Tab 9.2) which suggests that the behaviour of the stress-strain curve at an intermediary loading rate brings further information about the variation of the stress-strain curve with respect to the loading rate.

It is interesting to note that the value of α found in this case (ses Tab. 10.2) is very close to the α determined for the tests for which the D.I.C. was used. The characteristic time however, is very different. It is not a surprise to obtain different sets of parameters for the two calibrations since the stress-strain curves with and without D.I.C. are different for the reasons explained in section 7.4.

Parameter	Interpretation	Value	Units
α	order of derivation	0.90	
τ	characteristic time	480.5	s
C_{100}^{W}	elastic coefficient (W)	148.44	Pa
C_{200}^{W}	elastic coefficient (W)	0	Pa
C_{100}^{U}	elastic coefficient (U)	84.8	Pa
C_{200}^{U}	elastic coefficient (U)	137.5	Pa
a	generalized viscous coefficient	1269	$s^{-\alpha}$
b	generalized viscous coefficient	0	$s^{1-\alpha}$
c	generalized viscous coefficient	0.204	$s^{2-\alpha}$

Tab. 10.1: Identification of the parameters of the fractional model using the results of the unconfined compression tests at 120 mm min^{-1},12 mm min^{-1} and 1.2 mm min^{-1} (with the D.I.C.)

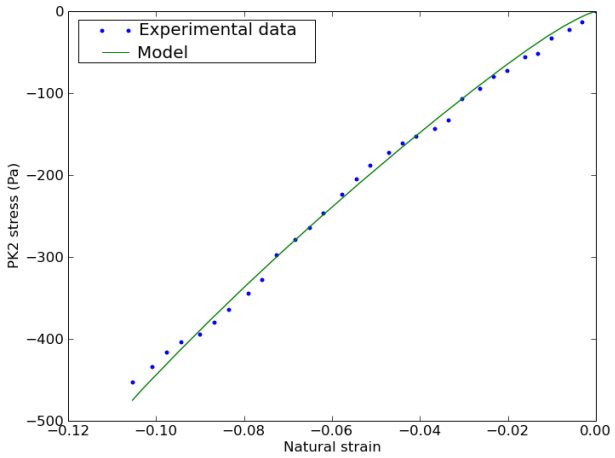

Fig. 10.1: Result of the calibration of the fractional differential model for the unconfined compression test at 120 mm min^{-1} using the D.I.C.

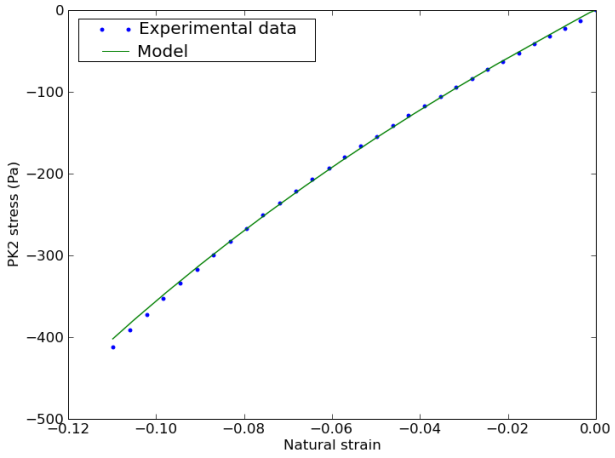

Fig. 10.2: Result of the calibration of the fractional differential model for the unconfined compression test at 12 mm min^{-1} using the D.I.C.

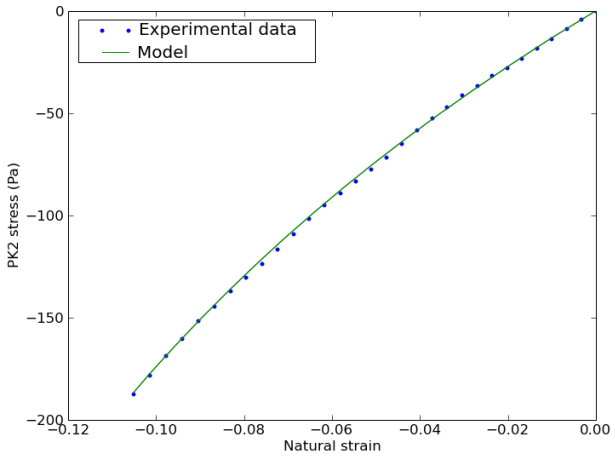

Fig. 10.3: Result of the calibration of the fractional differential model for the unconfined compression test at 1.2 mm min^{-1} using the D.I.C.

Parameter	Interpretation	Value	Units
α	order of derivation	0.89	
τ	characteristic time	21.3	s
C_{100}^{W}	elastic coefficient (W)	91.1	Pa
C_{200}^{W}	elastic coefficient (W)	248.4	Pa
C_{100}^{U}	elastic coefficient (U)	58.8	Pa
C_{200}^{U}	elastic coefficient (U)	44.6	Pa
a	generalized viscous coefficient	51.5	$s^{-\alpha}$
b	generalized viscous coefficient	0.85	$s^{1-\alpha}$
c	generalized viscous coefficient	1.21	$s^{2-\alpha}$

Tab. 10.2: Identification of the parameters of the fractional model using the results of the unconfined compression tests at 120 mm min^{-1},12 mm min^{-1} and 1.2 mm min^{-1} (without the D.I.C.)

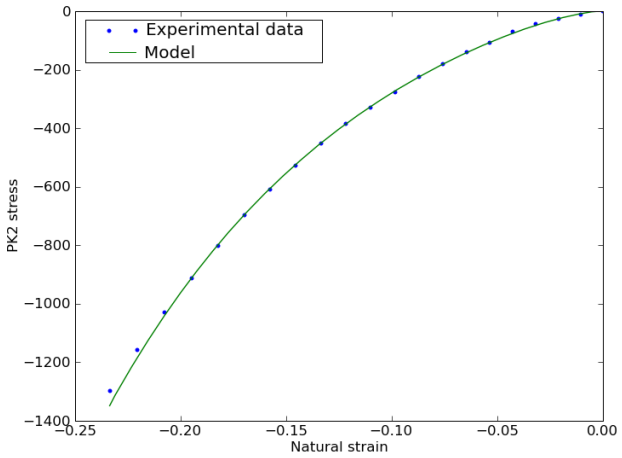

Fig. 10.4: Result of the calibration of the fractional differential model for the unconfined compression test at 120 mm min^{-1} using the outputs of the testing machine

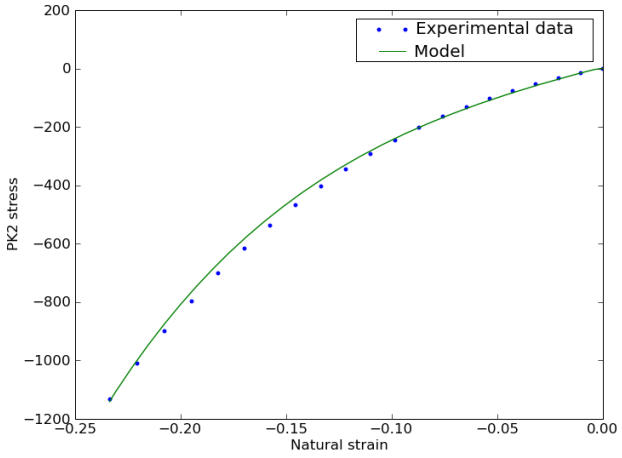

Fig. 10.5: Result of the calibration of the fractional differential model for the unconfined compression test at 12 mm min^{-1} using the outputs of the testing machine

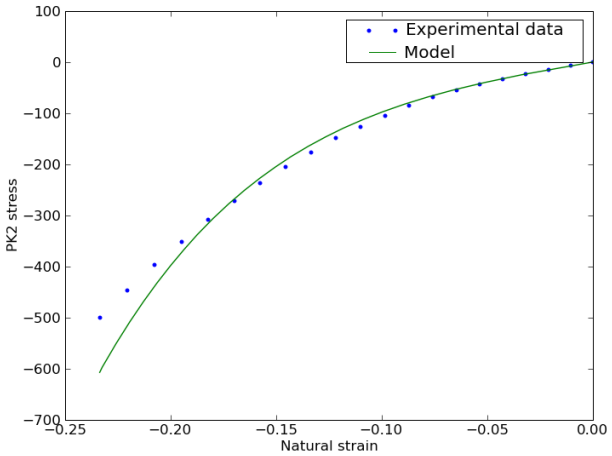

Fig. 10.6: Result of the calibration of the fractional differential model for the unconfined compression test at 1.2 mm min^{-1} using the outputs of the testing machine

10.3 Validation

The ability of the model based on the fractional derivative to fit the experimental data was proved by the calibrations performed above. But to be considered as good, a model must be validated after it was calibrated. To this end, the result of a numerical simulation of a cyclic test (comprising only one cycle) is compared to the experimental results (presented in section 7.3.3) in Fig. 10.10.

With the set of parameters of Tab. 10.2, the dissipated energy was negative, which is physically unacceptable. The parameter b was found to be the one allowing us to obtain a positive value of the dissipative energy and a behaviour of the cyclic force-displacement curve comparable to the experimental results. However, this modification changed the shape of the stress-strain curves predicted by the model for the unconfined compression tests. However, this change is rather limited, which indicates that the mere unconfined compression test do not constitute a sufficient data base to fully calibrate the model. With $b = -1.7$, the MRE was increased, particularly for the result corresponding to the highest loading rate but it remains quite good. The change is summarized in Tab. 10.3 and the corresponding curves are presented in Fig. 10.7 to Fig. 10.9. Visually, the numerical curves are in good agreeement with the experimental ones.

Loading rate	MRE (%, before)	MRE (%, after)
120 mm min^{-1}	1.3	7.4
12 mm min^{-1}	3.4	3.6
1.2 mm min^{-1}	9.7	9.6

Tab. 10.3: Modifications of the mean relative error due to the modification of the parameter b to fit the cyclic tests.

The examination of Fig. 10.10 shows a certain number of interesting facts:

- the model is able to predict that the final force (after unloading) is negative. However, the slope of the numerical curve at the beginning of the loading and at the end of the unloading is too large,
- the maximal value of the force lays between the extrema of the experimental data.

The qualitative behaviour of the model for the cyclic experiment can be considered as satisfactory, except for the initial and final slopes of the curve.

The second validation test proposed is the modelling of the relaxation experiment. The result of the simulation and the experimental data are plotted in Fig.10.11. The simulation is performed for the parameters of Tab. 10.2, except for b which is taken as $b = -1.7$. Since the relaxation behaviour is driven by the parameters α and τ, this has not a great importance.

The beginning of the computed relaxation curve does not fit the experimental data very well but the steady value is perfectly determined.

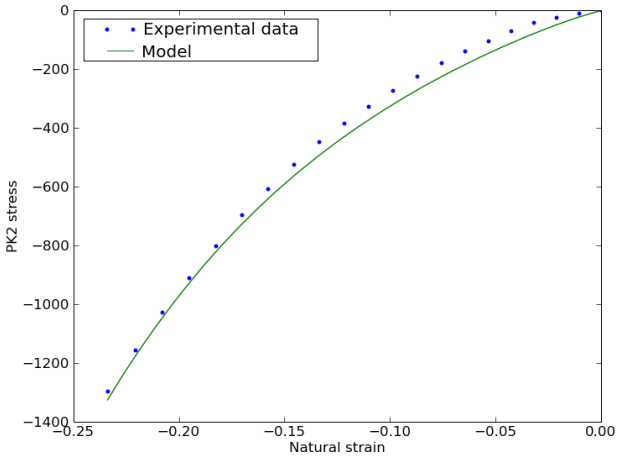

Fig. 10.7: Comparison of the model and the experimental data (unconfined compression test at 120 mm min^{-1}) after the modification of the parameter b to fit the cyclic test computed curve.

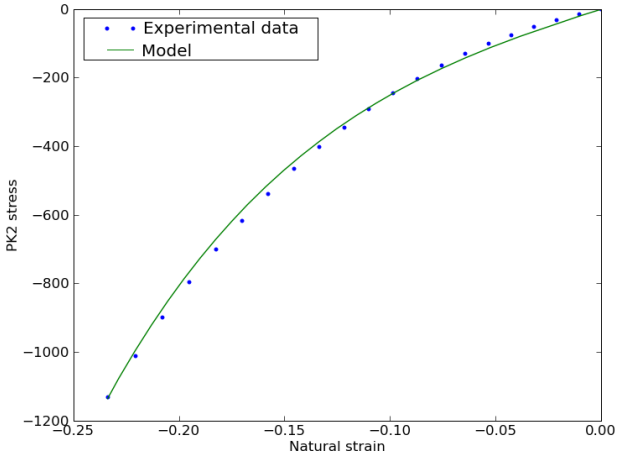

Fig. 10.8: Comparison of the model and the experimental data (unconfined compression test at 12 mm min^{-1}) after the modification of the parameter b to fit the cyclic test computed curve.

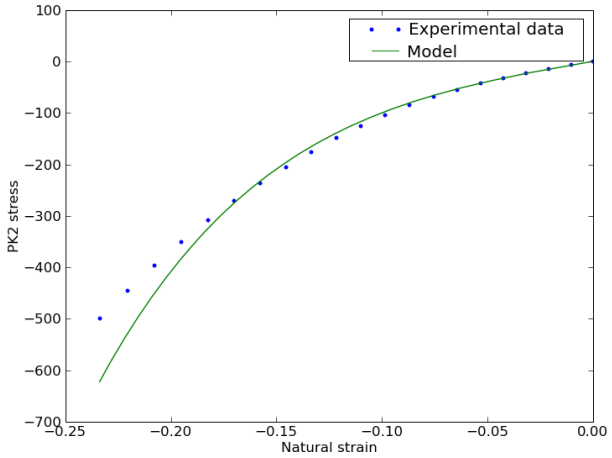

Fig. 10.9: Comparison of the model and the experimental data (unconfined compression test at 1.2 mm min^{-1}) after the modification of the parameter b to fit the cyclic test computed curve.

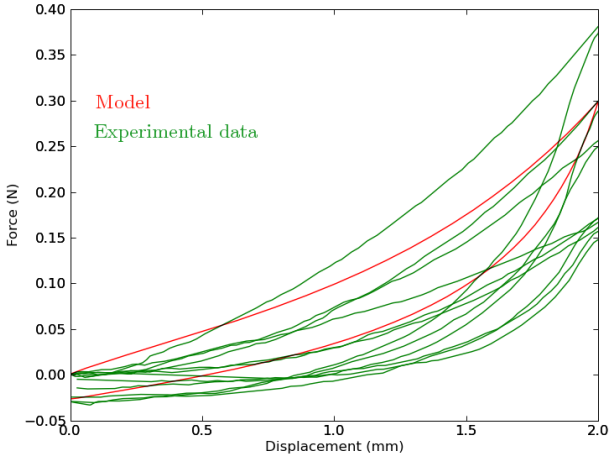

Fig. 10.10: Comparison of the numerical model and the experimental data for a cyclic experiment (one cycle) at 60 mm min^{-1}.

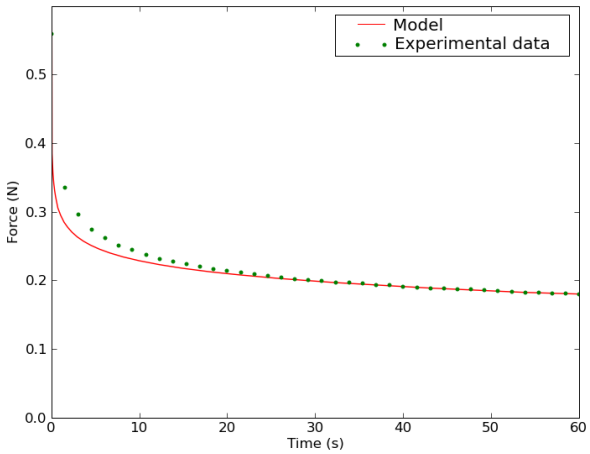

Fig. 10.11: Comparison of the numerical model and the experimental data for a relaxation experiment.

10.4 Conclusion

The proposed viscoelastic fractional model was calibrated on unconfined compression tests results at three different loading velocities over two orders of magnitude. The result of the calibration is very good. An attempt of validation of the model is proposed, using a cyclic test and a relaxation test. To account for the positive value of the dissipated energy during a cycle, one parameter had to be changed, which only slightly degraded the good agreement between the model and the experimental data for the compression tests. This modified model is able to predict the steady state value of the relaxation and the qualitative description of the cyclic test is in good agreement with the experimental data, excepted for the slopes of the curve at the beginning and the end of the test.

In absolute terms, the model should be calibrated with cyclic tests in tension and compression at different loading rates, completed with cyclic shear tests, again at different loading velocities. In this way, one can be sure that all the common effects related to viscoelasticity are taken into account. The quality of the model should then be judged on its ability to predict the deformations of the brain tissue in a real clinical case, as it was done by Wittek et al. (2005). Since there exists no standard protocol or universally accepted set of experimental results, this is the only objective way to evaluate the quality of a numerical model for the brain tissues.

CHAPTER 11
DISCUSSION OF THE NUMERICAL RESULTS

11.1 Introduction

Although the mathematical foundations of the fractional calculus go back to the 18th century, its applications in physics are relatively recent.

The fractional derivatives are mathematical powerful tools, known for their ability in the curve fitting domain. It was eventually proved in section 9.3 that a fractional calculus-based constitutive model for brain tissue is closer to the experimental data than the classical integer order differential model.

However, we have to admit that there is a price to this better curve fitting: firstly, the fractional derivatives are non-local, which dramatically increases the computational time and secondly the physical interpretation of some of the parameters of the model described by Eqn. 9.58 to Eqn. 9.60 is not straightforward. For instance, nothing indicates that the parameter b is the coefficient to play with to obtain a good modelling in cyclic test.

Contrarily to some classical hyper(visco)elastic models encountered in the literature, there is no theoretical proof that the proposed model follows the laws of thermodynamics. We can only prove that it does not violate any fundamental principle by simulating experiments and observing whether the results are acceptable or not in this sense. But given the results described in the previous chapter, no unacceptable behaviour has been encountered.

11.2 Calibration & validation

The original fractional calculus-based model presented in the present thesis provides very good quantitative results in calibration, with a mean relative error which does not exceed 7.5%. This MRE only slightly increased when one parameter was changed so that the qualitative behaviour of the model for a cyclic test fits the experimental observation. A recalibration of the model taking this experiment into account would probably lead to better results since b was changed by trials and errors, but the current result is satisfactory. As previously stated, it should be preferable to calibrate the model on cyclic tests in both tension and compression. Indeed, the behaviour of the brain tissue was proved to be different in tension and compression (see Miller and Chinzei (2002) and Franceschini (2006)).

But we have to keep in mind that the final application is the determination of the displacements and deformations that occur during a brain surgery, which is the ultimate validation test. Then, the requested model accuracy has to be consistent with the accuracy of the M.R.I. scanner used to acquire the pictures of the brain. Therefore, it should be the next logical step to implement the proposed constitutive equation in a finite element code and use it on a clinical case. If the result is not satisfactory, the model should be recalibrated using the aforementioned experiments and/or improved.

11.3 Possible improvements

In the literature, the Ogden strain energy density function was used instead of the extended Mooney-Rivlin strain energy density function which is not able to take account of the different behaviour in tension and compression (see Miller and Chinzei (2002) and references therein). This is the first possible improvement of the model.

The viscous part of the stress could also be considered as the sum of M viscoelastic modes, i.e. be of the form

$$\mathbf{S}^V = \sum_{i=1}^{M} \mathbf{Q}_i \tag{11.1}$$

with each mode $\mathbf{Q}_i$ being the solution of a fractional differential equation

$$D_t^{(\alpha_i)}\mathbf{Q}_i + \gamma_i \mathbf{Q}_i = \mathbf{F}_i(\boldsymbol{\zeta}, \dot{\boldsymbol{\zeta}}, \ddot{\boldsymbol{\zeta}}) \tag{11.2}$$

Considering the great curve fitting ability of the fractional derivatives, this solution would probably enable the model to perfectly fit a large number of experimental results but it would also dramatically increase the computational time, even if using the short memory principle.

Finally, the right hand side of Eqn. 9.59 could be replaced by a nonlinear function to be determined.

11.4 Implementation of the model in a finite element code

The implementation of the model in a finite element code is mandatory for the aimed application. However, a few issues will appear. Firstly, the solver of fractional differential equations is designed for a constant time step. It would be useful to make it more general so that this time step could be increased or decreased, depending on the convergence of the code at a given iteration. Otherwise, the time step should be manually adapted if the code failed to converge.

Secondly, the non locality of the fractional derivative increases the computational time compared to a more classical constitutive model, even when using the short memory principle. The number of variables to be stored in memory is also far more important in the case of a fractional model. The computation of the tangent matrix would more likely be the more costly operation in terms of computational time, whether it is performed analytically or using the perturbation method. But since the popularity of the use of fractional models has been increasing this last few years, no doubt that their implementation in finite element codes

will be investigated and that it will be possible to decrease both the computational time and memory space requirements in a next future.

11.5 Conclusion

The numerical modelling of the brain tissue using the fractional derivation operator gave promising results compared to classical models. It is an elegant and effective formulation that is suitable for the application in neurosurgery.

However, it is time and memory space consuming and the physical interpretation of the parameters is not easy.

But it needs, and probably deserves, more investigations on those two particular issues. Nowadays, it is not ready to be used in the neurosurgery operating room to provide the displacements and deformations of the brain in real time computation. But since there has been a increasing effort on the application of fractional calculus in the fields of engineering and physics for the last years, and considering the always increasing power of the computers, it should be the matter of a few years before it happens.

GENERAL CONCLUSIONS & PERSPECTIVES

he numerical modelling and the experimental characterization of the brain tissue is a very interesting and challenging field with numerous possible applications in neurosurgery and in the optimization of safety systems for the prevention of traumatic brain injuries.

In this thesis, we developed an original viscoelastic fractional model. We showed that for the same number of parameters, the fractional model fits the experimental data better than a model based on an ordinary differential equation. The fractional derivative-based model are commonly known for their excellent curve fitting property, and this was verified once again in the present document. The proposed model is able to reproduce the nonlinear, loading rate dependent behaviour of the brain tissue in compression for three different compression rate spreading over two orders of magnitude compatible with the loading rates encountered in neurosurgical applications. It also perfectly predicts the steady value of the force observed in a relaxation experiment. Finally, it gives a satisfactory result in simulating a cyclic experiment consisting in a compression phase followed by an unloading phase.

The good agreement between the fractional model and the experimental data comes from the non locality of the fractional derivative. This property increases the computational cost of the resolution of a fractional differential equation compared to an ordinary one. Therefore, we should state that nowadays, the fractional constitutive equation is not ready to be used in a finite element model for a real-time computation of the displacements and the deformations of a brain during a neurosurgery. However, regarding the growing interest about the application of fractional calculus in physics, and particularly in constitutive modelling of viscoelastic materials, as well as the development of efficient fractional differential equation resolution algorithms, it should be a matter of months before fractional model can advantageously replace classical ones.

Experimental results in the literature, and confirmed in the present thesis, showed that for the loading rate compatible with neurosurgical applications, the brain tissue behaves like a viscoelastic solid which soften when subjected to cyclic tests. Results in the literature also proved that the behaviour of the brain tissue is not the same in tension and compression. A fractional model should be able to reproduce these properties if given a suitable hyperelastic strain energy density function.

The experimental data exposed in the literature generally differ from one author to another. This is because no standard protocol exists for the testing of brain tissue. It proved to be sensitive to experimental conditions such as the temperature or the postmortem time. Furthermore, the brain tissue made of isotropic grey matter and anisotropic white matter is not an homogeneous material. The species from which the samples are taken also participates to the wide scatter observed in the literature, not to mention the intra species variability, which was clearly demonstrated in the present thesis.

Due to its softness, the brain tissue is very delicate to handle and great caution must be taken when carving the sample. In this thesis, we used the digital image correlation, a contactless optical method, to measure the displacements and strains in the sample during our experiments. To work properly, the D.I.C. requires the application of a speckle pattern on the sample's surface. A rigorous statistical analysis showed that, with the experiment protocol developed in this thesis, the application of this pattern did not change the mechanical properties of the brain for the duration of our experiments.

The use of the digital image correlation enabled us to bring an experimental proof of the incompressibility of the brain tissue, which, to our best knowledge, was never made before. The use of the D.I.C. also allowed us to underline the importance of the initial contact between the superior surface of the sample and the plate of the testing machine on the measured force/stress at the end of the compression experiments. Due to this imperfect contact, we also demonstrated why the stress-strain curves obtained using only the outputs of the testing machine are different from the ones obtained with the D.I.C. In unconfined compression tests, the imperfect contact leads to the underestimation of the stresses.

The results were obtained using a few assumptions, i.e. the homogeneity and isotropy of the brain tissue. The contact between the sample and the plates of the testing machine was assumed to be frictionless, which allowed us to consider that the sample kept its cylindrical shape throughout the tests, thus simplifying the subsequent computations. This hypothesis was visually confirmed by the observation of the shape of the samples before and after the tests.

As good and complete could be the set of experiments carried out to calibrate a given model, they do not replace the ultimate test: the validation on a real clinical case (if the considered application is the neurosurgery).

Future work would consist in the realization of simple tensile tests and cyclic tests in both tension and compression. Depending on the results, the model could be improved, the first change being the replacement of the extended Mooney-Rivlin strain energy density function by Ogden's one. If the fractional derivative is not able to reproduce the softening of the tissue, a state variable and its equation of evolution should be added. Finally, the validation on a clinical case is envisaged, which requires the implementation of the constitutive model in a finite element code. We should then investigate a way to compute efficiently the tangent constitutive operator.

It is also worth trying to see if the fractional model could be used in traumatic brain injury prediction. To this end, it should be recalibrated using the published results of shear tests. The next step would be to determine a damage criterion for the tissue.

BIBLIOGRAPHY

(2006). Introductory notes on fractional calculus. www.xuru.org.

Adolfsson, K. (2003). *Models and numerical procedures for fractional order viscoelasticity.* PhD thesis, Chalmers university of Technology.

Adolfsson, K. and Enelund, M. (2003). Fractional derivative viscoelasticity at large deformations. *Nonlinear dynamics*, 33:301–321.

Agrawal, O. (2006). Fractional variational calculus and the transversality conditions. *Journal of Physics A : Mathematical and General*, 39:10375–10384.

Aimedieu, P. (2004). *Contribution a la biomecanique des tissus mous intracraniens.* PhD thesis, Universite de Picardie Jules Verne.

Aimedieu, P., Grebe, R., and Idy-Peretti, I. (2001). Study of brain white matter anisotropy. In *23rd Annual EMBS International Conference*.

Ali, M., Törn, A., and Viitanen, S. (2002). A direct search variant of the simulated annealing algorithm for optimization involving continuous variables. *Computers and Operations Research*, 29:87–102.

Atanackovic, T. and Stankovic, B. (2008). On a numerical scheme for solving differential equations of fractional order. *Mechanics Research Communications*, 35:429–438.

Augustine, G., Cant, N., Casseday, J., and Einstein, G. (1999). *Neurosciences.* De Boeck Université.

Bagley, R. and Torvik, P. (1983). A theoretical basis for the application of the fractional calculus to viscoelasticity. *Journal of Rheology*, 27:201–210.

Bagley, R. and Torvik, P. (1984). On the appearance of the fractional derivative in the behavior of real materials. *Journal of Applied Mechanics*, 51:294–298.

Bagley, R. and Torvik, P. (1986). On the fractional calculus model of viscoelastic behavior. *Journal of Rheology*, 30:133–155.

Bandak, F. (1995). On the mechanics of impact neurotrauma: a review and critical synthesis. *Journal of Neurotrauma*, 12:635–649.

Barrault, M. and Le Bris, C. (1999). Optimisation numérique et différentiation automatique pour un problème industriel. Technical report, École Nationale des Ponts et Chaussées.

Bayly, P., Song, S., Ji, S., Mulcahy, N., Meyer, G., and Genin, G. (2003). Measurement of strain by mri tagging in physical models of brain injury. In *Summer Bioengieneering Conference*.

Bechir, H., Chevalie, L., Chaouche, M., and Boufala, M. (2006). Hyperelastic constitutive model for rubber-like materials based on the first seth strain measures invaiant. *European Journal of Mechanics A/Solids*, 25:110–124.

Bilston, L., Liu, Z., and Phan-Tien, N. (2001). Large strain behaviour of brain tissue in shear: some experimental data and differential constitutive model. *Biorheology*, 38:244–252.

Blank, L. (1996). Numerical treatment of differential equations of fractional order. Technical report, Manchester Center for Mathematics.

Bologna, M. (2004). Short introduction to fractional calculus. www.uta.cl/revistas/charlas/volumen19/Indice/MAUROrevision.pdf.

Boukamel, A., Méo, S., Débordes, O., and Jaeger, M. (2001). A thermo-viscoelastic model for elastomeric behaviour and its numerical application. *Archive of Applied Mechanics*, 7:785–801.

Brands, D. (2002). *Predicting brain mechanics during closed head impact - numerical and constitutive aspects* -. PhD thesis, Technische Universiteit Eindhoven.

Brands, D., Peters, G., and Bovendeed, P. (2004). Design and numerical implementation of a 3d non-linear viscoelastic constitutive model for brain tissue during impact. *Journal of Biomechanics*, 37:127–134.

Caputo, M. and Mainardi, F. (1971). A new dissipation model based on memory mechanism. *Pure and applied geophysics*, 91:134–147.

Cardoso, M., Salcedo, R., and Feyo de Azevedo, S. (1996). The simplex-simulated annealing approach to continuous non linear optimization. *Computers chem. Engng*, 20:1065–1080.

Carpinteri, A. and Mainardi, F. (2006). *Fractals and fractional calculus in continuum mechanics*. Springer.

Cescotto, S. and Fonder, G. (1979). A finite element approach for large strains of nearly incompressible rubber-like materials. *International Journal of Solids Structures*, 15:589–605.

Chakroun, M., Zagrouba, M., and Elloumi, I. (2004). Modélisation du comportement vibratoire de la matière cérébrale: modèle de maxwell semi-linéaire. *Rhéologie*, 6:67–73.

Cheng, S. and Bilston, L. (2007). Unconfined compression of white matter. *Journal of Biomechanics*, 40:117–124.

Chu, Y. and Bottlang, M. (2003). Finite element analysis of traumatic brain injury.

Chusid, J. (1996). *Correlative neuroanatomy and functional neurology.* Lange Medical Publications.

Clatz, O. (2002). Analysis and prediction of the brain deformation during a neurosurgical procedure. Master's thesis, ENS Cachan.

Clatz, O., Bondiau, P., Delingette, H., Sermesant, M., Warfield, S., Malandin, G., and Ayache, N. (2004a). Brain tumor growth simulation. Technical report, INRIA.

Clatz, O., Delingette, H., Bardinet, E., D., D., and Ayache, N. (2004b). Patient-specific biomechanical model of the brain : application to parkinson's disease procedure.

Cocozza-Thivent, C. (2002). Processus stochastiques niveau 1. Course slides. UFR de Mathématiques, University of Marne-la-Vallée.

Cotter, C., Smolarkiewicz, P., and Szczyrba, I. (2002). A viscoelastic fluid model for brain injuries. *International Journal for numerical methods in fluids*, 40:303–311.

Coupé, P., Hellier, P., and Barillot, C. (2005). Etat de l'art des methodes de correction des deformations cerebrales per-operatoires. Technical report, IRISA.

Darvish, K. and Crandall, J. (1999). Investigating nonlinear viscoelastic properties of brain tissue using the forced vibration method. In *Proceedings of the 23rd Annual Meeting of the American Society of Biomechanics.*

Darvish, K. and Crandall, J. (2000). A quasilinear viscoelastic model for brain tissue. pdf document.

Darvish, K. and Crandall, J. (2001). Nonlinear viscoelastic effects in oscillatory shear deformation of brain tissue. *Medical Engineering & Physics*, 23:633–645.

Davatzikos, C., Shen, D., Mohamed, A., and Kyriacou, S. (2001). A framework for predictive modeling of anatomical deformations. *IEEE Transactions on medical imaging*, 20:836–843.

Dealy, J. and Plazek, D. (2009). Time-temperature superposition - a users guide. *Rheology Bulletin*, 2:16–25.

Deng, W. (2007). Short memory principle and a predictor-corrector approach for fractional differential equations. *Journal of Computational and Applied Mathematics*, 206:174–188.

Diethelm, K. (1997a). An algorithm for the numerical solution of differential equations of fractional order. *Electronic transactions on numerical analysis*, 5:1–6.

Diethelm, K. (1997b). Generalized compound quadrature formulae for finite-part integrals. *IMA Journal of Numerical Analysis*, 17:479–493.

Diethelm, K. (2006a). An efficient algorithm for the evaluation of convolution integrals. *Computers and Mathematics with Applications*, 51:51–72.

Diethelm, K. (2006b). A survey of numerical methods in fractional calculus. course slides.

Diethelm, K. and Ford, N. (2003). Numerical solution of the bagley torvik equation. Technical report, Manchester Center for Computational Mathematics.

Diethelm, K., Ford, N., and Freed, A. (2002). A predictor-corrector approach for the numerical solution of fractional differential equations. *Non linear dynamics*, 29:3–22.

Diethelm, K., Ford, N., Freed, A., and Luchko, Y. (2005). Algorithms for the fractional calculus : a selection of numerical methods. *Computational Methods in Applied Mechanical Engineering*, 194:743–773.

Diethelm, K. and Freed, A. (2006a). The fracpece subroutine for the numerical solution of differential equations of fractional order. Technical report, TU Braunschweig & NASA RC.

Diethelm, K. and Freed, A. (2006b). Fractional calculus in biomechanics: a 3d viscoelastic model using regularized fractional-derivative kernels with application to the human calcaneal fat pad. *Biomechanics and Modeling in Mechanobiology*, 5:203–215.

Donnelly, B. and Medige, J. (1997). Shear properties of human brain tissue. *Journal of Biomechanical Engineering*, 119:423–432.

Dorea, C. (1997). On the efficiency of a continuous version of the simulated annealing algorithm. *Statistics & Probability Letters*, 31:247–253.

Drozdov, A. (1996). *Finite elasticity and viscoelasticity.* ISBN 9810224338.

Drozdov, A. (1998). *Mechanics of viscoelastici solids.* ISBN 0471975125.

Dubois, F. and Mengué, S. (2000a). Collocation mixte pour les équations différentielles nonlinéaires d'ordre fractionnaire. Preprint.

Dubois, F. and Mengué, S. (2000b). Schémas numériques implicites pour les équations semidifférentielles. Technical report, Conservatoire National des Arts et Métiers.

Ehlers, W., Markert, B., and Acartürk, A. (2003). Large strain viscoelastic swelling of charged hydrated porous media. Institute fo applied mechanics, University of Stuttgart.

El Sayed, T., Mota, A., Fraternali, F., and Ortiz, M. (2008). Biomechanics of traumatic brain injury. *Computational Methods in Applied Mechanics and Engineering*, 197:4692–4701.

Enelund, M. and Lesieutre, G. (1999). Time domain modeling of damping using anelastic displacement fields and fractional calculus. *International journal of solids and structures*, 36:4447–4472.

Fafard, M. (2004). Viscoélasticité tridimensionnelle via une approche de la thermodynamique des pocessus irréversibles. Course of the University of Laval.

Fancello, E., Ponthot, J., and L., S. (2006). A variational formulation of constitutive models and updates in non-linear finite viscoelasticity. *International Jounal for Numerical Methods in Engineering*, 65:1831–1864.

Fitzgerald, M. (1995). *Neuroanatomy: basic and clinical.* Saunders Company LTD.

Ford, N. and Simpson, A. (2001). The numerical solution of fractional differential equations : speed versus accuracy. Technical report, Manchester Center for Computational Mathematics.

Franceschini, G. (2006). *The mechanics of human brain tissue.* PhD thesis, University of Trento.

Franceschini, G., Bigoni, D., Regitnig, P., and Holzapfel, G. (2006). Brain tissue deforms similarly to filled elastomers and follows consolidation theory. *Journal of Mechanics and Physics of Solids*, 54:2592–2620.

Fung, Y. (1981). *Mechanical properties of living tissues.*

Galford, J. and McElhaney, J. (1970). A viscoelastic study of scalp, brain and dura. *Journal of Biomechanics*, 3:211–221.

Gao, C., Eng Hock Tay, F., and Nowinski, W. (2006). Modelling of the human brain with detailed anatomy for numerical simulation of surgical interventions. *Journal of Physics: Conference Series*, 34:985–989.

Garo, A., Hrapko, M., van Dommelen, J., and Peters, G. (2007). Towards a reliable characterisation of the mechanical behaviour of brain tissue: the effects of post-mortem time and sample preparation. *Biorheology*, 44:51–58.

Gefen, A., Gefen, N., Zhu, Q., Raghupathi, R., and Margulies, S. (2003). Age-dependent changes in material properties of the brain and braincase of the rat. *Journal of Neurotrauma*, 20:1163–1180.

Gefen, A. and Margulies, S. (2004). Are in vivo and in situ brain tissues mechanically similar? *Journal of Biomechanics*, 37:1339–1352.

Gemant, A. (1936). A method of analyzing experiment results obtained from elasto-viscous bodies. *Physics*, 7:311–317.

Gemant, A. (1938). On fractional differentials. *Philosophical Magazine*, 25:540–549.

González-Monroy, L. and Córdoba, A. (2000). Optimization of energy supply systems with simulated annealing : continuous and discrete descriptions. *Physica A*, 284:433–447.

Greenleaf, J., Fatemi, M., and Insana, M. (2003). Selected methods for imaging elastic properties of biological tissues. *Annu. Rev. Biomed. Eng.*, 5:57–78.

Hagemann, A., Rohr, K., and Stiehl, H. (2002). Coupling of fluid and elastic models fo biomechanical simulations of brain deformations using fem. *Medical Image Analysis*, 6:375–388.

Hastretier, P., Rezk-Salama, C., Nimsky, C., Lurig, C., Greiner, G., and Ertl, T. (2000). Registration techniques for the analysis of the brain shift in neurosurgery. *Computers & Graphics*, 24:385–389.

Hault, A., Drazetic, P., and Razafimahery, F. (2005). Etudes des phenomenes d'interaction fluide/structure lors d'un choc a l'interieur de la boite cranienne. In *17eme Congres Francais de Mecanique.*

Hawkins, T., Wittek, A., and Miller, K. (2004). Comparison of constitutive models of brain tissue for non rigid image registration. Technical report, University of Western Australia.

Holzapfel, G. (2001). *Nonlinear Solid Mechanics : A Continnum Approach for Engineering*. ISBN 0471823198.

Horaud, R. and Monga, O. (1995). *Vision par ordinateur*. Hermes.

Hrapko, M., van Dommelen, J., Peters, G., and Wismans, J. (2005). The mechanical behaviour of brain tissue: large strain responses and constitutive modelling. In *International IRCOBI Conference*.

Hrapko, M., van Dommelen, J., Peters, G., and Wismans, J. (2006). The behaviour of brain tissue in compression. pdf document.

Hrapko, M., van Dommelen, J., Peters, G., and Wismans, J. (2008). The influence of test conditions on characterization of the mechanical properties of brain tissue. *Journal of Biomechanical Engineering*, 130:1–10.

Hrapko, M., van Dommelen, J., Peters, G., and Wismans, J. (43). The mechanical behavior of brain tissue : large strain response and constitutive modelling. *Biorheology*, 2006:623–636.

Hu, T. and Desai, J. (2004). Characterization of soft-tissue material properties: large deformation analysis. *Lecture Note in Computer Science*, 3078:28–37.

Ingber, L. (1989). Very fast simulated re-annealing. *Mathematical Computer Modelling*, 12:967–973.

Ingber, L. (1993). Adaptative simulated annealing (asa). Technical report, Caltech. http://www.ingber.com/.

Jafari, H. and Daftardar-Gejji, V. (2006). Revised adomian decomposition method for solving systems of ordinary and fractional differential equations. *Applied Mathematics and Computation*, 181:598–608.

Kazmarec, M., Subramaniam, R., and Neff, S. (1997). The hydromechanics of hydrocephalus: steady-state solutions for cylindrical geometry. *Bulletin of Mathematical Biology*, 59:295–323.

Keunings, R. (2003). Finite element methods for integral viscoelastic fluids. *Rheology reviews*, x:167–195.

Kim, J. and Srinivasan, M. (2005). Characterization of viscoelastic soft tissue properties from in vivo animal experiments and inverse fe parameter estimation. In *MICCAI 2005*.

Kyriacou, K. and Davatzikos, C. (1998). A biomechanical model of soft tissue deformation, with applications to non-rigid registration of brain images with tumor pathology. In *MICCAI*.

Kyriacou, S., Davatzikos, C., Zinreich, J., and Bryan, R. (1999). Non linear elastic registration of brain images with tumor pathology using a biomechanical model. *IEEE Transactions on Medical Imaging*, 18:580–592.

Kyriacou, S., Mohamed, A., Milller, K., and Neff, S. (2002). Brain mechanics for neurosurgery: modeling issues. *Biomechan Model Mechanobiol*, 1:151–164.

Kyriacou, S., Shen, D., and Davatzikos, C. (2000). A framework for predictive modeling of intra-operative deformations : a simulation-based study. In *MICCAI*.

Lauret, C. (2007). Optical characterization of acceleration-induced strain fields in inhomogeneous brain slices. Master's thesis, Eindhoven University of Technology.

Lecomte, B. (2006). Simplified finite elements modeling of brain deformation. Master's thesis, University of Liège.

Libertiaux, V. (2005). Penalty methods for nearly incompressible hyperelastic materials. Technical report, M&S Department, University of Liège.

Libertiaux, V. (2006). Hyperviscoelastic constitutive law for fem code. Technical report, M&S Department, University of Liège.

Libmann, M. (1991). *Neuroanatomy made easy and understandable.* Aspen Publications.

Ling, Y. (1996). Uniaxial true stress-strain after necking. *AMP Journal of Technology*, 5:37–48.

Loret, B. and Simões, F. (2005). A framework for deformation, generalized diffusion, mass transfer and growth in multi-species multi-phase biological tissues. *European Journal of Mechanics A/Solids*, 24:757–781.

Loverro, A. (2004). Fractional calculus : history, definitions and applications for the engineer. Technical report, Department of Aerospace and Mechanical Engineering, Univerity Notre-Dame, IN USA.

Luchko, Y. and Gorenflo, R. (1998). An operational method for solving fractional differential equations with the caputo derivatives. Preprint.

Luo, Y., Zhang, Q., and Del Bigio, M. (2008). Recent progress in application of fem in study of non-penetrating brain injuries. *Advanced Theory in Applied Mechanics*, 1:225–240.

Magin, R. and Royston, T. (2010). Fractional-order elastic model of cartilage: a multi-scale approach. *Communications in Nonlinear Science and Numerical Simulation*, 15:657–664.

Matignon, D. (2005). Introduction au calcul fractionnaire. Notes de cours.

McLean, D., Mustapha, K., and Thomée, V. (2006). Numerical methods for some fractional-order partial differential equations. Slides.

Meaney, D. (2003). Relationship between structural modeling and hyperelastic material behavior : application to cns white matter. *Biomechan Model Mechanobiol*, 1:279–293.

Mehdizadeh, S., Khoshgoftar, M., Najarian, S., Farmanzad, F., and Ahmadi, S. (2008). Comparison between brain tissue gray and white matters in tension including necking phenomenon. *American Journal of Applied Sciences*, 12:1701–1706.

Menzel, A. (2005). Modelling of anisotropic growth in biological tissues. *Biomech Model Mechanbiol*, 3:147–171.

Metropolis, N., Rosenbluth, A., Rosenbluth, M., Teller, A., and Teller, E. (1953). Equations of state calculations by fast computing machines. *Journal of Chemical Physics*, 6:1087–1092.

Miettinen, K., Mäkelä, M., and Maaranen, H. (2006). Efficient hybrid methods for global continuous optimization based on simulated annealing. *Computers & Operations Research*, 33:1102–1116.

Miga, M., Paulsen, K., Hoopes, P., Kennedy, F., Hartov, A., and Roberts, D. (2000a). In vivo modelling of interstitial pressure in the brain under surgical load using finite elements. *Journal of Biomechanical Engineering*, 122:354–363.

Miga, M., Paulsen, K., Hoopes, P., Kennedy, F., Hartov, A., and Roberts, D. (2000b). In vivo quantification of a homogeneous brain deformation model for updating preoperative images during surgery. *IEEE Transactions on Biomedical Engineering*, 47:266–273.

Miller, A., Alston, R., and Corsellis, J. (1980). Variation with age in the volumes of grey and white matter in the cerebral hemispheres of man: measurements with an image analyser. *Neuropathology and Applied Neurobiology*, 6:119–132.

Miller, K. (1998). Finite deformation, linear and non linear viscoelastic models of brain tissue mechanical properties.

Miller, K. (1999). Constitutive model of brain tissue suitable for finite element analysis of surgical procedures. *Journal of Biomechanics*, 32:531–537.

Miller, K. (2000). Constitutive modelling of abdominal organs. *Journal of Biomechanics*, 33:367–373.

Miller, K. (2001). How to test very soft biological tissues in extension ? *Journal of Biomechanics*, 34:651–657.

Miller, K. (2002). *Biomechanics of brain for computer integrated surgery*. Publishing house of the Warsaw University of Technology.

Miller, K. (2005). Most recent results in the biomechanics of the brain. *Journal of Biomechanics*, 38:965.

Miller, K. and Chinzei, K. (1997a). Constitutive modelling of brain tissue : experiment and theory. *Journal of Biomechanics*, 30:1115–1121.

Miller, K. and Chinzei, K. (1997b). Modelling of brain tissue mechanical properties: bi-phasic versus single phase approach. In *Proceedings 3rd International Symposium Computational Methods in Biomechanics and Biomedical Engineering*.

Miller, K. and Chinzei, K. (2002). Mechanical properties of brain tissue in tension. *Journal of Biomechanics*, 35:483–490.

Miller, K., Chinzei, K., Orssengo, G., and Bednarz, P. (2000). Mechanical properties of brain tissue in-vivo : experiment and computer simulation. *Journal of Biomechanics*, 33:1369–1376.

Mohamed, A. and Davatzikos, C. (2005). Finite element modeling of brain tumor mass-effect from 3d medical images. In *MICCAI*.

Momani, S. (2006). A numerical scheme for the solution of multi-order fractional differential equations. *Applied Mathematics and Computation*, 182:761–770.

Momjian, S. and Bichsel, D. (2006). Elastic and poro-elastic models of ventricular dilatation in hydrocephalus. In *COMSOL Users Conference*.

Monson, K., Goldsmith, W., Barbaro, N., and Manley, G. (2005). Significnce of source and size in the mechanical response of human cerebral blood vessels. *Journal of Biomechanics*, 38:737–744.

Nagashima, T., Tada, Y., Hamano, S., Skakakura, M., Masaoka, K., Tamaki, N., and Matsumoto, S. (1990). The finite element analysis of brain oedema associated with intracranial meningiomas. *Acta Neurochir Suppl*, 51:155–7.

Nagashima, T., Tamaki, N., Matsumoto, S., Horwitz, B., and Seguchi, Y. (1987). Biomechanics of hydrocephalus: a new theoretical model. *Neurosurgery*, 6:898–904.

Nagashima, T., Tamaki, N., Takada, M., and Tada, Y. (1994). Formation and resolution of brain oedema associated with brain tumors. a comprehensive theoretical model and clinical analysis. *Acta Neurochir Suppl*, 60:165–7.

Nava, A., Mazza, E., Haefner, O., and Bajka, M. (2004). Experimental observation and modelling of preconditioning in soft biological tissues. Center of mechanics, ETH-Zurich.

Nutting, P. (1921). A new general law of deformation. *Journal of the Franklin Institute*, 191:679–685.

Odibat, Z. (2006). Approximations of fractional integrals and caputo fractional derivatives. *Applied Mathematics and Computation*, 178:527–533.

Ogden, R. (1984). *Non-linear elastic deformations.* Mineaola, N.Y.

Ogden, R. and Roxburgh, D. (1999). A pseudo-elastic model for the mullins effect in filled rubber. *Proc. R. Soc. Lond.*, 455:2861–2877.

Omori, K., Zhang, L., Yang, K., and King, A. (2000). Effect of cerebral vasculatures on the mechanical response of brain tissue: a preliminary study. In *ASME International Mechanical Engineering Congress*.

Ottensmeyer, M., Kerdok, A., Howe, R., and Dawson, S. (20xx). The effects of testing environment on the viscolastic properties of soft tissues. Technical report, CIMIT, Cambridge, MA.

Ozawa, H., Matsumoto, t., Ohashi, T., Sato, M., and Kokubun, S. (2001). Comparison of spinal cord gray matter and white matter softness: measurement by pipette aspiration method. *Journal of Neurosurgery*, 95:221–4.

Pamidi, M. and Advani, S. (1978). Nonlinear constitutive relations for human brain tissue. *Journal of biomechanics engineering*, 100:44–48.

Pascon, F. (2005). Constitutive equations for mechanical behaviour of brain tissues. Technical report, M&S Department, University of Liège.

Pervin, F. and Chen, W. (2009). Dynamic mechanical response of bovine gray matter and white matter brain tissues under compression. *Journal of Biomechanics*, 42:731–735.

Pioletti, D., L., R., Benvenuti, J., and P., L. (1998). Viscoelastic constitutive law in large deformations : application to human knee ligaments and tendons. *Journal of Biomechanics*, 31:753–757.

Pioletti, D. and Rakotomanana, L. (2000). Non-linear viscoelastic laws for soft biological tissues. *European Journal of Mechanical A/Solids*, 19:749–759.

Podlubny, I. (1997). The laplace transform method for linear differential equations of the fractional order. www.arXiv.org.

Podlubny, I. (1999). *Fractional differential equations*. London Academic Press.

Podlubny, I. (2005). Geometric and physical interpretations of fractional integration and differentiation. Course slides.

Podlubny, I., Dorcak, L., and I., K. (1999). On fractional derivatives, fractional-order dynamic systems and $PI^{\lambda}D^{\mu}$- controllers. In *Proc. of the 36th IEEE CDC San Diego*.

Podlubny, I. and Heymans, N. (2005). Physical interpretation of initial conditions for fractional differential equations with riemann-liouville fractional derivatives. www.arXiv.org. Submitted for publication in Rheological Acta.

Prange, M. and Margulies, S. (2002). Regional, directional and age-dependent properties of the brain undergoing large deformations. *Journal of Biomechanical Engineering*, 124:244–252.

Press, W. (1992). *Numerical Recipes in Fortran - The art of scientific computing*. Cambridge University Press.

Sack, I., Beierbach, B., Wuerfel, J., Klatt, D., Hamhaber, U., Papazoglou, S., Martus, P., and Braun, J. (2009). The impact of aging and gender on brain viscoelasticity. *NeuroImage*, 46:652–657.

Sacks, M. and Sun, W. (2003). Multiaxial mechanical behaviour of biological materials. *Annu. Rev. Biomed. Eng.*, 5:251–284.

Samuelides, M. (1995). *Calcul intensif : optimisation stochastique*. Supaero.

Sarron, J., Blondeau, C., Guillaume, A., and Osmont, D. (2000). Identification of linear viscoelastic constitutive models. *Journal of Biomechanics*, 33:685–693.

Schmidt, A. and Gaul, L. (2002a). Application of fractional calculus to viscoelastically damped structures in the finite element method. Preprint.

Schmidt, A. and Gaul, L. (2002b). Fe implementation of viscoelastic constitutive stress-strain relations involving fractional time derivatives. Universität Stuttgart.

Scott Blair, G. and Caffyn, J. (1949). An application of the theory of quasi-properties to the treatment of anomalous strain-stress relations. *The Philosophical Magazine*, 40:80–94.

Segawa, W. (1957). Stress-strain relations for viscoelastic large deformation. *Journal of the Physical Society of Japan*, 12:996–998.

Shuck, L. and Advani, S. (1972). Rheological response of human brain tissue in shear. *Journal of Basic Engineering*, 94:905–911.

Siarry, P. (2005). Adaptation des métaheuristiques pour l'optimisation continue.

Skrinjar, O., Nabavi, A., and Duncan, J. (2002). Model-driven brain shift compensation. *Medical Image Analysis*, 6:361–373.

Smith, J. and Garcia, J. (2009). A nonlinear biphasic model of flow-controlled infusion in brain: fluid transport and tissue deformation analyses. *Journal of Biomechanics*, doi:10.1016/j.jbiomech.2009.06.014.

Soula, M. and Chevalier, Y. (1998). La dérivée fractionnaire en rhéologie des polymères - application aux comportements élastiques et viscoélastiques linéaires et non linéaires des élastomères. *ESAIM : Proceedings - Fractional differential systems : models, methods and applications*, 5:193–204.

Terzaghi, K. (1943). *Theoretical soil mechanics.*

Ueno, K., Melvin, J., Li, L., and Lighthall, J. (1995). Development of tissue level brain injury criteria by finite element analysis. *Journal of Neurotrauma*, 12:695–706.

Velardi, F., Fraternali, F., and Angelillo, M. (2006). Anisotropic constitutive equations and experimental tensile behavior of brain tissue. *Biomech Model Mechanbiol*, 5:53:61.

Vigneron, L. (2009). *FEM/XFEM-based modeling of brain shift, resection and retraction for image-guided surgery.* PhD thesis, University of Liège.

Vigneron, L., Duflot, M., Robe, P., Warfield, S., and Verly, J. (2009). 2d xfem-based modeling of retraction and successive resections for preoperative image update. *Computer Aided Surgery*, doi: 10.1080/10929080903052677.

Vuskovic, V., Kauer, M., Dual, J., and Bajka, M. (1999). Method and device for in-vivo measurement of elasto-mechanical properties of soft biological tissues. *Machine Graphics and Vision*, 8:637–654.

Warfield, S., Haker, S., Talos, I., and Kemper, C. (2004). Capturing intraoperative deformations : research experience at brigham and women's hospital. *Medical Image Analysis*, x:xxx.

Weaver, J., Van Houten, E., Miga, M., Kennedy, F., and Paulsen, K. (2001). Mangetic resonance elastography using 3d gradient echo measurements of steady state motion. *Medical Physics*, 28:1620–1628.

Weinberg, E. and Kaazempur-Mofrad, M. (2005). A large-strain finite element formulation for biological tissues with application to mitral valve leaflet tissue mechanics. *Journal of Biomechanics*, Accepted April 2005:xxx–xxx.

Weiss, J. and Gardiner, J. (2001). Computational modeling of ligament mechanics. *Biomedical Engineering*, 29:1–70.

Wittek, A., Hawkins, T., and Miller, K. (2008). On the unimportance of constitutive models in computing brain deformation for image-guided surgery. *Biomech Model Mechanbiol*, doi: 10.1007/s10237-008-0118-1.

Wittek, A., Kikinis, R., Warfield, S., and Miller, K. (2005). Brainshift computation using a fully nonlinear biomechanical model. In *MICCAI*.

Wittek, A., Miller, K., Kikinis, R., and Warfield, S. (2007). Patient-specific model of brain deformation: application to medical image registration. *Journal of Biomechanics*, 40:919–929.

Wu, J., Dong, R., and Schopper, A. (2004). Analysis of effects of friction on the deformation behavior of soft tissues in unconfined compression tests. *Journal of Biomechanics*, 37:147–155.

Yadagiri, S. and Papi Reddy, C. (1985). Viscoelastic analysis of nearly incompressible solids. *Computers and Structures*, 20:817–825.

Yuste, S. and Acedo, L. (2003). On an explicit finite difference method for fractional diffusion equations. www.arXiv.org. preprint submitted to Elsevier Science.

Zhang, D. and Arola, D. (2004). Applications of digital image correlation to biological tissues. *Journal of Biomedical Optics*, 9:691–699.

Part V

Appendixes

APPENDIX A

HADAMARD FINITE PART INTEGRAL

Let's consider the following integral

$$I_H = \int_a^b \frac{f(t)}{(x-t)^\beta}\, dt \tag{A.1}$$

with $a \leq x \leq b$ and $m < \beta < m+1$. This integral diverges for $t = x$.

Let $g(t,x)$ be

$$g(t,x) = f(t) - \sum_{q=0}^{m} \frac{(t-x)^q}{q!} f^{(q)}(x) \tag{A.2}$$

We also need to define I and J such that

$$I = \int_a^{x-\varepsilon} \frac{f(t)}{(x-t)^\beta}\, dt \tag{A.3}$$

$$J = \int_{x+\varepsilon}^{b} \frac{f(t)}{(x-t)^\beta}\, dt \tag{A.4}$$

Taking Eqn.A.2 into account, Eqn. A.3 becomes

$$I = \int_a^{x-\varepsilon} \frac{g(t,x)}{(x-t)^\beta}\, dt + \sum_{q=0}^{m} \frac{(-1)^q}{q!} f^{(q)}(x) \int_a^{x-\varepsilon} (x-t)^{q-\beta}\, dt \tag{A.5}$$

$$= \int_a^{x-\varepsilon} \frac{g(t,x)}{(x-t)^\beta}\, dt + \sum_{q=0}^{m} \frac{(-1)^q}{q!} f^{(q)}(x)\, \frac{\varepsilon^{q-\beta+1} - (x-a)^{q-\beta+1}}{q-\beta+1} \tag{A.6}$$

The same reasoning holds for J leading to

$$J = \int_{x+\varepsilon}^{b} \frac{g(t,x)}{(x-t)^\beta}\, dt + \sum_{q=0}^{m} \frac{f^{(q)(x)}}{q!}\, \frac{(b-x)^{q-\beta+1} - \varepsilon^{q-\beta+1}}{q-\beta+1} \tag{A.7}$$

Let's now have a close look at the different terms. In the neighbourhood of x, $\frac{g(t,x)}{(x-t)^\beta}$ behaves like $\sum_{q=m+1}^{\infty} \frac{(-1)^q (x-t)^{q-\beta}}{q!} f^{(q)}$ or $\sum_{q=m+1}^{\infty} \frac{(x-t)^{q-\beta}}{q!} f^{(q)}$ depending on t being less or greater than x. Therefore, the first integral in I and J converges since the minimum exponent in the summation is equal to $m+1-\beta > 0$.

The terms $\varepsilon^{q-\beta+1}$ resulting from the integrations are singular up to $q = m-1$.

We finally define $FPI(\varepsilon)$ and $FPJ(\varepsilon)$ as the regular parts of I_H and $I_\infty(\varepsilon)$ and $J_\infty(\varepsilon)$ as its singular parts. Considering the preceding developments, they write

$$FPI(\varepsilon) = \int_a^{x-\varepsilon} \frac{g(t,x)}{(x-t)^\beta}\, dt + \sum_{q=0}^{m} \frac{(-1)^q}{q!} f^{(q)}(x) + \frac{(x-a)^{q-\beta+1}}{q-\beta+1} - \frac{(-1)^m}{m!} f^{(m)}(x) \frac{\varepsilon^{m-\beta+1}}{m-\beta+1} \quad \text{(A.8)}$$

$$FPJ(\varepsilon) = \int_{x+\varepsilon}^{b} \frac{g(t,x)}{(x-t)^\beta}\, dt \sum_{q=0}^{m} \frac{f^{(q)(x)}}{q!} \frac{(b-x)^{q-\beta+1}}{q-\beta+1} - \frac{f^{(m)}}{m!} \frac{\varepsilon^{m-\beta+1}}{m-\beta+1} \quad \text{(A.9)}$$

$$I_\infty(\varepsilon) = -\sum_{q=0}^{m-1} \frac{(-1)^q}{q!} f^{(q)}(x) \frac{\varepsilon^{q-\beta+1}}{q-\beta+1} \quad \text{(A.10)}$$

$$J_\infty = -\sum_{q=0}^{m-1} \frac{f^{(q)(x)}}{q!} \frac{\varepsilon^{q-\beta+1}}{q-\beta+1} \quad \text{(A.11)}$$

We finally can write the Hadamard finite part integral $FP(I_H)$ as

$$FP(I_H) = \lim_{\varepsilon \to 0} \left[FPI(\varepsilon) + FPJ(\varepsilon) \right] \quad \text{(A.12)}$$

APPENDIX B

SIMULATED ANNEALING

B.1 Introduction

The determination of the parameters of a numerical model can be thought as a minimization of the difference between the results from the model and the experimental data. The major issue of minimization problems is to find the global optimum and not a local one.

In the frame of this thesis, we chose to use a global minimization method, the simulated annealing which is briefly presented hereafter.

B.2 Metropolis dynamics

For the sake of simplicity, we will only concentrate on the solution of continuous problems such as $\min_{x \in \mathbb{R}^n} f(x)$.

When solving a continuous optimization problem with gradient methods, since the gradient of a function is a local quantity, gradient-based algorithms only provides local minima. They require a starting point and are thus initial conditions dependent. It may be sufficient in some cases, but sometimes a global minimization algorithm is indispensable. This is certainly the case when we have no idea of the initial values to give to the parameters of our problem.

Figure B.1 shows a function $E(x)$ with several local optima. If a local minimization algorithm is used, the starting point must be chosen in the green domain to find the global minimum at the first strike.

Descent algorithms

In gradient-based algorithms, a starting point is supplied by the user. The gradient of the function is then computed and the next point, candidate to be the local minimum, is taken in the direction opposite to the gradient. A translation in pseudo code is proposed in Algorithm 1.

An alternative approach, also valid in cases where the gradient cannot be computed, is exposed in Algorithm 2.

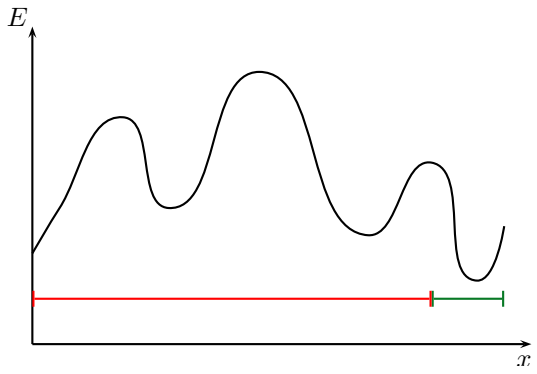

Fig. B.1: 1d function with several optima

Algorithm 1 Gradient based optimization

choose x_0 and dx
$x_{optimal} = x_0$
repeat
  Compute $g = \text{grad } x_{optimal}$
  $x_{optimal} = x_{optimal} - g * dx$
until convergence
end

Algorithm 2 Descent algorithm

choose x_0
$x_{optimal} = x_0$
choose $y \in \nu(x_{optimal})$
if $E(y) < E(x_{optimal})$ **then**
  $x_{optimal} = y$
end if
end

In Algorithm 2, ν stands for a problem dependent neighbourhood relationship. If it is chosen coarse, then each state is the neighbour of every other states but only the global minimum is solution of the problem. Conversely, if a fine ν is preferred, the algorithm will converge quickly but may be stuck in a local minimum. y is selected randomly in $\nu(x_{optimal})$.

There are different ways to define the neighbourhood relationship ν. To fix the ideas, let's consider a three variables minimization problem with the current solution $x_n = (v_1, v_2, v_3)$. Here are some possibilities to define the neighbour of x_n:

- add a random quantity ε to a randomly chosen variable v_i,
- add a random quantity ε to all variables,
- keep the last $N + 1$ points $(x_{n-N}, x_{n-N+1}, \cdots, x_n)$ and choose their centrum,

More details on the definition of a neighbourhood are given in the description of the two simulated annealing presented in section B.3 and section B.3.

Both Algorithm 1 and Algorithm 2 presented in this section only allow descents : any point whose value is greater than the actual minimum will be rejected. This very principle avoids an algorithm to "climb up a valley" and find a lower minimum in another valley.

Metropolis dynamics

The underlying idea of the Metropolis dynamics is to modify the descent algorithm, in a way that allows ascents in the process. Assuming $\beta = 1/T$[1], the Metropolis dynamics is described by Algorithm 3.

Algorithm 3 Metropolis dynamics

choose x_0
$x_n = x_0, n = 0$
loop
  choose $y \in \nu(x_n)$
  if $E(y) < E(x_n)$ **then**
    $x_{n+1} = y$
  else
    $x_{n+1} = y$ with probability $\exp(-\beta(E(y) - E(x_n)))$
  end if
  $n = n + 1$
end loop

This algorithm does not end, it rather defines a *Markov chain*[2] called the Metropolis dynamics (or the thermal relaxation). Metropolis et al. (1953) put this random dynamics forward during the 50's to compute equilibrium state in statistical dynamics.
According to the Metropolis dynamics, a point that gives a higher value of the function will be accepted as the new current state x_{n+1} with a probability $\exp(-\beta(E(y) - E(x_n)))$. It is then more likely to be accepted if the temperature is high and/or the difference $E(y) - E(x_n)$ is small. We can do the parallel with a particle, whose energy is proportional to T, wandering in an "energetic landscape" $E(x)$. If the energy of the particle is far greater than the depth of the valleys, then every single point is reachable. On the other hand, if the temperature is low, the particle can only fall in the valleys.
If the temperature is sufficiently high, all the states (i.e. all the values of x) are equiprobable, and the Metropolis dynamic amounts to a simple random walk in the state space. Generally, the most probable states at the thermal equilibrium are those of lowest energy. Hence, for $T \simeq 0$, the equilibrium state reached correspond to the global minima.

[1] T is called the *temperature* by reference to statistical mechanics
[2] For details, please consult Samuelides (1995)

B.3 Simulated annealing

The idea of the simulated annealing algorithm is to progressively cool down the temperature during the thermal relaxation process.

Proofs of convergence of the algorithm have been found for logarithmic cooling (see Samuelides (1995) and references therein):

$$T_n = \frac{A}{\log(n) + B} \tag{B.1}$$

However, those schemes converge slowly and in practice, geometrical schemes are used.

$$T_{n+1} = \alpha T_n \tag{B.2}$$

The simulated annealing algorithm is presented in Algorithm 4

Algorithm 4 Simulated annealing

choose x_0, M, α and T_{init}
$x_{optimal} = x_0$, $T = T_{init}$
$STOP$ = FALSE
while $STOP = FALSE$ **do**
  Perform thermal relaxation during M transitions
  if M is reached **then**
    cool down the temperature by a factor α
  else
    $STOP$ = TRUE (the system is frozen)
  end if
end while

Parameters of this scheme are the initial temperature, the temperature decrease factor α and the number of transitions at a constant temperature. A rule of the thumb is $\alpha \in [0.85, 0.95]$. The initial temperature is problem dependent. It is advisable to spend a little time adjusting it as a too low T_{init} will be likely to trap the system in a local minimum. A very high temperature (with respect to the maximum value of the function) will needlessly lengthen the computation time. In continuous problems, the number of allowed transitions M is generally fixed to $100K$ where K stands for the number of variables.

Different methods exist, each one with its advantages and drawbacks. Two algorithms will be presented here. The interested reader is invited to consult (Press (1992),Ali et al. (2002) and Siarry (2005))

Downhill simplex method

The downhill simplex method (DSM) (Press (1992)) requires only function evaluations, not derivatives.

A *simplex* is a geometrical figure with $N+1$ nodes in a N dimensional space ; i.e. a triangle in 2D and a tetrahedron in 3D. This simplex has to be non degenerated : the $N+1$ nodes have to be distinct and enclose a N dimensions volume.
The DSM requires a starting simplex supplied by the user. One way to obtain it is to choose a single point P_0 and take the N other points to be

$$P_i = P_0 + \mu e_i \tag{B.3}$$

where μ is a constant related to the problem's characteristic length scale and e_i is the i^{th} unit vector.
Basically, during the execution of the algorithm, the simplex will do the following moves, represented in Fig. B.2:

- reflection away from the node with the highest value,
- expansion in one direction,
- contraction in one (or several) direction(s),

Let's consider an example : given a starting simplex, the algorithm will compute the values of the function at the nodes. It will keep in memory the lowest (L), highest (H), and second highest (SH) points. The first move is a reflection : the point giving the worst result is moved through the opposite face of the simplex. If the value of the function at this new node is less than L, the algorithm performs an expansion in the same direction; otherwise, if the value is higher than SH, the method contracts the simplex. The DSM then consists in a geometrical figure performing and combining 3 simple moves to find a **local** minimum.

Modified downhill simplex method

In the modified downhill simplex method (MDSM) (Press (1992)), the moves described for the DSM are used. The implementation of the Metropolis dynamic is quite subtle : a positive, logarithmically distributed random variable, proportional to the temperature T is added to the value of the function at each node ; a similar random variable is subtracted from the value of the function at every point tried as a new vertex. This way, the method always accepts a true downhill step and sometimes accepts an uphill one.
For a finite temperature T, the simplex expands at the size of the region that is reachable at this temperature and performs a random walk. If the temperature is cooled down sufficiently smoothly, as it is recommended in simulated annealing methods, it is highly likely that the simplex will converge in the region containing the lowest minimum. As in all methods involving simulated annealing, the annealing schedule is the key point of the success or failure of the algorithm. Some possibilities are described in Press (1992) :

- reduce T to $(1-\varepsilon T)$ after every M moves where ε and M are determined by experiments
- budget a total of K moves, and reduce T after every M moves to a value $T = T_0(1 - k/K)^\alpha$, where k is the cumulative number of moves, and α is a constant. Larger values of α spend more iterations at lower temperature.

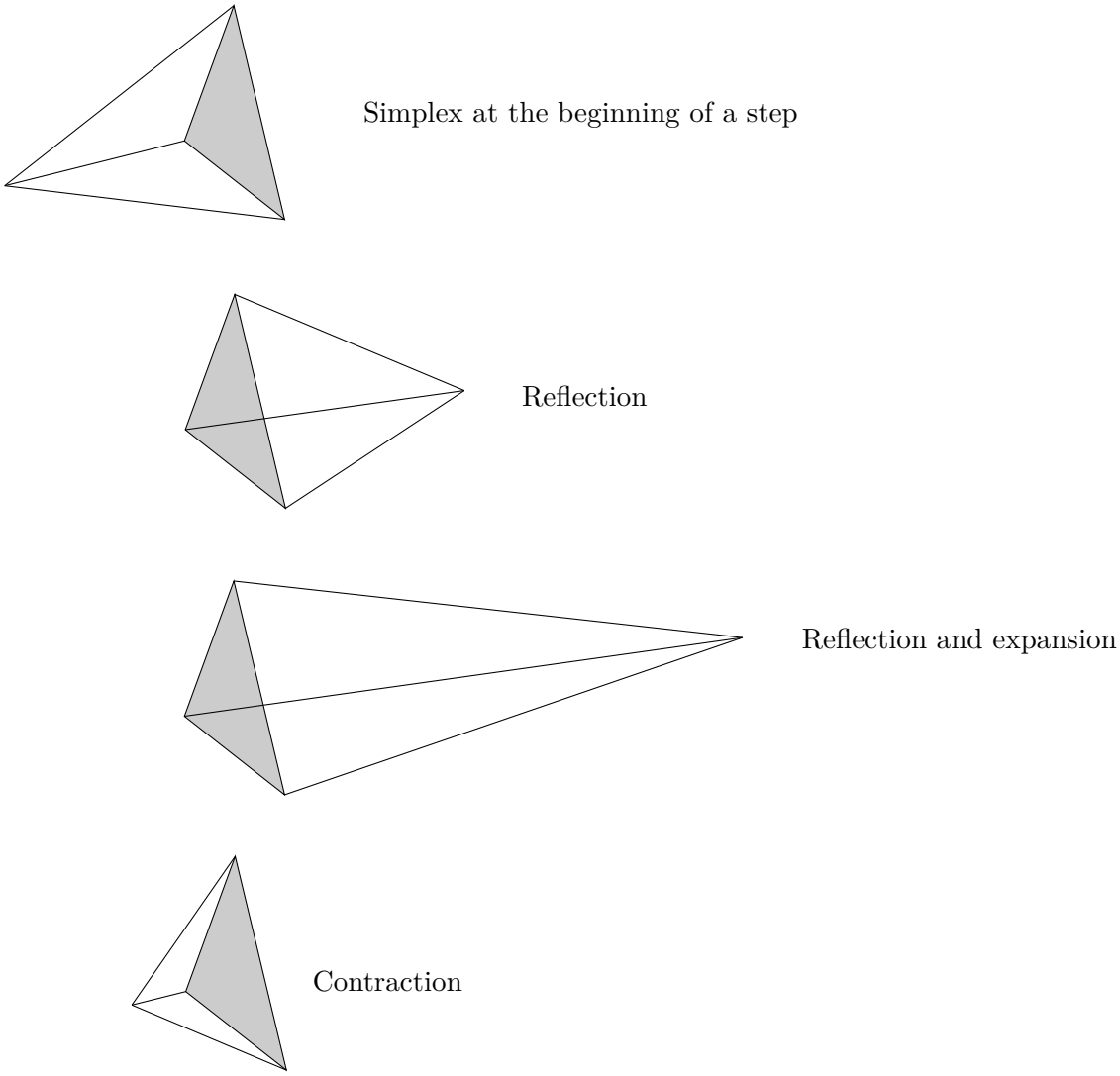

Fig. B.2: Basic moves performed by the DSM algorithm: case of 3D problem.

- After every M moves, set T to $\beta \times (f_1 - f_b)$, where β is an experimentally determined constant of order 1, f_1 is the current smallest value in the simplex and f_b is the best function ever encountered.

A good move also consists in occasionally restarting the algorithm and replacing one of the vertices by the best-ever point. This is not a universal piece of advice as it may sometimes have negative effects.

A drawback appears when dealing with constrained optimization problems : what if a vertex is taken out of the allowed domain after a simplex dilatation ? A random choice will alter the process and may lead to an unpredictable behavior. Indeed, there is, to our knowledge, no proof of convergence in that case.

Classical simulated annealing

The classical simulated annealing method (CSA) is certainly the most intuitive continuous simulated annealing. Let's remember that the main issue in continuous simulated annealing is to define a neighbourhood relationship. For a N dimensional minimization problem, the idea is the following : a N d vector (VM) contains the step length for each variable at step i. This step length is periodically adjusted so that half of all function evaluations in the uphill direction are accepted. Thus, a trial point X at step $i+1$ is of the form :

$$X_{i+1} = X_i + VM_i \tag{B.4}$$

VM is linked to T, so that the cooler the temperature, the smaller the step length. The annealing schedule is geometrical, $T_{i+1} = \alpha T_i$ with $\alpha \in [0.90\ 0.99]$.

A faster algorithm was developed by Ingber (1989) and is available on the web (Ingber (1993))

B.4 Conclusion

Simulated annealing algorithms are powerful tools which require a little experience to be very efficient. They are very convenient in the case of functions with multiple local minima. Since they are starting point-independent, they are very useful when no knowledge of the function is needed, contrarily to gradient methods which require an initialization "not too far" from the solution.

In the present thesis, the classical simulated annealing was preferred to the modified downhill simplex method. Indeed, the classical algorithm handles more easily the cases where a trial point y is not in the allowed domain, i.e. between the lower and upper bounds chosen for the parameters.

APPENDIX C

TIME-TEMPERATURE SUPERPOSITION

The time-temperature superposition (TTS) is used to determine the behaviour (typically the relaxation modulus or the creep modulus) of a viscoelastic material at times or frequencies that are not reachable via experimental procedures. This can be achieved thanks to the temperature dependence of the mechanical properties of viscoelastic materials.

Practically, the same experimental protocol is used to perform tests at different temperatures. The relaxation (or creep) modulus is plotted versus time (or frequency) using logarithmic scale for both axes. A curve is chosen as the reference and the other curves are shifted horizontally and vertically so that they all superpose to form the so called *master curve*. This master curve now covers more decades of time (or frequency). Fig. C.1 illustrates this technique.

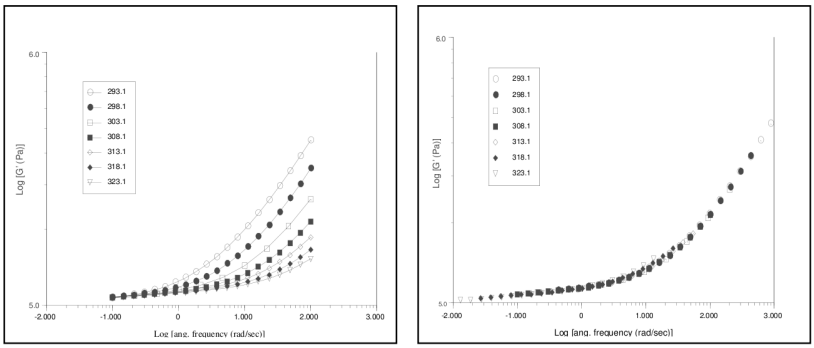

Fig. C.1: Illustration of the time-temperature superposition. The left picture shows the experimental data at different temperatures. The right picture shows the master curve.

This thermorheological simplicity involves that all the viscoelastic mechanisms have the same temperature dependence.

The horizontal and vertical shift factors are traditionally designated by a_T and b_T. b_T is

of the form

$$b_T = \frac{T_0 \rho_0}{T \rho} \tag{C.1}$$

where T is the temperature, ρ is the density and the subscript 0 designates the chosen reference state.

Different models exist for the horizontal shift factor a, amongst them the Arrhenius formulation

$$a_T = \exp\left[\frac{E_a}{R}\left(\frac{1}{T} - \frac{1}{T_0}\right)\right] \tag{C.2}$$

where E_a is called activation energy by analogy with the reaction rate theory in chemistry and R is the universal gas constant. The WLF (from Williams, Landel and Ferry) relationship can be used instead:

$$\log(a_T) = \frac{-c_1(T - T_0)}{c_2 + (T - T_0)} \tag{C.3}$$

where c_1 and c_2 are empirical constants.

More details about the TTS can be found in Dealy and Plazek (2009)

APPENDIX D

DIFFERENTIAL VERSUS INTEGRAL MODEL

This appendix consists in a article accepted for publication in the Journal of Computational and Applied Mathematics (doi:10.1016/j.cam.2009.08.060).

Differential versus integral formulation of fractional hyperviscoelastic constitutive laws for brain tissue modelling.

V. Libertiaux[a,*,1], F. Pascon[a,2]

[a] *Dpt ArGEnCo, University of Liège, Bat. B52, 1 chemin des chevreuils, 4000 Liège - Belgium*

Abstract

For years, interest has been constantly growing up in biological tissues modelling. Particularly, the mechanical study of the brain has become a major topic in the field of biomechanics. A global model of this organ, including a realistic mesh and suitable constitutive laws for the different tissues, would find applications in various domains such as neurosurgery, haptic device design or car manufacturing to evaluate the possible trauma due to an impact.
Several constitutive models have already been designed; regarding the strong strain-rate dependence of the stress-strain curves available in the literature, we decided to describe brain tissue as a viscoelastic medium through the use of the fractional derivation operator. Thanks to this approach, we can derive a convolution-based model with the Mittag-Leffler function as the regularized kernel.

Key words: fractional derivative, brain tissue modelling, viscoelasticity, Mittag-Leffler's functions

1. Introduction

Although the field of brain biomechanics has been investigated for more than 30 years, there is still no consensus within the scientific community on the optimal model for brain tissues. All agree that brain tissues do not behave like elastic solids, though such constitutive laws were used in some works [4],[13],[23]. There are two approaches: the poroelastic one and the viscoelastic one.

The poroelastic theory comes from soil mechanics. Indeed, soils are made of porous materials (partially) filled with water. Since brain is composed of hydrated tissues, authors like Miga [15],[16] followed this approach. According to him, there is indubitably viscoelasticity in brain tissues but a pure viscoelastic description would be limited given the inherent coupling between deformation and hydrodynamic behavior. Using a 20,000

*Corresponding author
Email addresses: vincent.libertiaux@ulg.ac.be (V. Libertiaux), f.pascon@ulg.ac.be (F. Pascon)
[1] F.R.I.A. fellow
[2] Postdoctoral Researcher at the Belgian Funds for Scientific Research (F.N.R.S.)

nodes geometrically realistic mesh of the brain, Miga & al. achieved a 75 to 85 percent predictive capability on the displacements of 20 beads inserted in a pig's brain during a *in vivo* compression test [15].

The literature is more abundant as far as viscoelastic models are concerned. Their strain-rate dependence makes them more likely to model the wide range of behaviors encountered as functions of the loading rate. Unlike poroelastic models which focus on neurosurgical applications only, viscoelastic models have been used in several domains. For examples, Sarron & al. [21] have designed a 2D multi-domain model to study the G loss of consciousness (GLOC) of fighter pilots. Brands & al. [3] focused on the design of a 3D nonlinear viscoelastic constitutive model for brain tissue during impact. They used a differential decoupled 3D constitutive law. Darvish and Crandall [5] proposed a model that agrees with the nonlinear viscoelastic behavior of the brain when subjected to deformation impulses with duration of only a few milliseconds.

Contrarily to the previous authors, Velardi [24] claims that viscous effects can be disregarded in impact loading as they have a limited influence on the short term response of the brain tissue. The model used by Velardi is hyperelastic and takes the anisotropy of the white matter into account.

Miller [17],[18] designed hyperviscoelastic models valid over a wide range of strain-rates in tension and compression. His constitutive equation was implemented in a FE model of human brain. The aim was to study the displacements due to the brain shift at the opening of the skull [25].

2. Notations

$D_t^{(\alpha)}$	Real-order derivative of order α with respect to t
$\mathbf{S}$	Second Piola-Kirchhoff stress tensor
$\mathbf{F}$	Deformation gradient tensor
$\mathbf{C} = \mathbf{F}^T\mathbf{F}$	Cauchy Green tensor
$\mathbf{g}$	Boldface latin letter: tensor quantity

3. Fractional calculus

The origin of the fractional derivative goes back to the end of the 17th century. It was first discussed by l'Hospital and Leibniz in 1695. Although it is not a recent concept, it was not before 1920 that fractional operators were used in a physical framework when Nutting [19] observed that stress relaxation of some materials might be modelled by fractional powers of time. Gemant [12] was the first who suggested explicitly to use fractional derivatives in the constitutive equation. Nevertheless, it is neither usual to deal with an expression such as $\left(\frac{d}{dt}\right)^{\alpha} f(t)$ where α is not an integer, nor to determine its physical meaning, if any.

Amongst the suitable definitions that fit the concept of real-order derivative, the Riemann-Liouville and Grunwald-Letnikov's formulations are the most famous. They can be obtained very easily from repeating the definitions of the n^{th} integral and derivative of a function $f(t)$ respectively. Thus, they write:

Riemann-Liouville

$$D_t^{(\alpha)} f(t) = \frac{1}{\Gamma(-\alpha)} \int_0^t \frac{f(x)}{(t-x)^{(1+\alpha)}}\, dx \tag{1}$$

Grunwald-Letnikov

$$D_t^{(\alpha)} f(t) = \lim_{h \to 0} \left[h^{-\alpha} \sum_{m=0}^{t/h} (-1)^m \frac{\Gamma(\alpha+1)}{\Gamma(\alpha-m+1)\Gamma(m+1)} f(t-mh) \right] \tag{2}$$

where $\Gamma(x)$ is referred to as the Eulerian gamma function :

$$\Gamma(x) = \int_0^\infty e^{-t} t^{x-1}\, dt \tag{3}$$

According to Podlubny [20], both definitions are equivalent for the fractional index p, $0 < p < n$, if the function $f(t)$ is $(n-1)$-times continuously differentiable in the interval $[0, T]$ and if $f^{(n)}(t)$ is summable in $[0, T]$. This property proves to be useful as definition (1) is more convenient for analytical calculus and (2) for numerical evaluation.

Looking at both formulations, it is straightforward that the main difference between classical integer order derivative operator and fractional one is that the latter is non local: all the previous values of the function f are required to compute $D_t^{(\alpha)} f$ at time t. Fractional derivation operators seem thus a good tool to model hereditary materials. Furthermore, the convolution kernel $(t-x)^{-(1+\alpha)}$ in expression (1) clearly exhibits the behaviour of a relaxation function.

The major drawback when dealing with Riemann's (or Grunwald's) operator in the modelling of physical processes is that the derivative of a constant is not zero but rather a real-order power of the independent variable (see [20]). This implies that the use of those operators in the frame of fractional differential equations will lead to impose fractional initial conditions to the problem, which do not have an immediate physical interpretation, unlike integer-order ones. The alternative is then to use another definition of the fractional derivative which returns zero when applied to a constant. The Caputo's derivative has been specifically designed for this. Its definition is given by expression (4)

$$D_t^{(\alpha)} f(t) = \frac{1}{\Gamma(n-\alpha)} \int_0^t \frac{D_x^n f(x)}{(t-x)^{\alpha+1-n}}\, dx, \quad n = \lceil \alpha \rceil \tag{4}$$

with $\lceil . \rceil$ meaning *the smallest integer greater than* .

Till the end of this paper, we will only use Caputo's derivative.

Let us now consider the general form of a linear fractional differential equation (FDE):

$$D_t^{(\alpha_n)} y(t) + \sum_{j=1}^{n-1} p_j(t) D_t^{(\alpha_{n-j})} y(t) + p_n(t) y(t) \quad = \quad f(t) \tag{5}$$

with initial conditions $y^{(k)}(0) = y_0^k, k = 0, 1, 2, \cdots, n-1$.
The first properties to ensure are the existence and uniqueness of the solution. This is the object of the following theorem:

> If $f(t) \in L_1]0,T[$, and $p_j(t)$, $(j = 1, 2, ..., n)$ are continuous functions in the closed interval [0,T], then the initial-value problem (5) has a unique solution $y(t) \in L_1]0,T[$

For more information, please consult [20].

Fractional constitutive models have been studied on a theoretical point of view by Adolfsson, Enelund and Olsson [1], [2]. Freed and Diethelm [8] applied fractional calculus to the modelling of calcaneal fat pad.
The non-local property of fractional derivatives is a difficulty to their direct application in classical incremental finite element codes. Some attempt have been done by Schmidt [22] and Enelund [10]. Techniques to reduce the computational times have been developped: the fixed memory principle (Podlubny [20]), the logarithmic memory principle (Ford and Simpson [11], Diethelm and Freed [9]) and the short memory principle (Deng [6]).

4. Fractional hyperviscoelastic laws

Hyperviscoelastic models have already been used within the framework of brain tissue modelling by Miller [17], [18]. The general from of such laws is written

$$\Phi \quad = \quad \int_0^t f_{rel}(t-\tau) \frac{\partial W_{hyper}}{\partial \tau} \, d\tau \tag{6}$$

where f_{rel} stands for a relaxation function and W_{hyper} for a strain-energy density function. In the case of [17], expression (6) takes the particular form:

$$\begin{aligned} \Phi \quad = \quad & \int_0^t \left\{ \sum_{i+j=1}^{N} \left[C_{ij0} \left(1 - \sum_{k=1}^{n} g_k \left(1 - e^{(\tau - t)/\tau_k} \right) \right) \right] \right. \\ & \left. \frac{\partial}{\partial \tau} \left[(I_1 - 3)^i (I_2 - 3)^j \right] \right\} \, d\tau \end{aligned} \tag{7}$$

Where C_{ij0} are hyperelastic coefficients, τ_k relaxation times and g_k relaxation moduli. N is the order of polynomial in strain invariants and n the number of relaxation terms needed to fit the experimental curves. Miller chose $N = n = 2$ and assumed $C_{ij0} = C_{ji0}$

and $C_{110} = 0$. We will adopt the same assumptions in our work.

The brain is generally considered as an incompressible material. The second Piola-Kirchhoff stress tensor is thus given by:

$$\begin{aligned} \mathbf{S} &= 2\frac{\partial \Phi}{\partial \mathbf{C}} - p\mathbf{C}^{-1} && (8) \\ &= 2\mathbf{S}' - p\mathbf{C}^{-1} && (9) \end{aligned}$$

where p is a unknown hydrostatic pressure to be determined by the boundary conditions and the equilibrium equations. The first term $\mathbf{S}'$ is thus

$$\begin{aligned} \mathbf{S}' = \int_0^t \left\{ \sum_{i+j=1}^{2} \left[C_{ij0} \left(1 - \sum_{k=1}^{2} g_k (1 - e^{(\tau - t)/\tau_k}) \right) \right] \right. \\ \left. \frac{\partial}{\partial \tau} \frac{\partial}{\partial \mathbf{C}} \left[(I_1 - 3)^i (I_2 - 3)^j \right] \right\} d\tau \end{aligned} \quad (10)$$

A differential equation equivalent to (10) can be obtained and is written

$$\ddot{\mathbf{S}}' + \beta \dot{\mathbf{S}}' + \frac{1}{\tau_1 \tau_2} \mathbf{S}' = \mathbf{G}(t) \quad (11)$$

provided that

$$\beta = \frac{1}{\tau_1} + \frac{1}{\tau_2} \quad (12)$$

$$\mathbf{G}(t) = \dot{\mathbf{p}}(t) + \frac{1 - g_1 - g_2}{\tau_1 \tau_2} \mathbf{F}_{\mathbf{p}}(t) \quad (13)$$

$$\mathbf{p}(t) = \sum_{i+j=1}^{2} C_{ij0} \frac{d}{dt} \frac{\partial}{\partial \mathbf{C}} \left((I_1 - 3)^i (I_2 - 3)^j \right) \quad (14)$$

where $\dot{\mathbf{p}}$(t) and $\mathbf{F}_{\mathbf{p}}$(t) are the time derivative and primitive of $\mathbf{p}$(t) respectively.

According to Podlubny [20] and Mainardi [14], the relaxative-oscillative behavior characteristic of second order differential equations can be reproduced using a single fractional-order derivative. The idea is thus to replace equation (11) with a suitable FDE:

$$\mathbf{S}^{\alpha} + b\mathbf{S} = \mathbf{H}(t) \quad (15)$$

where $\mathbf{H}(t)$ has the dimension $ML^{-2}T^{-2-\alpha}$ and is written

$$\mathbf{H}(t) = \dot{\mathbf{p}}(t) + \zeta \mathbf{F}_{\mathbf{p}}(t) \quad (16)$$

The fractional constitutive law for brain tissue then writes:

$$\begin{aligned} \mathbf{S} &= 2\mathbf{S}' - p\mathbf{C}^{-1} \\ D_t^{(\alpha)}\mathbf{S}' + b\mathbf{S}' &= \mathbf{H}(t) \end{aligned} \tag{17}$$

The algorithm used to solve this equation is due to Diethelm, Ford and Freed [7]. Equation (17) can be solved analytically, yielding to

$$\mathbf{S}'(t) = \int_0^t \underbrace{(t-u)^{\alpha-1} E_{\alpha,\alpha}(-b(t-u)^{\alpha})}_{(*)} \, \mathbf{H}(u)\, du \tag{18}$$

where $(*)$ can be interpreted as a relaxation function and $E_{\alpha,\alpha}$ is the Mittag-Leffler function. Expression (18) can then be regarded as a PK2 stress tensor derived from a strain energy density potential.

The convolution kernel in equation (18) is plotted in figure 1 for several values of $\alpha \in]0,2[$. It is immediately noticeable that the strictly decreasing functions obtained for $\alpha \in]0,1]$ present a weak singularity[3] for $u = 0$. However, the integral of the function exists in the sense of Hadamard finite part. As $\mathbf{H}(t)$ is a summable real-valued function and is bounded, integral (18) converges. For $\alpha \in]1,2]$, the functions start from 0 so that a null weight if affected to function g at current time t in the convolution product. Furthermore, they are oscillating for a sufficiently high value of α. Thus, to obtain a good relaxation behaviour, α must be taken in $]0,1]$.

The fractional power $(t-u)^{\alpha-1}$ in equation (18) alters the behavior of the Mittag-Leffler functions which are plotted in figure 2 for serveral values of α in $]0,2[$.

Such functions are better relaxation functions candidates for $\alpha \in]0,1[$: they are strictly decreasing and regular at the origin.

The convolution-based model is thus described by the equations:

$$\mathbf{S}(t) = \mathbf{S}'(t) - p\mathbf{C}^{-1}(t) \tag{19}$$

$$\mathbf{S}'(t) = \int_0^t E_{\alpha,\alpha}(-b(t-u)^{\alpha})\, \mathbf{H}(u)\, du \tag{20}$$

We end up with two original models (17) and (20) counting 5 parameters each. The first one is described by a fractional differential equation which can be solved analytically, resulting in expression (18). This convolution-based model presents a singularity at the origin which might not be satisfying from a physical point of view. That is why we designed a model with a regular kernel, described by equation (20), which cannot be related to a FDE anymore.

[3] Excepted for $\alpha = 1$, for which the classical exponential is retrieved

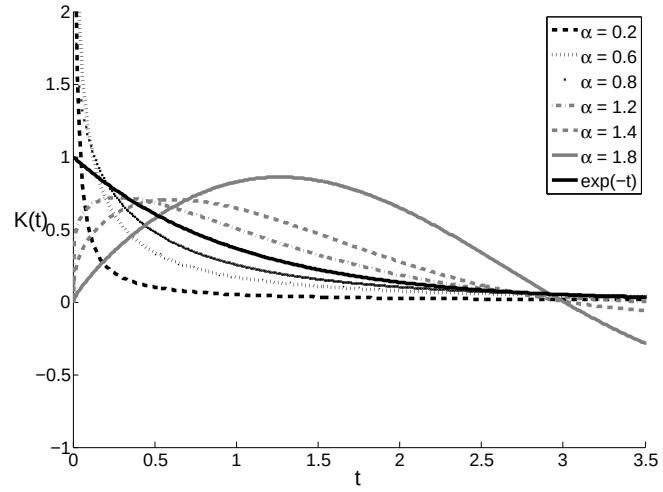

Figure 1: Convolution kernel of the relaxation-oscillation problem for $\alpha \in]0,2[$

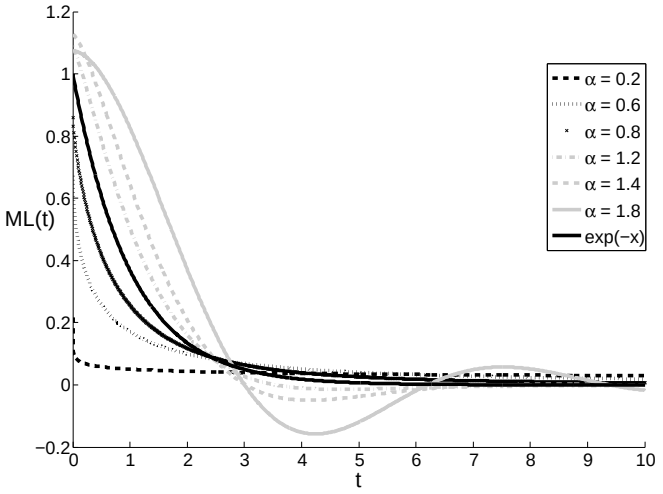

Figure 2: Mittag-Leffler functions $E_{\alpha,\alpha}(-t)$ for various $\alpha \in]0,2[$

5. Results

The parameter identification was achieved through a stochastic optimization (the simulated annealing algorithm). The experimental data come from Miller's unconfined compression tests at fast and medium loading velocities [17]. Let us recall that since we follow Miller's assumptions, there are only two hyperelastic coefficients. The following

values were obtained:

Differential		Convolution-based	
α	0.98	α'	0.7
b	$8.581\ 10^{-3}$	b'	0.011
C_{100}	3463.7	C'_{100}	1159.7
C_{200}	35.908	C'_{200}	100
ζ	$5.042\ 10^{-2}$	ζ'	$0.722\ 10^{-2}$

Table 1: Parameters values for the differential and the convolution-based models.

Figures 3 and 4 show the curves obtained from the models and the experimental data. The differential model presents a better curve fitting than the integral one. It almost perfectly fits the data for the medium loading velocity, while the prediction for the high loading velocity is very good up to a natural deformation equal to -0.25. The convolution-based model also gives a good result for the lower loading velocity but it is quite worse for the faster one. Only one Mittag-Leffler function does not seem to be enough to caracterize the relaxation of brain tissue. It could be possible to add another one with a different characteristic time and/or α but it would increase the computational time.
So, although the convolution formulation presents the advantages to be directly linkable to classical hyperviscoelasticity and to be based on a regular kernel, the differential model should be preferred as far as the curve fitting is concerned. It gives rather good curves fitting on brain tissue samples simple compression tests with the strain-rate varying on two orders of magnitude.

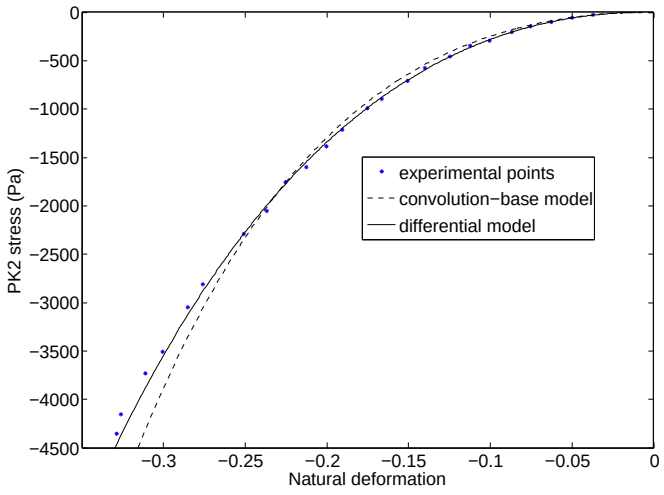

Figure 3: Lagrange stress vs natural strain for the unconfined compression experiment at strain rate $0.64s^{-1}$. The experimental data comes from [17].

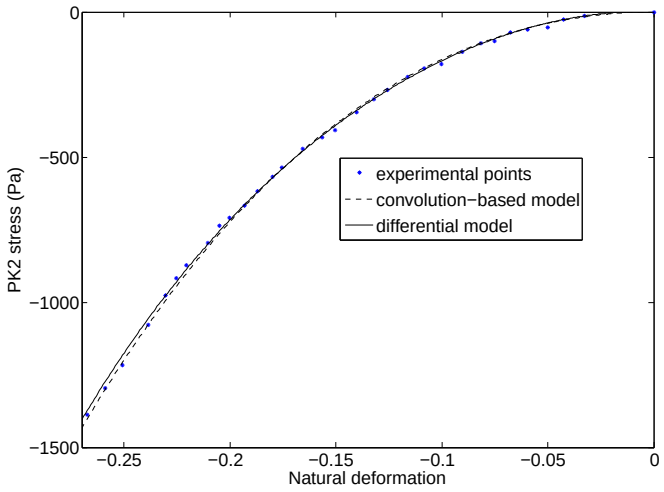

Figure 4: Lagrange stress vs natural strain for the unconfined compression experiment at strain rate $0.0064s^{-1}$. The experimental data comes from [17].

6. Acknowledgements

The authors thank the F.R.I.A. and the F.N.R.S. for the financial support given.

References

[1] K. Adolfsson. Models and numerical procedures for fractional order viscoelasticity. *Chalmers University of Technology*, 2003

[2] K. Adolfsson and M. Enelund. Fractional derivative viscoelasticity at large deformations. *Nonlinear dynamics*, 2003, 33:301-321

[3] D.Brands, G. Peters and P. Bovendeed. Design and numerical implementation of a 3D non-linear viscoelastic constitutive model for brain tissue during impact. *Journal of Biomechanics*, 2004, 37:127-134

[4] O. Clatz. Analysis and prediction of the brain deformation during a neurosurgical procedure. *Master thesis, ENS Cachan*, 2002

[5] K. Darvish and J.Crandall. Nonlinear viscoelastic effects in oscillatory shear deformation of brain tissue. *Medical Engineering and Physics*, 2001, 23:633-645

[6] W. Deng. Short memory principle and a predictor-corrector approach for fractional differential equations. *Journal of computational and applied mathematics*, 2007, 206:174-178

[7] K. Diethelm, N. Ford and A. Freed. A predictor-corrector approach for the numerical solution of fractional differential equations. *Nonlinear dynamics*, 2002, 29:3-22

[8] K. Diethelm and A. Freed. Fractional calculus in biomechanics: a 3D viscoelastic model using regularized fractional-derivative kernels with application to the human calcaneal fat pad. *Biomechanics and Modeling in Mechanobiology*, 2006, 5:203-215

[9] K. Diethelm and A. Freed. An efficient algorithm for the evaluation of convolution integrals. *Computers and mathematics with applications*, 2006, 51:51-72

[10] M. Enelund and G. Lesieutre. Time domain modeling of damping using anelastic displacement fields and fractional calculus. *International journal of solids and structures*, 1999, 36:4447-4472

[11] N. Ford and A. Simpson. The numerical solution of fractional differential equations : speed versus accuracy. *Internal report, Manchester Center of Computational Mathematics*, 2001

[12] A. Gemant. On fractional differentials. *Philosophical Magazine*, 1938, 25:540-549
[13] A. Hault, P. Drazetic and F. Razafimahery. Etudes des phenomenes d'interaction fluide/structure lors d'un choc a l'interieur de la boite cranienne. *17eme Congres Francais de Mecanique*, 2005
[14] F.Mainardi and A. Carpinteri. Fractals and fractional calculus in continuum mechanics. *Springer*, 2006
[15] M. Miga, K. Paulsen, P. Hoopes, F. Kennedy, A. Hartov and D. Roberts. In vivo modelling of interstitial pressure in the brain under surgical load using finite elements. *Journal of Biomechanical Engineering*, 2000,122:354-363
[16] M. Miga, K. Paulsen, P. Hoopes, F. Kennedy, A. Hartov and D. Roberts.
In vivo quantification of a homogeneous brain deformation model for updating preoperative images during surgery. *IEEE Transactions on Biomedical Engineering*, 2000, 47:266-273
[17] K. Miller. Constitutive model of brain tissue suitable for finite element analysis of surgical procedures. *Journal of Biomechanics*, 1999, 32:531-537
[18] K. Miller and K. Chinzei. Mechanical properties of brain tissue in tension. *Journal of Biomechanics*, 2002, 35:483-490
[19] P. Nutting A new general law of deformation. *Journal of the Franklin Institute*, 1921, 191:679-685
[20] I. Podlubny. Fractional differential equations, Ames, W.(ed.). *London Academic Press*, 1999
[21] J. Sarron, C. Blondeau, A. Guillaume and D. Osmont. Identification of linear viscoelastic constitutive models. *Journal of Biomechanics*, 2000, 33:685-693
[22] A. Schmidt and L. Gaul. Application of fractional calculus to viscoelastically damped structures in the finite element method. *Proceedings of the International Conference on structural dynamics modelling*, 2002, 297-306
[23] O. Skrinjar, A. Nabavi and J. Duncan. Model-driven brain shift compensation. *Medical Image Analysis*, 2002, 6:361-373
[24] F. Velardi, F. Fraternali and M. Angelillo. Anisotropic constitutive equations and experimental tensile behavior of brain tissue. *Biomechanics and Modeling in Mechanbiology*, 2006, 5:53-61
[25] A. Wittek, K. Miller, R. Kikinis and S. Warfield. Patient-specific model of brain deformation : application to medical image registration. *Journal of Biomechanics*, 2007, 40:919-929

APPENDIX E

THE Γ FUNCTION

The fractional calculus makes an intensive use of the Γ function. Some of its major properties are presented here.

Defintion

The gamma function $\Gamma(x)$ is defined by the integral

$$\Gamma(x) = \int_0^\infty e^{-t} t^{x-1}\, dt \tag{E.1}$$

This expression is valid for $\Re(x) \in \mathbb{R}_0^+$. The gamma function satisfies the functional equation

$$\Gamma(x+1) = x\Gamma(x) \tag{E.2}$$

The value $\Gamma(1)$ is easily calculated and is equal to 1. Then, using E.2, it comes for $x \in \mathbb{N}$

$$\Gamma(2) = 1\Gamma(1) = 1 = 1! \tag{E.3}$$
$$\Gamma(3) = 2\Gamma(2) = 2.1! = 2! \tag{E.4}$$
$$\Gamma(4) = 3\Gamma(3) = 3.2! = 3! \tag{E.5}$$
$$\vdots \tag{E.6}$$
$$\Gamma(n+1) = n\Gamma(n) = n.(n-1)! = n! \tag{E.7}$$

The gamma function thus interpolates the factorial operator for non integer values of x. Eqn. E.2 is also useful to compute $\Gamma(x), \Re(x) \in \mathbb{R}^-$.

Another property of the gamma function is that is has simple poles at the points $x = -n, n \in \mathbb{N}$. The demonstration requires to write $\Gamma(x)$ in the form :

$$\Gamma(x) = \int_0^1 e^{-t}t^{x-1}\,dt + \int_1^\infty e^{-t}t^{x-1}\,dt \tag{E.8}$$

The first integral in E.8 is evaluated by using the series expansion for the exponential function:

$$\int_0^1 e^{-t}t^{x-1}\,dt = \int_0^1 \sum_{k=0}^{\infty} \frac{(-t)^k}{k!}t^{x-1}\,dt \tag{E.9}$$

$$= \int_0^1 \sum_{k=0}^{\infty} \frac{(-1)^k}{k!}\int_0^1 t^{k+x-1}\,dt \tag{E.10}$$

$$= \sum_{k=0}^{\infty} \frac{(-1)^k}{k!(k+x)} \tag{E.11}$$

The second integral defines an entire[1] function of the complex variable x. Indeed, let's define $\varphi(x)$ by

$$\varphi(z) = \int_1^\infty e^{-t}t^{x-1}\,dt \tag{E.12}$$

$$= \int_1^\infty e^{(x-1)\log(t)-t}\,dt \tag{E.13}$$

Let $\mathcal{D}$ be an arbitrary bounded closed domain in the complex plane ($x = a + \imath b$) and denote $a_0 = \max_{x\in\mathcal{D}} \Re(x)$. Then, the following relations holds :

$$\left|e^{-t}t^{x-1}\right| = |e^{(x-1)\log(t)-t}| \tag{E.14}$$

$$= |e^{(a-1)\log(t)-t}|\,|e^{\imath b\log(t)}| \tag{E.15}$$

$$= |e^{(a-1)\log(t)-t}| \tag{E.16}$$

$$\leq e^{(a_0-1)\log(t)-t} \tag{E.17}$$

$$\leq e^{-t}t^{a_0-1} \tag{E.18}$$

And thus, the integral E.12 converges uniformly on $\mathcal{D}$. As this domain was chosen arbitrarily, the function $\varphi(x)$ is then an entire function in the whole complex plane.

Bringing togheter the preceding results, we can finally express the gamma function as

$$\Gamma(x) = \sum_{k=0}^{\infty} \frac{(-1)^k}{k!(k+x)} + \int_1^\infty e^{-t}t^{x-1}\,dt \tag{E.19}$$

$$= \sum_{k=0}^{\infty} \frac{(-1)^k}{k!(k+x)} + \text{ entire function} \tag{E.20}$$

It appears evident now that $\Gamma(-n), n \in \mathbb{N}$ are simple poles.

[1] A complex function is said to be *entire* if it is analytic at all finite points of the complex plane $\mathbb{C}$